UNIVERSITY OF CALIFORNIA
Santa Barbara

Interfacing Defect Qubits with Nanophotonics in Silicon Carbide

A dissertation submitted in partial satisfaction
of the requirements for the degree of

Doctor of Philosophy

in

Physics

by

Gregory Richard William Calusine

Committee in charge:

Professor David D. Awschalom, Chairperson

Professor Ania Bleszynski Jayich

Professor Chetan Nayak

December 2014

The dissertation of Gregory Richard William Calusine is approved:

Ania Bleszynski Jayich

Chetan Nayak

David D. Awschalom
Committee Chairperson

October 2014

Interfacing Defect Qubits with Nanophotonics in Silicon Carbide

by

Gregory Richard William Calusine

To my wife, Kate

without whom none of this would have been possible

Acknowledgments

First of all, I'd like to thank Professor David Awschalom for providing me with the opportunity to work in his group. His approach to research and developing young scientists produces a unique environment where new ideas are encouraged and scientific boundaries are stretched with regularity. His fearlessness and zeal at starting up new, cutting-edge projects using a wide variety of experimental techniques is an inspiration to scientists everywhere, especially within his group. I'd also like to thank him for all his support over the years, especially after moving to Chicago.

Second, I'd like to thank my committee members for taking time out of their busy schedules to serve on my committee and provide feedback. A special thanks goes out to Professor Ania Bleszynski Jayich for helping alleviate the loneliness that resulted from the Chicago move by allowing me to attend her group meetings.

Third, I'd like to thank all of the people I worked with directly over the years. Roberto Myers provided me with my introduction into the lab and helped me figure out how to get started in the world of spin physics research. Shawn Mack supplied me with many samples, doses of wisdom, and bits of comradery during our frustrating attempts to figure out what was going on with Mn spins in GaAs quantum wells. Will Koehl, often described as the intersection of physics and (quantum?) baller-dom, introduced me to the captivating puzzle of background literature on defects in wide band-gap semiconductors and never failed to keep me company on the way to my car after a long day. Bob Buckley was always there for a helpful conversation, whether on the topic of classes, research, or life. I am incredibly thankful to have had him around for my time at UCSB

and consider him a dear friend. Joe Heremans was a great asset to have around, especially for his keen eye for design and many helpful CAD drawings. Abram Falk was extremely helpful during our painful search for 'dirt centers' and shows a remarkable ability to always keep pushing a project forward. Alberto Politi was absolutely essential to our development of 3C SiC photonics and provided me with an insider's guide to Italian food and culture, which I would eventually find to be indispensable during my honeymoon in Italy.

I'd also like to thank the many coworkers I overlapped with and/or lived with during my time in the Awschalom lab. Brian Maertz was always there for me to commiserate about broken equipment and was never bitter after I defeated him in a wrestling match and/or watermelon fight. David Toyli always provided much needed no-nonsense viewpoints on research and I will be forever in awe at his combination of a deep grasp of science and remarkable ability to thoroughly plan every aspect of a project (one of the most difficult scientific skills to acquire!) David 'Raccoon Whisperer' Christle instigated many enjoyable lab shenanigans and provided me with many deep insights during our scientific discussions whenever I found a new bit of information and was all like 'I don't know what that is, I've never seen that...". Andrew Yeats has always impressed me with his resourcefulness and technical prowess, but I will never forgive him for eating all my danishes or for getting rid of my beloved pool table. Paolo Andrich may possibly be the nicest guy I've ever met, is an incredibly dedicated researcher, and is perhaps the only European fan of American football in the world. I am indebted to Amit Vainsencher for his fab advice and frank perspectives on research in general. Paul Klimov has always impressed me with his ability to work hard and play hard and his intense drive to produce

successful research. Felix Mendoza gave me some of my early introductions to the lab and was always there to lament about Philly sports with me. Greg Fuchs provided a lot of helpful scientific insight early on in my grad school career. Lee Bassett also provided some helpful scientific insight later on in my grad school career, in addition to teaching me his 'Lee Bassett Weightlifting Regimen.' Benji Aleman always provided much enthusiasm and gave me a lot of helpful encouragement throughout his time here. Last but not least, Joerg Bochmann inspired me with his deep drive to develop a thorough understanding of science and produce top-notch research and provided me with some of the most frank and helpful career advice I've received.

There were many members of the lab I intersected with less who I want to thank for their company, insight, and technical assistance: Viva Horowitz, Mark Nowakowski, Jesse Berezovsky, Chris Yale, Charlie de las Casas, Ken Ohno, Maiken Mikkelson, Nate Stern, David Steuerman, and Jayna Jones.

I sincerely hope that everyone I've mentioned (or possibly forgotten to mention) finds success and happiness in whatever they end up doing in their lives and careers.

For fear of forgetting someone I won't name everyone, but I'd like to thank my many classmates and friends who made my time in Santa Barbara enjoyable.

I'd also like to recognize and thank the many UCSB staff who provided invaluable help in navigating the labyrinth that is purchasing, grants, payroll and the like: David Prine, Dan Stack, Lynne Leininger, Daniel Daniels, Eva Deloa, Sonya Perez, and Stella Hahn. I especially want to thank Holly Woo for always providing the clearest path towards getting things done,

for encouraging me every step along the way, and for many enjoyable conversations. Research in our lab could not have progressed in the manner it did without her invaluable help.

Many of the cleanroom staff were crucial for their assistance in developing and troubleshooting the various processes we used to prepare samples: Adam Abrahamsen, Tony Bosch, Don Freeborn, Aidan Hopkins, Bill Mitchell, Brian Thibeault, Ning Cao, Bob Hanson, Lizzie Slaughter, and Peter Duda. These are the people behind the scenes of much of the successful research that UCSB has produced in engineering and the sciences.

I want to thank Glenn Schiferl and Rick Barber for their IT support throughout the years and for putting up with my uninformed IT questions. Paul Weakliem was crucial to my research through his assistance in setting up access to simulation software on the CNSI cluster. I wish to thank him wholeheartedly for his help and putting up with my badgering.

The UCSB physics machine shop staff also provide an invaluable service to the research community and deserve recognition for their contributions: Jeff Dutter, Doug Rehn, Mark Sheckherd, Mike Wrocklage, Guy Patterson, and Andy Segale.

I also want to recognize Mike Deal for his immense dedication to the thankless job of keeping Broida and PSBS up and running, despite UCSB Facilities' desire to destroy them. Mike showed an unparalleled dedicated to his job, including showing up in the lab at 2 AM one night out of concern for a failure in the air handling system. Without him, our research would have ground to a halt many, many times.

I'd like to give a special thanks to the companies who sold me products that actually worked the way they said they would. One can only dream of a day when every manufacturer of scientific equipment pursues

such high standards. I'd also like to thank Rick in New Jersey.

I want to thank my family for their support and love throughout my time in Santa Barbara, even despite the cross-country distance and my limited ability to visit them regularly. They have provided me with so much over the years that I can't appropriately put in words how grateful I am for them.

Lastly, I want to thank my beloved wife Kate. She deserves to be a co-author on everything I've ever produced because I simply could not have gotten to this point in my life without her. I love her dearly and am eternally in her debt for all the love and support she provided over the years.

Vitæ

Education

2007 B.A., Physics, University of Pennsylvania

2013 M.A., Physics, University of California, Santa Barbara.

2014 Ph.D., Physics, University of California, Santa Barbara.

Publications

"Cavity enhanced measurements of defect spins in silicon carbide photonic crystal cavities," G. Calusine, A. Politi, and D. D. Awschalom, (*in preparation*).

"Silicon carbide photonic crystal cavities with integrated color centers," G. Calusine*, A. Politi*, and D. D. Awschalom, *Applied Physics Letters* **105**, 011123 (2014).

"Electrically and mechanically tunable electron spins in silicon carbide color centers", A. L. Falk, P. V. Klimov, B. B. Buckley, V. Ivady, I. A. Abrikosov, G. Calusine, W. F. Koehl, A. Gali, and D. D. Awschalom, *Phys. Rev. Lett.* **112**, 187601 (2014).

"Polytype control of spin qubits in silicon carbide," A. L. Falk, B. B. Buckley, G. Calusine, W. F. Koehl, V. V. Dobrovitski, A. Politi, C. A. Zorman, P. X.-L. Feng, and D. D. Awschalom, *Nat Commun* **4**, 1819 (2013).

"Engineering and quantum control of single spins in semiconductors," D. M. Toyli, L. C. Bassett, B. B. Buckley, G. Calusine, and D. D. Awschalom, *MRS Bulletin* **38**, 139-143 (2013).

"Room temperature coherent control of defect spin qubits in silicon carbide," W. F. Koehl, B. B. Buckley, F. J. Heremans, G. Calusine, and D. D. Awschalom, *Nature* **479**, 84-87 (2011).

Fields of study

Major field: Physics

Interfacing Defect Qubits with Nanophotonics in Silicon Carbide

Professor David D. Awschalom

Abstract

Interfacing Defect Qubits with Nanophotonics in Silicon Carbide

by

Gregory Richard William Calusine

Defect based qubit systems like the nitrogen vacancy center in diamond have recently emerged as promising candidates for quantum technologies due to their combination of long coherence times, room temperature operation, and robust optical interface. In order to realize many of their proposed applications, defect qubits must be incorporated into scalable devices architectures consisting of photonic, mechanical, or electrical degrees of freedom. Despite much recent progress, many challenges remain for diamond growth and device fabrication. As an alternate approach, we engaged in a search for nitrogen vacancy center analogues in alternative materials with the hope of obtaining a greater degree of control over defect and material properties. Ultimately, we discovered that divacancy-related point defects in all three of the most common forms of silicon carbide- termed 4H, 6H, and 3C- act as analogues to the nitrogen vacancy center in diamond. We chose to focus our research primarily on defects in 3C silicon carbide (termed 'Ky5' defects) because of its availability as a single crystal heteroepitaxial thin film grown on silicon, an advantage that

greatly facilitates the fabrication of functional devices. We characterized the spin and optical properties of Ky5 defects in thin film geometries and observed many similarities to the nitrogen vacancy center. We performed the first measurements of spin dynamics in 3C silicon carbide and demonstrate coherent control of defect spins up to room temperature and observe coherence times of up to T_2 =22 μs.

To demonstrate their use in real devices, we designed, fabricated, and characterized photonic crystal cavities in 3C silicon carbide thin films with mode volumes of less than $(\lambda/n)^3$ and Q's as high as 1,500 with integrated Ky5 defects. Additionally, we performed simulations and analysis of the fabricated structures using observed structural imperfections to determine that the Q's are likely limited primarily by the non-vertical structure sidewall angle. Despite the modest Q's of these structures, they can be utilized to generate large local field intensities to enhance optical interactions with Ky5 qubit states within the cavities. We accomplish this by performing cavity enhanced photoluminescence excitation spectroscopy on cavity modes tuned to the zero phonon line of the defects and observe large (as high as 30x) increases in the luminescence and optically detected magnetic resonance signals originating from the defect states and ~2x faster rates of ground state spin initialization. In addition, we use these techniques to probe the photoluminescence dynamics of the Ky5 defects' optical pumping cycle, perform excitation wavelength dependent studies of spin and spectral inhomogeneity, and use the small mode volume and narrowband photoluminescence enhancements of the cavities to observe spectrally distinct subensembles of defects with linewidths as narrow as 25 GHz within the inhomogeneously broadened zero phonon line. Although much is still unknown regarding the properties of these defects, they show great promise

as a candidate system for defect qubit based quantum devices and technologies.

Contents

List of figures

List of tables

Chapter 1

Introduction

1.1 Why Do We Care About Quantum Systems?

Technologies based on quantum systems represent one of a few potential future hardware advances that could revolutionize information technology. As many types of computing hardware matured at the end of the 20th century, they became commodities rather than specialized products, and, as a result, much of the manufacturing base shifted to regions other than North America. Due to this economic shift, many historically relevant information technology companies ceased to fund aggressive, cutting edge basic research and the famous private research labs that were responsible for so many basic scientific and technological advances either received

smaller funding streams or were shuttered altogether. With the end of Moore's Law seemingly in sight, some policy makers are finally starting to do more than just pay lip service to the goal of pressing modern technology forward. As a result, many new directions for future technologies are currently being explored.

The development of quantum technologies has the potential to provide one route for expanding the capabilities of future technologies. On one hand, current cutting edge electronics and photonics hardware are reaching the limits of size and powers where quantum effects become important. On the other, quantum devices exhibit drastically different functionalities that are completely foreign to current technological paradigms. Most notably, quantum computers have the potential to threaten RSA key encryption security protocols[1] and quantum key distribution has the potential for perfectly secure communication protocols.[2] Many of the candidate systems with potential to realize these technologies have reached a high level of maturity and now the goal remains to develop them into forms that can proliferate throughout society.

The production of interacting ensembles of individually controllable quantum systems also has the potential to revolutionize basic science. Sensors based on quantum technologies show strong potential for enhanced

sensitivities and imaging applications.[3] [4] [5] Quantum simulation has reached a very high level of maturity, particular for simulating difficult to realize condensed matter Hamiltonians in atomic optical lattices.[6] [7] Generally, this highlights one of the recurring themes anytime a new technology starts to reach maturity: while it is clear that the new functionalities are likely to be useful for *something*, what that something is is difficult to predict.

1.2 Candidate Systems

Ever since the field of quantum information science first rose to prominence, many systems have been investigated as candidates for quantum technologies. Here is a brief list of some of the most prominent systems and their advantages/disadvantages:

- NMR systems: One of the first systems to realize quantum information protocols was ensembles of nuclei interacting through electron mediated coupling in molecules.[8] This system's advantages were its relative simplicity and long coherences times. However, it is not easily scalable past what has been previously demonstrated and requires thermalization in a large magnetic field for state initialization.
- Optically active quantum dots: Self assembled quantum dots in III-

V materials have long shown promise for quantum applications due to their strong transition dipole moments (10-100 Debye) and fairly easy incorporation into III-V devices like diode structures and optical cavities.[9] [10] Achieving strong coupling to an optical cavity in these systems is fairly pedestrian at this point. However, these systems suffer from scalability problems due to the inability to controllably pattern high quality emitters and additionally tend to have short coherences times relative to other systems.

- Photons: Many early quantum information schemes were first demonstrated using photons. Photons are advantageous due to their extremely long coherence times (typically set by an effective T_1 that results from optical losses) and ease of single qubit gates (waveplates). Additionally, advances in integrated photonics have greatly reduced the footprint of the necessary hardware [11]. However, as usual, their very weak interactions that yield advantages in terms of coherence make it extremely difficult to implement multi-qubit gates.
- Superconducting qubits: Superconducting qubits are currently the most likely candidate for actually building a quantum computer due to their advantages of conventional fabrication, easy scalability, control over almost every parameter of the qubits and their interactions,

and the purely electrical means by which they are manipulated.[12] Their only disadvantages are actually not that pressing; the requirement for low temperature and the size of the devices. Due to recent advances in dilution refrigerator technology, these issues aren't a significant impediment to progress.

- Trapped ions: Trapped ions have been a mature quantum technology for a long time, culminating recently in the Nobel Prize being awarded to Dave Wineland, a leader in the field (along with Serge Haroche for his work on Rydberg atoms). Trapped ions have very mature protocols for most criteria for a quantum technology and have even recently been scaled up to 14 qubit systems and have demonstrated some basic few-body quantum simulations.[7] However, challenges in incorporating wafer-based electrodes in UHV chambers may prevent easy scaling to larger numbers of qubits.
- Neutral atoms: Neutral atoms have been utilized recently both for basic quantum networking protocols [13] and as ensembles in optical lattices for quantum simulation of condensed matter Hamiltonians [6]. They are a very mature system and exhibit long coherence times but unfortunately also requires UHV chambers and complex laser systems that may prevent easy scaling.

- NV centers and divacancies: Quantum applications of NV center-like systems will be the focus of this work and will be discussed in detail later.
- Electrostatically gated quantum dots: These systems are relatively simple in that they are formed from gating 2 dimensional electron gases to form localized puddles of electrons [14]. They have the advantages of purely electrical control and a very mature understanding of the corresponding physics, but suffer from short coherence times and geometrical constraints on control lines. However, the recent realization of SiGe based quantum dots seems to have solved some of the problems with short coherence times.[15]
- Electron and nuclear spins in silicon: Electronic and nuclear states in silicon exhibit extremely long coherences times and have the huge advantage of being CMOS compatible.[15] However, developing schemes to scale to multiple interacting qubits has been a challenge.
- Others: There are many other candidate systems that play some role in quantum information applications, including rare-earth ions [16], newly investigated dopant systems in a host of varied materials [17], and mechanical devices [18]. See many of the above reviews for references to these systems or see [19].

Although some systems mentioned above seem to be the most relevant for certain applications like quantum cryptography or quantum computing, future likely technologies may require the use of multiple systems in order to utilize each system's advantages and overcome problems resulting from their disadvantages. As a result, much recent work has pushed towards finding ways to interact disparate systems in controlled, scalable ways.

1.3 Why Solid State?

Solid state systems afford distinct advantages over other types of candidate quantum systems, primarily in terms of scaling. One driving force for this is the possibility of using existing semiconductor infrastructure to generate large scale or large volume implementations of quantum technologies. Outsourcing hardware generation in the way the electronics and photonics industries have done can save time, money, and lead to more reproducible outcomes and this has led some of the traditionally 'bulky' systems like quantum optical networks [20] and trapped ion systems [21] to be realized in compact forms that can be generated by hardware 'foundries'. Modularity also helps significantly for scaling; most cleanroom processes can be just as easily used to generate thousands of sub-systems as they can generate one. I found this to be a particularly compelling argument when

I heard Professor John Martinis, an expert in superconducting qubits, remark in a talk: "Now that I've talked about one qubit, how do we add more qubits? We use L-Edit!" This is in stark contrast to systems like the NV center and single photon qubits where the production of multiple, interacting qubits is exceedingly difficult. Furthermore, the compact nature of solid state systems typically allows for enhanced spatial resolution and mitigates practical challenges, especially for sensors. [3]

However, solid state systems come with their own challenges. Inhomogeneity is often a big problem induced by interactions with the extra 'stuff' around. Under the right conditions in a UHV chamber, almost every rubidium-87 atom is identical; producing two identical quantum dots or NV centers is a huge outstanding challenge in solid state quantum information. Semiconductor lattices often act as an artificial 'vacuum' for solid state qubits but unfortunately no crystal is perfect and this has consequences for scaling these systems. Furthermore, many qubits that rely on solid state systems suffer from charge fluctuations at surfaces or within the bulk, leading to both static and non-static fields that degrade qubit performance. Still, for many technologies the benefits of solid state implementations outweigh the costs.

1.4 Basics of Quantum Information

The basic units of the physics of quantum information are the two-level system and the harmonic oscillator state (or Fock state). A wise young professor who was teaching a class I attended once made the frank statement (paraphrased): "Almost everything in physics can be described as either a two level system or a harmonic oscillator. You can get pretty far by knowing only these two systems and how they interact." Developing an understanding of these two systems was crucial to the development of quantum mechanics; two level systems (or, spin) were elucidated by the famous Stern-Gerlach experiments and consideration of quantized harmonic oscillator modes led to the resolution of the Ultraviolet Catastrophe that had plagued modern physics in the early 20th century. In terms of quantum information science, these two systems make up the basic building blocks of a 'quantum computer', 'quantum sensor', or a 'quantum network'.

Two level systems are generally described as a superposition of two distinct states

$$| \psi \rangle = \alpha \, |\uparrow\rangle + \beta \, |\downarrow\rangle \tag{1.1}$$

where the 'up' and 'down' states are the usual eigenstates of the Hamilto-

nian

$$\frac{\hbar\omega_0}{2}(|\uparrow\rangle\langle\uparrow| - |\downarrow\rangle\langle\downarrow|) \tag{1.2}$$

with an energy splitting of $E = \hbar\omega_0$. These states can consist of any number of two-level systems (including harmonic oscillator states if anharmonicity is added to the system to produce an un-even splitting in the 'ladder states', as is typically done with superconducting qubits), although the most common example is a spin $\frac{1}{2}$ state with a splitting given by:

$$E_{\pm} = \pm\frac{1}{2}g\mu_B\hbar B_z \tag{1.3}$$

In equation 1.1, α and β are typically complex numbers and can be parameterized by two values θ and ϕ in the following manner:

$$|\ \psi\ \rangle = \cos\frac{\theta}{2}\ |\uparrow\rangle + e^{i\phi}\sin\frac{\theta}{2}\ |\downarrow\rangle \tag{1.4}$$

This depiction in terms of angles provides a convenient picture by which we can think of two level systems that is typically termed the 'Bloch Sphere' and is depicted in Figure 1.1.

One of the defining aspects of quantum mechanics that leads to all sorts of interesting behavior and uses for computing is the concept of a superposition state mentioned above. In brief, this is what allows for the speed up in computation time afforded by a quantum computer or simulator: instead of just performing operations on a single input, one is

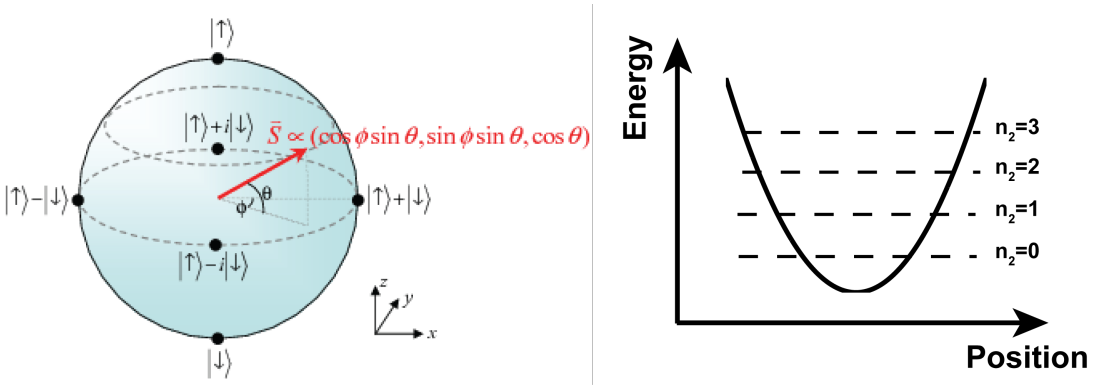

Figure 1.1: The 'Bloch Sphere' (left) and harmonic oscillator potential and energy level structure(right)

performing parallel operations on multiple superimposed states and generating non-classical correlations ('entanglement') that simply does not exist for classical systems.[1] This is a large driving force behind identifying and manipulating quantum two level systems.

Harmonic oscillator states generally describe bosonic modes and are described as a 'ladder' of number or 'Fock' states shown in Figure 1.1 and described as:

$$| \psi \rangle = | n \rangle \tag{1.5}$$

where n is a number corresponding to the eigenstate of the Hamiltonian and energy spectrum given by:

$$H = \hbar\omega(a^\dagger a + \frac{1}{2}) \Rightarrow E_n = \hbar\omega(n + \frac{1}{2}) \tag{1.6}$$

The operators a and $a^\dagger$ are mathematically described by the following

relations and can generally be thought of as operators that add or subtract quanta from the Fock state:

$$a^\dagger \mid n \rangle = \sqrt{n+1} \mid n+1 \rangle \qquad a \mid n \rangle = \sqrt{n} \mid n-1 \rangle \tag{1.7}$$

The systems that are most widely described as harmonic oscillator states are optical modes, vibrational modes of interacting ions, or mechanical modes of a MEMs or NEMs stucture. While there are schemes where these types of systems act as qubit states, they are more commonly used as a means of mediating interactions between two level systems.[22] [7]

The Hamiltonian describing the fundamental interaction between a two-level system (here described as 'e' instead of $\uparrow$ to draw connections to an excited electronic state) and a harmonic oscillator mode is given by the ubiquitous Jaynes-Cummings Hamiltonian:

$$\begin{aligned} H =& H_{atom} + H_{field} + H_{int} \\ =& \hbar\omega_0 \mid e\rangle\langle e \mid + \hbar\omega_0 \, a^\dagger a + i\hbar\Omega \left(\mid e\rangle\langle g \mid a- \mid g\rangle\langle e \mid a^\dagger \right) \end{aligned}$$

This Hamiltonian is the starting point for understanding the vast majority of processes involved in quantum information systems, including coherent manipulation ('Rabi oscillations'), spontaneous emission, enhancements of spontaneous emission (the 'Purcell effect'), and coherent interactions between two-level systems and discrete optical modes (the 'strong coupling'

regime).

1.5 Organization

This thesis is organized as follows: Chapter 2 will give a general introduction to creating, manipulating, and measuring defect qubits and a few example applications of defect qubit systems. Chapter 3 will describe the basic physics of the diamond nitrogen vacancy center, currently the most promising defect qubit candidate and the model system whose physics forms the basis for our search for other defect qubit candidates in more technologically amenable materials. Chapter 4 will describe this search and the initial studies on divacancies in 4H and 6H silicon carbide. Chapter 5 will describe work done in discovering and characterizing a defect qubit candidate, the Ky5 divacancy-related center, in 3C silicon carbide, a material whose primary advantage over others is its availability as a heteroepitaxial thin film on silicon. Chapter 6 will describe our initial demonstration of functional devices in 3C SiC with integrated defect qubits: photonic crystal cavities with incorporated Ky5 centers. Chapter 7 will describe recent work on using our previously fabricated and characterized photonic crystal cavities to enhance measurements of Ky5 defect qubits. Chapter 8 will summarize the work presented in this thesis and

discuss future directions and challenges for defect qubit applications.

Chapter 2

General Defect Qubit Properties and Applications

2.1 General Introduction to Defects

The study of defects has a long history within condensed matter physics. Since progress in solid state physics has often run parallel to corresponding progress in material science, many of the issues related to residual defects in otherwise perfect crystal lattices have been relevant to the physics community. Also, since defects often play an important role in real world devices, the study of device physics inevitably includes considering the role of near-band and deep level states induced by point defects. Much of this research is aimed towards eliminating defects that have deleterious effects on bulk electronic properties. However, some research has focused

on the intentional incorporation of defects, typically for optics applications. The first laser relied on optical transitions of point defects (chromium) in sapphire (also know as Ruby). Also, many currently used laser technologies rely on localized defects in host lattices such as titanium in sapphire and neodymium in Yittrium Aluminum Garnet. Erbium doped fiber amplifiers play an important role as optical signal repeaters for the modern telecommunications industry. Similarly, it goes without saying that the modern semiconductor industry would not exist if not for controllable introduction and knowledge of shallow dopant states (donors and acceptors).

In more recent years, the field of quantum information has turned to a few defect systems as candidates for new quantum technologies. The diamond nitrogen vacancy center is one such candidate and this system, along with its recently discovered analogues in silicon carbide, will be discussed at length later. Other systems that have been explored for their quantum applications are bound electrons in III-V materials[23], which are advantageous due to the engineerability of III-V systems, phosphorus donors in silicon, which shows remarkably long coherences times [24], and rare earth ions, which are capable of storing single photon states for significant periods of time[25].

We shall primarily focus on deep level defects. These systems usu-

ally exhibit energy levels far removed from the conduction or valence band edges such that they are typically incapable of being easily ionized to or from states within the bands. They typically fall into one of two categories: intrinsic and extrinsic point defects. Intrinsic defects typically consist of defects or defect complexes made up of constituents that are inherently present to the lattice. These can include antisites, interstitials, vacancies, divacancies, vacancy-antisite complexes, so on. Extrinsic defects involve atomic species that would not be present in a perfect material. Any dopant fits this requirement and these dopants can often join with intrinsic defects to form complexes (like the NV center, for instance). Extrinsic defects are generally a bit easier to study because they can be more easily correlated with how a material has been treated. However, sometimes even the purest material contains residual quantities of extrinsic defects. For instance, chromium is frequently found in even the purest sapphire and magnesium oxide wafers due to the incorporation of chrome in stainless steel.

Defects are typically studies using a number of tools. Here is an abbreviated list of the most commonly used techniques:

- Electron transport: deep level defects often play the role of charge traps that can affect the ability of electrons to move through band

states within a semiconductor.

- Electron Paramagnetic Resonance: this technique is commonly used to characterize the net spin of the defect state.
- Deep Level Transient Spectroscopy: this method is frequently used to determine the position of states within the gap by measuring temperature dependent capacitance changes.
- Optics: if defects are optically active, they can be studied through photoluminescence, absorption, or other forms of spectroscopy.
- Density Functional Theory: this theoretical tool is often the best and sometimes only method of calculating defect properties.
- Group Theory: point group symmetries can often be used to characterize system level degeneracies and predict optical spectra by restricting selection rules.

In general, these methods are used to fully characterize the defect properties to determine the level structure within the host band gap, determine the charge state of the system, study its spin properties, characterize optical properties, or to consider the likely stability of a given defect species.

2.2 Defect Creation

A large body of literature exists that is devoted to studying the controlled creation of point defects in a variety of materials. These studies were largely motivated by the impetus to eliminate defects in order to produce high quality semiconducting and insulating materials for electronics applications. Thankfully, this body of knowledge also benefits researchers attempting to intentionally incorporate defects as candidates for defect qubits. I will focus the discussion on the two primary method by which researchers intentionally produce intrinsic and extrinsic defects: high energy electron irradiation and ion implantation. However, it should be noted that there exist a number of more or less exotic approaches. These include intentional and unintentional incorporation during growth, neutron irradiation (if you have a spare nuclear reactor lying around, which many former soviet republics do), and high temperature approaches like diffusion and additive coloration (heating a binary crystal in an overpressure of one of the constituent atoms).

Electron irradiation is the most typical method used for producing low densities of defects suitable for the isolation of single sites. The interactions of high energy electrons with solid materials is a fairly well understood process and several tools exist for determining the relevant process param-

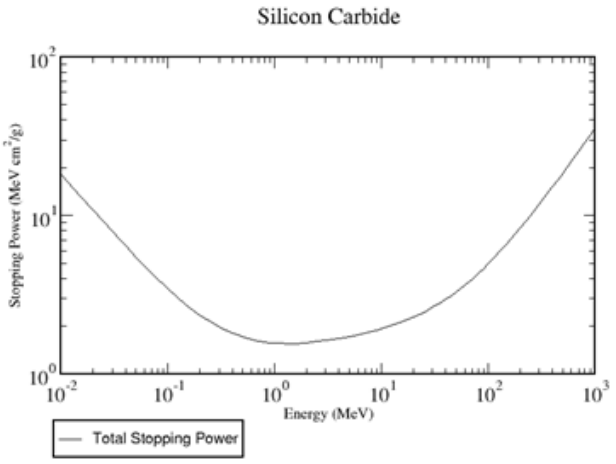

Figure 2.1: High energy electron stopping power vs. energy for silicon carbide.

eters, including the ESTAR database[26] and CASINO[27]. The ESTAR database is a calculation tool for determining the stopping power of a given material when exposed to an electron beam of a given energy. An example plot for silicon carbide is show in Figure 2.1.

The important point to take away from the plot is the window of relatively small change in energy of the beam from 1 to 10 MeV. In this window, the beam generally passes straight through the material with a uniform chance of interaction, thus producing an isotropic distribution of damage events within the crystal. Typically, we use facilities that utilize beam energies of 2, 5, or 10 MeV to produce doses of 10^{13} to 10^{15} electrons per square centimeter in order to produce isolated single defects distributed evenly throughout the crystal depth, although recent work on delta doping

has allowed for controllable depth localization of NV centers[28]. Achieving higher doses can be more difficult as beam currents are typically kept low in order to reduce effects from local heating. Accordingly, doses in the 10^{17} to 10^{18} range can cost upwards of 10,000 dollars at a commercial irradiation facility. In order to achieve these high doses at a reasonable cost and turnaround time, we implemented our own electron irradiation setup in the UCSB Free Electron Laser (FEL). The FEL uses a 6 MeV electron beam with a current capable of producing a 10^{18} electron dose with in approximately 10 hours. See Figure 2.2 and Figure 2.3 for images of the setup. While preliminary work was done to characterize the system, it was never used exhaustively for defect production.

In contrast, CASINO yields energy loss distributions typically for lower energies that produce damage dependent on depth within the crystal based off of Monte Carlo simulations of defect scattering trajectories(see Figure 2.4). This information is primarily useful for the potential application of the typically 300 keV electron beams found in transmission electron microscopes for controllable patterning of defects within a thin film[29]. In particular, if the defects can be produced without subsequent annealing[30], this could enable deterministic patterning of single site defects on the nanoscale.

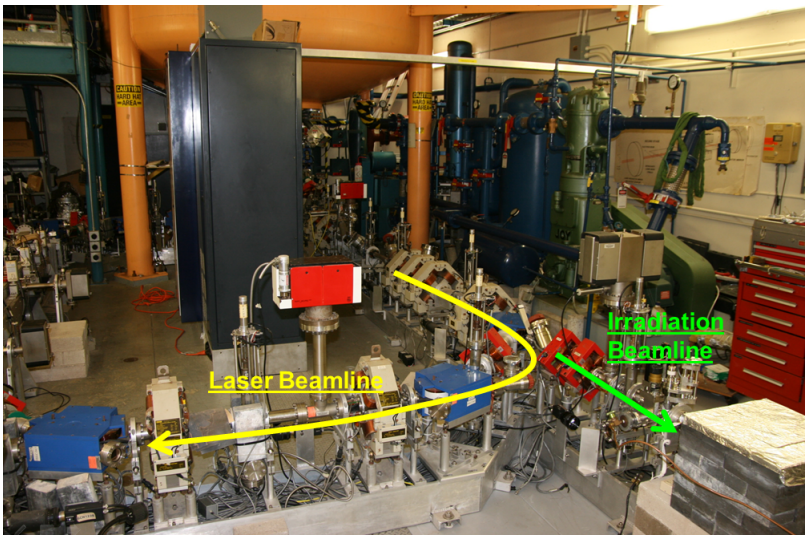

Figure 2.2: UCSB Free Electron Laser irradiation beamline.

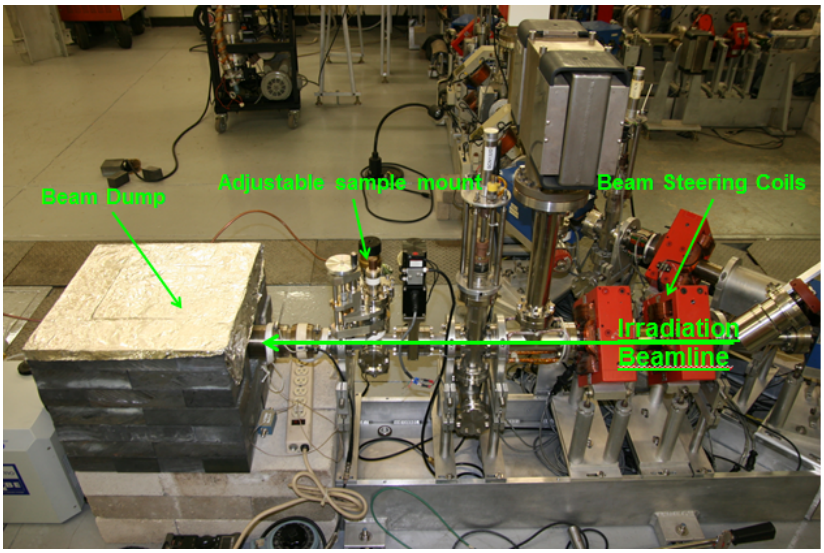

Figure 2.3: UCSB FEL electron irradiation sample chamber.

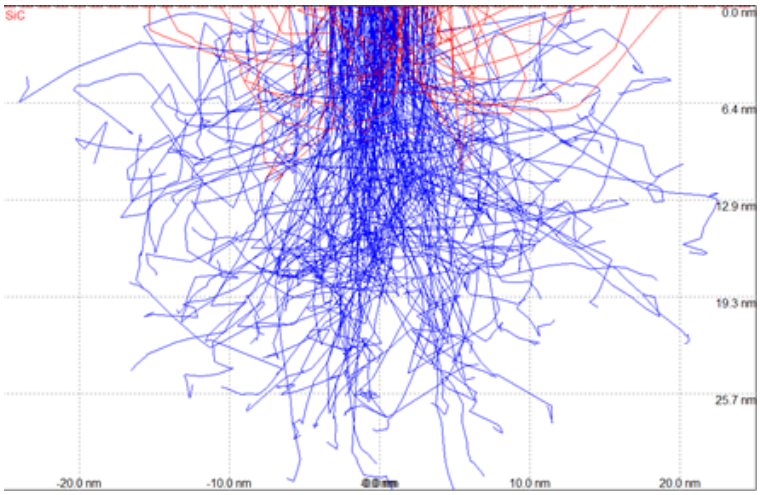

Figure 2.4: Monte Carlo simulations of electron scattering calculated using CASINO.

The other approach typically used to induce defects within a crystal is ion implantation. This process has in the past been utilized by the semiconductor industry for the spatially localized introduction of dopants into semiconductors. This spatial control is also what make the process attractive for deterministic production of localized defects qubits for device and sensing applications. The spatial control of depth is tuned by changing the ion energy and species. The freely available SRIM software[31] provides an easy to use calculator for determining the optimal ion energy for specified geometries. The software typically outputs a distribution of vacancies produced through irradiation damage that can generally be used to tailor the final distribution of incorporated defects within the material.

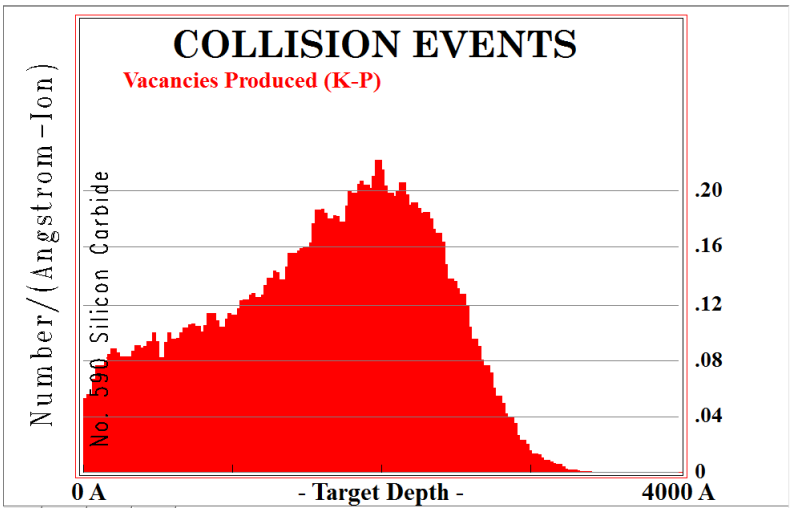

Figure 2.5: Vacancy distribution vs. depth for carbon atoms implanted into SiC calculated using SRIM.

Figure 2.5 gives an example of such an output. Additionally, the stronger interaction of heavy ions with most materials means that damage can be masked to spatially modulate the vacancy density. This has enabled the controlled placement of single NV centers at predetermined locations[32], a process commonly cited as one of the advantages that defects qubits have over random distributed quantum dots. However, due to the non-ideal optical properties of defects produced in this manner, this claim is debatable.

As mentioned previously, post-irradiation annealing is generally crucial to producing defects. This process has the benefit of allowing for diffusion processes that induce different point defects to join and also for healing some or all of the residual damage left behind by the irradiation process.

In general, different point defects begin diffusing at different temperatures and have different levels of final stability. A huge body of literature exists related to these processes. For our purposes, processes are typically determined empirically based on previous evidence from the literature. For instance, the optimal annealing process for 4H and 6H silicon carbide divacancies was determined to be a 900 degrees C anneal for 30 minutes in an argon atmosphere in order to produce the brightest sample. Additional care must generally be taken to prevent samples from deteriorating due to impurities in the inert atmosphere. Fortunately, we were able to take advantage of the existence of various vacuum annealing systems to perform annealing up to temperatures of 2200 degree C for SiC samples. This allowed for post-irradiation tailoring of the divacancy density by inducing the formation of higher order defects (trivacancies, etc) or to reduce background defect densities in order to search for single defects[33]. Similar annealing processes have been developed with NV centers in order to reduce spectral diffusion[34].

2.3 Defect Excitation

One of the primary reasons for the rapid expansion of research in the field of defects is the simple means by which they can be excited. Due

to the existence of a broad blue-shifted phonon sideband, NV centers can typically be excited off-resonantly over a broad range of wavelength(450-600 nm) and defects in silicon carbide can typically be excited over the range of 800 nm to 1100 nm. Both these wavelength ranges are particularly convenient due to the wide availability of green (532 nm) lasers for NV centers, and Ti:Sapphire or Nd:YAG lasers for silicon carbide defects. Furthermore, sources in this range are also typically available as compact solid state packages or as fiber-coupled butterfly diode laser. This is similar in many ways to semiconductor quantum dots, which can be excited with most wavelengths above the material bandgap. Defects, however, have the advantage that no band states are required for their excitation process and this can avoid strong background luminescence resulting from band edge emission. Off-resonant excitation of localized defect states typically results in only local excitations involving the promotion of the defect electrons to higher excited states followed by the relaxation within the excited state due to the emission of phonons. The defect properties that lead to this blueshifted phonon excitation band will be discussed in a later section.

There do exist, however, many reasons to resonantly excite defect states. Interactions between NV centers and laser fields resonant with the defects' zero phonon line have been utilized to study the NV center excited

state structure[35], achieve near unity ground state spin polarization and single shot readout[36], and to coherently manipulate the defect spin states optically.[37] Accordingly, most quantum information applications involving NV center-like defects rely on schemes involving resonant excitation. The lasers available for these experiments tend to be more complicated: they usually exhibit extremely narrow linewidths ($<$ 300 kHz), typically tune over narrow range (up to 10 nm mode-hop free tuning on some models, up to 100 nm coarse tuning with 5-30 GHz mode hop free tuning on others), and require special stabilization routines to maintain wavelength and power stability. Additionally, resonant excitation typically results in a higher rate of charge conversion (which essentially results in non-permanent photo-bleaching). However, the advantages described above usually outweigh the added difficulties associated with resonant excitation.

A few other, more specialized excitation methods are also occasionally used. Because of the versatility of above-gap excitation for characterizing most semiconductors, some past studies have utilized excitation ranging down to the UV wavelength range. This excitation process involves a combination of band-to-defect state relaxation that is usually not well understood. For instance, the first observation of the Ky5 defect bands in 3C SiC resulted from above gap excitation[38]. This method has proved

particular convenient for performing characterization of a broad range of 3C SiC epilayers. Because the silicon substrate typically exhibits fluorescence levels that can swamp the defect signal, above gap excitation in the UV range allows one to characterize a given epilayer's defect fluorescence level without complicated processing due to the short attenuation length of above gap excitation. Furthermore, this may provide clues that electrically pumped band edge carriers could be used to excite defect fluorescence.

Electrical excitation has indeed recently been demonstrated in diamond and silicon carbide[39] [40] by incorporating defect states into LED structures. Electrical pumping had previously been only limited to III-V based systems.[9] This approach is particularly relevant for the prospects of demonstrating a room temperature, electrically pumped single photon source.

2.4 Defect Detection

Detection schemes for optically active deep level defect qubits typically focus on photoluminescence readout mechanisms. Most initial research on the NV center was performed using EPR spectrometers to detect the defect spin states [41] and it was only after the correlation between the spin and optical properties was established that researchers began studying NV

center fluorescence using ODMR. For many candidate defect qubit systems like those in silicon carbide, the vast majority of the literature focused on EPR methods and the full model of the connection between the optical and spin properties has not yet been established. In general, EPR is a more straight forward method to characterize spin sublevels because it does not involve any convolution with the defect optical properties. However, typical EPR spectrometers like the Bruker X-band model in the UCSB NMR lab is only sensitive to $\sim 10^9$ total spins at the very least; ODMR, as demonstrated for NV centers and other defects with a net spin, can be sensitive down to the single spin level. Electrical methods have also been utilized in the past, motivated primarily by the desire to eliminate the deleterious effects that deep levels often have on real semiconductor devices. Deep Level Transient Spectroscopy is a method based on changes in capacitance resulting from deep level state depletion and is frequently used to establish deep level properties [42]. Additionally, direct spin-dependent charge relaxation in SiC MOSFETS has been observed [43]. However, these and the plethora of other methods applicable to III-V systems are beyond the scope of this work so I will focus on fluorescence detection methods.

Optical detectors generally fall into two categories: analog detectors and photon counting units. Due to their low sensitivity, analog detectors

are usually applied only to large ensembles of emitters or for measurement techniques that involve interactions with a laser field. The former case applies to much of the initial work we performed on defects in silicon carbide; a high sensitivity (Noise Equivalent Power ~30 fW/$\sqrt{Hz}$) with low bandwidth (~20 Hz) was the most reasonable, cost-effective choice for the initial experiments. Higher bandwidth, lower sensitivity diodes were used in some early studies of NV center optical dynamics [44]. Similar diode detectors were utilized for studies of spectral hole burning [45], Raman heterodyne detection,[46] and recent work involving faraday rotation in NV centers[37].

Photon counting units are further divided into two categories: array detectors and point detectors. The most common type of array detector is the CCD array. These types of CCD cameras are commonly applied in spectroscopy applications and can be liquid nitrogen cooled to reduce background count rates. Silicon CCDs are typically used for visible and near-infrared spectroscopy (400nm-1100nm) and InGaAs CCDs are optimized for infrared detection (900nm-1700nm). These systems suffer from rather low bandwidth (~1 Hz) due to the need for mechanical shutters but are still preferable to point detectors for PL spectroscopy using a spectrometer due to the large number of wavelengths sampled in one exposure.

Point detector photon counting units are typically the main workhorse detector used for visible and near-infrared single defect studies due to their combination of high quantum efficiency and high bandwidth. Silicon avalanche photodiode single photon counting modules are available with very high quantum efficiencies (greater than 70 percent at 700 nm), low timing jitter (down to 50 ps), low dark counts (as low as 25 cts/s), and reasonable cost (5K for top of the line specifications). Silicon devices typically exhibit negligible quantum efficiency for infrared photons so for defects like those found in silicon carbide that emit in the telecom bands, other alternatives must be used. InGaAs photon counting modules are commercially available but typically require gated operation due to high rates of dark counts (although idQuantique has recently developed a free-running model with good specifications). Accordingly, most telecom range single photon-based research has required access to superconducting nanowire single photon counting units. These systems have only recently become commercially available and are typically very expensive (50-100K U.S. dollars, at least) both to purchase and operate due to the need for cryogenics (wet or closed cycle). They do, however, exhibit a good quantum efficiency of approximately 25 percent over a broad wavelength range (900nm-1900nm) and very low dark counts (less than 1 ct/s). These de-

tectors were crucial for sensitive, high bandwidth measurements of silicon carbide defects and for the isolation of single defect sites.

2.5 Defect Manipulation

The next crucial ingredient in studying defect qubits and implementing quantum information schemes is the ability to coherently manipulate defect states, distinct from the largely incoherent excitation and measurement processes. The majority of these methods of manipulation take advantage of the 'atom-like' structure of localized defects within the semiconductor lattice and mimic processes previously exploited for studying and controlling neutral atom and trapped ion systems. I will focus the discussion around methods used in NV center-like systems research but these methods have been applied to a variety of other defects. Here is a brief survey of the most common methods of manipulation:

- Microwave manipulation: The NV center and its analogues in SiC form well defined triplet spin states both in their ground and excited states with magnetic dipole transitions connecting the $m_s = 0$ and $m_s = \pm 1$ states. Accordingly, this method of manipulation is the primary means by which single qubit gates are applied to defect states [47]. Both CW and pulsed methods of microwave manipulation have

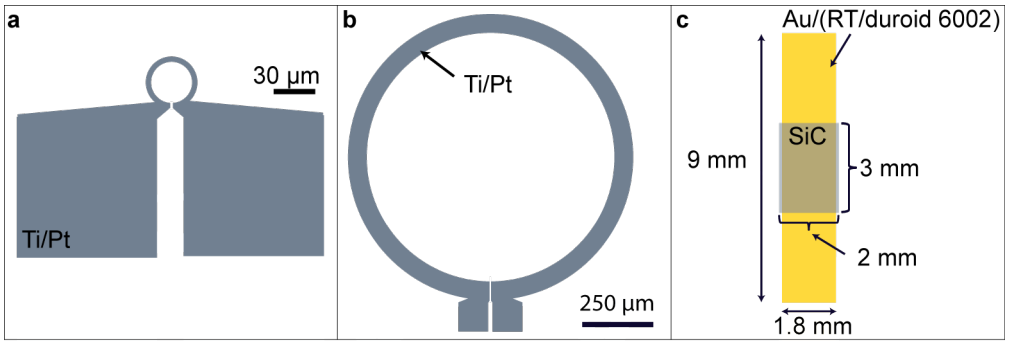

Figure 2.6: Metallization wires used to apply microwave fields for spin resonance experiments in SiC.

reached a high degree of maturity for spin control. Perhaps the only downside to this method is the inherently small degree of localization of magnetic fields. However, implementation of microwave structures for spin manipulation is fairly simple for both on and off chip architectures. See Figure 2.6 for examples of three different metal structures used for microwave manipulation of SiC defects.

- Optical manipulation: Under the right conditions (low-temperature, small degree of inhomogeneous broadening), direct manipulation of the spins and orbital states can be achieved through the use of resonant laser excitation. In particular, for NV centers, recent research in this area has led to the demonstration of optical Rabi oscillations [48] and optical (AC) stark shifts [37]. These methods are promis-

ing and/or necessary for many quantum information schemes (see the laser sections on basic quantum information schemes). In principle, the optical control fields can be localized on very small scales using photonic or plasmonic structures but in general, laser-based approaches require more complicated and expensive hardware than microwave manipulation.

- Electrical manipulation: Although the direct degree of coupling of the NV center and SiC divacancy spin sublevels to electric fields is rather weak, nevertheless they can be used to perform both DC shifts[49] of excited state energies and even coherent spin manipulation in the defect ground state sublevels [50]. DC level shifts of the excited state are a crucial tool for combating spectral inhomogeneity for the production of indistinguishable photons, while AC electric field manipulation may allow for spin manipulation on very small length scales due to the ability to strongly confine electric fields on the nanoscale.

- Strain manipulation: Similar to electric field manipulation, strain fields can also be applied to manipulate defect spin states.[51] This has recently been demonstrated in both diamond and silicon carbide. The most exciting prospects for this process involve potentially cou-

pling defects to strain field in fabricated nanomechanical resonator. [52].

2.6 Incorporation into Functional Devices

One key outstanding challenge for the defect qubit field is their interface with other degrees of freedom such as optical or mechanical modes. Incorporating defect qubits into useful geometries and functional devices is crucial to almost all of their applications and is certainly essential for scalability. Here is a brief description of each of the most common types of architectures researchers are pursuing:

- Photonic structures: This approach is, up to now, the most commonly explored line of research due to the inherent optical interface between the spin and optical degrees of freedom of NV center-like defects. The structures fall into one of two categories: structures for broadband or narrowband spectral enhancement. Structures intended for broadband enhancement are typically sought to increase the total photon yield of an individual emitter and in diamond, have come in the form of solid immersion lenses [53], nanoposts [54], and plasmonic resonators [55]. Nanopost structures have the additional merit of being well suited for incorporation into scanning probe ge-

ometries. Structures that result in narrowband enhancement are typically desired for quantum optics applications. These structures typically include micron scale ring resonators [56] and nanoscale photonic crystal cavities[57] [58]. Due to the fact that the majority of photon emission goes into the broad sideband transitions of the NV center, strong Purcell enhancements are necessary to funnel emission into the narrow zero phonon line for applications involving indistinguishable or narrow band single photon production. These applications typically involve structures with high quality factors and small mode volumes and if these parameters can be sufficiently optimized, the potential for 'strong coupling' exists. If this regime could be accessed, it would open up a number of possibilities for interfacing the long-lived spin coherence of the NV center ground state with optical degrees of freedom for a host of quantum information applications, some of which were discussed previously. See Figure 2.7 for an example of a fabricated 3C SiC photonic crystal cavity containing Ky5 defect qubits.

- MEMs, NEMs: NV center-like systems also typically interact with strain degrees of freedom in their ground and excited states and this opens up the possibility for interactions with mechanical systems.

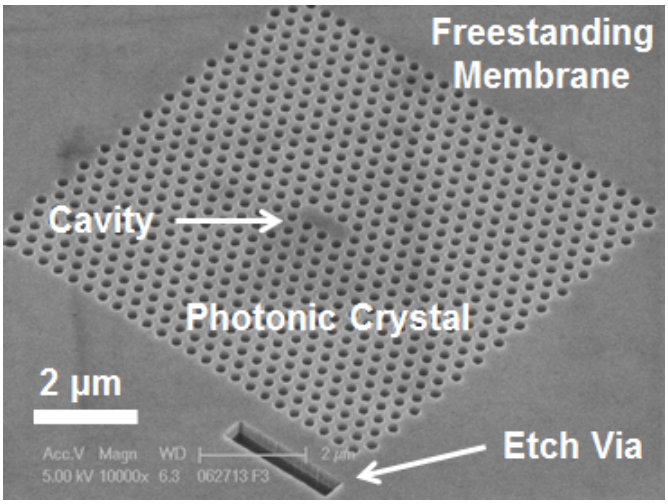

Figure 2.7: L3 photonic crystal cavities fabricated out of 3C SiC containing Ky5 defect qubits.

Figure 2.8 shows an example of such a structure: a series of cantilevers fabricated out of 3C SiC that contain Ky5 defect qubits. Applications of these systems range from sensing of local strains[52] to mechanical cooling[59] to coherent interactions between mechanical resonators and single defects [60]

- LED's: In order to produce a scalable single photon source, one would ideally like to be able to generate the photons through an electrical means. This has previously been demonstrated for III-V semiconductor quantum dots [9] and has recently been applied to NV centers [39] and defects in SiC [40].

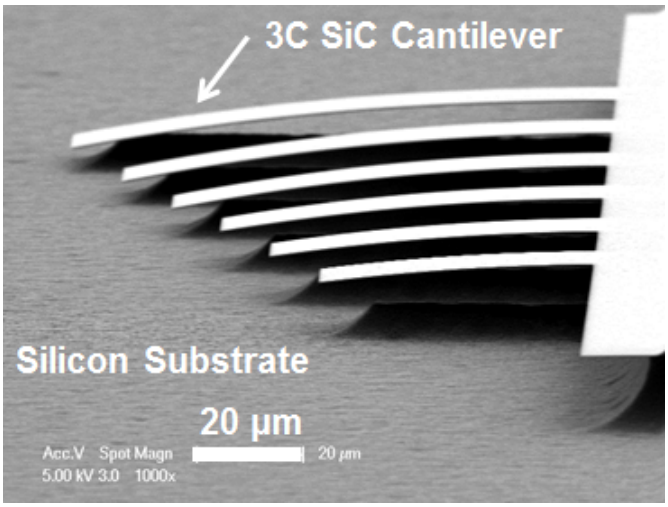

Figure 2.8: Cantilevers fabricated out of 3C SiC containing Ky5 defect qubits. Courtesy of B. Aleman

2.7 Single Site Isolation

One of the main driving forces behind studying deep level defects for quantum information applications is the potential for single site isolation. After many decades of research studying the properties of NV centers, researchers isolated single emitters in the late 90's [47]. This research expanded for many years and eventually led to isolation of other single emitters in diamond and other materials [61] [62] [17] [63]. See Figure 2.9 for a typical spatial scan of a low density sample of SiC exhibiting isolated single emitters. The single emitter nature of a given isolated emission site is typically verified through the emission photon statistics (see Section 2.7), as shown in Figure 2.10 . There are a number of motivations behind study-

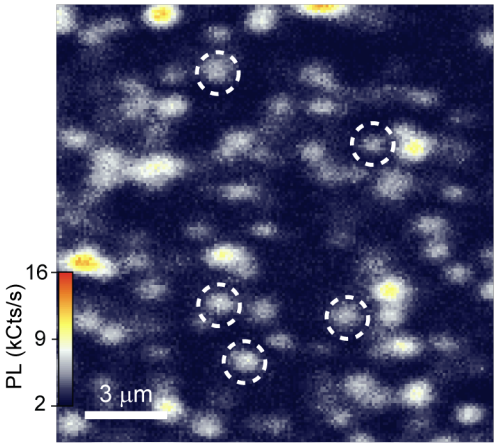

Figure 2.9: Scanning confocal PL map of a low defect density 4H SiC sample.

ing single emitters in place of ensembles. From a basic science perspective, this allows one to (mostly) eliminate the effects of inhomogeneous broadening which can prevent the study of many intrinsic defect properties. I qualify this state with 'mostly' because most measurement procedures still involve time averaging schemes that can still produce inhomogeneity as a result of non-static properties. This inhomogeneity can come in many forms, including spectral inhomogeneity, inhomogeneity in spin dynamics and splitting parameters, and spatial inhomogeneity resulting in experimental non-idealities (a particularly harmful problem in experiments involving optical cavities and sensing schemes).

For quantum information applications, single emitters are a crucial component of most schemes. In particular, many quantum key distribution

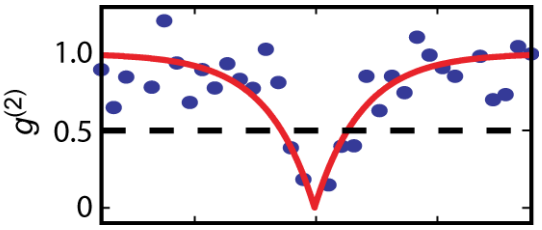

Figure 2.10: Second-order coherence function of single defects in SiC exhibiting photon anti-bunching.

schemes rely on the use of single photon states for perfectly secure communication. A basic demonstration of the BB84 scheme has previously been implemented using single photons generated by NV centers. Other schemes (like projective entanglement, for instance [64]) require indistinguishable single photons, which can be more difficult to achieve and often requires local tuning of individual defect transitions. For sensing applications, ensemble approaches can be used, but these result in spatial averaging of the measured field and reduced coherence times resulting from ensemble dephasing. However, for many quantum information and sensing schemes, if an ensemble of N truly indistinguishable defects could be produced with long spin coherences times, one can gain a $\sqrt{N}$ enhancement of the desired effect. For quantum information schemes, this results from the $\sqrt{N}$ enhancement of the coupling factor in the Tavis-Cummings model. For sensing schemes, this results from the larger signal to noise that results from a higher photon count rate (the signal typically scales as the square

root of the count rate leading to a sensitivity that scales inversely with the square root of the number of emitters).

The isolation of single emitters usually results from the use of extremely low emitter density samples and confocal microscopes with fine spatial resolution (a small excitation and collection volume). Examples of scanning confocal microscope setups will be given in later chapters. In brief, a laser of sufficient power to saturate the emission of a single defect is typically spatially scanned through the volume of a crystal using a microscope objective and the emitted photoluminescence is passed back through the same microscope objective, filtered to reject the pump laser, and passed to a sensitive photodiode module. It is vitally important that the sample have an emitter density lower than 1 emitter per cubic micron and that the sample background emission signal be much lower then single emitter signal. These two criteria can be very difficult to access for most materials and defects.

2.8 Single Photon Emitters

One of the main defining quantum properties of NV centers and single defects is their non-classical photon emission. This manifests itself as a statistical property of the light field produced by the emitters that can

be described by the second order photon correlation function $g^{(2)}$. Single photon sources generally exhibit antibunching, or $g^{(2)} < 1$. This property cannot be described using classical electromagnetic theory and therefore is regarded as a 'quantum property' (beyond the obvious particle-like nature of the light field). Single photon states are generally applicable to a number of quantum information schemes, including the BB84 quantum key distribution protocol [2] and entanglement of spatially separated quantum states [65]. Some of these protocols have recently been realized for NV centers, including the BB84 protocol [66], two-photon interference [67], and projective entanglement [64].

The normalized second order photon correlation function is defined as

$$g^{(2)}(\tau) = \frac{\langle n_c(0) n_d(\tau)\rangle}{\langle n_c(0)\rangle\langle n_d(0)\rangle} = \frac{\langle c^\dagger(0)c(0)d^\dagger(\tau)d(\tau)\rangle}{\langle c^\dagger(0)c(0)\rangle\langle d^\dagger(0)d(0)\rangle} \tag{2.1}$$

where $c^\dagger(c)$ are the raising(lowering) operators for the photon field of the output arm of the 50:50 beamsplitter given the label 'c'. $a, b(c, d)$ are the input (output) channels for the 50:50 beamsplitter. In order to relate the beamsplitter outputs to the input, we use the following relationships between the input and output operators:

$$c = \frac{-ia + b}{\sqrt{2}} \qquad d = \frac{a - ib}{\sqrt{2}} \tag{2.2}$$

We are generally interested in the zero time delay correlation function

$g^{(2)}(0)$. For the input Fock state $\psi =\mid n,\ 0\ \rangle$, using equation 2 and performing a little algebra, one can show that

$$g^{(2)}(0) = \frac{\langle n(n-1)\rangle}{\langle n^2\rangle} = 1 - \frac{1}{n} \tag{2.3}$$

For a single emitter, only one photon is emitted within the decay time of the excited state lifetime. Thus at any given time the input state is $\mid \psi \rangle =\mid 1\,0 \rangle$ yield $g^{(2)}(0) = 0$ (see Figure 2.11 (left)). If multiple photons are emitted, the state $\mid \psi\rangle =\mid 20\rangle$ yields $g^{(2)}(0) = 1/2$. Hence, it commonly accepted that for $g^{(2)}(0) < 1/2$, the source is considered a 'single emitter'.

For the case of identical emitters, the input state to the beamsplitter is $\mid \psi\rangle =\mid 1\,1\rangle = a^\dagger b^\dagger \mid 0\,0\rangle$ (see Figure 2.11 (right)). This can be rewritten as

$$a^\dagger b^\dagger \mid 0\,0\,\rangle = \frac{ic^\dagger + d^\dagger}{\sqrt{2}}\frac{c^\dagger + id^\dagger}{\sqrt{2}} \mid 0\,0\,\rangle \tag{2.4}$$

$$= \frac{1}{2}(c^\dagger c^\dagger + id^\dagger d^\dagger) \mid 0\,0\,\rangle = \frac{1}{\sqrt{2}}(\mid 2\,0\,\rangle + i \mid 0\,2\,\rangle) \tag{2.5}$$

Hence the two photons always exit the same arm of the beamplitter and the coincidence counts between the two photon counting channels drops to zero when the photons arrive at the beamsplitter at the same time. This yields the famous 'Hong-Ou-Mandel' result from quantum optics: a dip in the coincidence counts from the two channels of the output ports of a 50:50 beamsplitter. The magnitude of the dip is a measure of the indis-

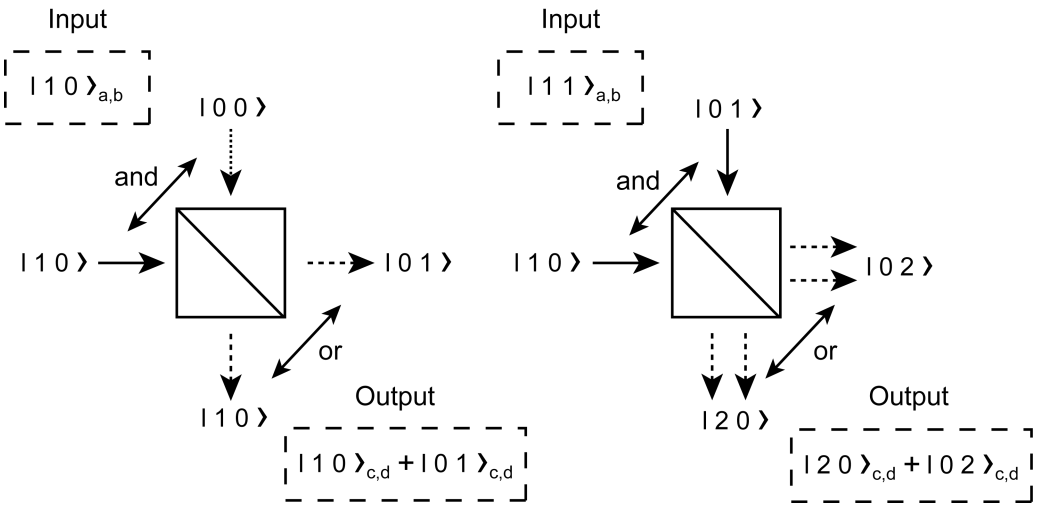

Figure 2.11: Comparisons between input and output states of different sets of Fock states incident on a 50:50 beamsplitter.

tinguishability of the incident photons. See Figure 2.11 for a schematic of these two situations.

Although much progress has been recently demonstrated for NV center based single photon sources, they still face significant challenges. Typically one would prefer to work with single photons in the telecom range to take advantage of the low loss in silica fibers through the 1-1.5 micron wavelength range and the near-unity photon detection capabilities of super conducting nanowire detectors (which is necessary for some quantum information schemes). Accordingly, it would be advantageous to be able to convert photon frequencies through the use of bulk non-linear optics [68] or on-chip material nonlinearities [69]. Additionally, NV centers typically

emit over a broad spectral range (~200 nm bandwidth) which can pose a challenge for some optical systems. Incorporating NV centers into optical cavities [70] can improve the situation by providing narrowband enhancement and emission into a well defined optical mode although this approach certainly has many challenges with regard to ease and defect stability.

The challenge of achieving stable NV centers is particularly problematic for schemes that involve photon interference because this leads to spectrally distinguishable emission. NV centers with stable spectral emission are the exception rather than the norm [71] and this becomes particularly problematic in fabricated microcavities. However, some recent progress has been made towards improving the emission stability of individual NV centers. [34]

For a detailed discussion of the successes and challenges in the field of single photon emitters, see [72].

2.9 Cavity QED

Most of the interesting behavior and applications of single emitter systems arise when a single emitter is coupled to single mode of an optical cavity. To understand this behavior we consider a two level system interacting with an optical mode through the typical Jaynes-Cummings

Hamiltonian:

$$H = \hbar\omega_0 \mid e \rangle\langle e \mid + \hbar\omega_0(a^\dagger a + \frac{1}{2}) + \hbar g_0 \mid e \rangle\langle g \mid a - \hbar g_0^* \mid g \rangle\langle e \mid a^\dagger \quad (2.6)$$

where ω_0 is the transition frequency, a and $a^\dagger$ are the cavity mode raising and lower operators, and g_0 is the emitter-field coupling constant. We have set the transition frequency equal the the frequency of the cavity mode for convenience. To characterize the system's eigenmodes and dynamics, it is necessary to take into account the loss mechanisms that result from spontaneous emission and cavity photon loss. These can be taken into account through a Master equation approach:

$$\frac{d}{dt}\rho = \frac{1}{i\hbar}[H, \rho] - \frac{\gamma}{2}(\sigma_+\sigma_-\rho - 2\sigma_-\rho\sigma_+ + \rho\sigma_+\sigma_-) - \frac{\kappa}{2}(a^\dagger a\rho - 2a\rho a^\dagger + \rho a^\dagger a) \quad (2.7)$$

where γ is the excited state decay constant, $\sigma_\pm$ are the Pauli raising and lowering operators, and κ is the cavity field decay constant. This can be treated as an effective non-hermitian Hamiltonian of the following form:

$$H_{eff} = H - i\hbar\frac{\gamma}{2}\sigma_+\sigma_- - i\hbar\frac{\kappa}{2}a^\dagger a\rho \quad (2.8)$$

If we only consider the two states $\mid e\,0 \rangle$ and $\mid g\,1 \rangle$ signifying the states where the excitation is either in the emitter or the cavity, this can be easily

cast into the simple form:

$$H_g = \hbar \begin{pmatrix} -i\frac{\gamma}{2} & g_0 \\ g_0^* & -i\frac{\kappa}{2} \end{pmatrix} \tag{2.9}$$

The eigenvalues of this Hamiltonian can be obtained as:

$$E_{\pm} = -i\frac{\kappa+\gamma}{4} \pm \sqrt{\mid g_0 \mid^2 - \Big(\frac{\kappa-\gamma}{4}\Big)^2} \tag{2.10}$$

In the limit where $g_0 \gg \kappa/2, \gamma/2$, the 'strong coupling' limit is reached. In this limit, the square root term in the eigenvalues can be real, yielding eigenstates that are combinations of both the cavity excitation and the emitter excitation. The values set by this eigenenergies are real and therefore the behavior is oscillatory; excitations can be swapped from the emitter to the cavity and back before the excitation has decayed from the system through either spontaneous emission or cavity loss. In the other limit where $g_0 \ll \kappa/2$ or $g_0 \ll \gamma/2$, we have the 'weak coupling' or 'Purcell enhancement' regime. In this regime, the two eigenenergies are purely imaginary, leading to decaying excitations. These eigenenergies and decay rates are given by:

$$E_1 = -i\frac{\kappa_g}{2} \qquad \kappa_g \approx \kappa - \frac{4 \mid g_0 \mid^2}{\kappa} \tag{2.11}$$

$$E_2 = -i\frac{\gamma_g}{2} \qquad \gamma_e \approx \gamma + \frac{4 \mid g_0 \mid^2}{\kappa} \tag{2.12}$$

The first eigenstate is more 'cavity-like' and the second is more 'emitter-like'. We focus on the second state and consider how the cavity affects the emitter's behavior. The emitter decay rate has now been enhanced to be:

$$\gamma_e = \gamma(1 + F_p) \qquad F_p = \frac{4 \mid g_0 \mid^2}{\kappa\gamma} \tag{2.13}$$

which can be seen by considering that this eigenvalue's eigenstate primarily consists of the emitter excitation state($\kappa \gg \gamma$ in most solid state systems). This extra term F_p is considered the rate at which the emitter is decaying into the cavity mode. If we compare the rate at which the emitter would otherwise emit in a material of index n

$$\gamma_n = \frac{n\mu^2\omega_0^3}{3\pi\epsilon_0\hbar c^3} \tag{2.14}$$

To the cavity emission rate

$$\gamma_c = \frac{4 \mid g_0 \mid^2}{\kappa} = \frac{2\mu^2\omega_0^3}{\epsilon_0\hbar n^2 V_m \kappa} \tag{2.15}$$

We derive the well known 'Purcell Enhancement' that results from change in optical density of states the emitter can couple to as a result of the cavity:

$$\frac{\gamma_c}{\gamma_n} = \frac{3}{4\pi^2}\left(\frac{\lambda}{n}\right)^3 \frac{Q}{V_m} \tag{2.16}$$

Intuitively, we can understand this behavior as a result of the modified optical density of states that results from the cavity's presence. This can be

understood heuristically by considering the two common methods for calculating spontaneous emission: Fermi's Golden Rule or Wigner-Weiskopff formalism.

Fermi's golden rule can be states that the transition rate from a state i to a state f is given by :

$$T_{i \to f} = \frac{2\pi}{\hbar} \mid a \mid^2 \rho(\omega) \tag{2.17}$$

where a is the transition matrix element and $\rho(\omega)$ is the density of states at that frequency. The cavity alters this density of states, and thus the transition rate.

The Wigner-Weisskopf approach to calculating spontaneous emission is preferable to Fermi's golden rule in its degree of rigor. Without going into details (see [73]), as with Fermi's Golden Rule, it involves an integral over available optical modes in order to calculate the transition rate from one state to another. The presence of cavity alters this integral, leading to altered emission rates.

NV center type emitters with significant phonon sidebands have additional caveats when it comes to Purcell enhancements. The ZPL is the only homogeneously broadened transition that can efficiently couple to a high Q cavity mode yet this emission line only constitutes ~3% of the total defect emission band. As a result, one has to realize that the decay rate given by

equation 2.16 is made up of of a term for the total emission rate without a coupled cavity mode and a cavity coupled term (the Purcell term). However, the Purcell term includes the single photon Rabi frequency for just the ZPL dipole strength in the numerator while the entire excited state decay is in the denominator:

$$\gamma_e = \gamma(1 + F_p) = \gamma(1 + \frac{4 \mid g_0 \mid^2}{\kappa\gamma}) \tag{2.18}$$

Another way to look at this is as though the Purcell Factor for a single emission line is reduced by the ratio of that line's rate to the total radiative rate:

$$F_P \rightarrow F_P \left(\frac{\gamma_{ZPL}}{\gamma_{tot}}\right) \tag{2.19}$$

We can re-write the Purcell term only in terms of the enhancement of the ZPL emission in the cavity mode relative to free space/bulk as:

$$\gamma_e = \gamma + \frac{4 \mid g_0 \mid^2}{\kappa\gamma_{ZPL}}\gamma_{ZPL} = \gamma + F_{ZPL}\xi_{ZPL}\gamma_B \tag{2.20}$$

where γ_B is the bulk emitter decay rate where we have defined the fraction of emission into the ZPL ξ_{ZPL} (the "Debye-Waller" factor) as

$$\xi_{ZPL} = \frac{\gamma_{ZPL}}{\gamma_B} \tag{2.21}$$

We can now obtain an expression for the enhancement of the ZPL emission relative to bulk in terms of experimentally measurable parameters:

$$F_{ZPL} = \left(\frac{\tau_0}{\tau_e} - \frac{\tau_0}{\tau_{off}}\right)\frac{1}{\xi_{ZPL}} \tag{2.22}$$

where we τ_0 is the total PL decay lifetime of the emitter in bulk, τ_e is the total PL decay lifetime when the emitter is coupled to the cavity, and τ_{off} is the total PL decay lifetime when the emitter is not coupled to the cavity mode (this is distinct from the bulk emission rate due to the fact that the local dielectric environment of the emitter is altered by being in the cavity even when not coupled to it). This provides a simple method for extracting F_{ZPL}: measure the Debye-Waller factor and PL decay rate in bulk and then measure the decay lifetime when the ZPL is not coupled to the cavity mode and then tune the mode or emission to the mode wavelength to obtain enhanced decay lifetime. ZPL Purcell enhancements of ~70 and 62 have been measure for 2D [70] and 1D [74] photonic crystal cavities, respectively.

Although these reported results provide significant Purcell enhancements, the cavity Q's demonstrated for these mode volumes are still more than an order of magnitude away from achieving the onset of the strong coupling regime. For nanoscale cavities with mode volumes on the order of $\sim(\lambda/n)^3$, Q's of approximately 10^5 are necessary to achieve strongly coupling to an NV center. The highest Q's reported for these sized structures with operating wavelengths near the NV center ZPL are around 6000, with Q's of 1000 being more typical. Despite this, some of the applications de-

scribed in later sections are achievable in the the Purcell regime.

However, the expression for F_p above assumes that the emitter is on resonance with the cavity wavelength, positioned at the electric field maximum of the cavity and that the dipole polarization matches the cavity mode polarization. While it is not difficult to achieve resonance with tuning of the cavity or emitter wavelength, the second two criteria are very difficult to achieve. The non-ideal Purcell factor F_r has the form:

$$F_r = F_p \left| \frac{E(r) \cdot \mu}{\mid E_{max} \mid\mid \mu \mid} \right|^2 \frac{1}{1 + 4Q^2(\frac{\lambda}{\lambda_{cav}} - 1)^2} \tag{2.23}$$

Spatial positioning within the cavity mode maximum is extremely difficult due to diffusion during annealing for top-down fabricated defects and $< 111 >$ oriented material is required to achieve the proper emitter polarization. All the factors mentioned above pose significant challenges for doing cavity QED with NV center like systems.

Cavity quantum electrodynamics is a rich field and this has only scratched the surface. However, the strong coupling and Purcell regimes form the basis for many of the applications for solid state optical emitters, some of which will be discussed briefly in the next few sections. Purcell Enhancements are generally applicable for enhancing any applications that rely on the production of single photons for quantum optics applications and the strong coupling regime allows for a number of different coherent

interactions between light fields and matter qubits. For a more rigorous set of derivations and more details discussions of the various applications, see [75].

2.10 Projective Entanglement

One of the most promising implementations of optically active defect qubits involves projective entanglement of two separate qubits into an entangled state. The primary advantage of this scheme is that it does not require the direct interaction between the two qubit; the crucial step in the process is the interference between indistinguishable photons from the two distinct systems. In this sense, the process is projective and not deterministic. Nevertheless, schemes exist to exploit this process for quantum information applications[65]. The basic experimental setup is demonstrated in Figure 2.12: The systems we wish to entangle consist of two ground state levels making up a qubit state with an excited state connected to one of the ground state levels two states through optical transitions. Each qubit is incorporated into a cavity for practical reasons but this is not strictly necessary. Single photons emitted from the qubits are incident on a 50:50 beamsplitter where they interfere and pass to photon counters in the two exit ports of the beamsplitter.

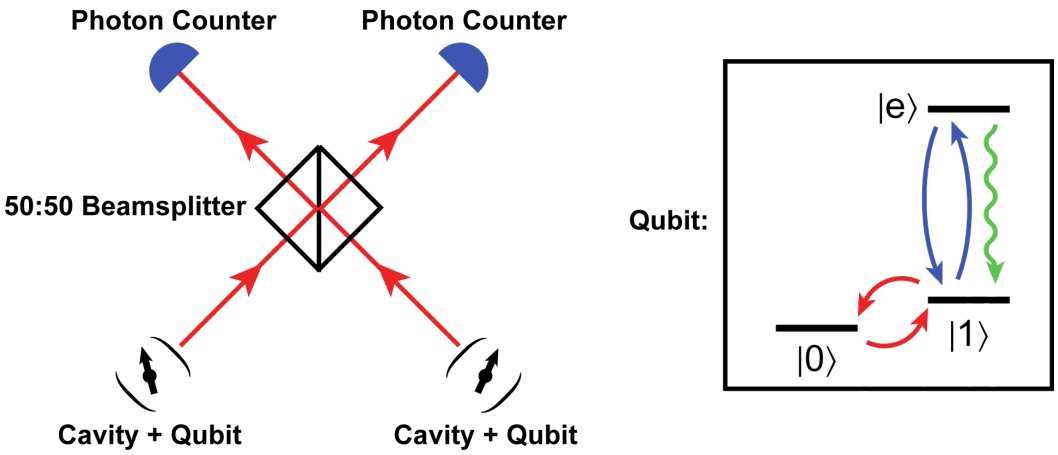

Figure 2.12: Experimental configuration for projective entanglement using two optically active qubit systems.

We begin by initializing each of the two qubit states into the state:

$$| \Psi \rangle = \frac{1}{\sqrt{2}}(| 0 \rangle + | 1 \rangle) \tag{2.24}$$

This could be accomplished in a number of ways but for the case of the NV center, it could be performed by optically pumping the state to either the $m_s = 0$ or $m_s = 1$ state and applying a $\pi/2$ pulse to the system. Next, an optical π pulse is applied to the $| 1 \rangle \rightarrow | e \rangle$ transition, putting each qubit in the state:

$$| \Psi \rangle = \frac{1}{\sqrt{2}}(| 0 \rangle + | 1 \rangle) \Rightarrow \frac{1}{\sqrt{2}}(| 0 \rangle + | e \rangle) \tag{2.25}$$

The composite state of the system can now be written as

$$| \Phi \rangle = | \Phi_1 \rangle \otimes | \Phi_2 \rangle = \frac{1}{2}(| 00 \rangle + | 0e \rangle + | e0 \rangle + | ee \rangle) \tag{2.26}$$

Ultimately, the scheme is reliant on the detection of a single photon at either of the two beamsplitter output ports. At this point, we can neglect the $| 00 \rangle$ and $| ee \rangle$ states as they act as 'failed' instances of the protocol. The state we care about is

$$| \Phi \rangle \propto (| 0e \rangle + | e0 \rangle) \tag{2.27}$$

Now the states each decay within the fluorescence lifetime of the excited state and this process can be described by including the state of the photon field:

$$| \Psi_{tot} \rangle = (| 0e \rangle + | e0 \rangle) \mid vac \rangle \Rightarrow (| 01 \rangle a^\dagger + | 10 \rangle b^\dagger) \mid vac \rangle \tag{2.28}$$

where a and b designate the photon creation operators for two input channels of the 50:50 beamplitter. As described previously in the section on photon statistics, we can re-write the input photon creation operators in terms of the output operators as:

$$a^\dagger = \frac{1}{\sqrt{2}}(ic^\dagger + d^\dagger) \qquad b^\dagger = \frac{1}{\sqrt{2}}(c^\dagger + id^\dagger) \tag{2.29}$$

Rewriting the previous state in terms of these operators yields, with some

re-arranging of terms, the state:

$$\begin{aligned} \mid \Psi_{tot} \rangle \propto & (\mid 01 \rangle (ic^\dagger + d^\dagger) + \mid 10 \rangle (c^\dagger + id^\dagger)) \mid vac \rangle \\ = & (\mid 10 \rangle + i \mid 01 \rangle) c^\dagger + (i \mid 10 \rangle + \mid 01 \rangle) d^\dagger \end{aligned}$$

We now see that we have our final state in a superposition of two state: one where a single photon clicks on either of the two photon counters. Once that happens, the state of the qubits is projected onto one of the two maximally entangled states adjoining the photon creation operators. Furthermore, this process can be concatenated to further entangle extra qubits, if an series of such qubit nodes is available. The simplicity of this process lead to its realization in a recent experiment with two distinct NV centers in separate cryostats entangled of a distance of approximately 3 meters[64].

2.11 State Transfer Via Flying Qubits

One of the most conceptually straight forward approaches to building up a 'quantum network' involves the exchange of phase coherence between localized states ('nodes') and photons ('flying qubits').[22] This approach relies on the ability to coherent control the dynamics of a Λ system typically through applied optical control fields. Optical cavities are a crucial part

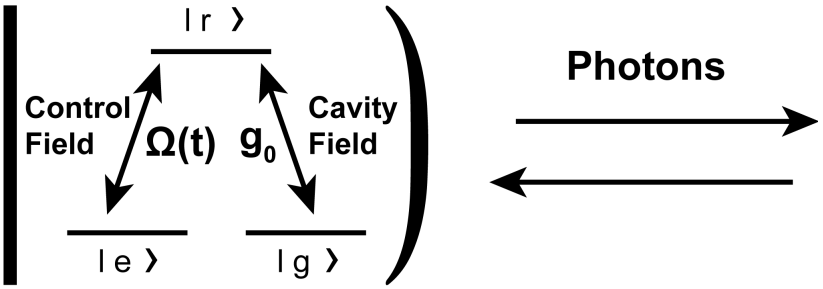

Figure 2.13: Configuration of a quantum node for a stimulated Raman adiabatic passage approach to building a 'quantum network'.

of this process because they act as a coherent interface that transmits the output photon to a well defined optical mode. This mode can then be transferred to another node through a fiber network or through an on-chip waveguide. To demonstrate the basics of this process, we considered a three level Λ system where one leg of the system is driven by a control field and the other is coupled to a single mode of an optical cavity. This scheme is based on the process of stimulated Raman adiabatic passage. Figure 2.13 demonstrates the states and control fields involved.

The resulting Hamiltonian for this situation can be written in the $\mid e,0\,\rangle, \mid r,0\,\rangle, \mid g,1\,\rangle$ basis as:

$$H(t) = \begin{pmatrix} 0 & \Omega^*(t)/2 & 0 \\ \Omega(t)/2 & \Delta - i\gamma/2 & g_0 \\ 0 & g_0 & 0 \end{pmatrix} \tag{2.30}$$

The state $\mid g,0\,\rangle \Rightarrow \mid r,0\,\rangle$ is assumed to be decoupled from the control

field through a relative detuning or polarization selection rule. One can see that the state

$$\mid \Psi(t) \rangle = g_0 \mid e, 0 \rangle - \frac{\Omega(t)}{2} \mid g, 1 \rangle \tag{2.31}$$

is an eigenstate of the above Hamiltonian for all times. Therefore, under the conditions for adiabatic transfer, the system can be transferred from being initially in the $\mid e, 0\rangle$ state ($\Omega(t) = 0$) to the state $\mid g, 1\rangle$ ($\Omega(t) \gg g_0$). Therefore, if the state is initially in a superposition of the ground states $\mid g, 0 \rangle$ and $\mid e, 0 \rangle$ with amplitudes α and β, this phase coherence can be transferred to the photon state:

$$(\alpha \mid e \rangle + \beta \mid g \rangle) \mid 0 \rangle \Rightarrow \mid g \rangle(\alpha \mid 1 \rangle + \beta \mid 0 \rangle) \tag{2.32}$$

In practice, the situation is much more complicated. All the above scheme does is demonstrate in a toy model the basics of how such a scheme works. This photon state would then need to be transferred out of the cavity and coherently re-absorbed by another node. Thankfully, this approach, when taking cavity losses into account, can solve this problem by appropriate engineering of the control pulse. In principle this allows one to generate single photons of an arbitrary envelope into a external mode and then utilize the time-reverse of the process to facilitate coherent re-absorption. For a more detailed discussion, see [75] and the references therein. It is in

general easier to deal with polarization superpositions rather than number state superpositions as flying qubits and this entire process has recently been realized for this scheme [76].

2.12 Mediating Photon-Photon Interactions

One promising route towards utilizing qubit-cavity systems relies not on using the local qubit as the node, but instead uses it to mediate interactions between photon-qubit states. Photons generally act as very good qubits due to their very weak interactions with their surroundings but mediating interactions between photons is generally very difficult. Many of the most common schemes rely on material non-linearities that are incredibly weak at the single photon level. Strongly coupled qubit-cavity systems, however, can demonstrate highly non-linear behavior down to the single photon level. One proposal based on these interactions that has shown recent progress relies on using coupled cavity-qubit system to produce a π phase shift in the phase of the polarization of one photon state contingent on the polarization of another photon state. The basic building block of this process relies on producing a controlled phase shift in the polarization of a photon contingent on the state of the cavity-qubit system as follows.

The following discussion is based on the proposal in [77]. It was previously demonstrated that this controlled phase flip operations, along with single qubit operations, makes up a complete set of operations needed for universal quantum computation. The operator describing this shift is:

$$U_{aj}^{CPF} = e^{i\pi|0\rangle\langle 0|\otimes|h\rangle_j\langle h|} \tag{2.33}$$

Producing this operation is the main challenge of this process. For a coupled-cavity emitter system, with some work, one can show that the resulting different phase shift for a photon reflected from the cavity with or without the emitter on resonance is $\sim \pi$ for an emitter in the strong coupling regime with $g_o^2 > \frac{\gamma\kappa}{4}$. For further details, see [75]. The follow discussion will demonstrate how this operation between a matter qubit and a photon can be used to generate operations between photons, described by the following operator:

$$U_{jk}^{CPF} = e^{i\pi|h\rangle_j\langle h|\otimes|h\rangle_k\langle h|} \tag{2.34}$$

First, we prepare the matter qubit in a superposition of states, only one of which is resonant with the cavity mode and capable of producing the controlled phase flip:

$$| \Phi_{ai} \rangle = \frac{1}{\sqrt{2}}(| 0 \rangle + | 1 \rangle) \tag{2.35}$$

We then perform the following series of composite operations that will perform the photon-photon phase flip:

$$U_{jk}^{CPF} \mid \Psi_{jm} \rangle \otimes \mid \Phi_{ai} \rangle = U_{aj}^{CPF} \, R_a(-\pi/2) \, U_{ak}^{CPF} \, R_a(\pi/2) \, U_{aj}^{CPF} \tag{2.36}$$

This process consists of a matter-photon phase flip on one photon labeled 'j', followed by a $\pi/2$ rotation of the matter qubit state, followed by a matter-photon phase flip on a second photon labeled 'k'. This process is then 'reversed' to leave the matter qubit and initial photon state in its original form by then performing a $-\pi/2$ rotation on the matter qubit followed by another matter-photon phase flip on the first photon. The net effect of this process for an initial photon with 'H' polarization yields:

$$\begin{aligned} | \psi_H \rangle = | \Psi_{jm} \rangle \otimes | \Phi_{ai} \rangle = & \frac{1}{2}(| 0 \rangle + | 1 \rangle) \otimes | H \rangle_j \otimes (| H \rangle_k + | V \rangle_k) \\ & \Rightarrow \frac{1}{2}(| 0 \rangle + | 1 \rangle) \otimes | H \rangle_j \otimes (- | H \rangle_k + | V \rangle_k) \end{aligned}$$

The net effect of this process for an initial photon with 'V' polarization yields:

$$\begin{aligned} | \psi_V \rangle = | \Psi_{jm} \rangle \otimes | \Phi_{ai} \rangle = & \frac{1}{2}(| 0 \rangle + | 1 \rangle) \otimes | V \rangle_j \otimes (| H \rangle_k + | V \rangle_k) \\ & \Rightarrow \frac{1}{2}(| 0 \rangle + | 1 \rangle) \otimes | V \rangle_j \otimes (| H \rangle_k + | V \rangle_k) \end{aligned}$$

This demonstrates the phase flip of the second photon contingent on the state of the first. If the first photon is in a superposition of polarizations, this process can be used to entangle the two photons. This and similar processes have been demonstrated for quantum dots in photonic crystal cavities[78] and neutral atoms coupled to bulk[13] and microcavities[79].

2.13 Conclusions

While great progress has been made recently in applying defect qubits to many of the application described in this chapter, significant challenges remain with regards to the difficult of fabrication and stability of individual defects. While the focus of this thesis will be on moving on to new systems beyond the NV center to facilitate many of the applications above, the NV center is still the gold standard for defect qubits and a thorough understanding of its properties is crucial to making progress with new candidate systems.

Chapter 3

The Diamond Nitrogen Vacancy Center

3.1 Introduction

Although none of the work presented in this thesis was performed using the negatively charged nitrogen vacancy center (NV center) in diamond, understanding the background physics and details of this system was crucial to identifying and studying the newly discovered defect qubits in silicon carbide. The goal of the initial work on silicon carbide was to discover new systems that exhibit electronic structure and behavior analogous to the NV center so it was crucial to both understand the current state of NV center research and also the history of what experiments led to this knowledge. Much of this behavior had been studied in other point

defects in solids and in small molecule systems prior to the development of a (near) complete understanding of the NV center before but the NV center provides a relatively clean model system by which we can understand most of the types of defect properties we consider relevant to defect qubits. Furthermore, much of the work on silicon carbide has been and is focused on confirming NV center-like behavior or assumes as much. Accordingly, it is worthwhile to present some of the details of the NV center electronic structure, behavior, and applications as background to the work in silicon carbide.

3.2 NV center electronic structure

The basic structure of the negatively charged nitrogen vacancy center can be understood from the perspective of considering the proper symmetrical combinations of the local dangling bonds. [80] We begin with the local dangling bond orbitals from the three carbon atoms adjacent to the vacancy which we label $a - c$ and the orbital from the nitrogen dangling bond which we label d. The nitrogen vacancy center has the point symmetry group C_{3v} so we need to construct combinations of the orbitals that

transform as irreducible representations of this symmetry group. They are:

$$u = d - \lambda v$$
$$v = \frac{a+b+c}{\sqrt{3+6S}}$$
$$e_x = \frac{2c-a-b}{\sqrt{6-6S}}$$
$$e_y = \frac{a-b}{\sqrt{2-2S}}$$

where S and λ are the overlap integrals of a with b and d with v, respectively. The orbitals labeled u and v correspond to the A_1 representations and the e_x and e_y orbitals correspond to the E representation. First-principle calculations are generally required to determine the energetic ordering of states in this type of analysis. In this case, calculations indicate that the u state is the lowest energy and that it falls within the valence band of the diamond host. The other states fall within the bandgap and the e_x and e_y states are degenerate and highest in energy. See Figure 3.1 for a diagram of the energetic ordering.

The basic properties of the NV center are well described by a six electron model where three electrons are contributed from the three carbon orbitals, two electrons are contributed from the nitrogen orbital, and one extra electron is captured from the host lattice. The single electron orbitals described above can be filled according to Hund's rules to produce

the multi-electron states that form the basis for the NV center model. Figure 3.1 (a) shows one such filling for the ground state, lowest energy configurations. The properly symmetrized forms of these states can be expressed as

$$
\begin{aligned}
\mid S_x\rangle &= \frac{-i}{\sqrt{2}}(\mid e_x\, e_y\,\rangle + \mid \bar{e_x}\, \bar{e_y}\,\rangle) \\
\mid S_y\rangle &= \frac{-1}{\sqrt{2}}(\mid e_x\, e_y\,\rangle - \mid \bar{e_x}\, \bar{e_y}\,\rangle) \\
\mid S_z\rangle &= \frac{1}{\sqrt{2}}(\mid e_x\, \bar{e_y}\,\rangle + \mid \bar{e_x}\, e_y\,\rangle)
\end{aligned}
$$

where the barred orbitals indicate a spin up electron and the unbarred orbitals indicate spin down. We have omitted the spin configuration for the other orbitals because they are the same for each of these three states. In this picture, one does have to take consider the spin configuration for the other orbitals for excited states (see Figure 3.1 (b)).

The two most important terms in the ground state Hamiltonian that define its spin physics of the NV center are the spin-spin interaction and the Zeeman interaction. The spin-spin interaction originates from the dipole interaction of the un-paired electron spins and can be written as

$$H = S \cdot D \cdot S \tag{3.1}$$

where $S = S_1 + S_2$ is the total spin operator and D is a tensor. It can be

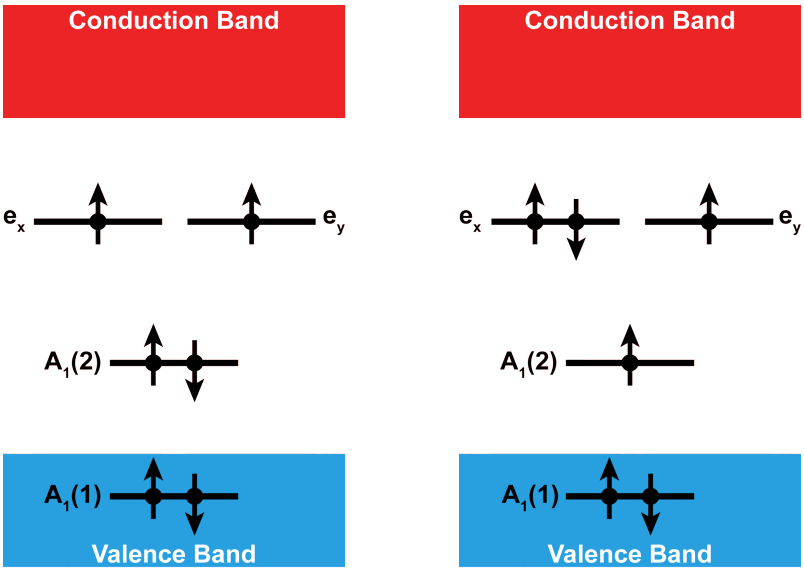

Figure 3.1: Composite electronic configuration for the NV ground state (left) and excited state (right).

shown that this term in the Hamiltonian reduces to

$$H = D(S_z^2 - 1) \tag{3.2}$$

and the calculation of D can be reduced to the form

$$D \propto \langle \frac{r^2 - 3z^2}{r^5} \rangle \tag{3.3}$$

where the brackets indicate an averaging integral over the wavefunction of the electron state. Performing this integral requires first-principle approaches but in general this quantity can be measured quite easily. For the NV center, this term produces a difference in frequency between the $m_s = 0$ and $m_s = \pm 1$ ground states of 2.876 GHz.

The Zeeman term takes the typical form

$$H_{Zeeman} = g\mu_B B \cdot S \tag{3.4}$$

and splits the ground state $m_s = \pm 1$ levels by a frequency of 2.8 MHz/gauss.

The basic ground state Hamiltonian then takes the form:

$$H_g = D(S_z^2 - 1) + g\mu_B B \cdot S \tag{3.5}$$

which can be expressed in matrix form in terms of the S_x, S_y, S_z basis described above as

$$H_g = \begin{pmatrix} 0 & -ig\mu_B B_z & g\mu_B B_x \\ ig\mu_B B_z & 0 & ig\mu_B B_y \\ -g\mu_B B_x & ig\mu_B B_y & -D \end{pmatrix} \tag{3.6}$$

If we make a change of basis to the familiar $m_s = 0$ and $m_s = \pm 1$ through the relation

$$H_{0,\pm 1} = U H_{S_z, S_x, S_y} U^{-1} \tag{3.7}$$

where U is the transformation matrix

$$H_g = \begin{pmatrix} \frac{1}{\sqrt{2}} i & \frac{1}{\sqrt{2}} & 0 \\ 0 & 0 & 1 \\ \frac{1}{\sqrt{2}} i & -\frac{1}{\sqrt{2}} & 0 \end{pmatrix} \tag{3.8}$$

and apply a magnetic field solely along the z-axis, we end up with the familiar diagonalized Hamiltonian for spin 1 system with a zero field splitting

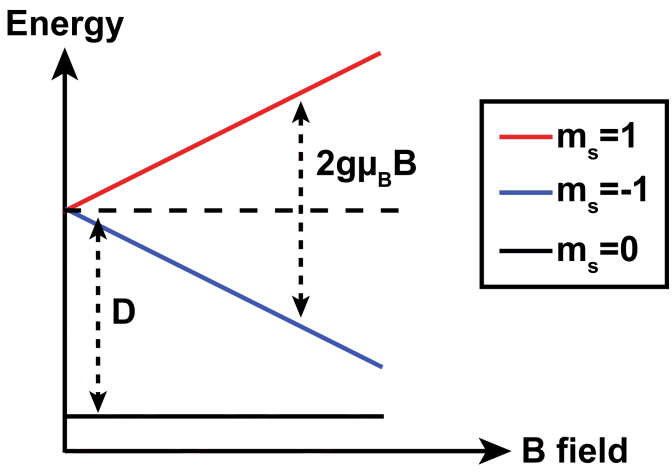

Figure 3.2: Energy level for the NV center ground state with an applied magnetic field along the defect symmetry axis.

between the $m_s = 0$ and $m_s = \pm 1$ state:

$$H_g = \begin{pmatrix} ig\mu_B B_z & 0 & 0 \\ 0 & -D & 0 \\ 0 & 0 & -ig\mu_B B_z \end{pmatrix} \tag{3.9}$$

where a magnetic field splits the $m_s = \pm 1$ states linearly with the applied field and the $m_s = 0$ state stays at a fixed energy. This behavior is depicted in Figure 3.2.

3.3 Optical Properties

The NV center optical spectrum (both absorption and emission) takes a rather peculiar form. It consists of a single relatively sharp transition

referred to as the zero phonon line (ZPL) accompanied by a series of broadened phonon peaks red-shifted (blue-shifted) from the ZPL emission (absorption). These phonon side peaks broaden to the point of indistinguishability as one moves farther in energy from the zero phonon line. The presence of these phonon side bands indicates strong electron-phonon coupling and has broad implications for most applications of the NV center. This electron-phonon coupling can be described with the following Hamiltonian:

$$H = \frac{\omega_0}{2}\sigma_z + \epsilon b^\dagger b + \frac{V}{2}\sigma_z(b + b^\dagger) \tag{3.10}$$

where ω_0 is the ZPL transition frequency, σ_z is the z Pauli matrix, ϵ is the phonon energy, V is the electron-phonon coupling coefficient, b and $b^\dagger$ are raising and lowering operators for the phonon mode. Rewriting the Hamiltonian using the following set of operators:

$$b_1 = b + \frac{V}{2\epsilon} \qquad b_2 = b - \frac{V}{2\epsilon} \tag{3.11}$$

yields the form:

$$H = \frac{\omega_0}{2}\sigma_z - \frac{V^2}{4\epsilon} + \epsilon(\sigma_{11} b_1^\dagger b_1 + \sigma_{22} b_2^\dagger b_2) \tag{3.12}$$

From this we see that the Hamiltonian is such that there are effectively two separate phonon modes with the same energy spacing, one for the ground state and one for the excited state. This results in the energy level diagram

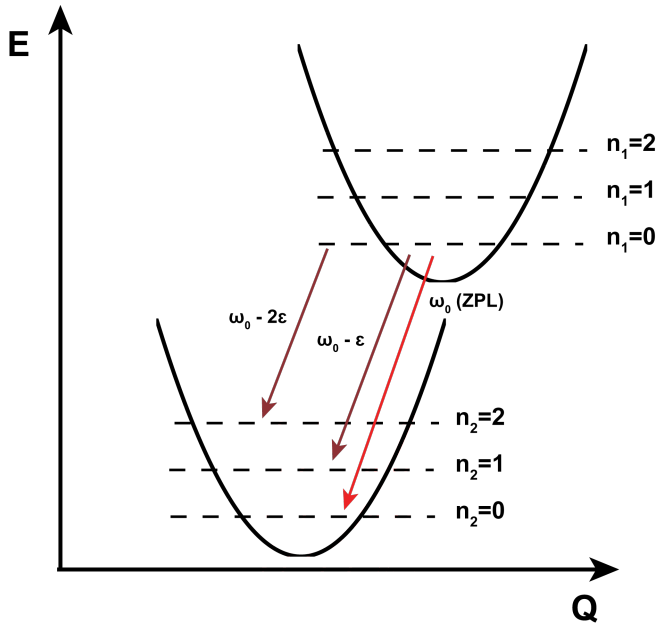

Figure 3.3: Configuration coordinate diagram depicting the combination of orbital and phonon structure of the NV center levels.

depicted in Figure 3.3.

To understand the emission spectrum, we consider the system as starting in the lowest phonon state $\mid i \rangle$ of the excited state manifold. Specifying this as the '1' state, we see that this is an eigenstate of the b_1 operator:

$$b_1 \mid i \rangle = 0 \tag{3.13}$$

From the definition of b_1 and b_2 we see that $\mid i \rangle$ is also a coherent state

$$b_2 \mid i \rangle = -\frac{V}{2\epsilon} \mid i \rangle \tag{3.14}$$

With this information and using the notation:

$$z = \frac{V}{\epsilon} \tag{3.15}$$

we can write $\mid i \rangle$ in terms of the ground state phonon states as:

$$\mid i \rangle = e^{-\frac{z^2}{2}} \sum_{n=0}^{\infty} \frac{(-z)^n}{\sqrt{n!}} \mid e, n_{b_2} \rangle \tag{3.16}$$

We then consider an optical transition to the state:

$$\mid f \rangle = \mid g, m_{b_2} \rangle \tag{3.17}$$

which yields:

$$\mid \langle f \mid ex \mid i \rangle \mid^2 = \mu_{12}^2 \frac{z^{2n}}{n!} e^{-z^2} = \mu_{12}^2 \frac{S^n}{n!} e^{-S} \tag{3.18}$$

where μ_{12} is the optical transition dipole moment and S is known as the 'Huang-Rhys' factor. S signifies the mean number of phonons emitted during relaxation from the excited state to the ground state and determines the relative rate of each transition involving the number of phonons produced in the ground state. The $n = 0$ transition is the zero phonon line. Typically, the larger the phonon number involved in the transitions, the broader the transition linewidth. This means that the zero phonon line is the only optical transition that is Fourier transform limited, a fact that has implications for quantum information applications. Figure 3.4 shows the

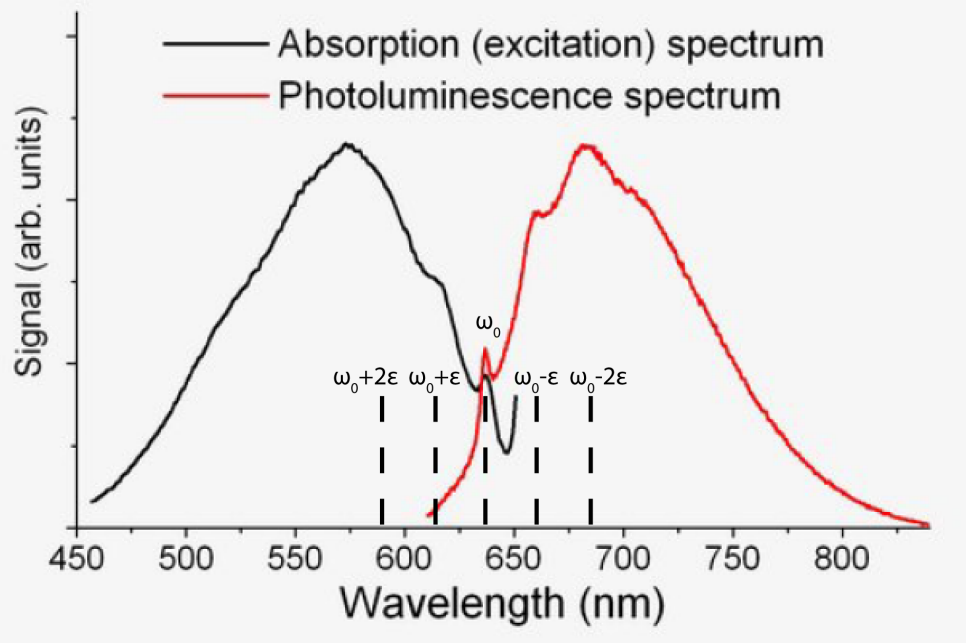

Figure 3.4: The NV center absorption (black line) and emission (red line) spectrum. The dashed lines signify the first few phonon-assisted transitions. Adapted from Wikipedia.

absorption and emission spectrum of the NV center at room temperature and signifies the first few phonon transitions (the individual lines are more distinct at low temperature).

Another means of quantifying the fraction of emitted light into the ZPL that is commonly used is entitled the 'Debye-Waller' factor. This is typically expressed as the fraction of the total emission in the emission band that falls in the ZPL and for the NV center is typically around 3 percent. The Debye-Waller factor ξ_{DW} is related to the Huang-Rhys factor

S by the relation $\xi_{DW} = e^{-S}$.

As was mentioned previously, the presence of the phonon sideband has broad consequences for applications of NV-center like systems. The first and most obvious is the broad range of emission wavelengths. This fact can have some practical implications for the optics involved. A larger issue is the fact that typically only about 3 percent of the emission of the defect goes into the ZPL. This is particularly relevant for applications involving narrowband cavities as this presents an inherent reduction in the Purcell factor of about 30 times. Similarly, this small fraction of ZPL emission limits the rate of production of indistinguishable photons from distinct emitters.

However, the implications are not all bad. From the perspective of basic defect physics, if one performs resonant excitation studies, one can reject the ZPL wavelength range and monitor the sideband emission. This provides a convenient method of monitoring absorption or other properties of the interaction between the excitation and system. This method has been used extensively to study the properties of the NV center excited state [35] and to observe optical Rabi oscillations [48].

The NV center typically exhibits a radiative optical lifetime of approximately 13 ns [81]. This quantity can be used to determine the optical

dipole strength μ of the ZPL transitions using the formula:

$$| \mu |^2 = \frac{3\pi\xi_{ZPL}\epsilon_0\hbar c^3}{\gamma n\omega^3} \tag{3.19}$$

where ϵ_0 is the permittivity of free space, c is the speed of light in a vacuum, γ is the radiative lifetime of the NV center, ξ_{ZPL} is the Debye-Waller factor, n is the index of refraction of diamond (~2.4), and ω is the transition frequency. This yields a dipole strength of $\mu \approx 1$ Debye for the zero phonon line (remember to divide by an additional factor of two to account for the two orthogonal dipole transitions). This number is a fair bit lower than the typical dipole strength exhibited by semiconductor quantum dots (10-100 Debye) and and results from the factor ξ_{ZPL} that signifies that only a small fraction (~3%) of the total emission emits into the most relevant optical transition, the zero phonon line.

3.4 Basic Level Structure

Despite the individual subtleties associated with each sublevel of the NV center electronic level structures, the basic model by which one can understand most of the NV center behavior is depicted in Figure 3.5/

The large band gap of the diamond host lattice (~5.5 eV) acts as a sort of 'artificial vacuum' in which the highly localized electronic states act as an 'artificial atom'. In this regard, the host electronic structure can essentially

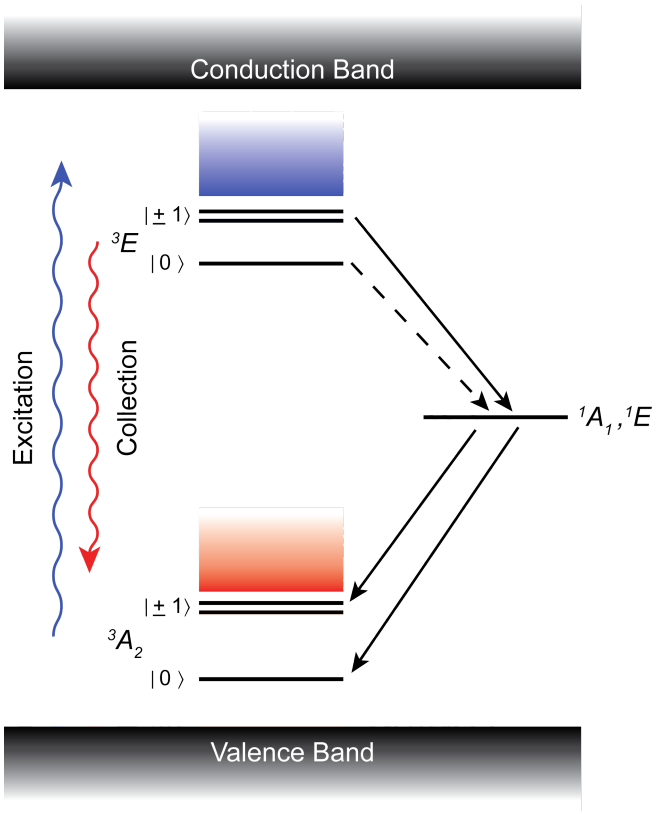

Figure 3.5: Effective level structure for the NV center at room temperature.

be ignored (although it does play a role in models of charge dynamics that explain the charge instabilities experienced by the NV center, particularly during resonant excitation). The ground state triplet level is labeled by its symmetry designation $^3A_2$ and is connected via the NV center's dominant optical transitions to the excited state triplet which is labeled by its ^3E symmetry. These optical transitions are depicted as blue shifted or red shifted from the direct transitions between the triplet states via the phonon assisted processes discussed earlier. Also present is a series of excited state

singlet levels labeled $^1A_1$ and ^1E that make up the defect's 'intersystem crossing'. These states are still under investigation as to their ordering and positioning with respect to the other defect levels but they are the basis for most of the NV center's optical spin polarization cycle, as will be discussed in a later section. The important point to be made regarding these states is that there is a small amount of spin orbit coupling in the system that mixes a small degree of singlet character with the triplet states and vice-versa. This has the net effect of allowing transitions to occur that cause relaxation from the triplet excited state to the single intersystem crossing followed by further relaxation to the ground state. The preferential relaxation to the intersystem crossing from the $m_s = \pm 1$ states over the $m_s = 0$ states is the basis for the off resonant spin initialization and readout mechanism in the NV center.

3.5 NV Center Fine Structure and Other Interactions

The NV center's Hamiltonian becomes quite complex when one accounts for interactions with other local fields and the solid state environment. The vast majority of these details are beyond the scope of this thesis but are worth mentioning in order to become familiar with the other

degrees of freedom that can both complicate and benefit NV center measurements and applications. For a detailed review, see [82].

- Nuclear Interactions: The NV center ground state and excited state both experience interactions with any non-zero spin nuclei in the vicinity of the electron wave function. This included both the 0.4% spin $= \frac{1}{2}$ ^{15}N abundance nitrogen nucleus that is part of the NV center complex and spin $= \frac{1}{2}$ ^{13}C atoms that have a natural 1.1 % abundance within the diamond lattice[83]. The nuclear interactions can help identify extrinsically incorporated NV centers [84] or act as a long lived memory qubit[85] but have the negative side effect of occasionally complicating measurements that only address the electronic degrees of freedom.
- Electric Fields: Electric fields can act as on- or off-diagonal terms in the ground [86] and excited state Hamiltonian of the NV center [87]. While the effect is generally weak in the ground state, local electric field (especially non-static ones) can significantly effect the stability of the the excited state [34]. The electric field sensitivity of the NV center can also allow for electric field sensing [88].
- Strain: Strain effects are significant for NV centers in that they can produce deviations from perfect axial symmetry, producing off-axis

strain splittings in the ground state [89], or they can affect the spin-splittings of the NV center excited states [82]. However, strain is often a useful tool for studying NV center optical transitions [90] or for coupling spin states to mechanical resonators [52].

- Temperature: One of the NV center's primary advantages over other quantum systems is its long coherence times even at room temperature. Temperature does play a significant role for many quantum optical applications in that the defect's ZPL transitions become inhomogeneously broadened above 20K, requiring low temperature for most coherent light-matter interactions. Additionally, the ground state zero field splitting is temperature dependent [91], leading some practical issues in sensing applications. However, this temperature dependence can also be used to locally sense temperature with high accuracy and nanoscale resolution. [92]

3.6 Excited State Structure

One important aspect of the NV center electronic structure that has up until this point been ignored is the excited state level structure. The NV center's excited state actually consists of two orbital states that each form a spin triplet. These two states have orthogonal polarizations that

form dipoles oriented perpendicular to the Nitrogen-Vacancy axis.[93] Accordingly, one must in general account for the aspects of this geometric projection when measuring or considering NV centers oriented along the $< 111 >$ axis in $< 100 >$ oriented material. For $< 111 >$ oriented material, these dipole are in the sample plane. This fact is particularly relevant for the possibility of coupling single NV centers photoluminescence to the optical modes of photonic structures which typically have in-plane fields. Figure 3.6 shows the excited state level structure at a finite magnetic field and finite strain, resulting in a splitting of the degeneracy of the spin and orbital states.

While aspects of this fine structure were observed in various experiments in bulk diamond (typically spectral hole burning experiments [94]), the emission and absorption lines were only recently observed directly for single NV centers. This is due to the fact that it was only recently that high quality single crystal diamond was made to be widely available with optical transitions nearing the transform limited values of 13 MHz. Previously, linewidths of many tens of GHz were observed even for single defects in bulk crystals.[95] Additionally, even in narrow linewidth sample, many of these transitions could not be observed without coincident microwave excitation.

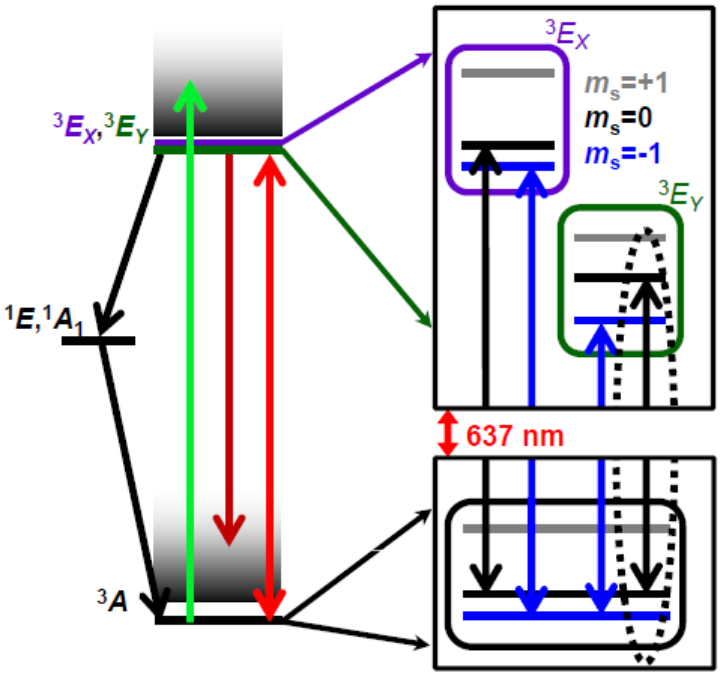

Figure 3.6: Fine Structure of the NV center excited state. Provided courtesy of Bob Buckley.

The properties of these transitions hold a significant degree of relevance for quantum information applications. First, for coupling optical transitions to optical modes, one typically wants to work in the limit where the emitter linewidth is significantly smaller than the cavity linewidth. Second, only one of these transitions, the $m_s = 0$ optical transition for the E_x doublet branch, acts as a good cycling transition. All the other transitions either exhibit significant non spin-conserving transitions to other ground state spin levels or couple to the intersystem crossing, resulting in

optical pumping out of the resonantly excited state. For this reason, most of these transitions are not observable except while undergoing microwave excitation. The fact that there exists at least a single good cycling transition provides two important functionalities. First, since the transition has a small but still finite chance to transition the $m_s = \pm 1$ states, one can continuously drive this transition to achieve perfect spin polarization in the other states. Once the spin flips to the other states, it decouples from the light field and stays polarized for a time equal to T_1. Second, this decoupling from the light field allows for single shot read out of the defect spin state. With proper consideration of statistics, one is able to distinguish between the brightness of the defect in a time shorter than the time it takes to re-polarize under optical pumping.[96] This idea is particularly relevant for non-NV center defects because even if they exhibit poor contrasts due to their respective intersystem crossings, resonant excitation can always achieve unity polarization if good cycling transitions can be isolated.

3.7 Optical Dynamics

As was previously mentioned, the NV center's optical dynamics under off-resonant excitation are one of the primary reasons that it is useful as a

controllable quantum system. Understanding this process is essential for understanding how the NV center works and we shall later use this basic model to understand SiC defect dynamics. In short, a small degree of mixing between the triplet levels and the singlet intersystem crossing allows for transitions between the two sets of levels that are otherwise forbidden by selection rules. The asymmetry in this process between $m_s = \pm 1$ and $m_s = 0$ spin states is what generates the schemes by which NV center can achieve ground state spin polarization through exposure to light and also provides the readout mechanism by which the brightness of the emitter correlates with its spin polarization. Following the model put forth by [44] and further refined by [96], one can model the NV center dynamics using level structure shown in Figure 3.7.

where we have grouped the $m_s = \pm 1$ states together as a single set of levels due to their equivalence with zero applied magnetic field and the singlet levels have been distilled down to a single intersystem crossing level. In this picture, we model the NV center dynamics through a single rate equation model with the rates depicted in 3.1. For simplicity, I have labeled each transition as k^*_{ij}. These transitions actually consist of two rates k_{ij} and k_{ji}.

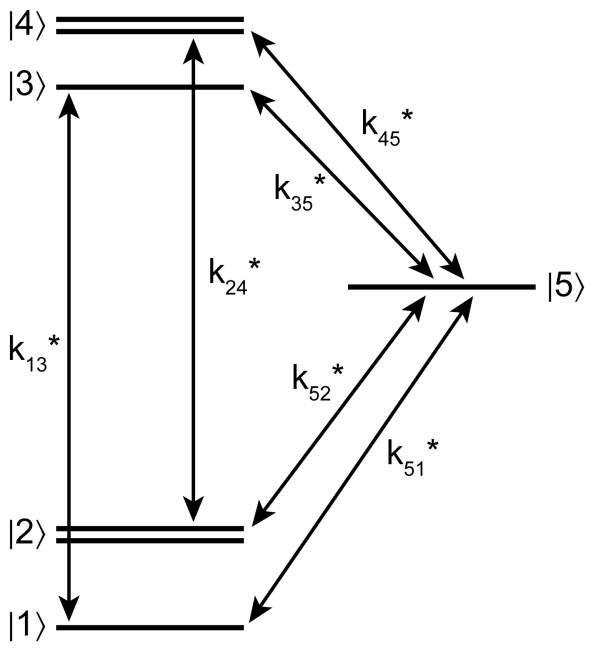

Figure 3.7: Diagram depicting the rates governing the NV center optical polarization and readout cycle.

The governing rate equations are given by:

$$\frac{dn_i}{dt} = \sum_j k_{ij} n_j - k_{ji} n_i \tag{3.20}$$

Since the majority of transitions result from spontaneous emission, the only transitions that involve a positive change in energy of the system are those driven by the excitation laser, k_{13} and k_{24}. Following [44], these rates are parametrized by $k_{13} = k_{24} = k * k_{42} = k * k_{42}$. Also included in the model (although not pictured) are the non spin-conserving transitions like k_{32}

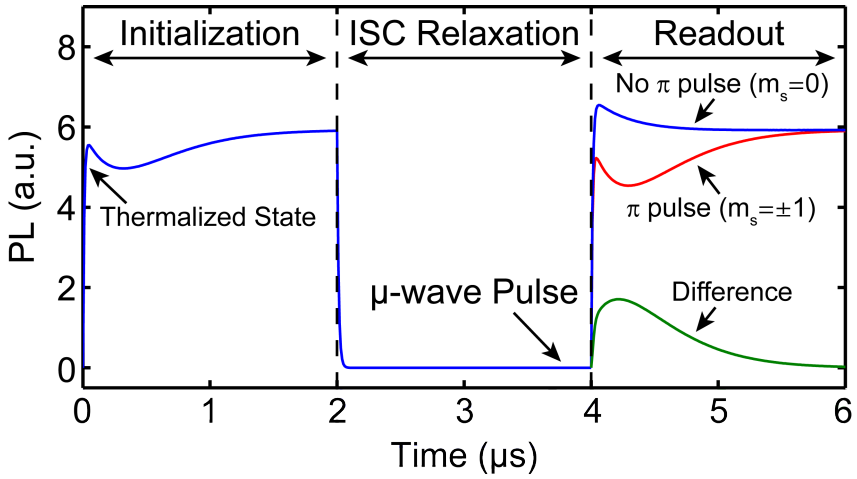

Figure 3.8: Photoluminescence dynamics for a NV center initially in a thermal population that is polarized by an optical pulse and then produces a different optical signal dependent on whether or not a Pi pulse is applied between optical pulses.

and k_{41} with their corresponding 'excited' counterparts, which account for the non-unity steady state polarization in the ground state after prolonged optical cycling. This set of linear, first order differential equations can be easily solved numerically in MATLAB or Mathematica. Figure 3.8 shows the resulting photoluminescence dynamics which agree well with observations [44] [96] [97].

The system is initially prepared in an equal (thermal population) fraction of all three spin states. The system is first excited for a period of time to initialize it and the luminescence reaches a steady state after a few microseconds. Then, the excitation is turned off. The luminescence in the visible transitions ceases immediately although relaxation still occurs

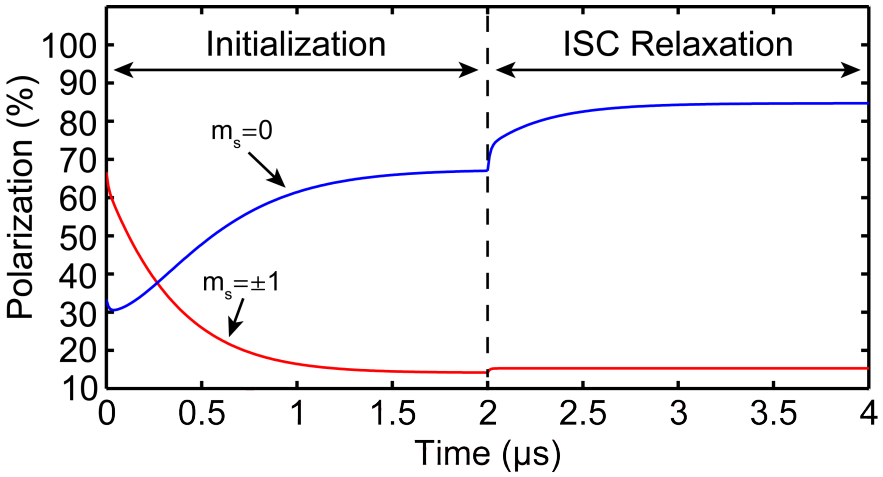

Figure 3.9: Ground state polarization dynamics resulting from a polarizing optical pulse.

from the intersystem crossing states to the ground state. Prior to a second excitation pulse, the system is either left in the $m_s = 0$ state or a π pulse is applied to transfer population to the $m_s = \pm 1$ states. When the second excitation pulse turns on, if the system was left in $m_s = 0$ state, it exhibits a brighter PL signal than if the system was transferred to the $m_s = \pm 1$ states. The difference in signal is also shown. Figure 3.9 shows the associated populations in the ground state spin sublevels during the initial excitation pulse and the following period of no excitation. During the dark period, a fraction of the system in the intersystem crossing levels decays to the ground state.

Table 3.1 summarizes the rates used to model the behavior shown

above, as determined by [44].

More recent work [96] has refined these measured values but the

Table 3.1: NV Center Dynamics Model

Transition	Rate(μs^{-1})
$k_{31} = k_{42}$	77
$k_{41} = k_{32}$	1.5
k_{45}	30
k_{35}	0
k_{51}	3.3

underlying behavior retains the same general features.

3.8 Coherent Manipulation and Coherence Times

The NV center ground state is a triplet state but one usually selects only two of the states ($m_s = 0$ and $m_s = +1$ or $m_s = -1$) for use as two-level quantum system. As mentioned previously, one usually engages in coherent manipulation of these states through the use of magnetic dipole transitions. To understand the basic of this process, we begin with the Master equation for the density matrix of a two level system given by:

$$\frac{d}{dt}\rho = \frac{1}{i\hbar}[H, \rho] + \Lambda\rho \tag{3.21}$$

where

$$\Lambda\rho = -\frac{\Gamma}{2}(\sigma_+\sigma_-\rho - 2\sigma_-\rho\sigma_+ + \rho\sigma_+\sigma_-) \tag{3.22}$$

where Γ is a decay constant and $\sigma_\pm$ are the Pauli raising and lowering operators.

This set of equations can be derived for a few different considerations and/or approximations (see your favorite quantum optics textbook). The important point of this starting point as opposed to even more semi-classical pictures is to gain insight into the decay dynamics governed by Γ. When driven by a harmonic perturbation parametrized by a 'Rabi frequency' Ω , one can show that the equations of motion for the density matrix components are given by:

$$\begin{aligned}
\frac{d}{dt}\rho_{aa} &= -\Gamma\rho_{aa} + \frac{i\Omega}{2}(e^{-i\omega t}\rho_{ba} - e^{i\omega t}\rho_{ab}) \\
\frac{d}{dt}\rho_{bb} &= \Gamma\rho_{aa} - \frac{i\Omega}{2}(e^{-i\omega t}\rho_{ba} - e^{i\omega t}\rho_{ab}) \\
\frac{d}{dt}\rho_{ab} &= -(i\omega_{ab} + \frac{\Gamma}{2})\rho_{ab} + \frac{i\Omega}{2}e^{-i\omega t}(\rho_{bb} - \rho_{aa})
\end{aligned}$$

where 'a' signifies the upper state of the two-level system , ω_{ab} is the angular transition frequency corresponding to the energy splitting of the two level system, and ω is the frequency of the harmonic perturbation.

If we ignore the perturbation (turn off the manipulation field) we have:

$$\begin{aligned}
\frac{d}{dt}\rho_{aa} &= -\Gamma\rho_{aa} \\
\frac{d}{dt}\rho_{bb} &= \Gamma\rho_{aa} \\
\frac{d}{dt}\rho_{ab} &= -(i\omega_{ab} + \frac{\Gamma}{2})\rho_{ab}
\end{aligned}$$

which can be solved to yield

$$\begin{aligned}
\rho_{aa}(t) &= \rho_{aa}(0)e^{-\Gamma t} \Rightarrow \rho_{aa}(0)e^{-\frac{t}{T_1}} \\
\rho_{bb}(t) &= 1 - \rho_{aa}(0)e^{-\Gamma t} \Rightarrow 1 - \rho_{aa}(0)e^{-\frac{t}{T_1}} \\
\rho_{ab}(t) &= \rho_{ab}(0)e^{-(i\omega_{ab}+\frac{\Gamma}{2})t} \Rightarrow \rho_{ab}(0)e^{-(i\omega_{ab}+\frac{1}{T_2})t} \Rightarrow \rho_{ab}(0)e^{-(i\omega_{ab}+\frac{1}{T_2^*})t}
\end{aligned}$$

Here we see that off-diagonal elements of the density matrix ('coherences') relax with a decay constant $2/\Gamma$ and the population (diagonal) terms relax with a decay constant Γ. In practice, this exact relationship does not generally hold and we assign the decay time T_1 to the population decay (energy loss) and T_2 to the decay time for loss of coherence. This sets the oft-cited but rarely explained relationship $2T_1 \geq T_2$. In most real situations, $T_1 \gg T_2$. Furthermore, dephasing, i.e. inhomogeneity that looks like coherence decay, often plays an additional role in the dynamics of a two level system and we use another phenomenological decay constant T_2^* to describe this value. Accordingly, $T_2 \geq T_2^*$. The arrows above indicate the assignment of these values.

We generally measure these parameters through the use of coherent control experiments that involve time dependent manipulation of the two-level system followed by a projection of the spin state. This is achieved through the use of driven Rabi oscillations whose form can be obtained from the above equations if decay is neglected:

$$\mid c_a(t) \mid^2 = \sin^2\left(\frac{\Omega_R t}{2}\right)$$

This approximation of neglected decay usually holds for typical periods of driven Rabi oscillations and coherence times in NV center-like systems. To obtain the value of T_2^*, we usually perform a Ramsey experiment. This involves initializing the spin state into one pole of the Bloch sphere, then applying a $\pi/2$ pulse to put it on the equator. This is done with a frequency that is slightly detuned from the resonance. As a result, in the rotating frame, the spin lies on the equator but is precessing at a frequency equal to the difference between the applied frequency and the transition frequency. After a fixed time, the state is rotated back to the original orientation on the Bloch sphere and the projection is read out. This signal decays with a time constant of T_2^* and oscillates due to the small frequency difference. While this measurement can in principle be done at zero detuning, any inaccuracy in determining the transition frequency or small frequency shifts during the measurement will result in long period oscillations that would

prevent accurate determination of the exponential decay.

T_2 is typically measured using a Hahn echo sequence that is similar to the Ramsey sequence but applies a 'refocusing' π pulse halfway through the experiment and is performed using pulses with zero frequency detuning. T_1 is typically measured by polarizing the spin and then simply monitoring this polarization vs. time by projecting the state onto the polarized state. Eventually the system reaches thermal equilibrium with a time constant equal to T_1. Additional schemes exist that can extend the coherence of the two level system (i.e. Dynamical Decoupling) for enhancing various quantum applications. In general, the T_2 time is connected to the method used to measured it and the values listed below are Hahn echo T_2 times.

Here is a representative sampling of various spin dynamics parameters for the NV center:

- T_1, ensemble, room temp : 7.7 ms [98]
- T_1, ensemble, 40K: 3.8 s [98]
- T_2, typical sample, single center, room temp: 600 μs [99]
- T_2, isotopically purified sample, single center, room temp: 1.8 ms [100]
- T_2^* typical sample, single center, toom temp: 1.7 μs [101]

3.9 Sensing

One of the most promising applications of defects is for high-sensitivity, nanoscale sensing, even up to room temperature. Research in this area began with considerations for magnetic field sensing[102] but soon similar protocols were discovered for sensing electric fields, temperature, strain, and orientation[4]. While other systems exist with better demonstrated sensitivities, few exist that exhibit the same combination of sensitivity, spatial resolution, and room temperature operation. In this section, I will discuss the basics of sensing magnetic fields with NV center-like systems. Similar ideas have been applied to sensing the other quantities mentioned above. All sensitivity numbers quoted here should be considered to be among the best values reported but exact values vary significantly for different operating conditions. A poor sensitivity in a configuration that is easily implemented for actual sensing (i.e. a scanning probe) may, in many instances, be preferable to a high sensitivity in a 'clean' environment (i.e. deep within a bulk diamond) that is incapable of actually being utilized for real applications.

The first and most easily understood form of NV center sensing is for sensing DC magnetic fields. It relies on the simple fact that the NV center ground state ODMR lines are split linearly in an applied magnetic field.

Accordingly, to determine the smallest possible measurable frequency shift we consider a ODMR intensity line of the form:

$$I(\nu_m) = R\Big[1 - \alpha F(\frac{\nu_m - \nu_0}{\Delta\nu})\Big] \tag{3.23}$$

where I is the signal intensity, ν_m is the frequency at which we are measuring, ν_0 is the center frequency of the resonance line, $\Delta\nu$ is the linewidth, R is the rate of detected photons per second, α is the contrast of the line(difference in count rate for the 'dark' state), and F is a function describing the lineshape (typically Gaussian or Lorentzian).

All expressions given here are based on the premise of extracting the minimum possible frequency shift, and therefore the minimum possible field shift by comparing the fluctuations in the count rate (typically considered to be photon shot noise limited) to the slope of the count rate vs. frequency:

$$\gamma\delta B_{min} = \delta\nu_{m,min} = \frac{\delta\beta}{max \mid \frac{\partial\beta}{\partial\nu_m} \mid} \tag{3.24}$$

where B_{min} is the smallest measurable field change, γ is equal to $g\mu_B$, $\delta\nu_{m,min}$ is the minimum measurable frequency shift, and β is the number of photons collected per measurement time $\beta = It_m$. One can show that for this scenario, the sensitivity can be expressed as:

$$\eta_{esr} = \delta B_{min}\sqrt{t_m} = P_f \frac{h}{g\mu_B}\frac{\Delta\nu}{\alpha\sqrt{\beta}} \tag{3.25}$$

This method of magnetic field sensing is by far the simplest to implement. The best sensitivities achieved using this method are $\eta_{dc} \approx 2\mu T/\sqrt{Hz}$. [103]

An alternate approach to DC magnetic field sensing is to use a scheme based on Ramsey interferometry. This technique is essentially the same as performing a Ramsey fringe experiment but instead one applies a fixed, known detuning which is then altered by the measured field. Thus a different amount of phase is acquired during a given pulse sequence and this phase can be related to the measured magnetic field. Similar considerations to above yield the expression:

$$\eta_{esr} = \delta B_{min}\sqrt{t_m} = \frac{\hbar}{g\mu_B}\frac{1}{\alpha\sqrt{\beta T_2^*}} \tag{3.26}$$

This method improves over CW methods and achieves $\eta_{dc} \approx 300nT/\sqrt{Hz}$. [103]

Similar considerations can be applied to a Hahn echo sequence, although in that case the phase of the measured signal must flip with the same frequency as defined by the π pulse within the Hahn echo sequence. As a result, this technique is applicable to measuring AC fields. In the Ramsey case, the optimal measurement time was set by T_2^*. For the case

of the Hahn echo sequence, the optimal measurement time is T_2, allowing for a greater reduction in base sensitivity. The expression for the AC magnetic field sensitivity of this technique is:

$$\eta_{esr} = \delta B_{min}\sqrt{t_m} = \frac{\pi\hbar}{2g\mu_B}\frac{1}{\alpha\sqrt{\beta T_2}} \tag{3.27}$$

This method achieves the lowest sensitivities reported of $\eta_{ac} \approx 30nT/\sqrt{Hz}$.[104]

Chapter 4

NV center analogues in SiC

Some figures and sections of this chapter are adapted with permission from the publications: "Room temperature coherent control of defect spin qubits in silicon carbide," W. F. Koehl, B. B. Buckley, F. J. Heremans, G. Calusine, and D. D. Awschalom, Nature **479**, *84-87 (2011) and "Polytype control of spin qubits in silicon carbide," A. L. Falk, B. B. Buckley, G. Calusine, W. F. Koehl, V. V. Dobrovitski, A. Politi, C. A. Zorman, P. X.-L. Feng, and D. D. Awschalom, Nat Commun* **4**, *1819 (2013).*

4.1 Defect State Criteria

As mentioned previously, we began studying defects in SiC in order to identify defects like the NV center in materials that provide additional functional and engineering capabilities to more rapidly advance the use

of defect qubits for applications in quantum information and sensing. In order to search for NV center analogues, one must first identify the salient features of the NV center that provide it with the extraordinary spin and optical properties that it exhibits. These features are summarized in [105] in the context of how one would search for new NV center-like systems and consist of the following:

- Suitable Qubit States: The defect complex must in some way have a set of long-lived states that can form a psuedo-spin 1/2 system that can be controlled via single qubit gates. For the NV center, this consists of spin-sublevels of a triplet ground state but other level structures are suitable, such as the ubiquitous meta-stable triplet states [63]. Another possibility explored in that reference is the use of the electronic state as an interface between optical degrees of freedom and a nuclear spin that provides the qubit states.
- Optical Polarization Cycle: Rather than relying on relaxation at low temperatures for qubit initialization, it is generally fruitful to have an optical polarization cycle that results in polarization of the qubit state. For the NV center, these processes can be either off resonant [44], as discussed earlier, or resonant [36] with the ZPL. In the resonant case, the scheme is applicable to a broad class of systems with

a set of Λ states.

- Optical Readout Mechanism: This process is essentially the compliment of the previous case, although other readout mechanisms exist such as Faraday rotation [37], direct spin-dependent absorption, or the Raman heterodyne process [46], among others.
- Distinct Optical Transitions: In this case, distinct is meant to signify that the optical transitions are within the host band gap and avoid coupling to band states. Otherwise, there exists a large chance of charge instabilities involving electron exchange between the defect and host states.
- Thermally Isolated States: In general, if too many distinct states (whether spin or orbital) are clustered together in such a manner that thermal excitation can cause transitions, there exists a strong chance that polarization or coherence between states will be degraded.

4.2 Defect Host Criteria

Further constraints exist on the host material for new defect qubit candidates. These criteria primarily function to allow the crystalline host to act as a good 'vacuum' for the atom-like defect states with the added functionality provided by solid state engineerability. Again, these proper-

ties are summarized in [105] and consist of the following:

- Wide Band Gap: This criterion assures that energy level splitting between the host valence and conduction bands is such that it affords enough of a gap so that optical transitions can exist that do not overlap with band to band or bound state to band state transitions.
- Small Spin-Orbit Coupling: Spin-orbit coupling generally tends to limit spin coherence times by coupling local phonon excitations to spin fluctuations. This criteria holds for group IV materials like diamond, silicon, and silicon carbide.
- High Quality Crystals: In general, low quality materials that exhibit high densities of paramagnetic and structural defects do not provide a good host for isolated spin systems. Paramagnetic defects provide a background bath of spins that can interact with the defect qubit levels through dipolar coupling, leading to increased rates of decoherence. Additionally, the presence of such states can affect the defect qubit optical interface by providing a source of background PL (and therefore, extra photon shot noise) and by inducing local charge fluctuations that can affect the optical stability of the defect qubit both in terms of overall charge stability and spectral line energies. Structural defects cause similar problems resulting from dangling bond

states. This criteria also applies to non-bulk materials; the availability of a given host material as a high quality heteroepitaxial layer greatly facilitates the incorporation of defect qubits into devices.

- Isotopic Engineering: Background nuclear spin baths can also provide a source of local spin fluctuations affecting the defect spin coherence. In III-V quantum dots, this generally provides a very significant limit to the spin coherences times which are typically limited to 1-10 ns due to interactions with ~10^5 local nuclear spins. Point defects generally interact with fewer local nuclei but nevertheless, the reduction in background nuclear spins has great benefits for extending coherence time. [100]

4.3 Previous Work

As with early work on the diamond NV center, previous results from photo-enhanced electron spin resonance studies gave indications that these defects form spin 1 ground states that can be optically polarized. Similar to the controversy over the diamond NV center, researchers initially could not detect the EPR signature of these spin 1 defects without optical illumination, suggesting that the defects exhibit a metastable triplet state, as was the case with many small molecules. However, studies with increased

defect densities eventually determined that the spin 1 sublevels were in fact the defect ground state [106]. Some previous ODMR studies in 6H and 3C SiC also suggested the possibility that defects in SiC may exhibit properties similar to the NV center. [107] [108] [109]

For 4H SiC, photo-induced EPR measurements, annealing experiments, and comparisons to theoretical calculations determined that the four UD-2 luminescence lines (PL1-PL4) originate from four distinct forms of the neutral divacancy, which is an uncharged defect complex consisting of a carbon vacancy adjacent to a silicon vacancy [110] [33] [111], $[V_{Si} - V_C]_0$. Two forms of the divacancy, which are often given the labels (hh) and (kk), are oriented along the c axis of the crystal. The other two, (hk) and (kh), are oriented along the basal bond directions (See Figure 4.1). These four defects give rise to the P6b/P6'b (c-axis) and P7b/P7'b (basal) spin-resonance signals that are often observed in electron spin resonance studies of 4H-SiC, and that have been shown to correspond to spin 1 ground states that can be spin-polarized with incident light [106] [112] [111].

Additionally, previous theoretical work had suggested that the divacancy in SiC may exhibit properties similar to the NV center [105] [113]. These studies suggested that the divacancy in SiC should share with the NV center some of the most relevant properties pertaining to use as a defect

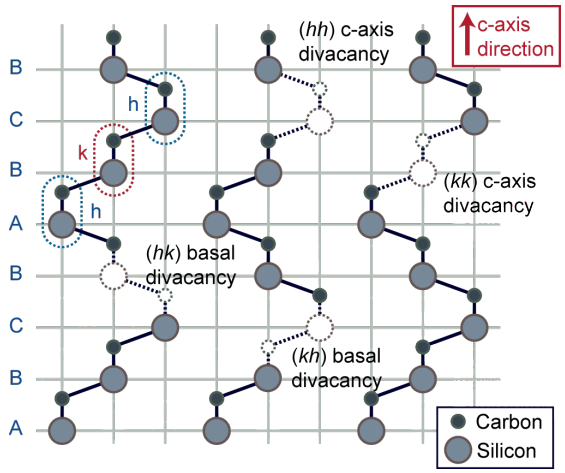

Figure 4.1: Different possible orientations for divacancy point defects in 4H SiC.

qubit: a spin 1 state with C_{3v} symmetry, triplet-triplet optical transitions, and a localized wavefunction. These and future DFT studies on the divacancy in SiC successfully calculated many of the defects other properties like the energy of the ZPL and zero field splitting in the ground state.

4.4 Experimental Setup

Samples were measured in a liquid helium flow cryostat with optical and microwave access, as depicted in Figure 4.2. The sample temperatures could be varied between 20 and 300 K. 853 nm diode laser light was used for sample excitation, and was pulsed using an acousto-optic modulator (AOM) for time-dependent measurements. A 14mm focal length lens or a 60X microscope objective focused the light on the sample surface with

spot diameters of approximately 15 or 1 μm, respectively. The 14 mm focal length lens allows for collection from a greater number of emitters for larger signals at the cost of greater inhomogeneity in applied field. The laser power was 20 mW at the sample surface. Two infrared detectors were used to measure photoluminescence: a liquid-nitrogen-cooled InGaAs CCD camera with a .5 m focal length spectrometer (for taking spectra) or a femtowatt photoreceiver with an analogue voltage output (for optically detected magnetic resonance measurements). Analogue voltages were measured and processed digitally using a data acquisition system (DAQ). Both detectors had an 800-1,700nm operating range. Microwaves were supplied to the cryostat by a signal generator and were modulated using a digital delay generator and a selection of microwave switches and mixers. A permanent magnet was used to apply a magnetic field along the c axis of the material. Samples were diced from a 365-mm-thick wafer of HPSI 4H-SiC purchased from CREE, and had dimensions of roughly 2mm x 3 mm. Ring-shaped microwave sources 34 μm and 1mm in diameter were patterned on the surfaces of two samples using standard photolithographic techniques. In both cases, a 10/90 nm Ti/Pt metallization was used. A third sample was mounted on top of a 1.8 mm wide by 9mm long microwave stripline made from RT/duroid 6002 plated with 1.8 μm of Au. All microwave de-

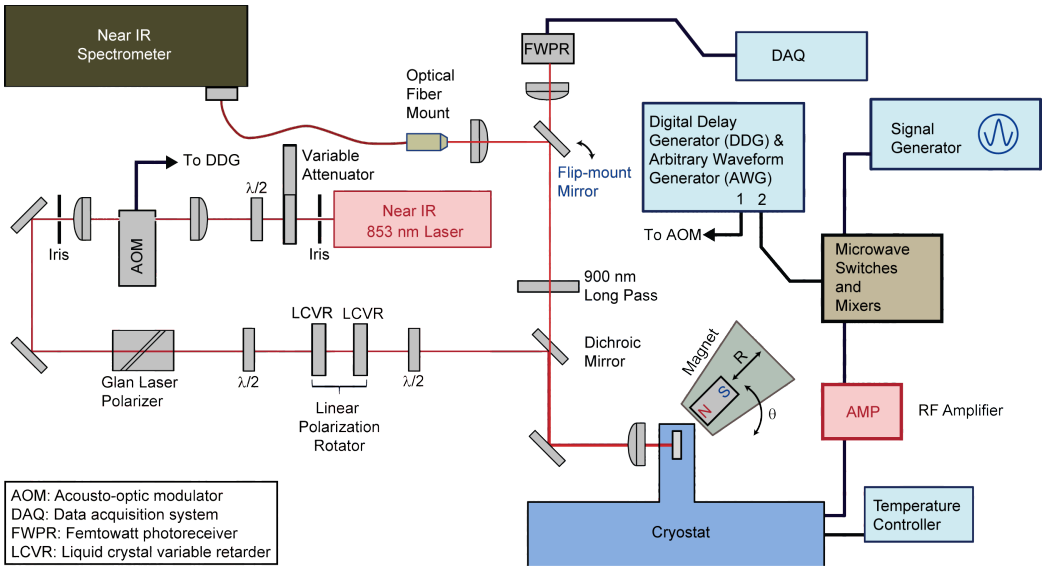

Figure 4.2: Experimental setup used for initial measurements on divacancy defects in 4H SiC.

vices were connected via wire bonds to the microwave line in the cryostat.

4.5 4H Divacancy Photoluminescence

The first evidence of divacancies in 4H SiC that we observed consisted of NV center like luminescence bands in the infrared. To observe this, we studied samples diced from a 2-inch wafer of high-purity semi-insulating (HPSI) 4H-SiC. The samples were optically excited with below-bandgap light from an 853nm (1.45 eV) diode laser. Photoluminescence spectra taken at sample temperatures ranging from 20 to 300K are shown in Fig-

ure 4.3. At 20 K, several sharp lines with energies ranging from 1.09 to 1.20 eV are apparent, along with a series of broader features found from 0.9 to 1.20 eV. At low temperatures, luminescence from a single species of optically active defect commonly consists of a sharp ZPL and a broad sideband composed of lower energy phonon replicas of the ZPL. Several overlapping spectra are observed in Figure 4.3 due to the presence of multiple different defect orientations and species. An expanded view of the 20K photoluminescence from 1.09 to 1.20 eV can be seen in Figure 4.4, where six sharp lines have been given the labels PL1-PL6. Four of these, PL1-PL4, form a group of lines known in previous literature by the singular label, UD-2 [114]. The other two, PL5 and PL6, are close to one another in energy and share several features. This suggests that PL5 and PL6 are related, but their origins are currently under investigation. At higher temperatures, all six lines simultaneously broaden and decrease in height, so that they are almost completely indistinguishable from the phonon sidebands by 200 K. However, luminescence from a subset of these defects' phonon sidebands is still clearly visible up to 300 K.

One of the primary methods of identifying a given defect's orientation consists of studying its spin resonance behavior as a function of orientation of known crystal axes with respect to a magnetic field. In this case, defect

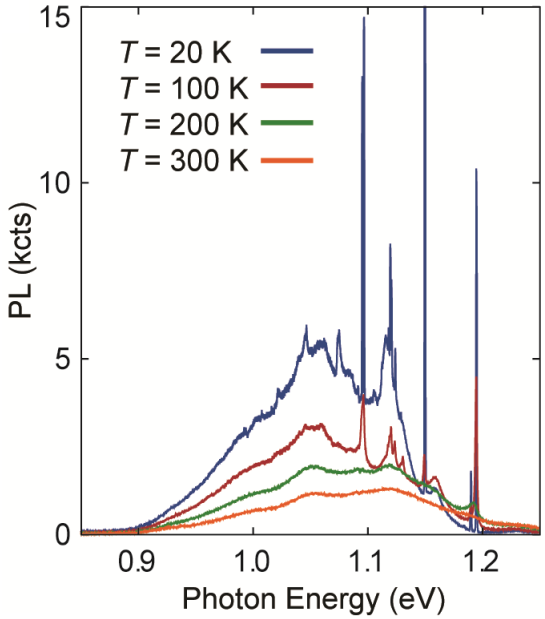

Figure 4.3: Wide range PL spectrum of high purity, semi-insulating 4H SiC under 850 nm illumination.

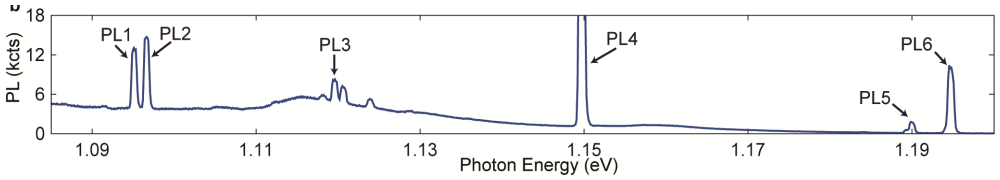

Figure 4.4: Narrow range PL spectrum showing the various ZPL's for divacancies and unknown defects in 4H SiC.

axes can be directly determined by applying a static magnetic field to the sample. In each panel of Figure 4.5, we plot total luminescence originating from one ZPL as a function of applied magnetic field at 20 K. No microwave radiation was applied. The five traces in each panel correspond to different magnetic field angles (θ), where the angle was measured relative to the defect axis of PL6 and was in the plane defined by this defect axis and $<1\ 1\ 0\ 0>$. (Defect axes for PL1, PL2, and PL6 were all found to be collinear within the precision of the experimental apparatus, and were oriented along the c axis of the material.) As seen in Figure 4.5 (a) when $\theta = 0^o$, a sharp decrease in PL1 luminescence occurs at a magnetic field corresponding to hD/($2\mu_B$), where h is Planck's constant, B is the Bohr magneton, and D is the axially symmetric spin-splitting measured in through ODMR. This phenomenon is also observed in Figure 4.5 (b) and 4.5 (d), although in Figure 4.5 (b) it appears as an increase in luminescence. As θ is increased, these sharp features broaden, and an additional broad feature of undetermined origin appears at a lower magnetic field that then opens up with increased angle as well. Similar behavior is seen in the diamond NV center when the defects spin sublevels are tuned to a level anti-crossing (LAC) by an external magnetic field aligned roughly along the defect axis.[115] In such case, dips in luminescence are observed due to a combination of

spin mixing, spin precession, and optical spin polarization. The results in Figure 4.5 are therefore consistent with a model in which the neutral divacancy possesses a spin-1 ground state that can be optically polarized through an intersystem crossing, like the diamond NV center. [106]

Figure 4.5 (c) shows the results of the same ML experiment performed on PL4. No sharp features are seen at 0^o, but rather there is a monotonic decay that occurs most rapidly at low magnetic fields (30-150 G). This lineshape does not change dramatically as a function of θ, and is similar to the decay seen in diamond N-V luminescence when θ is large [115]. Similar results were observed for PL3 and PL5. This indicates that PL3, PL4, and PL5 all originate from basal defects with defect axes at large angles to the c-axis, as is also implied by the ODMR data in Figure 4.7. Ultimately, these results indicate that the previously observed divacancy defects studied in the literature correspond to the behavior observed here as indicated by their luminescence spectra and orientations.

With systems involving singlet-triplet transitions it is important to have some idea of the relative ordering of the states in order to determine the system ground state. Inconsistent determinations of this ordering led to previous controversies as to whether the NV center was a triplet ground state or triplet intersystem crossing ('phosphorescent triplet state'). In

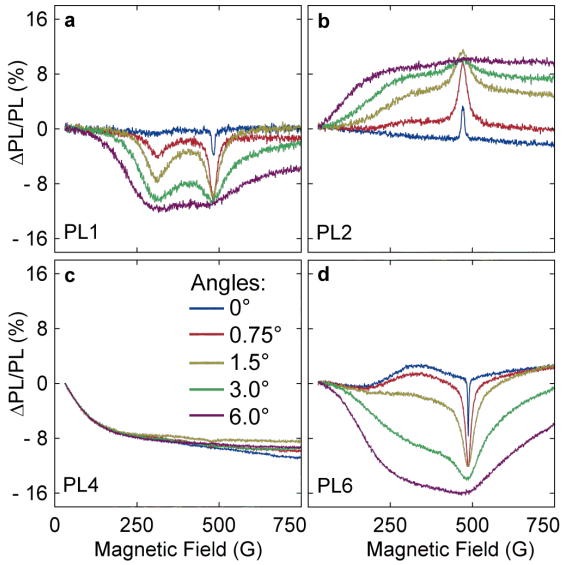

Figure 4.5: Level anti-crossing data for 4 divacancy species in 4H SiC

order to rule out the possibility of system being a phosphorescent triplet state, we performed optical lifetime measurements using a superconducting nanowire detector. Phosphorescent states generally have long lifetimes in the microsecond to millisecond range, whereas the NV center has a lifetime ~12 ns. Figure 4.6 shows the fluorescence decay curves for PL1-PL6. The optical lifetimes for PL1-PL6 are measured to be 15 ns, 15 ns, 12 ns, 14 ns, 13 ns, 14 ns respectively, with uncertainties of 3 ns coming from the fits. The data are horizontally offset for clarity.

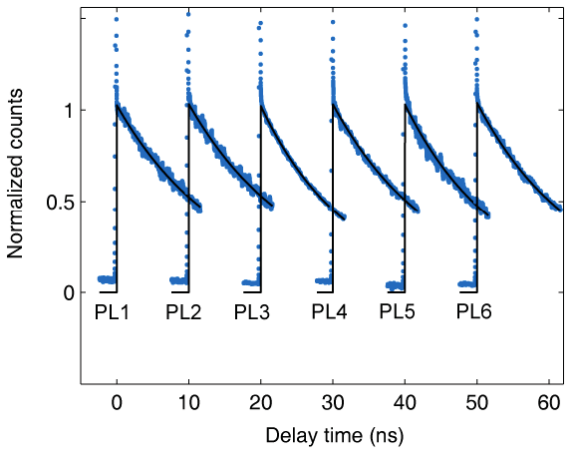

Figure 4.6: Photoluminescence decays curves for PL1-PL6 when excited with a pulsed Ti:Sapphire laser and measured with superconducting nanowire detector.

4.6 ODMR in 4H SiC

ODMR data taken from an ensemble of defect spins at 20K are shown in Figure 4.7. The direction of the microwave driving field varied across the spin ensemble, so that spins oriented in any direction could be driven in the same field geometry. An ODMR scan in which the microwave frequency was varied between 0-2 GHz can be seen in Figure 4.8. In this case, all PL in the 900-1700 nm range was collected for the measurement. If we spectrally filter the luminescence collected during the ODMR measurement, we can determine which spin resonances are associated with each one of the six ZPL features labeled in Figure 4.4. Spin resonances are observed when isolating all six lines. In Figure 4.7 we see a sharp decrease in PL1 lumi-

nescence resulting from microwave-induced transitions between sublevels of the (hh) c-axis divacancy ground state spin. The central frequency of this resonance corresponds to the axially symmetric spin splitting (D) of this defect spin state. There is a similarly shaped increase in PL2 luminescence centered at a frequency corresponding to D for the other form of the c-axis divacancy, (kk). The two center frequencies agree with published values for the axially symmetric spin splitting (D) of P6b and P6'b, which have been identified as the ESR signatures of the (hh) and (kk) forms of the divacancy respectively. Additionally, the locations of the satellite features are consistent with previous observations of P6b/P6'b hyperfine resonances induced by neighboring ^{29}Si nuclei. [112] [111]

A pair of resonances is observed Figure 4.7, which show ΔPL/PL for PL3 and PL4, respectively. Each figure corresponds to one of the two basal forms of the divacancy. Owing to the hexagonal crystal structure of 4H-SiC, these basal defects possess a lower symmetry than their c-axis counterparts and have their vacancy-vacancy axis mis-aligned with the c-axis. Their ground state spins therefore exhibit a transverse anisotropy spin splitting (E) in addition to D. This results in two zero-field resonances at frequencies defined by (D $\pm$ E). The two PL4 resonances are located at 1.3156 and 1.3528 GHz, while the PL3 resonances are at 1.140

and 1.304 GHz, all at 20 K. This puts the midpoints between each pair of resonances at 1.3342 and 1.222 GHz, which are close to published values of D for P7b and P7'b respectively. We measure E, which corresponds to half the distance between a pair of resonances, to be 18.6 and 82 MHz for PL4 and PL3 respectively. This is substantially different from recently reported values of 270 and 30 MHz [112] [111]. The reason for this discrepancy is unclear, but observed values of E for the basal divacancies vary throughout the literature, in some cases changing drastically due to sample misalignment during measurement. [33]

PL5 and PL6 also give rise to ODMR signals in this frequency range. The PL6 resonances in Figure 4.7 have a similar shape to those of the c-axis divacancies (PL1 and PL2), suggesting perhaps that all three originate from a similar defect structure and orientation, and are centered at 1.3650 GHz at 20 K. For PL5, two separate resonances are found at 1.3559 and 1.3689 GHz (Figure 4.7), and so resemble the basal divacancy orientations (PL3 and PL4) which have both D and E terms. Some of the spin resonances seen in Figure 4.7 manifest as decreases in luminescence, while others appear as increases. This suggests that the spin selection rules that lead to optical spin polarization vary by defect type [116]. However, in all cases, both unknown defect species represented by PL5 and PL6 have spin

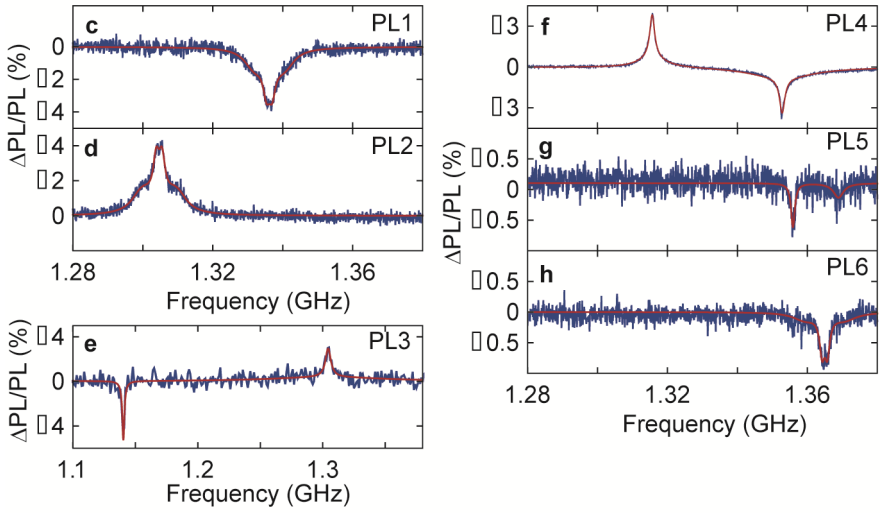

Figure 4.7: ODMR signature of the 6 observed divacancy related defect species in 4H SiC.

resonances which decrease the defect luminescence.

In figure 4.9, we track the ODMR resonance frequencies of all three c-axis defects as a function of magnetic field applied along the c axis of the crystal. Each of the zero-field ODMR features observed in figure 4.9 results from two degenerate spin transitions. At non-zero fields these degenerate transitions split apart by an energy expected from a spin 1 Zeeman model. All three resonances exhibit a linear magnetic field dependence with a slope of magnitude $\sim 2\mu_B/h$. Figure 4.9 is therefore consistent with previous data linking PL1 and PL2 to the neutral c-axis divacancy, a defect which has a spin 1 ground state with a g-factor of 2.003 [112] [111]. Because this data is optically detected, it cannot be used to conclusively determine the spin

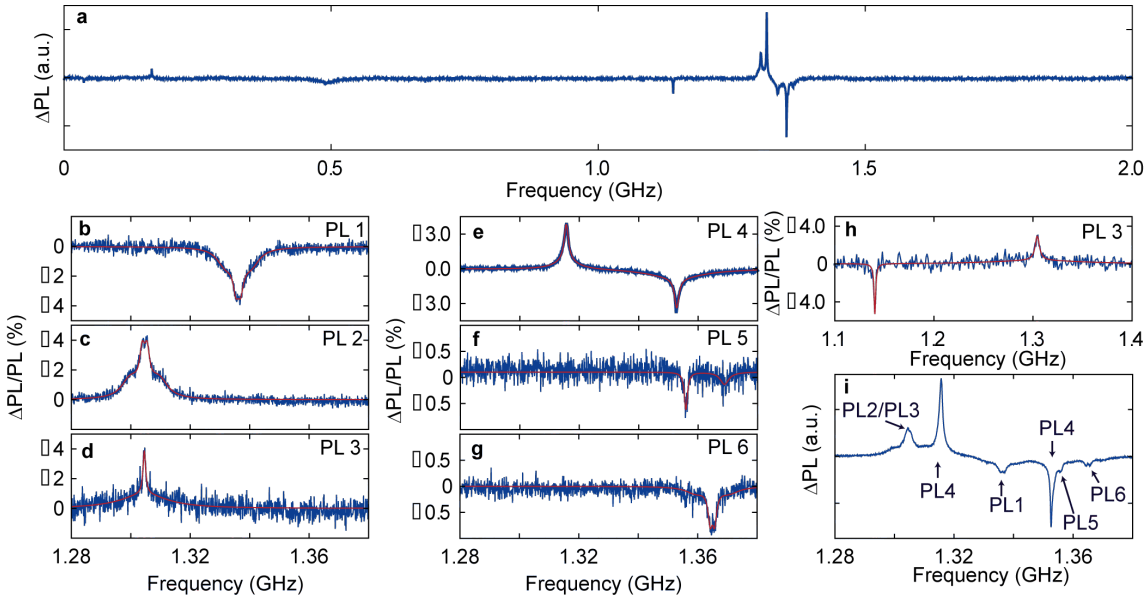

Figure 4.8: ODMR spectrum from 4H SiC through the whole range of 0-2 GHz.

state of the resonance associated with PL6. That is to say that a slope of magnitude $2\mu_B/h$ is consistent with any $\Delta m_S = \pm 1$ resonance for which the g-factor is ~2. Therefore, while we may tentatively identify the PL6 resonance as a spin 1 system due to the many similarities it shares with the PL1 and PL2 resonances, we can only say conclusively that it is a spin system with S>1/2.

The observed ODMR resonances do not respond uniformly to elevated temperatures. In Figure 4.10, we see the temperature dependence of the zero-field ODMR features shown in Figure 4.7. We see that the PL3/PL4 (basal divacancy) resonances are no longer observed at 100 K,

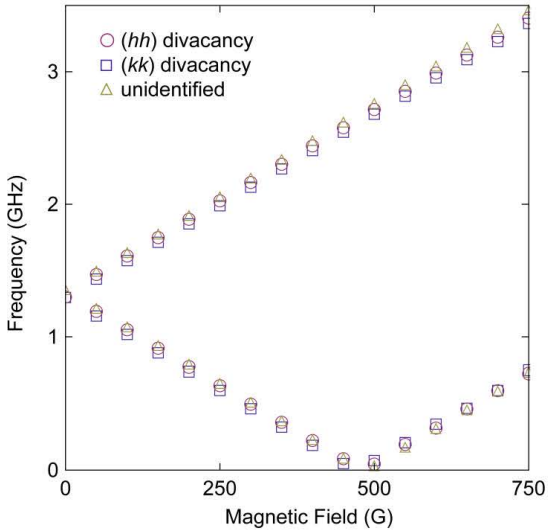

Figure 4.9: Positions of ODMR resonance frequencies for c-axis defects with a magnetic field applied along the defect symmetry axis.

while the PL1 and PL2 (c-axis divacancy) resonances begin to decrease in magnitude at 250 K and 200 K respectively. The PL5 and PL6 resonances persist to room temperature, and decrease in magnitude by only about 30% between 20-300 K. These resonances correspond to the basal and c-axis unidentified defects, respectively.

4.7 4H SiC Spin Dynamics

In order to characterize the spin dynamics of the various divacancy-related defects in 4H SiC, we switch from continuous wave measurements

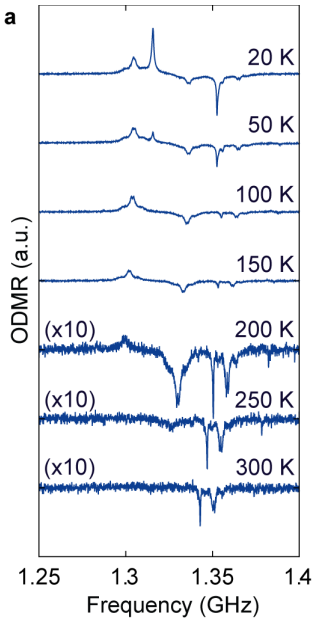

Figure 4.10: Temperature dependence of the divacancy-related ODMR features in 4H SiC.

to pulsed measurements. Pulsed measurements are primarily undertaken through modulation of the applied microwave signal through the use of high bandwidth microwave switches. These switches are controlled by the output of a digital delay generator or an arbitrary waveform generator. Figure 4.11 shows the pulse pattern we use for various spin dynamics measurements.

These measurements were performed using a high sensitivity femtowatt photo receiver with a fairly high sensitivity and low noise equivalent power (7.5 x 10^{-15} W/Hz$^{1/2}$). However, this received had a very low band-

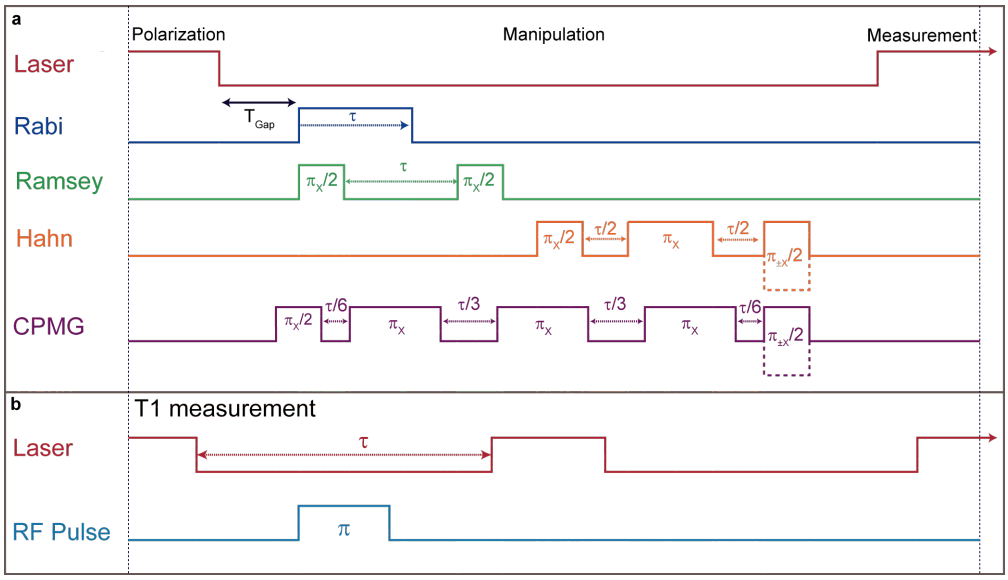

Figure 4.11: Pulse sequences used for coherent manipulation of 4H point defect spin sublevels.

width of about 25 Hz. Accordingly, some spin-dependent aspect of these patterns was modulated and lock-in techniques were used to extract the signal from patterns repeated many times within the modulation period. For ODMR, Rabi, and Ramsey measurements, the microwave signal amplitude was modulated on and off to lock in to the spin dependent signal. For Hahn and CPMG pulse sequences, the phase of the final pulse was modulated using a microwave mixer to perform a lock-in measurement that dependent on the direction of the final spin rotation (what pole of the Bloch sphere the state was rotated to). Each laser pulse both read out the brightness of the defects (and therefore provides a measure of the

spin projection) and then re-polarized the spin state for the next sequence repetition. Most parameters like laser pulse length and relaxation times were optimized empirically.

Rabi oscillation resulting for coherent manipulation of PL4's ODMR transitions are shown in Figure 4.12. We performed this measurement at various powers and observed that the drive frequency increased linearly with the square root of microwave power, as expected from the Rabi formula [117]. A Ramsey pulse sequence [118] is used to observe free induction decay of the same defect ensemble at 20K, and the resulting dynamics are fitted to reveal an inhomogeneous spin coherence time of $T_2* = 1.44 \pm 0.02$ μs for the ground state spins. The Ramsey decay oscillates because the driving field was detuned from resonance by 3.33 MHz. Data from Hahn echo and 3-π pulse Carr-Purcell-Meiboom-Gill (CPMG) pulse sequences [118] are shown as well, revealing homogeneous spin coherence times of $T_2 = 184 \pm 1$ μ s and $T_{CPMG} = 357 \pm 3$ μs at 20K in our samples. This is the same order of magnitude as T_2 for diamond nitrogen vacancy center ensembles surrounded by a spin bath composed of ^{13}C nuclear spins and background paramagnetic impurities [99].

The c-axis forms of the neutral divacancy offer a more direct comparison to the diamond nitrogen vacancy center because they share the same

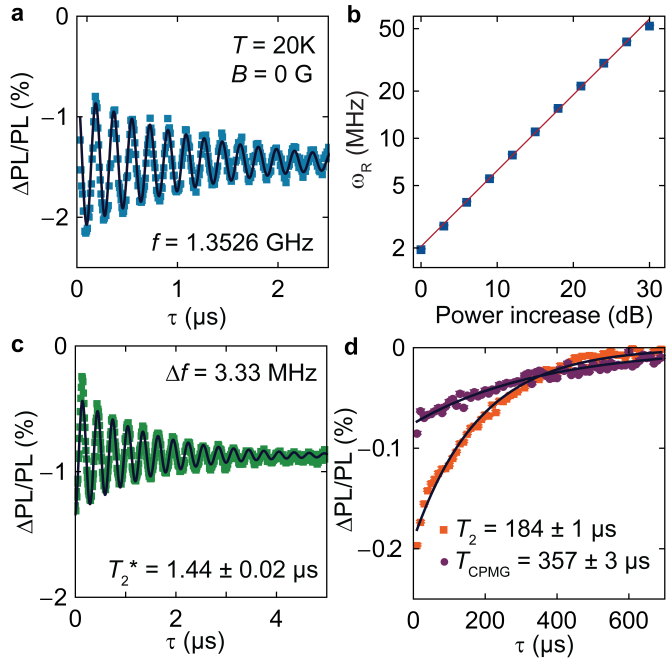

Figure 4.12: Rabi, Ramsey, and Hahn spin dynamics curves in 4H SiC. Also, the measured power dependence of the measured Rabi frequency.

symmetry and are predicted to have a similar electronic structure [113]. Rabi and Ramsey oscillations are shown for the (hh) divacancy at 200K and 52G in Figure 4.13. Periodic modulations of the Hahn echo envelope are observed in 4.13 that appear when a magnetic field is applied along the c-axis of the crystal. These modulations increase in frequency as the magnetic field is increased, and fits to the data at a given field reveal that they contain two frequency components equal to the Larmor frequencies of ^{29}Si and ^{13}C nuclei. These modulations therefore represent coherent interactions between the (hh) divacancy spins and the surrounding nuclear spin

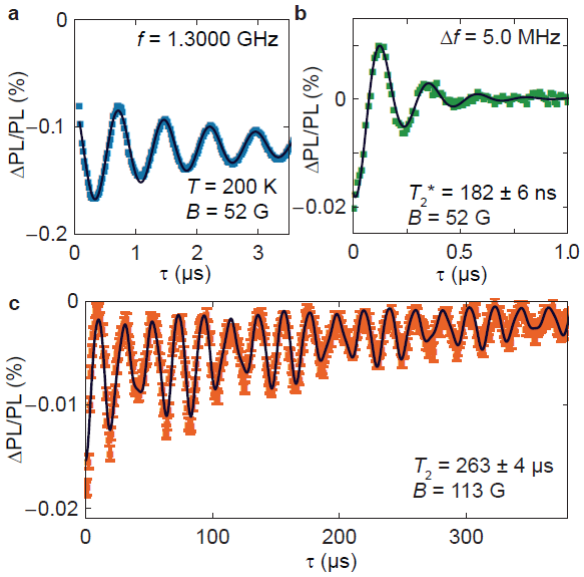

Figure 4.13: Rabi, Ramsey, and Hahn spin dynamics curves for c-axis divacancies at 200K.

bath [119], similar to what has been observed for nitrogen vacancy centers [101].

Similar measurements were performed on the unidentified defects corresponding to PL5 and PL6 at room temperature, a shown in Figure 4.14 and Figure 4.15 . These measurements were made at 300K and 0 G, with an in-plane driving field along the $<1\bar{1}00>$ crystal direction. Although the c-axis defect spins oscillate at one frequency, the basal defect spins do not. This beating effect is observed because the basal defect spins exist in three orientations that couple unequally to the in-plane driving field. The Hahn echo measurements also show coupling to nuclear species for these defects

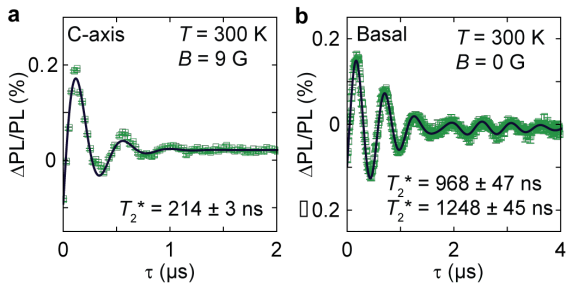

Figure 4.14: Room temperature Ramsey decays of the unidentified defects in 4H SiC.

and this fact maybe applied to identifying these defects, similar to previous work performed to definitively identify the divacancy. [120]

4.8 Other Forms of SiC

Initial studies on divacancy related defects in SiC were limited to 4H SiC primarily due to the fact that high purity, semi-insulating wafers purchased directly from CREE already contained divacancy related defects. However, there are two other forms of SiC that are ready available as commercial products: forms termed '6H' and '3C'. Like 4H, 6H begets this label due to the periodicity of the stacking of its hexagonal layers. 3C, on the other hand, can still be formed from stacking 3 repeated hexagonal layers but this results in a cubic, zincblende structure so it is labeled with a 'C'. See Figure 4.16 for a depiction of the different stackings.

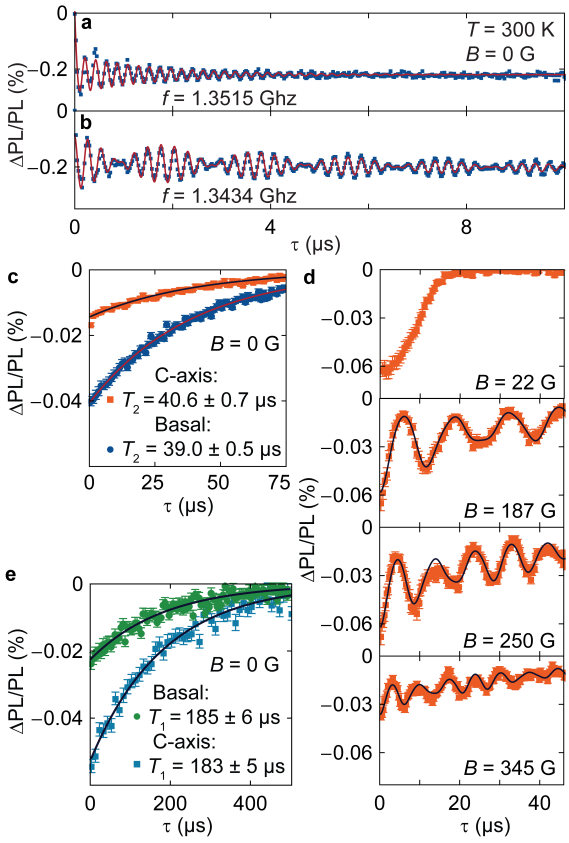

Figure 4.15: Room temperature Rabi oscillations, Hahn echo decays, T1 measurements, and nuclear Hahn echo modulation for the unidentified defects in 4H SiC.

Figure 4.17 shows a comparison of the infrared zero phonon lines for implanted 4H, 6H, and 3C crystals. All three crystals show what is likely divacancy related (this still needs to be definitively proven for 6H and 3C SiC) luminescence throughout this energy range with a number of PL lines equal to the number of inequivalent lattice sites, aside for the two unidentified lines PL5 and PL6 in 4H SiC. In other words, 6H has 6

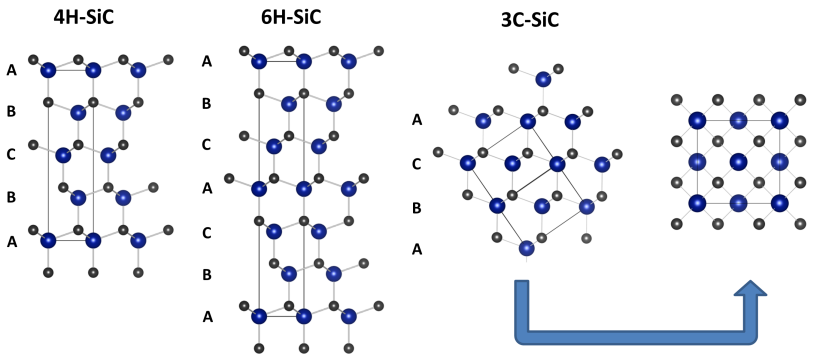

Figure 4.16: Depiction of how the different crystal stackings leads to the bulk crystal structure of the three most common forms of SiC.

inequivalent possible divacancy lattice site while 3C has just one. For the remainder of this section, we will focus on 6H as 3C will be discussed in a later chapter.

Figure 4.18 shows a broader spectrum of the 6H defects. The spectrum looks qualitatively similar to the wide 4H shown earlier. One initial reason we did not study 6H further was the presence of a series of lines related to vanadium out past 1300 nm. These lines result from vanadium incorporated into the growth in order to produce insulating material (to compensate for residual n-dopants). Typically these lines have presented a bright background that swamped defect PL. In this plot, we electron irradiated sample at an extremely high electron dose of 10^{18} electrons per square centimeter in order to produce bright 6H PL. This spectrum was

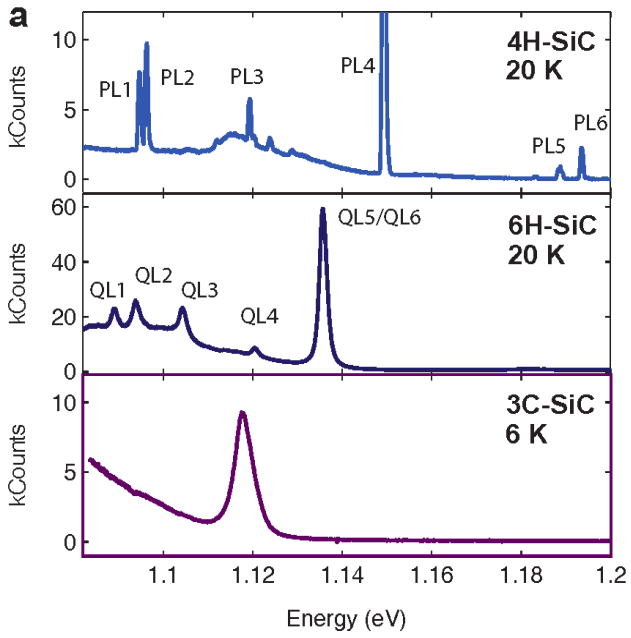

Figure 4.17: Comparison between the different divacancy-related zero phonon lines of the three most common forms of SiC.

taken with a 1 second exposure and was the brightest sample we have yet to produce in SiC. Alternatively, the problems associated with the vanadium emission can be alleviated with the right lock-in detection parameters.

Similarly, 6H SiC shows a series of ODMR lines through the 1.1 to 1.5 GHz range (see Figure 4.19). As with 4H, some of these lines are c-axis defects and some are basal, as can be seen by the non-uniform splitting in the magnetic field dependent plot. Additionally, some lines persist up to room temperature.

These defects seem to exhibit similar spin polarization cycles as the

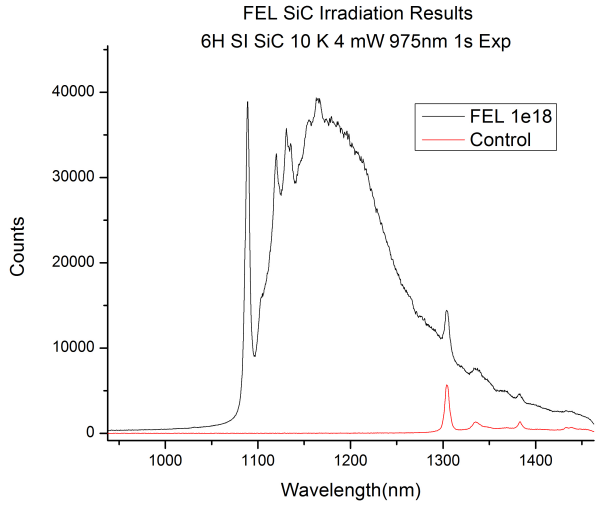

Figure 4.18: Photoluminescence spectrum of highly electron irradiated 6H SiC.

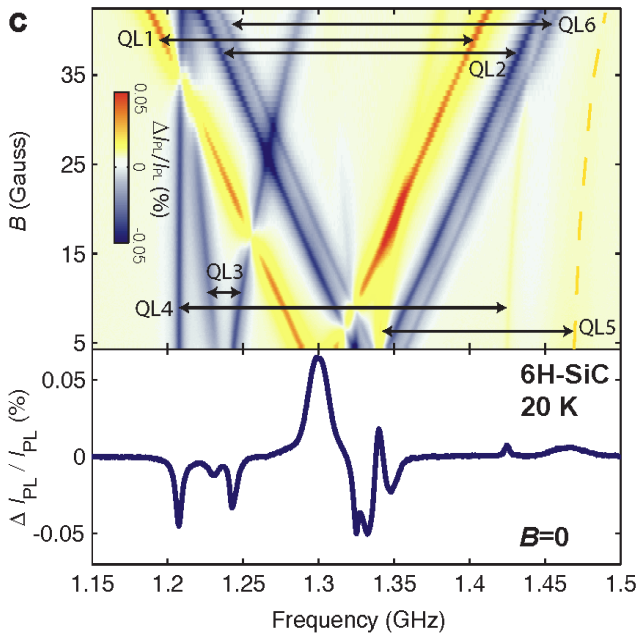

Figure 4.19: Low field ODMR spectrum of defects in 6H SiC. .

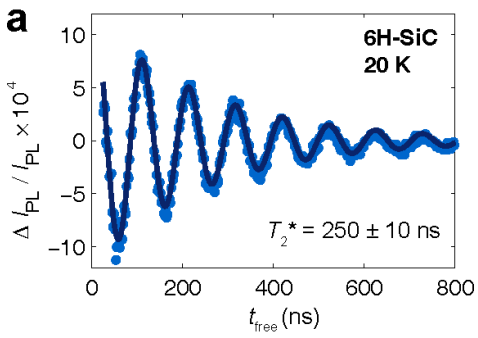

Figure 4.20: Rabi oscillations of divacancy related defects in 6H SiC.

4H defects and thus can be coherent controlled as well, as shown in figure 4.20.

Figures 4.21 and 4.22 show Hahn echo decays for the 6H defects and a summary of their coherence times for different implantation doses, respectively.

The table shown in Figure 4.23 summarizes the 'zoo' of defects in each of the three common polytypes of SiC and their basic properties.

4.9 Defect-Defect Interactions in 6H SiC

One of the additional functionalities available in SiC that is not readily available in diamond is the presence of multiple optically addressable electronic state that can be independently controlled and measured within

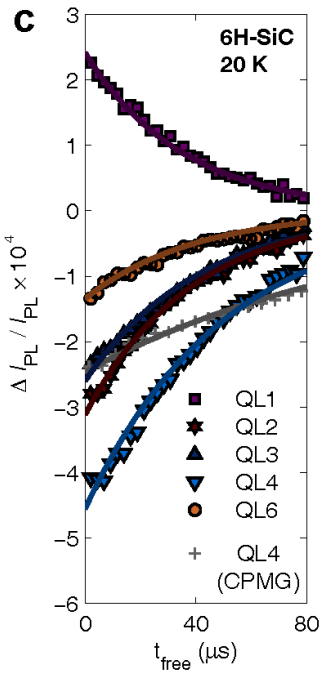

Figure 4.21: Hahn echo decay curves measured for divacancy related defects in 6H SiC.

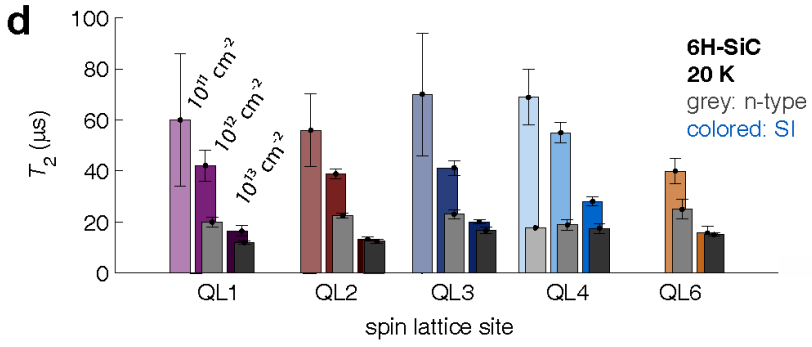

Figure 4.22: Summary of Hahn echo coherence times for defects in 6H SiC for different implantation doses.

PL/ODMR label	Otherwise known as....	Identification	Orientation	optical energy (eV)	ODMR 1 (GHz) (*)	ODMR 2 (GHz) (*)	D (GHz)	E (GHz)	room temp?	20K?
				4H-SiC						
PL1	P6b	(hh) divacancy	c-axis	1.095	1.336	-	1.336	< 1 Mhz	implanted	yes
PL2	P6'b	(kk) divacancy	c-axis	1.096	1.305	-	1.305	< 1 Mhz	no	yes
PL3	P7b/P7'b	basal divacancy	basal	1.119	1.140	1.304	1.222	0.082	yes	yes
PL4	P7b/P7'b	basal divacancy	basal	1.150	1.316	1.353	1.334	0.019	no	yes
PL5		unknown	c-axis	1.189	1.356	1.389	1.373	0.017	yes	yes
PL6		unknown	basal	1.194	1.365	-	1.365	< 1 Mhz	yes	yes
PL7		unknown	basal	-	1.333	-	-	-	yes	yes
				6H-SiC						
QL1		UD-2	c-axis	1.088	1.300	-	1.300	< 1 Mhz	no	yes
QL2		UD-2	c-axis	1.092	1.334	-	1.334	< 1 Mhz	yes	yes
QL3		UD-2	basal	1.103	1.228	1.243	1.236	0.008	yes	yes
QL4		UD-2	basal	1.119	1.208	1.425	1.317	0.109	no	yes
QL5		UD-2	basal	1.134	1.340	1.465			yes	yes
QL6		UD-2	c-axis	1.134	1.347	-	1.347	< 1 MHz	no	yes
QL7		unknown	c-axis	-	1.345 (**)	-	1.345 (**)	< 5 MHz	yes	no
QL8		unknown	c-axis	-	1.371 (**)	-	1.371 (**)	< 5 MHz	yes	no
QL9		unknown	basal	-	1.332 (**)	1.365 (**)	1.349 (**)	.017 (**)	yes	no
				3C-SiC						
RL1	Ky5	unknown	[111]	1.12	1.336		1.336	< 1 Mhz	Substrate-dependent	yes

* At *B*=0 and at 20K, unless noted.
** Room temperature frequency. ODMR lines not visible at low temperatures.

Figure 4.23: A summary of the various properties of the divacancy-related defects in the three most common forms of SiC.

the same optical excitation spot. This allows for the use of techniques like Double Electron-Electron Resonance (DEER) to studying how multiple defects spin species interact in the same crystal. Figure 4.24 shows the measurement scheme used to perform this experiment and the resulting behavior.

Figure 4.24 (a) shows an example of a Hahn Echo sensing technique

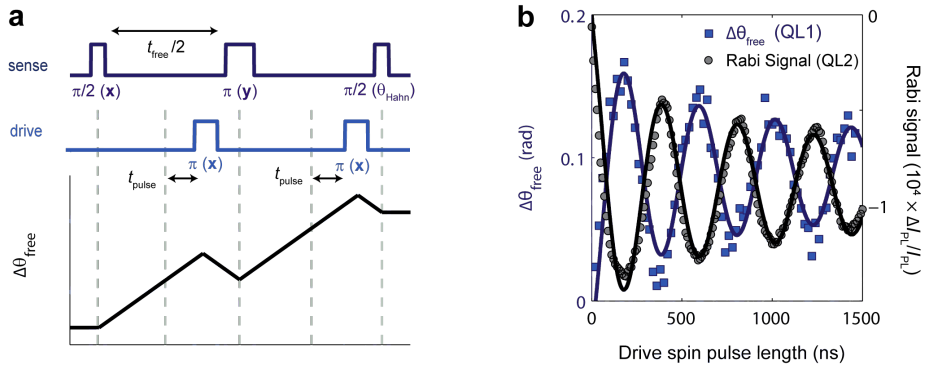

Figure 4.24: DEER measurement scheme (a) and corresponding Rabi and DEER signals for the QL1 and QL2 defects (b).

that uses one defect species to sense a second 'driven' species. The first 'sense' species accumulates phase that is proportional to the spin polarization of the 'drive' species, which is flipped during the pulse sequence to perform a sensitive AC measurement of the interaction. The DEER signal can be express as:

$$DEER\,Signal = \cos(2\pi\Delta f(2t_{pulse}) + \theta_{Hahn})e^{-2t_{pulse}/\tau} \tag{4.1}$$

where Δf is the frequency shift due to the drive species that results in the phase accumulated for the sense species. Figure 4.24 (b) shows the complementary DEER signal on the 'sense' species and the driven Rabi oscillations of the 'drive' species. This demonstrates one of the first realizations of new experimental functionalities that SiC exhibits that is not easily accessible in diamond based systems.

4.10 High Purity Material and Single Defects

Of course, all measurements shown previously were performed on large ensembles of defects. For almost all applications of defect qubits, one would prefer to work with single sites for spatial resolution for sensing and single photon emission for quantum applications. This milestone has recently been reached in high purity material obtained from collaborators with extremely low background impurity and structural defect densities. See Figures 2.9 and 2.10 for spatial scans of isolated emitters in 4H SiC and the corresponding anti-bunching curve demonstrating that the sites are indeed single emitters, respectively. This milestone can be further combined with controlled patterning of implanted spins demonstrated in [32] and [121] (see Figure 4.25) to controllably fabricate single defect qubits and incorporate them into device geometries.

Additionally, samples from the same source with high defect densities showed very long coherences times, even in excess of 1 ms (See Figure 4.26). This value is comparable to what has been achieved for single NV centers in isotopically purified diamond [100]. This material, however, consists of ensemble measurements with a non-zero nuclear background.

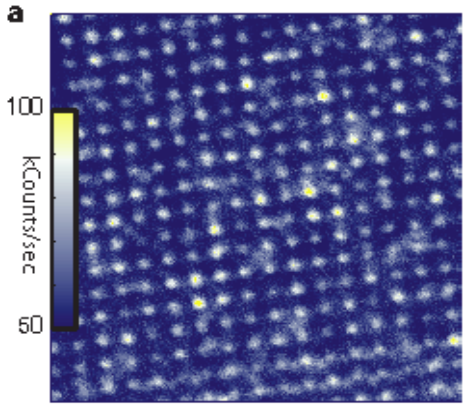

Figure 4.25: An array of ensembles of defects implanted through a hard mask in 4H SiC.

This further adds to the promise shown by defects in silicon carbide for most applications currently being pursued for the diamond NV center.

4.11 Conclusions

This early work on NV center analogues in SiC demonstrates the potential benefits of finding new defect qubit systems. Although much is still unknown regarding the defects' properties, they appear to be in many ways comparable to the NV center in a material with many added benefits. The presence of multiple defect species allows for the study of interacting ensembles of spins [121] and some of the defects' sensitivity to external parameters are greater than for the NV center [122]. However, 4H and 6H

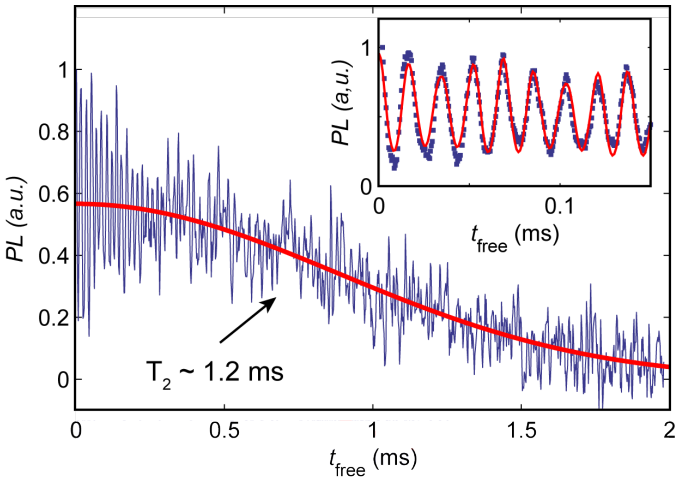

Figure 4.26: Hahn echo decay curve for an ensemble of defects in high purity 4H SiC demonstrating very long spin coherence times. Plot courtesy of D. Christle.

SiC are still only available as bulk materials without an underlying sacrificial layer, a fact that limits one's ability to easily make devices out of these crystals. A combination of the 'smart-cut' technique and high temperature annealing may allow for production of devices [123] with high quality defect spins. This has not yet been demonstrated, so a more straightforward approach is to use the form of SiC already available as a heteroepitaxial film: 3C SiC.

Chapter 5

Defect Qubits in 3C Silicon Carbide

Some figures and sections of this chapter are adapted with permission from the publications: "Polytype control of spin qubits in silicon carbide," A. L. Falk, B. B. Buckley, G. Calusine, W. F. Koehl, V. V. Dobrovitski, A. Politi, C. A. Zorman, P. X.-L. Feng, and D. D. Awschalom, Nat Commun **4**, *1819 (2013) and "Silicon carbide photonic crystal cavities with integrated color centers," G. Calusine*, A. Politi*, and D. D. Awschalom, Applied Physics Letters* **105**, *011123 (2014).*

5.1 Motivations

The primary reason for searching for NV center analogues in other

materials is to access defect and host functionalities that are either very hard or impossible for the NV center in diamond. As discussed previously, the lack of heteroepitaxy is a significant challenge for incorporating NV centers into devices in diamond. 3C SiC has a significant advantage over diamond not only because it grows heteropitaxially, but also because the preferred growth substrate is silicon. This opens up the possibility of using the many cleanroom processes and tools thats were developed for silicon-based processes for building 3C SiC devices. Hence we began this line of research in order to pursue these possibilities and potentially develop a truly scalable defect qubit device architecture.

One added benefit of working with SiC over diamond is the fact that large amounts of material is commercially available for a relatively low cost. Aside from the obvious device scaling arguments, having access to large sample areas makes almost every aspect of fabrication and process development much easier as compared to working with samples that are on the millimeter scale. Figure 5.1 compares the size of a typical diamond sample with a commercially available 3C SiC on Si wafer.

An area of diamond samples equivalent to the wafer area of the pictured 3C SiC wafer would cost approximately 2.2 million USD, as compared to a price of ~1000 US dollars for the SiC wafer. Figure 5.2 shows a

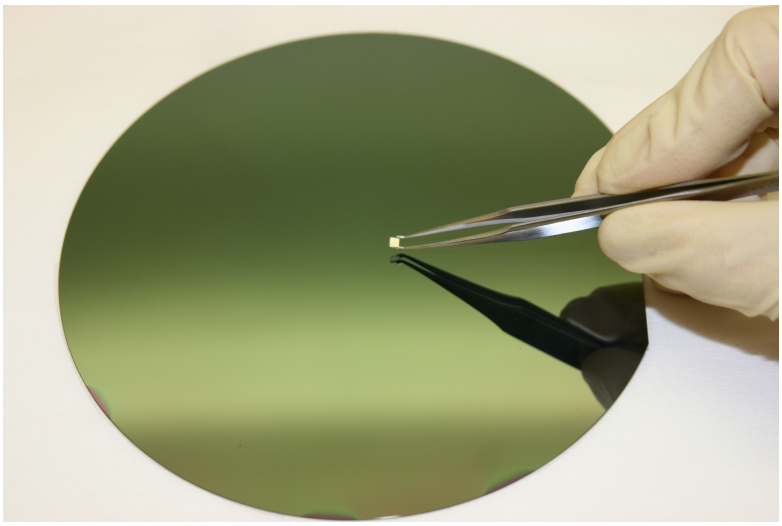

Figure 5.1: Comparison between a typical diamond sample and a commercially available wafer of 3C SiC

3C SiC wafer being used to admire the author's beautiful face.

5.2 Previous Work

Due to its relatively recent production as a high quality film and in contrast to 4H and 6H silicon carbide, there exist very few papers on spin resonance and luminescence of defects in 3C SiC. A PL band similar to the one we observe has been observed previously [38] but was found to be associated with a spin-1/2 ODMR signal. Another study [109] has associated this band with a spin-1 ODMR signal but observed a zero-field splitting 50-80 MHz different than the one we observe and did not determine a spectral dependence for this ODMR signal. The PL bands

Figure 5.2: A 3C SiC wafer reflecting the author's handsome face.

from both of these reports and the spin-1 ODMR signal we observe depend on the sample annealing temperature in a similar manner, indicating that they are likely related. An electron paramagnetic resonance study [124] has observed a spin-1 defect in 3C SiC with zero-field splitting and symmetry similar to the one we observe which persists up to room temperature. It tentatively attributed this signal to a neutral divacancy. This assignment results from the established defect symmetry along the $< 111 >$ axis and the fact that it shares a nearly identical zero field splitting with a form of the divacancy in 4H SiC that has a locally cubic environment. The defect structure is shown in Figure 5.3.

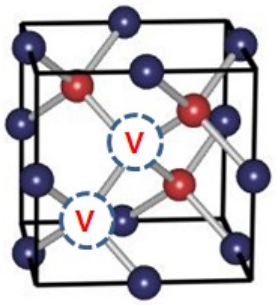

Figure 5.3: The local crystal structure of a divacancy in 3C SiC.

5.3 3C SiC Defect Luminescence

Although heteroepitaxial growth affords a functional advantage for 3C SiC, it also presents complications for certain measurements. The first challenge that presented itself when this research began was the realization that the silicon substrate exhibited bright fluorescence when excited by the near-infrared laser used to excite the SiC defects. This fluorescence originates from near band edge defects and easily swamps the luminescence that originates from the 3C layer. This luminescence is shown in Figure 5.4.

In order to overcome this impediment, we developed a method to remove the underlying substrate and eliminate the background fluorescence. While it is normally a straight forward process to back etch a silicon wafer with a wet etchant like KOH to form a membrane in a heteroepitaxial layer,

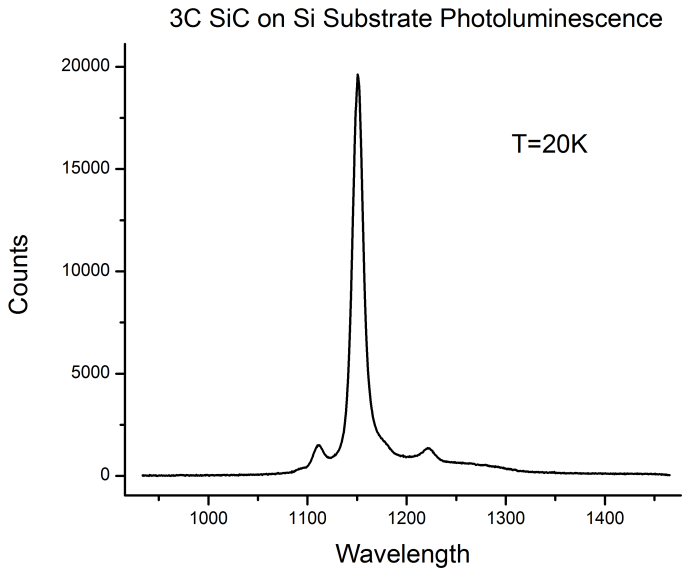

Figure 5.4: Background Si fluorescence originating from the substrate of 3C SiC-on-Si wafers.

this process could not be used for etching completely through a small 4 mm by 4 mm sample without eating away at the sample edges. Instead, we developed a process to pattern the backside of the sample and use the Bosch process to etch through the ~500 micron thick wafer. This process is shown in Figure D.1.

First, the rough backside of the wafer is polished to a smooth finish to promote adhesion of the hard mask. Next, a 3.5 micron thick silicon oxide layer is evaporated onto the backside of the wafer using a low temperature PECVD process. To pattern the hard mask, a thick, 3.3 micron

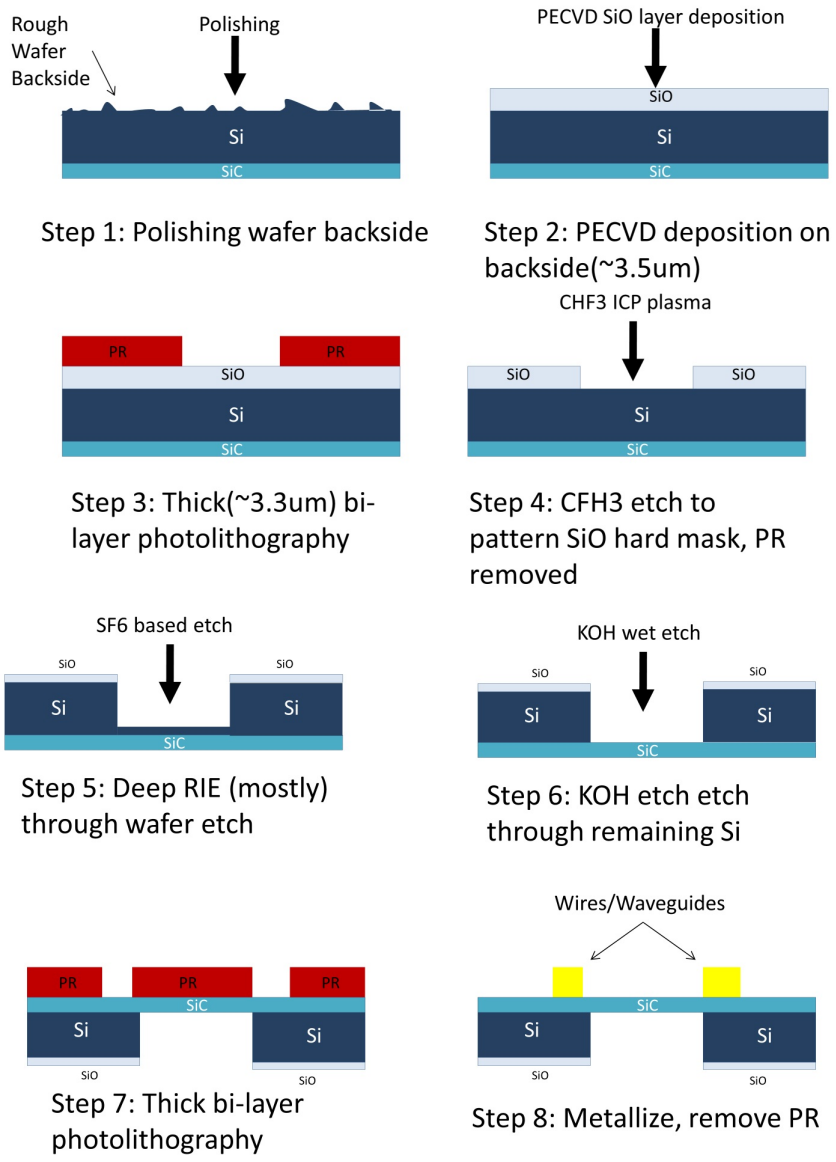

Figure 5.5: Process for creating windows in 3C SiC through a back-etch process.

bilayer photolithography process is used to develop a rectangular window pattern on the wafer backside. The photoresist then masks a CFH3 based etch in order to transfer the pattern to the silicon oxide layer. This layer then acts as another mask to etch the window pattern into the silicon via the Bosch process. This process alternately etches the silicon and passivates the etched sidewalls in order to perform a nearly vertical etch almost all the way through the 500 micron thick wafer. A thin layer of silicon is left on the backside of the window in order to prevent any potential etching of the window by the Bosch process. This was a precautionary measure; no etching of the window by the Bosch process was observed. Next, a brief KOH wet etch is used to remove the remaining silicon on the backside of the window. To finalize the structure for spin dependent measurements, the sample is then processed on the topside of the wafer in order to produce on-chip wires for applying large local magnetic fields to the sample. Figure 5.6 shows an optical image of the resulting free standing membrane.

This process produces a free standing layer with no silicon substrate below it. This process can be preferable to other methods of SiC PL isolation because it allows for the use of non-microscope objectives with large focal depths without the risk of exciting any background fluorescence. Alternately, one can use a thick film and a high NA objective to reject most

Figure 5.6: Free-standing window of 3C SiC surrounded by metallization for optically detector magnetic resonance experiments.

of the Si PL. If one chooses the sample thickness such that the implanted layer is within the focal depth of the lens but the substrate is not, this avoids excitation of the substrate and can reject the majority of the unwanted luminescence. Figure 5.7 shows the spectrum of a thin implanted layer in a 3.85 micron film with confocal excitation and collection. There is a small peak at 1125 nm resulting from the silicon substrate but it is negligible compared to the defect luminescence. Alternately, one can instead perform measurements at 70K. At this temperature, the silicon carbide fluorescence diminishes by only a factor of two from 20K but the silicon

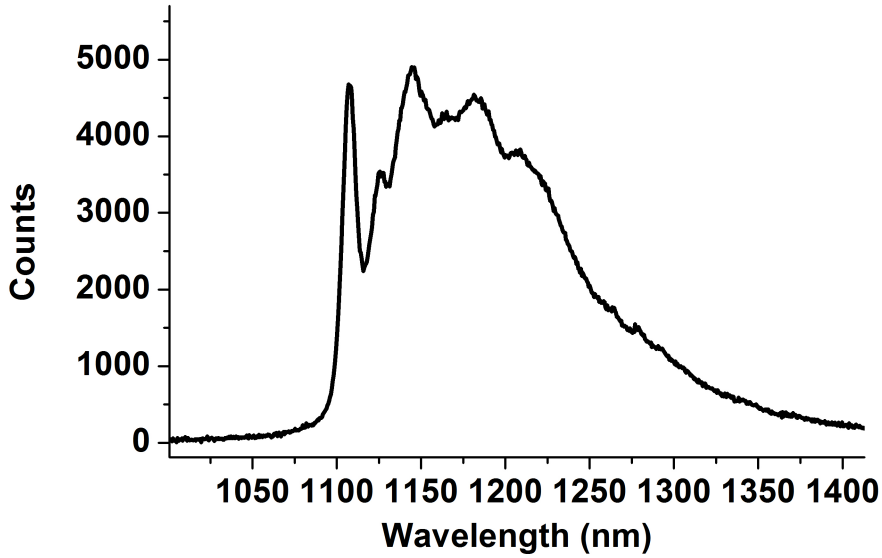

Figure 5.7: PL spectrum of Ky5 centers in a thick 3C SiC film (3.85 microns) taken with confocal excitation and collection.

fluorescence at 1125 nm becomes negligible (see Figure 5.8).

Yet another method to reject the silicon substrate PL applies mainly to materials characterization: UV excitation. As mentioned previously, this method of characterization relies on the fact that far above gap excitation only excites a shallow depth of material due to the high degree of absorption/attenuation of the excitation. This method was used to quickly characterize various doping levels and materials sources without needing to back-etch every sample. The spectra looked qualitatively similar to those shown above. One other implication for this method is the promising fact

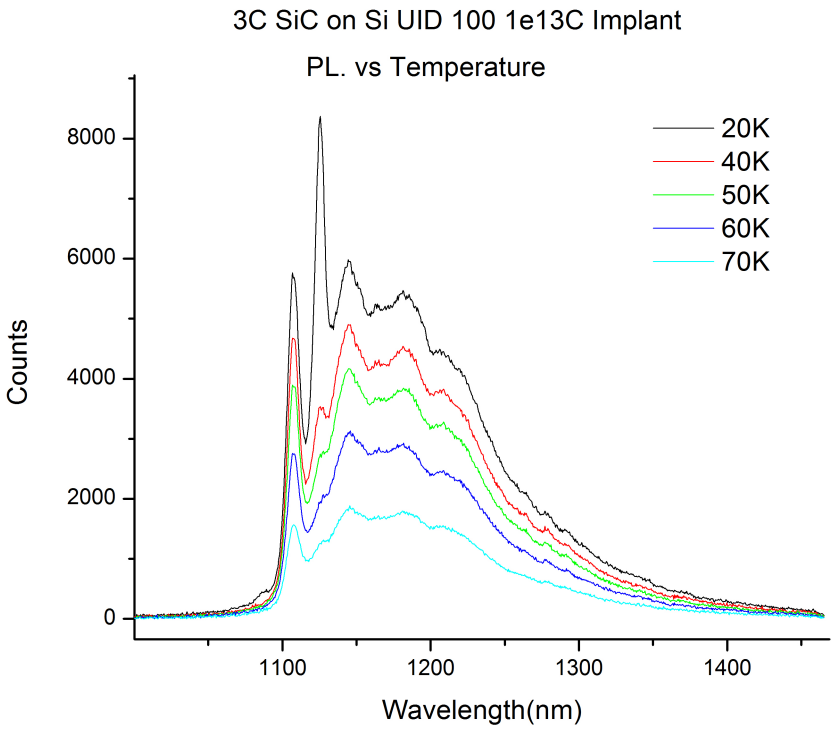

Figure 5.8: Temperature dependence of the Ky5 luminescence band.

that band edge excitation can result in defect emission. This may indicate that electrical pumping of defect luminescence is possible through relaxation processes involving band states.

Another important aspect of the defect luminescence is the difference in the spectrum between thick films and thin films. Due to the 20% lattice mismatch between 3C SiC and silicon, the material quality of the grown film typically improves as the thickness of the film increases. As a result, the material close to the silicon interface typically exhibits large amounts

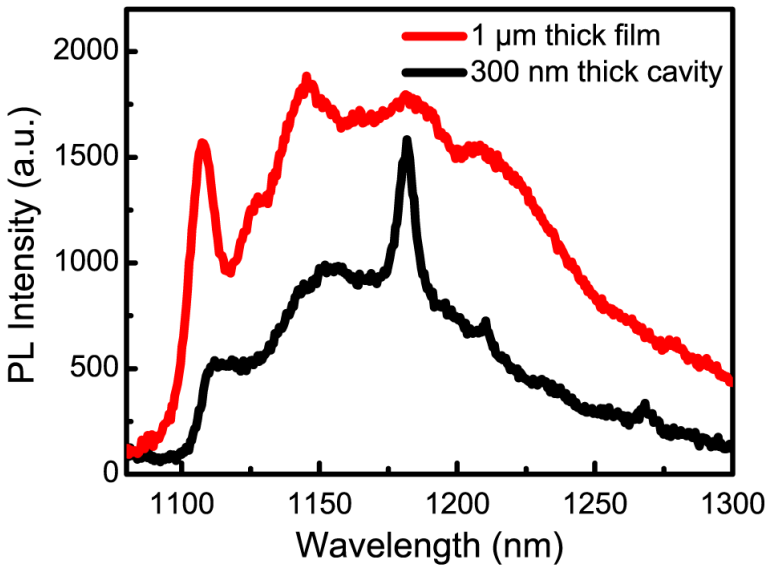

Figure 5.9: A comparison of Ky5 luminescence for a 1 micron thick film and a 300 nm thick film that were implanted with the same recipe.

of inhomogeneous broadening. Figure 5.9 compares the same implantation distribution for a 1 micron thick film with a 300 nm film. This broadening will be discussed further in a later section.

We also performed pulsed excitation studies of the Ky5 luminescence band to verify that it exhibits optical lifetimes comparable to the NV center in order to corroborate the suspicion that it has a triplet ground state. As discussed previously, this is important to verify that the defect level structures isn't instead composed of a meta-stable triplet state. Figure 5.10 shows the photoluminescence decay curve of the Ky5 luminescence band when excited with 150 femtosecond pulses from a Ti:Sapphire laser

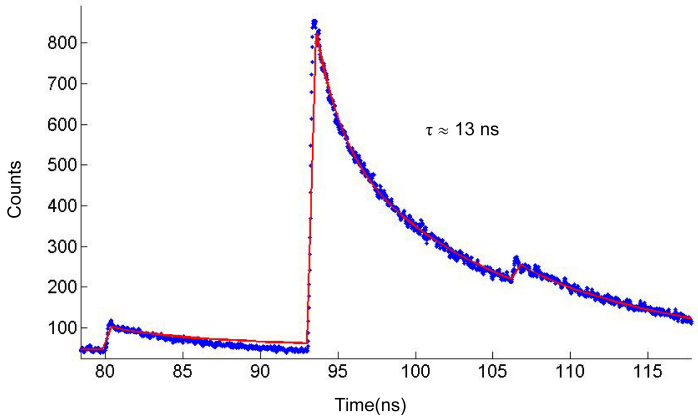

Figure 5.10: Fluorescence decay curve for Ky5 defects demonstrating an optical lifetime similar to the NV center.

tuned to 920 nm. A pulse picker is used to limit the repetition rate of the excitation and the imperfect extinction of the picked pulses yields the observed pulses before and after the main pulse. Like the NV center, this emitter exhibits a decay curve with an approximately 13 ns lifetime.

5.4 Doping and Orientation Variations

One crucial parameter affecting the formation of defects with a given charge state is the Fermi level of the material. While this process is typically well studied theoretically using DFT calculations, it is typically not well studied experimentally. In determining the optimal material for formation of Ky5 centers, we briefly explored the parameter space of available

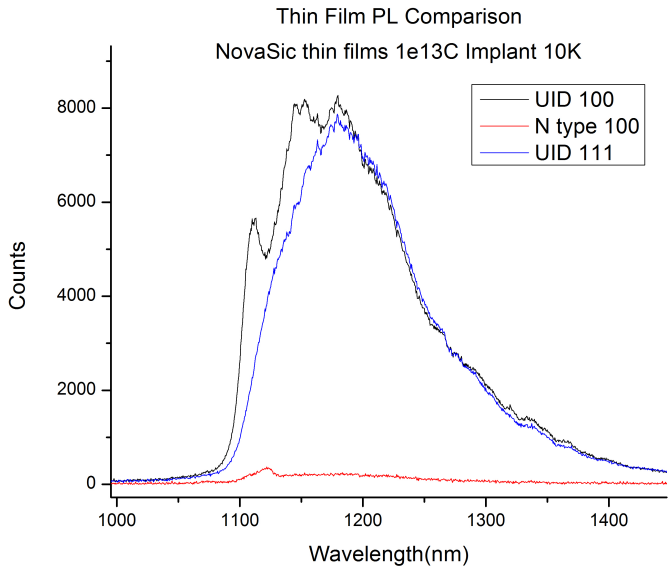

Figure 5.11: Comparison of different doping levels and materials orientations for thin films considered for optical cavity fabrication.

material in order to not waste time on non-optimal material. Figure 5.11 shows a comparison of PL from thin films (~300 nm) for different wafers obtained from NovaSic. The black curve corresponds to unintentionally doped (nitrogen dopants at a density of below 10^{16} per cubic cm), 100 oriented material we primarily focused on, the red curve to N-type material (nitrogen dopants at a density of approximately 10^{19} per cubic cm), and the blue curve to unintentionally doped (nitrogen dopants at a density of below 5×10^{16} per cubic cm) $< 111 >$ oriented material.

In general, it was observed that the more highly N-doped the ma-

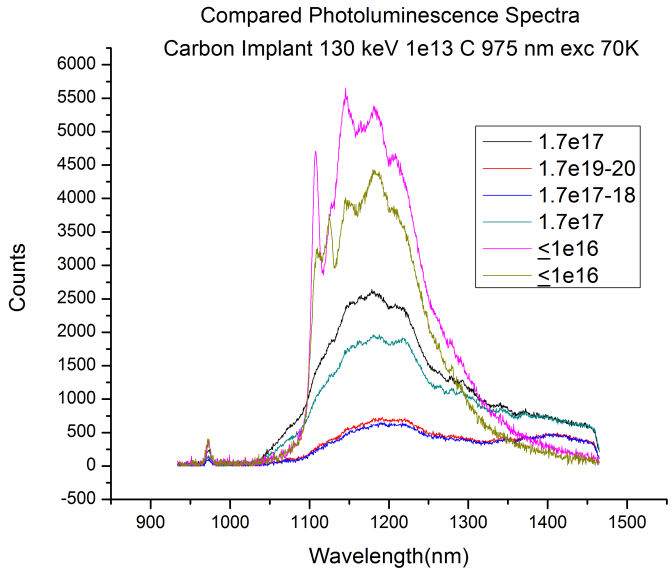

Figure 5.12: Comparison of Ky5 defect PL for different doping levels for material of the same orientation.

terial was, the weaker the defect PL (and therefore, the lower likelihood of defect formation in the proper charge state or stronger non-radiative pathways). Figure 5.12 compares material for a variety of different doping levels, although the first four colors originated from a collaborator in Australia. The two lowest doping levels are both from NovaSic. The yellow curve is for a 1 micron thick layer while the pink curve is for a 3.85 micron thick layer.

Additionally, it is noteworthy that some samples showed distinct zero phonon lines while others did not. The main clue as to the origin of

this behavior comes from the Novasic material comparisons. $< 100 >$ and $< 111 >$ oriented material showed comparable amplitudes for the phonon sidebands but the $< 111 >$ material exhibited no distinct zero phonon line. Since $< 111 >$ films generally exhibit more structural defects than $< 100 >$ material, it is likely that residual strains and inhomogeneous broadening is the source of this difference in spectra.

5.5 Low Temperature Spin Properties

Similar to divacancy related defects in the other forms of SiC, the Ky5 center exhibits an optically detected magnetic resonance line in the low GHz range around 1.33 GHz. The exact value of this resonance depends on temperature and local strain. Figure 5.13 shows the zero field continuous wave ODMR signal from Ky5 emission band at 6K. Also shown is the magnetic field dependence of this signal for a small magnetic field applied along the 100 axis. In contrast to the other forms of silicon carbide, the Ky5 defect exhibits only one PL and ODMR line because, like the NV center, it has 4 equivalent lattice sites along the $< 111 >$ axes of the cubic 3C SiC crystal. In this case the field is not parallel to the symmetry axis of the defect and for larger fields would cease to exhibit a linear splitting. This does, however, confirm the expectation that this single line splits into only

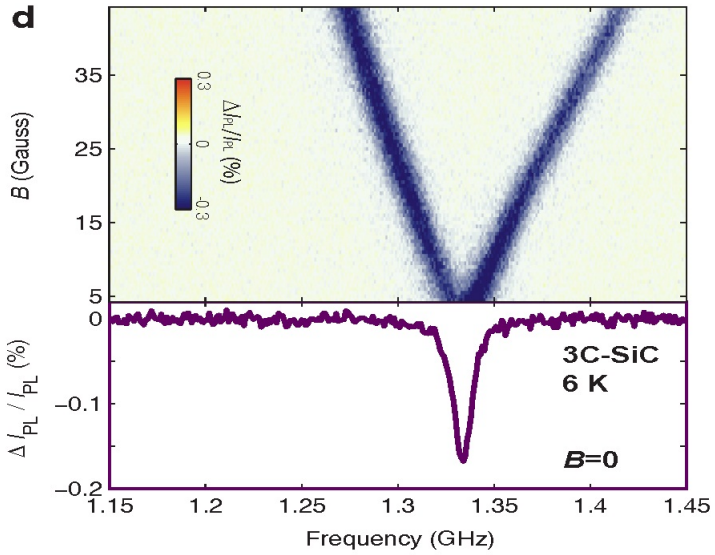

Figure 5.13: Low field ODMR for Ky5 defects with a field along the $< 100 >$ axis.

two lines for this field geometry since all four site experience an equivalent magnetic field projection on and off the defect axis. Later measurements with a magnet along the $< 111 >$ axis further confirm the expected orientation dependence of the ODMR splittings. The magnitude of the PL change is largely limited by the measurement technique used and should not be considered the maximal contrast observable for ensembles of single defects. We typically observed a 10 to 30 times higher PL contrast with better laser rejection and higher sensitivity detection using the SNSPD, and even this value may be improved further.

Figure 5.14 shows the spectral dependence of this ODMR signal. This measurement confirms that the ODMR signal corresponds to observed

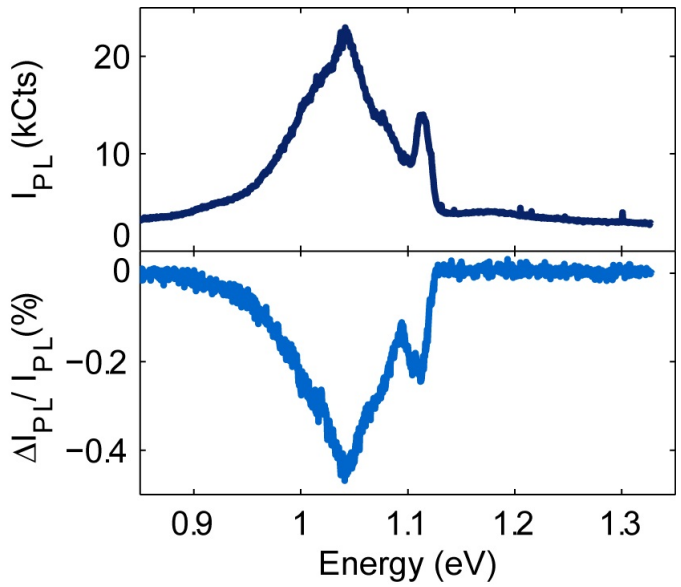

Figure 5.14: The spectral dependence of the ODMR corresponding to Ky5 defects.

emission band. As there may be a series of weaker emission bands present that are contributing to the overall PL signal, this measurement is crucial for confirming the expectation that the observed emission band is related to the measured spin levels. This measurement is generally useful for determining the various contributions to a complicated emission and ODMR spectra, as was demonstrated for 4H SiC [125].

Furthermore, the application of pulsed microwave excitation allows for demonstrations of coherent control over defect ground state spin sub-levels and characterization of their time-domain spin properties. Figure 5.15 shows coherently driven Rabi oscillations in the ground state of the Ky5 defects at zero field and low temperature. The importance of this demon-

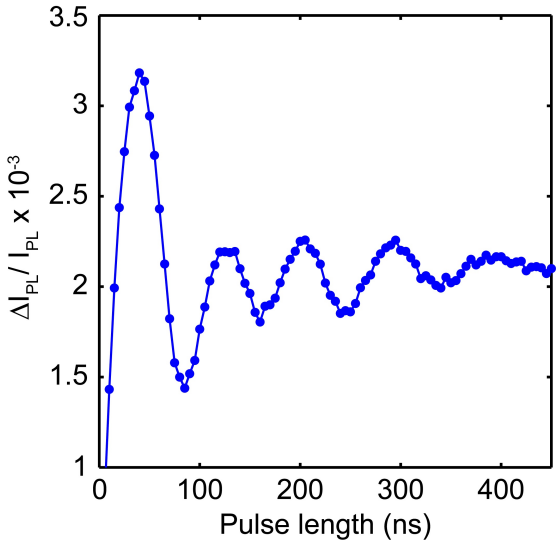

Figure 5.15: Rabi oscillations for Ky5 defects in 3C SiC.

stration is that it allows for the calibration of microwave pulses for engaging in spin manipulation for defect characterization, sensing, or other spin-dependent applications.

Figure 5.16 shows the results of a Ramsey measurement using $\pi/2$ pulses calibrated from driving Rabi oscillations at a fixed detuning. The resulting inhomogeneous spin coherence time T_2^* is ~50 ns. This value is short compared to the typically 250 ns to 1000 ns T_2^* times observed for 6H and 4H SiC at low temperature. This underlines the need for on-chip metalization, as discussed previously. Although ODMR can typically be observed when the sample sits on a stripline like those used for 4H and

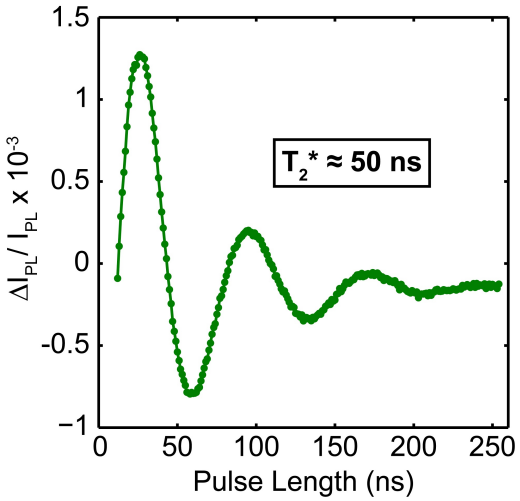

Figure 5.16: Ramsey oscillations for Ky5 defects in 3C SiC.

6H measurements, the field strengths are not strong enough to drive Rabi oscillations with periods on the time scale of the T_2^* time.

The observed Hahn spin-echo time $T_2 = 22$ μs, however, is typically within a factor of 2 of the roughly 40 μs observed in 6H SiC defects at low temperature. Figure 5.17 shows a comparison of the Hahn echo decay curves for the two different doping levels we typically measured (10^{13} and 10^{12} ions per square centimeter). The 10^{13} curve has a decay time of ~11 μs while the 10^{12} curve has a decay time of 22 μs. These results represent the first measurements of spin coherence times in this material. In contrast, previous measurements on high purity semi-insulating 4H SiC showed T_2 as long as 185 μs at low temperature. Although the defect qubit

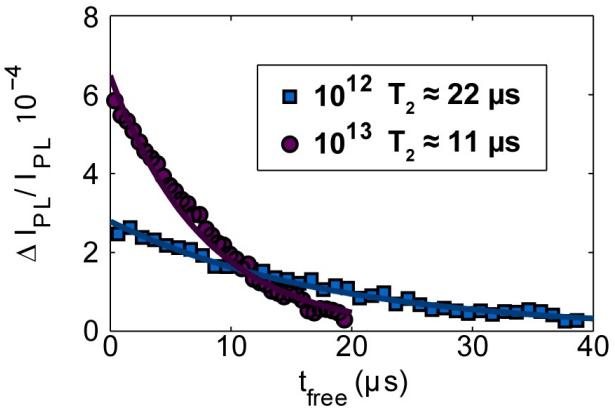

Figure 5.17: Comparison between Hahn echo decay curves for different doping levels in 3C SiC.

properties in 3C SiC are generally worse than those in 4H SiC, the argument for studying and utilizing 3C SiC is the same as the one made for using non-ideal forms of diamond; the functional gains resulting from the material properties may significant outweigh the negatives associated with degraded qubit properties.

5.6 Room Temperature Measurements

Typically, the photoluminescence signal of the Ky5 defect in the majority of the material we studied (from Novasic) starts to drop off in amplitude by liquid nitrogen temperatures and then disappears by 100K. This is likely an indication of the onset of non-radiative processes that quench

defect luminescence. While this may eliminate the ability to perform room temperature sensing experiments, the Ky5 defect can likely still be used for most NV center applications at low temperature. Low temperature are a necessary requirement for applications involving resonant collection or manipulation of the NV center zero phonon line and for many sensing applications, low temperature may be advantageous in order to avoid thermal drifts.

However, we did observe weak room temperature behavior in one sample obtained from collaborators that was implanted with nitrogen (the same sample did not show equivalent behavior when implanted with carbon). Although we could not reproduce this behavior in other materials, this points to the possibility that non-radiative process is not a fixed property of the system; with further study, we may be able to be limited or eliminate it to facilitate room temperature applications. Figure 5.18 shows the temperature dependence of the ODMR signal from the above-mentioned sample. The ODMR peak exhibits a thermally dependent shift and degree of quenching as the temperature is raised to 300 K.

The ODMR signal does not, however, truly disappear at room temperature. Figure 5.19 shows the ODMR signal taken at 300K. This signal was

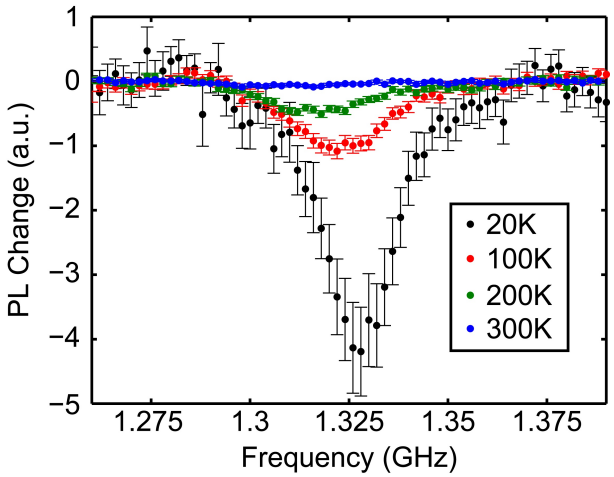

Figure 5.18: Temperature dependence of ODMR signal from Ky5 defects in 3C SiC.

very weak and required ~12-24 hours of averaging to obtain even a modest signal to noise. The peak was, however, completely reproducible.

Additionally, this weak ODMR signal allows for room temperature coherent control of the defect states, as depicted in Figure 5.20. Again, these measurements required very long averaging times and high microwave powers to observe Rabi oscillations. This plot is truncated after 45 ns because after that time temperature dependent signals resulting from heating start to swamp oscillatory behavior. This result, while promising, would require additional study in order to determine whether room temperature measurements of these defects might ever be easily realized. The fact that only nitrogen implanted samples exhibited this behavior points to the fact that

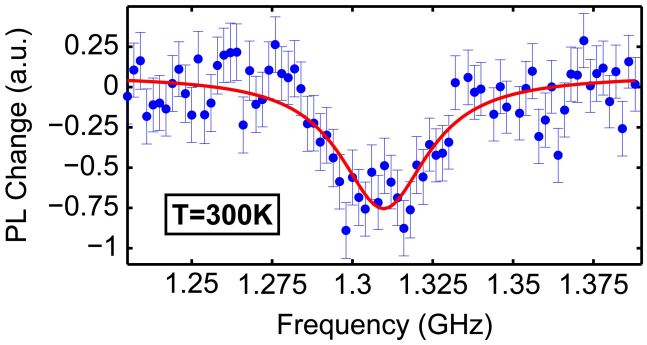

Figure 5.19: Room temperature ODMR from Ky5 defects in 3C SiC.

residual dopants or the differing Fermi level of the material (nitrogen is an n-type dopant in 3C SiC) may be providing non-radiative pathways. Higher purity material may eliminate these pathways. Furthermore, these pathways may only be present for off-resonant excitation. Resonant excitation may allow for one to bypass these loss mechanisms and allow for room temperature operation. Regardless, it is still the case that many applications involving defect qubits require low temperatures for either narrow spectral lines or stable sensing conditions.

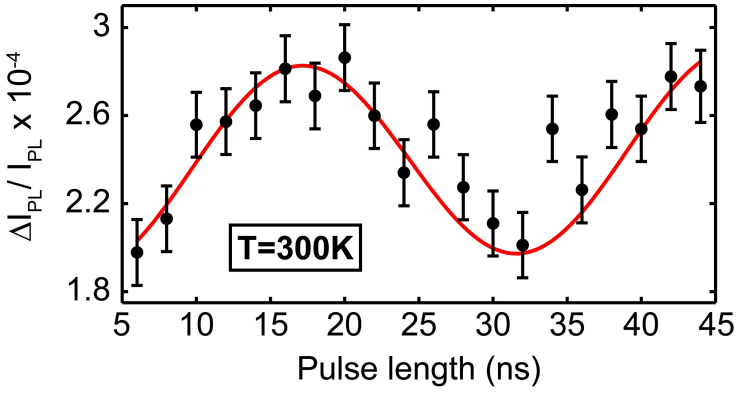

Figure 5.20: Room temperature rabi oscillations from Ky5 defects in 3C SiC.

Chapter 6

Photonic Crystal Cavities in 3C SiC

Some figures and sections of this chapter are adapted with permission from the publication: "Silicon carbide photonic crystal cavities with integrated color centers," G. Calusine, A. Politi*, and D. D. Awschalom, Applied Physics Letters* **105**, *011123 (2014).*

6.1 Introduction

The cubic form of SiC, 3C, has one distinct advantage over other potential hosts for NV center-like systems: it is available as a high quality heteroepitaxial thin film on up-to 6 inch wafers of silicon. Heteroepitaxial growth of III-V and SOI systems have made them the gold standard for

device fabrication and as a result, many quantum information approaches have focused on these hosts. Diamond, although it exhibits reasonably good spin qubits, is very much hindered in terms of scaling because of the lack of heteropitaxy. Currently, the production of diamond nanostructures involves rather complicated processes that involve thinning down polished 50 micron membranes to sub-micron dimensions all while maintaining good adhesion of the film to a sacrificial substrate. While this process has led to some great successes, it is difficult and costly. The cost of a single 4mm by 4 mm, 50 micron thick diamond substrate is the same as a 4 inch wafer of 1 micron thick 3C SiC epilayer. Additionally, the overwhelming majority of cleanroom tools are intended for use with wafer scale dimensions; working with small pieces is often very challenging (photoresist edge beads become a significant problem!). The advantage of having the sacrificial substrate be a silicon wafer also affords many other practice advantages. Most notably, releasing structures is very simple and can be achieved by a variety of methods, include backside wet etching (KOH or TMAH), backside deep etching via the Bosch process, or gas phase undercutting of structures through the use of XeF2 gas etchers.

The primary reason for pursuing this line of research is to circumvent the issues in diamond fabrication mentioned previously. Previous studies

that sought out new defect qubit candidates in SiC were motivated by the possibility of finding systems in hosts with added capabilities and functionalities not easily achievable in diamond. In particular, one of, if not the primary, goal is to incorporate defect qubits into devices in a scalable manner. The most clear application for devices in interfacing with defect qubits is to alter their local photonic environment. Because the form of defect qubits we focus on are initialized, manipulated, and read-out optically, photonic engineering stands to provide a number of advantages. These uses include:

- Increasing narrowband or broadband collection efficiency
- Enhancing optical coupling to a well defined spatial mode
- Increasing the effective optical depth for absorption based measurements
- Intense local fields for on-chip frequency conversion
- Purcell enhancements for improved single photon sources
- Defect based lasing for enhanced readout
- Strong coupling for quantum information applications

Many of these goals are ambitious but have the potential to realize many applications of defect qubits that have remained extremely difficult to

achieve. The largest outstanding challenge at the moment is the lack of knowledge of the details of the defect qubit optical properties and the fact that a single emitter has not yet been isolated in this form of silicon carbide. However, some progress has been made recently towards overcoming these challenges and the risks associated with this line of research are likely worth the potential rewards. In this chapter, we present our recent work on the design, fabrication, and characterization of photonic crystal cavities in 3C SiC thin films with incorporated Ky5 color centers.

6.2 Previous Work

Very little previous work exists on the development photonic crystal cavities in 3C SiC. At the time of starting our research into the development of photonic crystal cavities in 3C SiC, there had been no previous demonstrations of optical resonators in 3C SiC. There were, however, a few papers on the design, fabrication, and characterization of photonic crystal cavities in 6H SiC developed through the 'smart cut' process [126] [127]. One important outcome of this research is the demonstration that SiC photonic crystal cavities exhibit roughly a factor of 10x less shift in wavelength for a given temperature change around room temperature, leading to greater thermal stability for photonic applications. Recently, this same

process was used to produce photonic crystal cavities with Q's of 10,000 [123] capable of on-chip second harmonic generation. Also, another group recently reported the production of microdisk resonators using an electrochemical etching method [128]

In the course of performing this line of research, a few other groups have recently demonstrated ring-resonators [129], microdisks [130] [131], and photonic crystal cavities in 3C SiC [132].

6.3 Band Structure

Figure 6.1 shows the band structure of the 2D triangular lattice of holes that forms the photonic crystal. The MIT Photonic-Bands (MPB) package[133] was used to produce the band diagram and determine the position of the band gap. It shows the first four transverse electric (TE)-like modes of a SiC slab with hole radius r=0.29a and thickness h=0.85a for a lattice constant a. The bandgap opens for frequencies between approximately 0.3 ($2\pi c/a$) and .38 ($2\pi c/a$), where c is the speed of light. The resonant frequencies of the simulated H1 and L3 cavities are highlighted by the corresponding dashed lines.

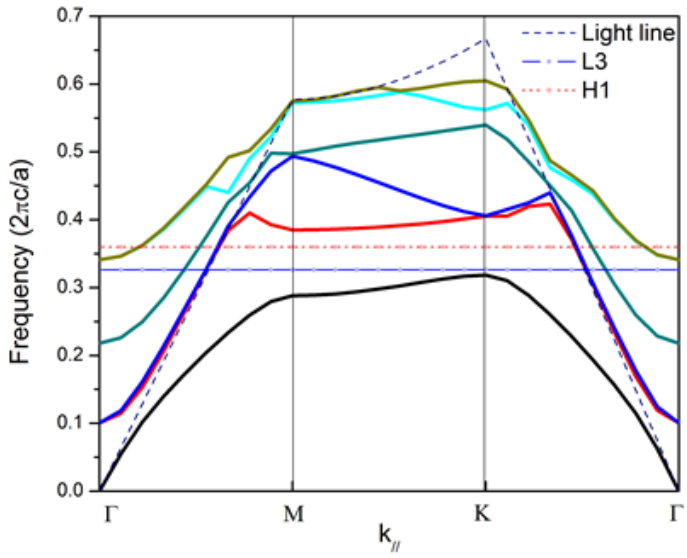

Figure 6.1: Calculated band structure for the photonic crystal lattice used for producing photonic crystal cavities.

6.4 Cavity Designs

The photonic crystal cavities consist of sets of missing and altered holes within the array of holes used to produce te previously described photonic crystal structures. Finite-difference time-domain (FDTD) simulations were used to determine the hole parameters necessary to produce modes within the spectral range of the zero phonon line of the Ky5 optical transitions and to optimize the position and size of the holes around the cavity for optimal cavity Q and mode volume. For both the H1 and L3 cavity types, the lattice hole radius 'r' and lattice periodicity 'a' are fixed by the relation r=0.29a.

Following the method in [134], we obtained an optimized Q of ~45,000 for the H1 structure when the radius of the four nearest vertically adjacent holes to the cavity are reduced to 0.22a and the horizontally adjacent holes are displaced outwards by a distance 0.2a. The optimal Q is obtained with a film thickness of 0.8a. Simulations indicate that the theoretical mode volume is $\sim(\lambda/n)^3$. This cavity's primary advantages are its high theoretical Q and its large degree of far field coupling within the numerical aperture of the objective we used (NA=.7).

We similarly optimized the L3 structure by shifting the position of the side holes of the cavity [135] by 0.21a and reducing their size [136] by 0.12a. This results in a theoretical quality factor Q ~17,000 at a film thickness of 0.85a with mode volume ~0.9 $(\lambda/n)^3$. These values compare favorably to the unoptimized L3 cavity design which achieves a Q factor of ~1,600 for a mode volume of $(\lambda/n)^3$. This cavity's main advantages are its relative insensitivity to fabrication imperfections and its relatively large degree of coupling to far field Gaussian laser modes. Figure 6.2 depicts the electric field profiles of both cavity designs and their corresponding fabricated structures.

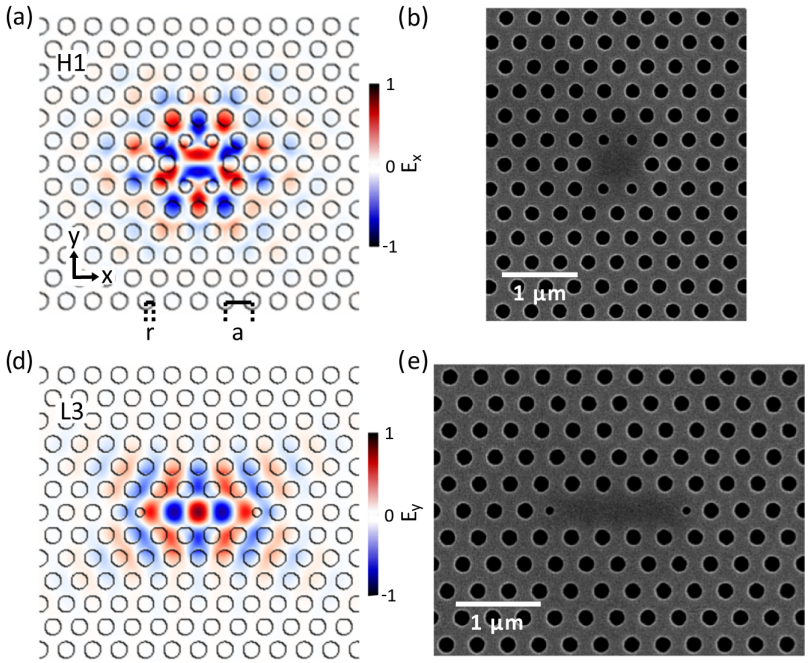

Figure 6.2: Electric field profile and fabricated structures for H1 and L3 photonic crystal cavities.

6.5 Cavity Fabrication Process

To fabricate photonic crystal cavities with incorporated color centers, we start with a 1 micron thick film of commercially available, $< 100 >$ oriented 3C silicon carbide grown epitaxially on a 100 mm $< 100 >$ oriented silicon wafer from NovasSic [137]. The film is initially thinned down to a thickness of 300 nm through a series of SF6 and Ar/Cl inductively coupled plasma (ICP) etches. In order to produce a vacancy distribution vertically centered in the middle of the film, the film is implanted with ^{12}C ions at an

energy of 110 keV, an incidence angle of 7 degrees, and a dose of 10^{13} ions per square centimeter. The film is then annealed at 750C for 30 minutes in an argon atmosphere to induce vacancy migration in order to promote the formation of Ky5 color centers. We found that this implantation and annealing procedure was optimal for producing the highest possible density of Ky5 centers in the material. Prior to implantation, the material exhibited no color center luminescence signal.

In order to fabricate the photonic crystal structure, the 300 nm SiC film is first covered with a hard mask consisting of 100 nm of aluminum capped with 10 nm of titanium deposited onto the sample using electron beam evaporation. The titanium layer is added to prevent oxidization of the aluminum and improve the consistency of the process. The sample is then spin-coated with 340 nm of ZEP520 electron beam lithography resist and a conductive polymer layer (AQUASave) to eliminate charging effects during the resist exposure that can distort the written pattern. Multiple arrays of devices are patterned on a 5-by-5-mm sample using a 100 keV electron beam lithography system. These arrays include duplicates in the case of local process failures and geometrically tuned patterns to map out the structure parameter phase space.

The conductive polymer is then removed, and the pattern is then

transferred to the SiC layer through a multi-step ICP etch. First, a BC_3/Cl_2 etch transfers the developed resist pattern to the Al/Ti layer. Then, without removing the sample from the etch chamber, an SF_6 plasma etch is performed at an ICP power of 900 W and a bias of 200 W to transfer the pattern to the SiC. This etch process was vital to the success of the structure formation. It was found empirically to minimize the degradation of the hard mask edges during the aggressive but nearly vertical SF_6 etching of the silicon carbide thin film. The SF_6 etch immediately followed the BCl_3/Cl_2 etch without removing the sample from the ICP chamber in order to avoid continued etching of the hard mask by unpassivated chlorine. The hard mask layers and any etch by-products remaining on the hole sidewalls are then removed through subsequent wet etches in Ti etchant, Al etchant, and buffered hydrofluoric acid (HF). Without the extra HF exposure, the process was found to leave residual etch residues lining the cavity holes. Finally, the sample is exposed to a short gaseous XeF_2 etch to isotropically remove the silicon substrate directly underneath the photonic crystal pattern in order to release the structure from the membrane (the undercut is approximately 25 microns). If further tuning of the cavity resonances is necessary, the structure thickness can be reduced further with a very short (5-10 second) short SF_6 or Ar/Cl ICP etch steps. A complete process flow

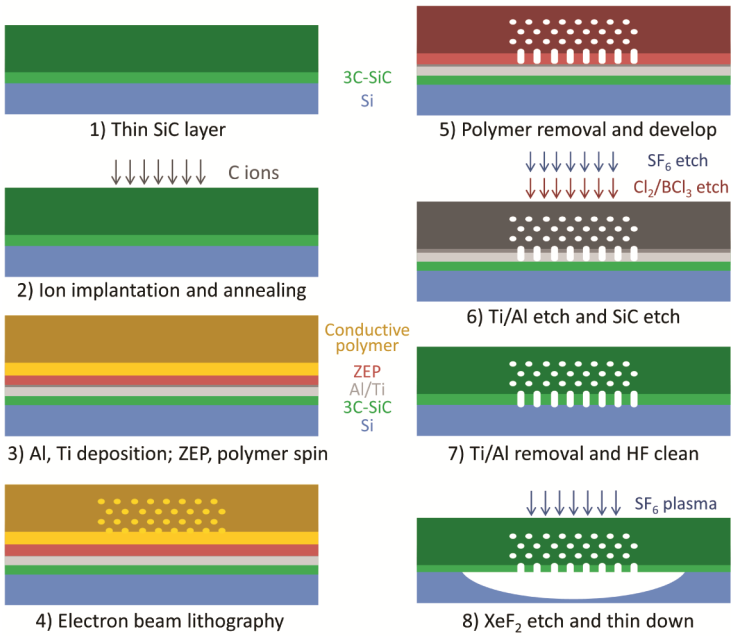

Figure 6.3: Fabrication process flow for producing photonic crystal cavities in 3C SiC.

of the fabrication procedure is shown in Figure 6.3.

6.6 Fabricated Structure Characterization

Figure 6.2 shows the results of the fabrication process for an H1 and an L3 cavity design. The structures exhibit a sidewall angle of approximately 85 degrees, typical of the values observed in the literature for similar etch conditions (see Figure 6.4). [138] Ultimately, as will be discussed later, it was found that this parameter plays a significant role in reducing the Q's of the structures. We did not appreciate this fact until it was too late to

change our process so we were not able to fully explore possibilities for achieving more vertical sidewalls. This may be achieved through the use of higher power etches and/or more robust hard masks (Cr and Ni are much more resilient to SF_6 etching but require more involved patterning processes). 90 degree sidewalls have been reported for certain special etch conditions. [139] The periodic holes defining the structure are uniform in radius and accurate in their positioning to within the spatial resolution of the SEM (~1.5 nm). The thin film's surface roughness increases from 0.5 nm rms to 1.2 nm rms as a result of processing, as determined by atomic force microscopy. The main contribution to this slight roughening was due to the SF_6 etch. The 500 W power and 200 W bias Ar/Cl (4:1, respectively) ICP etch used for membrane thinning increases the surface roughness from .5nm rms to .8 nm rms. Small variations in the hole shapes with an rms radial deviation of 2.75 nm are typically observed and the hole sidewalls show slight striations likely due to degradation of the aluminum hard mask edges during the high power etch needed to produce vertical sidewalls. These small hole variations and the other small scale structure on the surface are not expected to be significant enough to affect the cavity Q's [140] [141], but a direct analysis via FDTD would be impossible due to the small scale of the features (the required simulation meshing would

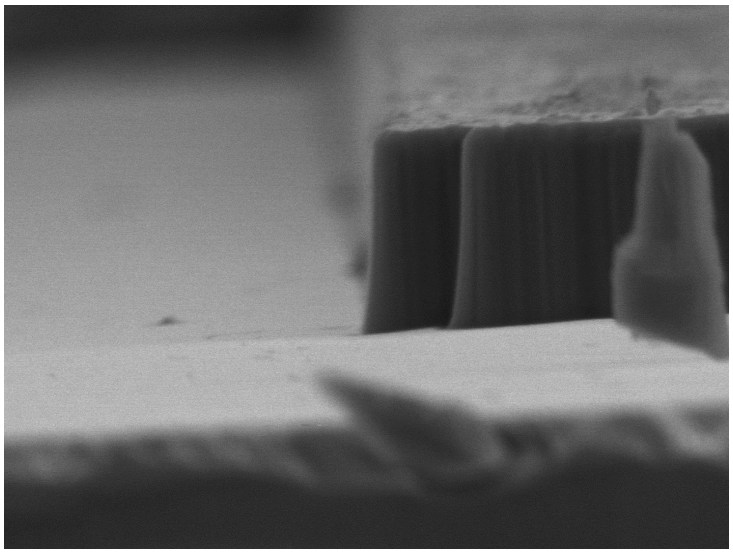

Figure 6.4: Approximately 85 degree sidewall angle that results from our SF6-based etching recipe.

lead to extremely long simulation times).

6.7 Cavity Characterization Setup

The structures were characterized in a home built scanning confocal microscope equipped with a helium flow cryostat with optical access as depicted in Figure 6.5. A flip mirror in the excitation path allows for switching between a 1060-nm diode laser for off-resonant excitation of the defects' photoluminescence via the blue shifted absorption side-band and a 1085-to-1185-nm tunable 300-kHz linewidth Littmann-Metcalf diode laser

for high resolution cross-polarized resonant scattering spectroscopy. Laser excitation is passed through a 0.7 numerical aperture microscope objective lens mounted on a series of coarse scanning stages. A fast-steering mirror (FSM) is incorporated into the optical path in order to alter the beam incidence angle on the back aperture of the objective, thus allowing for fast spatial scanning with a resolution of approximately 1 micron to determine the optical response of the various parts of the structure. Figure 6.6 shows the spatial dependence of the off-resonant reflectivity and photoluminescence from the structure. Photoluminescence and scattered laser light are collected through the same objective and reflected to a series of fiber couplers by a polarizing beam splitter.

For photoluminescence measurements, the light emitted by the defects is long pass filtered and coupled into a single-mode or multi-mode fiber. The light is then passed to either a 300 mm focal length spectrometer fitted with a liquid nitrogen cooled InGaAs CCD array for taking broadband spectra with a resolution of ~1 nm or a 1 meter focal length spectrometer fitted with the same CCD array with a resolution of ~.1 nm. The light can also be collected out of an alternate exit port on the 1 m focal length spectrometer and coupled to a superconducting nanowire single photon detector through a single mode fiber. Stray excitation light that

couples into the collection path is filtered with a dichroic mirror and can be utilized for spatial mapping of the photonic crystal cavity structure in order to place the laser excitation at the position of the cavity (Figure 6.6). All photoluminescence measurements were performed at a temperature of 20K. The incorporation of color centers directly into the cavity allows us to use the off-resonantly pumped defect luminescence band to excite the cavity modes over a broad range of wavelengths that are inaccessible to commercially available superluminescent diodes.

Cross-polarized resonant scattering provides a complementary characterization method for probing cavities without incorporated emitters or to study the response of the cavity [142] or internal emitters [143] to an externally incident Gaussian input beam. For cross-polarized resonant scattering measurements, a vertically polarized laser beam is reflected off a cavity rotated at 45 degrees with respect to the laser polarization axis. The cavity scatters a fraction of the incident power into the far field with an orthogonal (horizontal) polarization and it then passes into the collection path via a polarizing beam splitter. This light is then collected through a single mode fiber that is coupled to a femtowatt photoreceiver. An optical chopper wheel is used to modulate the incident laser intensity for lock-in detection. Wavelength dependent power fluctuations are actively

corrected for by a feedback loop consisting of a power meter and automated variable neutral density (ND) filter. When the laser wavelength is swept through the cavity resonance wavelength, a Fano lineshape is observed in the scattered laser intensity. This method of cavity characterization complements photoluminescence based methods in that it is capable of much higher resolution and can be used to characterize cavities that lack incorporated emitters or are at room temperature. Due to SiC's relatively small thermo-optic coefficient [144], only small (~1 nm) shifts in the cavity resonance were observed between 20K and 295 K. Comparable structures in silicon typically show about a factor of 10 times larger wavelength shift over this temperature range.

6.8 Cavity Characterization Results

One benefit of having an ensemble of emitters within the cavity is that their broadband emission provides a wide-band source of excitation. This allows one to characterize the cavity modes over a broad range of wavelengths set by the spectral range of the emission band (1100-1300 nm). Figure 6.7 shows a typical broadband photoluminescence spectrum (red line) at low temperature (20K) resulting from off-resonant excitation

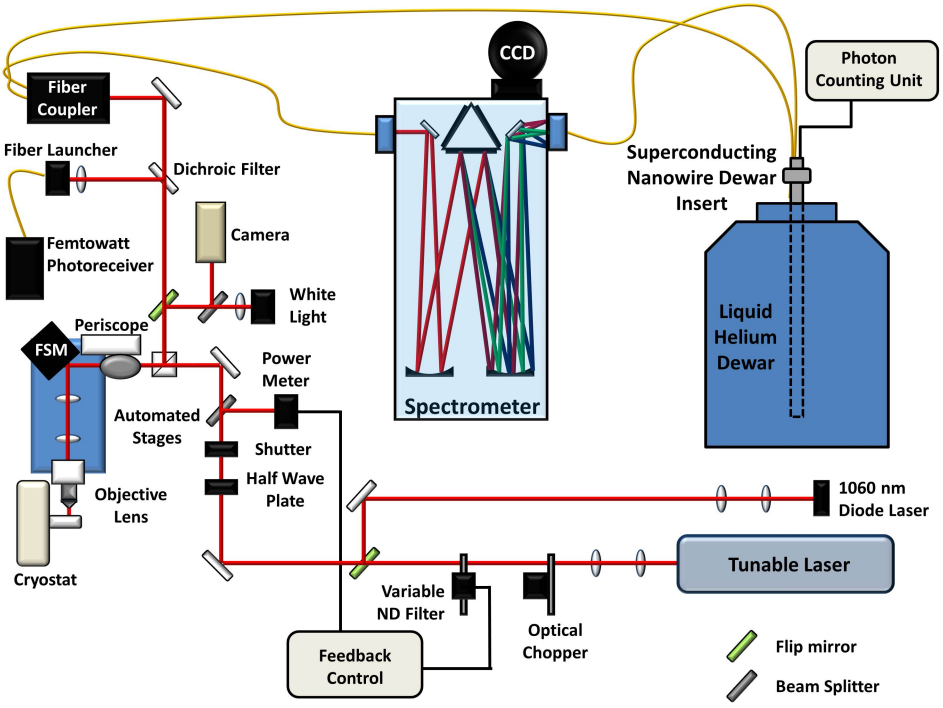

Figure 6.5: Setup used for characterizing photonic crystal cavities in 3C SiC.

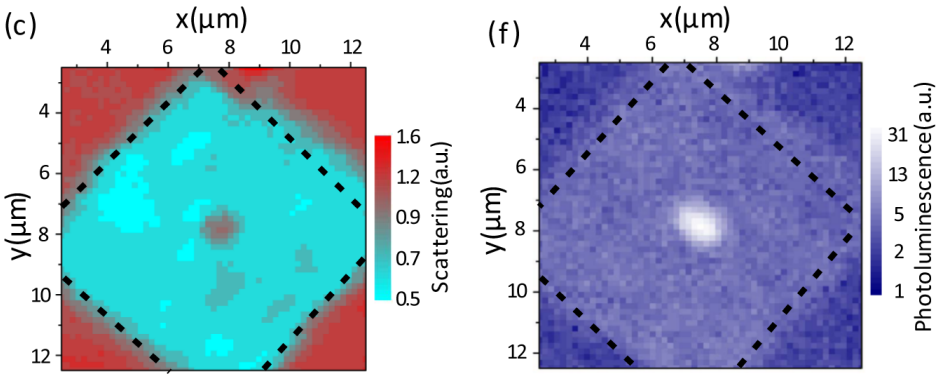

Figure 6.6: Spatial scans of off-resonant laser reflectance and resonant photoluminescence originating from photonic crystal cavity structures.

of color centers in an unprocessed 1 micron thick 3C silicon carbide layer that has been implanted and annealed. The spectrum consists of a zero phonon line centered at 1118 nm and a broad phonon-assisted emission sideband that extends deeper into the infrared. Also shown in the figure is a spectrum (black line) originating from a 300 nm thick H1 photonic crystal cavity with incorporated Ky5 defects that has a cavity resonance around 1180 nm. While qualitatively similar, the zero phonon line broadens from 4.6 nm FWHM to 28.2 nm FWHM in both patterned and unpatterned thin films, likely due to increased inhomogeneous broadening caused by the decreased crystalline quality of the material grown closer to the silicon interface.[145] This decreased crystalline quality results from the large (~20%) lattice mismatch between silicon and 3C SiC.

While this added spectral inhomogeneity may be a significant problem for scalable production of identical cavity-emitter systems, there are a number of potential solutions to this problem. First, one could utilize a combination of the Bosch process and back-etching to produce cavities in the material at the top of the thick film. Second, local DC stark shifts are generally necessary for combating spectral inhomogeneity in NV centers and recent studies suggest that silicon carbide defects exhibit stronger coupling to electric field [122]. Third, post-release annealing at high tem-

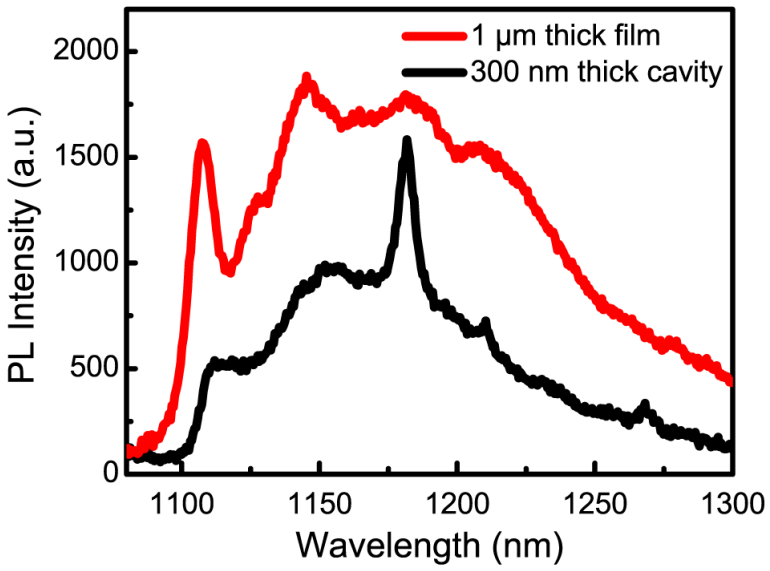

Figure 6.7: Comparison of inhomogenous broadening resulting from using 3C SiC thin films.

peratures may provide a means to heal some of the remaining structural defects in the film (I have already seem some suggestive evidence that this may be the case). Furthermore, one should note that residual strain is a significant problem for diamond membrane thin films; a recent study of NV centers in optical cavities observed almost 300 GHz strain splittings in the excited state as compared to the typically observed slitting of a few GHz in high quality single crystal bulk material.

Figure 6.8 shows the cavity resonance of an unoptimized L3 cavity with the resonance wavelength tuned to the peak of the Ky5 zero phonon

line. The tuning results from geometric tuning of the properties of an array of fabricated structures both to achieve cavities coupled to the zero phonon line and to determine the optimal cavity parameters. The measured Q's portrayed here are among the best we measured but the values were fairly typical of all fully exposed patterns. The measured Q of ~900 is less than the value of ~1,600 predicted by FDTD simulations. In the same plot, we show the cross-polarized resonant scattering spectrum of the same cavity, confirming the cavity properties measured via photoluminescence. Similar values are observed for room temperature cavities. Optimizations of the L3 cavity improve the measured cavity Q over the unoptimized case, as shown in Figure 6.9, but the resulting value is approximately an order of magnitude smaller than the predicted Q of ~17,000.

Similarly, for the optimized H1 cavity design we observed a maximum Q of ~1,000 despite a simulated value of ~45,000 (Figure 6.10). The reasons for these discrepancies will be discussed later. This H1 design does, however, provide a greater degree of far field coupling than the other designs, resulting in a 10-times enhancement of narrowband photoluminescence collection as compared to emission falling outside the spectral range of the cavity. This will be useful for studying spectral inhomogene-

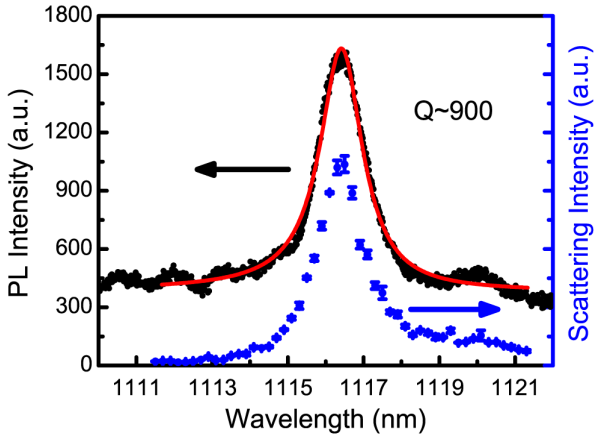

Figure 6.8: Photoluminescence spectrum and cross polarized resonant scattering spectrum for an unoptimized L3 cavity.

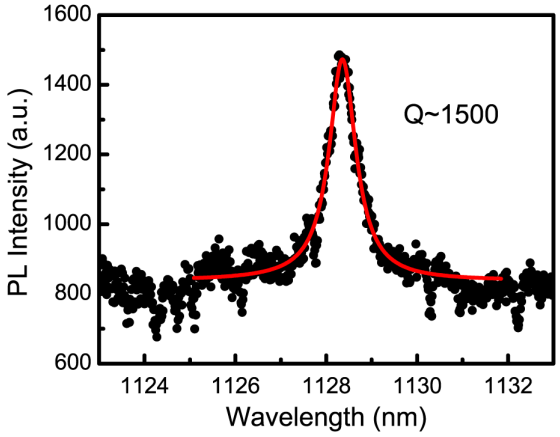

Figure 6.9: Photoluminescence spectrum for an optimized L3 cavity design.

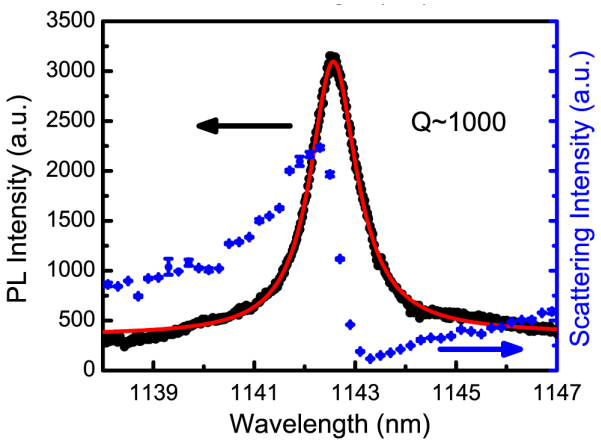

Figure 6.10: Photoluminescence spectrum and cross polarized resonant scattering spectrum for the H1 cavity design.

ity which will be discussed in a later chapter. Additionally, we observed that the H1 cavity supports additional modes red-shifted from the fundamental with similar Q's but much smaller mode volumes. In the case of the fundamental mode in the optimized H1 cavity, the cross-polarized resonant scattering spectrum exhibits a far more asymmetric Fano lineshape, indicating a greater degree of coupling between the cavity-dependent and -independent scattering channels. This is likely due to suppressed far field coupling to external Gaussian modes as a result of the odd cavity mode parity along the y-axis (as defined in Figure 6.2). This is further confirmed in the cavity resonant excitation measurements shown in later chapters.

6.9 Cavity Imperfection Simulations

A number of factors may contribute to the observed discrepancy between the simulated and measured Q's of our fabricated structures. Direct absorption by the defects' optical transitions is unlikely to be a primary limitation of the experimentally measured Q's because the structures' optical resonances show similar Q's at room temperature, in films with lower defect densities, and in films that were not irradiated and annealed to form Ky5 emitters. Furthermore, based on the estimated absorption coefficient in material similar to ours [129], our reduction in Q is likely not dominated by other material absorption processes. To estimate the effects of material absorption, we perform simulations on structures where the imaginary index of refraction of the thin film was set to a value of $n_i = 7 \times 10^{-5}$. This value was determined by relating the measured absorption coefficient in [129] to the imaginary index of refraction through

$$n_i = \frac{\alpha\lambda}{4\pi} \tag{6.1}$$

where α is the absorption coefficient and λ is the cavity wavelength. The material used in reference [129] originates from the same source as our material and is therefore likely to exhibit the same degree of sub-band gap absorption. Since the reductions in Q for these simulations is not

significant enough to explain our observed values (see Table 6.1), instead various structure imperfections inherent to the fabrication process-such as sidewall angle, variations in the size or position of the holes of the photonic crystal, or roughness on the surfaces or sidewalls-are the most likely source of scattering losses in excess of the radiative losses intrinsic to the cavity designs.

Table 6.1: Analysis of cavity Q factors for various fabrication imperfections

Cavity design	Ideal	Absorption	Sidewall 88 deg	Sidewall 85 deg	Sidewall 82 deg	Hole radius variations	Hole position variations
L3	1660	903	1333	794	523	1673	1634
L3 Optimized	17084	9153	7363	2198	1059	16383	16090
H1 optimized	45058	14443	15186	2362	672	33122	41682

Table 6.1 also shows the simulated Q for a given cavity geometry with geometric imperfections added to the simulated structure. Simulations of the effects of cavity imperfections on the structure Q's were performed with Lumerical's FDTD Solutions software package. All simulation conditions were checked for convergence and compared to results from the literature in order to verify their validity. Adding small, normally distributed random variations in the photonic crystal hole radii and positions to the simulations results in only small deviations from the ideal structure

Q factor for the L3 cavities (1%-5%) and slightly larger deviations for the H1 design (up to 26%). Random variations in the hole radii of the photonic crystal were introduced by adding or subtracting small increments from the radii so that the values were normally distributed around a mean corresponding to the structure's ideal hole radius. The magnitude of these variations was adjusted to match the values observed from image analysis of SEM micrographs that corresponded to the resolution limit of the SEM of 1.5 nm and should be considered an upper bound on the actual values for the fabricated devices. Random variations in the positions of the photonic crystal holes were introduced in a similar manner. Again, the standard deviation of the simulated distribution matched the measured distribution, which corresponded to the resolution of the SEM. The Q values quoted in Table 6.1 are the mean of ten simulations for different random configurations for each structure and deviation type. Table 6.2 compares the ideal cavity Q values with the simulated mean Q values and standard errors. The modest predicted reduction in Q's makes it unlikely that this contribution is dominant. Furthermore, the surface and sidewall roughness of 1.2 nm and 2.75 nm rms, respectively, that we observe in our fabricated devices is not likely to limit cavities with Q's of less than 10^5 . [140] [141]

Table 6.2: Analysis of cavity Q factors for various fabrication imperfections

Cavity design	Ideal	Hole Radius Variations	Radius Variation Q Standard Error	Hole Position Variations	Position Variation Q Standard Error
L3	1660	1673	10	1634	15
L3 Optimized	17084	16383	403	16090	326
H1 optimized	45058	33122	2435	41682	2249

Sidewall angle, however, has a pronounced effect on the Q factor for all three structures. Given the sidewall angle of approximately 85 degrees that we observe with SEM imaging, it is very likely that this is the limiting factor in reducing our Q's from the expected values. [146] Sidewall angle was introduced into the simulations by replacing the cylindrical photonic crystal holes with conical holes with a lower radius corresponding to the unperturbed value and an upper radius determined by the desired sidewall angle. In fabricated samples, this conical shape of the photonic crystal holes results from a combination of the ICP etch process not being completely vertical and degradation of the hard mask in the proximity of the holes during the etch. Simulations predict that for sidewall angles less than 85 degrees, the optimized H1 cavity has a lower Q than that of the optimized L3, contrary to what is predicted for vertical sidewalls. This qualitatively matches the behavior we observe in our fabricated structures (see Figure 6.11). At about 85 degrees sidewall angle the H1 cavity mode's

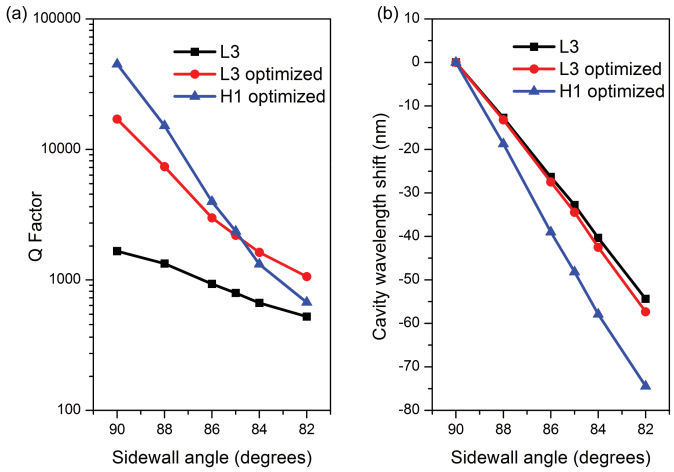

Figure 6.11: Simulated degradation in the cavity Q and change in resonant wavelength for non-vertical sidewall angles.

Q decreases to below that of the optimized L3 design despite having a higher Q for the unperturbed structure. This fact, in conjunction with the observed dependence of the structure Q's on the other imperfections, indicates that sidewall angle is likely the dominant factor limiting the Q's of our fabricated structures. Figure 6.11 also shows the dependence of the structure wavelength on sidewall angle. Furthermore, the large shift in wavelength that results from non-vertical sidewalls can cause the fundamental cavity mode to shift below the color centers zero phonon line. This shift needs to be compensated for in order to place the mode within the defect emission band for coupling to the internal emitters.

6.10 H1 Mode Structure

One other noteworthy feature of the H1 cavity is the presence of another mode red shifted ~20 nm from the fundamental mode as depicted in Figure 6.12. This mode typically exhibited a Q of ~1,000, similar to that of the fundamental mode, although with a small degree of coupling to the far field. Simulations of this mode yield a Q of approximately 3,000, a small mode volume of .16 $(\lambda/n)^3$ and a mode profile depicted in Figure 6.13. While this mode does exhibit a Q to mode volume ratio that is almost a factor of 10 higher than the fundamental for our measured Q's, the placement of the mode field maxima within the photonic crystal holes would limit the achievable coupling of the mode to the optical transitions of color centers internal to the film. In general, higher order modes afford an extra degree of functionality for applications like frequency conversion [147] or resonant excitation [148].

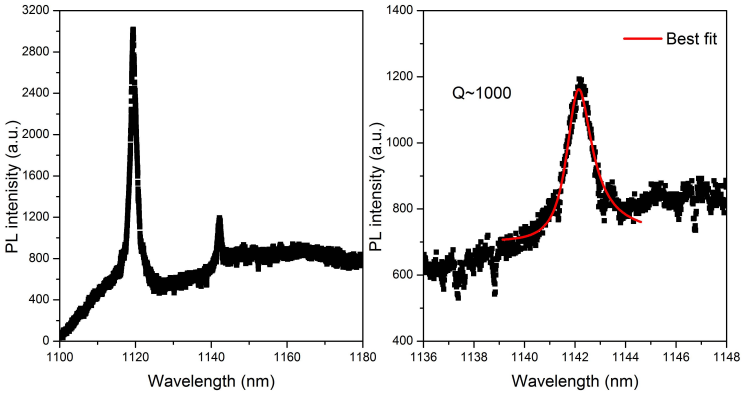

Figure 6.12: PL spectrum showing the fundamental H1 cavity mode and an additional red-shifted mode.

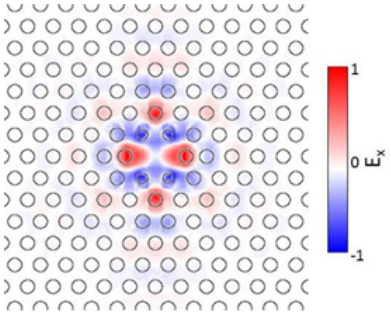

Figure 6.13: Simulated electric field profile for the red-shifted mode observed in H1 cavities.

Chapter 7

Cavity Enhanced Excitation of SiC Defect Qubits

"Cavity enhanced measurements of defect spins in silicon carbide photonic crystal cavities," G. Calusine, A. Politi, and D. D. Awschalom,(*in preparation, for most current results and details, see publication*).

7.1 Motivations

A primary motivation in the search for new solid state defect qubits is the desire to scalably incorporate these systems into devices that provide functionalities that are not available in bulk materials. Many color center defect qubits cannot easily be incorporated into devices because their material hosts are not available in heteroepitaxial forms. Color cen-

ter defect qubits in SiC are a promising candidate for solid state quantum technologies due to their combination of long coherence times [149], room temperature operation[125], and a host material for which mature growth[150] and fabrication protocols exist[151]. In particular, the ability to engineer the local photonic environment of optically active, solid state qubits is crucial to most scalable applications in the field of quantum information.[152] [70] The availability of SiC as a single crystal heteroepitaxial layer on silicon in the form of 3C SiC opens up the possibility of combining the favorable properties of SiC defect qubits with the fabrication advantages of III-V semiconductor systems. This may enable on-chip architectures for generating[153], routing[70], manipulation[154], and detection [155] of single photon emission from defect qubits in SiC. Most schemes rely on the use of high quality factor (Q), small mode volume cavities in order to achieve Purcell enhancements[70] [156] for efficient single photon generation or to access the strong coupling regime to produce the nodes in quantum network.[22] To date, only modest Q's have been demonstrated for small mode volume cavities in heteroepitaxial SiC thin films.[130] [132] [157] However, due to their potential for producing intense local optical fields[158], low and modest Q microcavities have alternatively been explored as a means to produce large local optical stark shifts[159],

frequency conversion through non-linear processes[69] [147], enhanced absorption and interactions lengths [160] [161], enhanced Raman scattering [162], on-chip optical traps[163], or to compensate for inefficient on-chip coupling or absorption a given excitation wavelength. The variety of these applications highlights the diverse functionalities enabled by interfacing solid state qubits with on-chip photonic structures.

As of yet, there have been no demonstrations of the use of SiC devices for enhancing spin-dependent phenomena. In this chapter, we demonstrate the use of on-chip nanophotonic cavities for enhanced excitation of color center defect qubits to enhance photoluminescence, CW and pulsed optically detected magnetic resonance (ODMR) signal amplitudes, and ground state spin polarization rates. Furthermore, we show that the small optical mode volumes and enhanced excitation and collection efficiencies provided by the cavities can be used to study inhomogeneous broadening of defect qubit ensembles in this and similar systems. The ability to efficiently and easily engineer the local photonic environment of color center defect qubits has the potential to greatly facilitate applications utilizing these systems in the fields of quantum information and sensing.

7.2 Absorption Enhancement in Fabry-Perot Cavities

Fabry-Perot cavities provide an intuitive way to think about the enhanced fields and absorption that an optical cavity generates. One can consider this from a few different perspectives that all yield equivalent outcomes for the cavity enhancement factor. The first method is to consider the uniform internal absorber as an added source of loss. The definition of an cavity finesse F yields the following relation:

$$F = \frac{\pi}{T + A} \tag{7.1}$$

where T is the transmission of the cavity mirrors and A is the rate of cavity loss. Using temporal coupled mode theory, one can derive the following expression for the power transmitted through a Fabry-Perot cavity with losses:

$$\frac{P_t}{P_i} = \Big(\frac{T}{T + A}\Big)^2 \tag{7.2}$$

where P_t is the power transmitted by the Fabry-Perot resonator and P_i is the power incident on the resonator. Adding an additional source of loss equivalent to the attenuation coefficient multiplied by the distance between the mirrors αd yields

$$\frac{P_t}{P_i} = \Big(\frac{T}{T + A + \alpha d}\Big)^2 \approx \Big(\frac{T}{T + A}\Big)^2 \Big(1 - 2\frac{\alpha d}{T + A}\Big) \tag{7.3}$$

The resulting change in transmitted power is

$$-2\frac{\alpha d}{T+A} = -\frac{2F}{\pi}(\alpha d) \tag{7.4}$$

Compared to the free space attenuation of αd, this indicates that the total absorption is enhanced by a factor of $(2F/\pi)$.

Equivalently, we could consider the rate of absorption due to the absorbing medium. This is defined by some rate R of absorption per photon per unit time and is multiplied by the total interaction time τ_i of a photon in the cavity to yield the probability of absorption. For a single pass through a distance d of material the total interaction time is nd/c for a material of refractive index n. For any cavity, the cavity photon lifetime is defined by

$$\tau_i = \frac{2Q}{\omega} = \frac{2\tau_{rt}F}{\omega t} = \frac{\tau_{rt}F}{\pi} = \left(\frac{2F}{\pi}\right)\left(\frac{nd}{c}\right) \tag{7.5}$$

where τ_{rt} is the round trip time of a photon in the cavity, Q is the quality factor of the cavity, ω is the frequency of the cavity, and t is the optical period. Again, this demonstrates a factor of $(2F/\pi)$ enhancement of the absorption in the cavity.

One final, and perhaps most rigorous, manner in which to derive the enhanced absorption is to consider the enhanced rate of excitation directly. We consider the field enhancement and thus, enhanced rate of absorption in a Fabry-Perot cavity in free space. The absorption rate is proportional

to the electric field squared in the cavity which is related to the cavity parameters through the relation [164]:

$$|E|^2 = \frac{4QP_{in}}{2\pi\omega\epsilon_0 V} \tag{7.6}$$

where P_{in} is the power input to the resonator, ω us the cavity frequency, ϵ_0 is the permittivity of free space, and V is the volume of the mode. The input power can be expressed as

$$I_0 A = \frac{c\epsilon_0 |E_0|^2 a}{2} \tag{7.7}$$

where a is the area of the input field.

Thus we can express the ratio of the enhanced electric field squared to the input electric field squared by

$$\frac{|E|^2}{|E_0|^2} = \Big(\frac{4Q}{2\pi\omega\epsilon_0 V}\Big)\Big(\frac{cn\epsilon_0 a}{2}\Big) = \Big(\frac{Qca}{\pi\omega V}\Big) \tag{7.8}$$

Since a/V is the length L of the resonator, we have

$$\frac{|E|^2}{|E_0|^2} = \Big(\frac{Qc}{\pi\omega L}\Big) \tag{7.9}$$

For a Fabry-Perot cavity,

$$Q = \frac{2\pi\omega L}{cT} \tag{7.10}$$

yielding

$$\frac{|E|^2}{|E_0|^2} = \Big(\frac{2}{T}\Big) = \frac{2F}{\pi} \tag{7.11}$$

which again demonstrates that the rate of absorption is enhanced by a factor of $(2F/\pi)$.

7.3 Cavity Field Enhancements

In this chapter, we observe large PL and ODMR signal enhancements from Ky5 defect qubits incorporated into 3C SiC photonic crystal cavities as a result of the intense optical fields generated by resonant cavity excitation. This field enhancement effect is directly analogous to those observed in Fabry-Perot cavities which are routinely used to generate large intracavity fields for a variety of optical applications[165]. Microcavities, however, have added complications due to the need for specialized engineering methods for efficient input coupling from external optical modes [166]. In general, the local field intensity inside a microcavity scales as $\propto \frac{\eta Q}{V_m}$ for a fixed incident power where η is the input power coupling efficiency and V_m is the cavity mode volume.

As with most analysis of photonic devices, the starting point for calculating the local field intensity enhancement is the equation governing the mode energy amplitude derived from temporal coupled mode theory[167]:

$$\frac{\partial \alpha}{\partial t} = -\Big(i\omega_c + \frac{1}{\tau_{tot}}\Big)\alpha + \kappa s_{in} \tag{7.12}$$

where $|\alpha|^2$ is the total energy in the cavity mode, ω_c is the cavity mode frequency, τ_{tot} is the cavity field lifetime, κ is the input coupling coefficient, and $|s_{in}|^2$ is the power incident on the cavity. Solving for the steady state behavior of the cavity every amplitude with an input field at a frequency ω yields

$$a = \frac{\kappa s_{in}}{i(\omega - \omega_c) + \frac{1}{\tau_{tot}}} \tag{7.13}$$

For an input field with a frequency equal to the cavity mode frequency, we can express the energy in the cavity mode as

$$|\alpha|^2 = \frac{|\kappa|^2 |s_{in}|^2}{\left(\frac{1}{\tau_{tot}}\right)^2} \tag{7.14}$$

$|\kappa|^2$ can be related to the far field overlap between the cavity radiation profile and profile of the incident Gaussian beam η through the relation

$$\frac{|\kappa|^2}{\left(\frac{1}{\tau_{tot}}\right)} = \frac{\eta}{2} \tag{7.15}$$

where η is defined by the mode overlap integral

$$\eta = \frac{|\int E_1^* E_2 dA|^2}{\int |E_1|^2 dA \int |E_2|^2 dA} \tag{7.16}$$

E_1 and E_2 are the far field radiation patterns of the cavity mode radiation pattern and the Gaussian input beam, respectively. The time reversal symmetry of Maxwell's equations dictates that this quantity yields the fraction of the power in the input beam that couples into the cavity mode

(up to the factor of two dividing η because the cavity emits equally in both vertical directions for symmetric structures).

Equation 7.14 can now be expressed as

$$|\alpha|^2 = \frac{\tau_{tot}\eta|s_{in}|^2}{2} \tag{7.17}$$

Since $\tau_{tot} = 2Q/\omega_c$ where Q is the quality factor of the cavity mode, we can rewrite this expression as

$$|\alpha|^2 = \frac{Q\eta|s_{in}|^2}{\omega_c} \tag{7.18}$$

The power in the gaussian input beam can be related to the irradiance I_0 through

$$|s_{in}|^2 = \frac{1}{2}\pi I_0 w_o^2 \tag{7.19}$$

where w_o^2 is the input beam waist for which η is calculated. I_0 is related to the field intensity through

$$I_0 = \frac{cn_b\epsilon_0}{2}|E_0|^2 \tag{7.20}$$

where c is the spead of light, n_b is the background index of refraction outside the cavity, ϵ_0 is the permittivity of free space, and $|E_0|^2$ is the modulus squared of the incident electric field in the Gaussian beam.

Putting this all together yields

$$|\alpha|^2 = \frac{Q\eta\pi w_o^2 c\epsilon_0 n_0|E_0|^2}{4\omega_c} \tag{7.21}$$

Because

$$\frac{\pi c}{\omega_c} = \frac{\lambda_c}{2} \tag{7.22}$$

where λ_c is the cavity wavelength, we have

$$|\alpha|^2 = \frac{Q\eta\lambda_c n_o \epsilon_0 w_o^2 |E_0|^2}{8} \tag{7.23}$$

To relate related the input field intensity to the local field intensity at the cavity maximum we use the definition of the cavity mode volume to yield the relation:

$$|\alpha|^2 = \frac{1}{2} V_m \epsilon_o n_c^2 |E_c|^2 \tag{7.24}$$

where V_m is the cavity mode volume, n_c is the cavity index of refraction, and $|E_c|^2$ is the modulus squared of the electric field in the cavity mode. Equating (12) and (13) yields

$$\frac{|E_c|^2}{|E_0|^2} = \frac{Q\eta\lambda_c n_o w_o^2}{4 n_c^2 V_m} \tag{7.25}$$

Equation 7.25 demonstrates the important structure parameters affecting the local field enhancement resulting from far field excitation of a photonic crystal cavity: the quality factor Q, the far field coupling factor η, and the mode volume V_m. These factors are, in general, interrelated and depend on each other significantly (in addition to the other factors like the refractive index and geometry), so one must be careful to optimize multiple factors

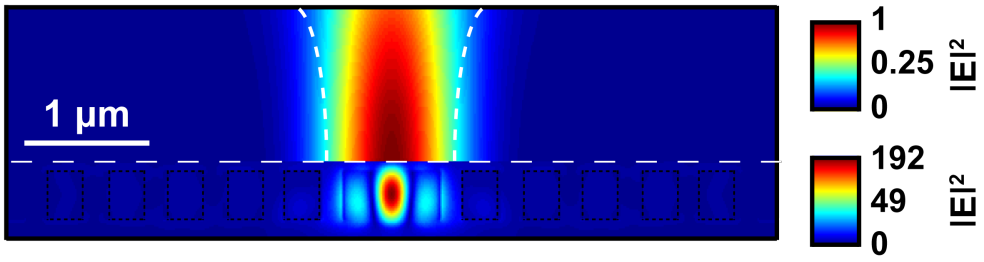

Figure 7.1: Schematic depicting the FDTD simulation geometry.

like the Q and far field coupling concurrently to maximize the achievable cavity field amplitude. While some factors like the Q, the wavelength λ, and the beam parameters can be measured experimentally, factors required for calculating the field enhancement like the input coupling efficiency η and mode volume V_m are difficult to measure directly and typically must be extracted from simulations[168]. Furthermore, FDTD simulations can be used to *directly* extract the field enhancement through direct numerical calculation of the response of the cavity to an incoming Gaussian beam. We set up simulations with the geometry depicted in Figure 7.1 to extract the various cavity parameters and calculate the local field enhancement directly.

A pulsed Gaussian source excites the cavity mode from above and a series of field monitors in the simulation extract the cavity parameters and the field enhancement. The beam waist of the Gaussian excitation is set equal to the measured value from our experiments and its polarization is

set to match that of the dominant component of the cavity far field losses. In Figure 7.1., we see the enhanced local field of an unoptimized L3 cavity, resulting in a square modulus of the electric field that is almost 200 times higher than for the peak intensity of the input Gaussian source with unity amplitude and beam waist equal to our experimentally measured value of 1.1 μm. All simulations were tested for convergence by varying the relevant parameters to ensure simulation accuracy. All parameters were extracted from a single simulation run by properly apodizing the relevant field monitors to extract cavity parameters independent of the excitation conditions. The input coupling efficiency was extracted by numerically performing the integral in equation 7.16 for the S and P polarized far field profiles of the mode under consideration and the Gaussian excitation used to excite it. The field monitor for extracting the field enhancement is not apodized and outputs the steady state field profile even for a pulsed source.

The resulting field intensity enhancement of 191.52 agrees within ~1 percent of the value of calculated from equation 7.25 for the basic L3 cavity ('L3 Basic') using the input parameters extracted from simulations. A similar agreement is observed for the Shrink hole cavity design ('L3 Shrink') although discrepancies between the simulations and calculations of 18.7% and 13.4% are observed for the simulations with added sidewall angle('L3

86 deg.') and material absorption('L3 Abs.'), respectively. These discrepancies likely arise from simulation artifacts resulting from problems with extracting the mode volume for moderate Q cavities.

Higher Q modes can, in principle, exhibit significantly higher field enhancements. However, for planar photonic crystal cavities, this tends not to be the case, as one typically increases the Q of a photonic crystal cavity by reducing the far field coupling, resulting in a lower input coupling efficiency. For instance, the optimized L3 design presented in [157] exhibits a greater than a factor of 10 increase in Q over the un-optimized design but exhibits only a 25% higher field enhancement due to a compensating decrease in input coupling efficiency and a larger mode volume. This limitation can be circumvented by using on-chip coupling through local waveguides which can achieve $\eta \approx 90\%$ for Q's comparable to our measured values [169] or by using structures that have been specially designed to simultaneously optimize Q and far field coupling.[170]

Table 7.1 summarizes the relevant cavity parameters for the different geometries simulated and compares the calculated field enhancement to the simulated value. The '86 deg' cavity was simulated with an 86 degree sidewall tilt, similar to what we observe for our cavities and which likely explains the deviations between the simulated and measured Q's of our

fabricated structures.[157] For this geometry, extra care was taken to account for the differences in far field profile in the vertical and horizontal direction in determining the calculated field enhancement. The 'L3 Abs' cavity included the estimated absorption coefficient for our measured material in the material used for the photonic crystal cavity simulation. An extra factor of $(Q_a - Q_{tot})/Q_a$ multiplies equation 7.25 to account for the non-radiative component of the cavity losses in the derivation of equation 7.25 where Q_a is the Q factor that accounts only for non-radiative losses and Q_{tot} is the total Q of the cavity mode. For this and the other cavity geometries, the in-plane losses were found to be negligible compared to the far field losses.

For some simulations the agreement with the semi-analytic theory is

Table 7.1: Cavity Field Enhancement Parameters

Design	Wavelength(nm)	Q	V_m $((\lambda/n)^3)$	η	$\|E_c\|^2$ Calculated	$\|E_c\|^2$ Simulated
L3 Basic	1110	1655	.679	.096	193.48	191.52
L3 Shrink	1122	17444	.907	.015	253.28	255.35
L3 86 deg.	1084	931	.743	.105	114.29	96.30
L3 Abs	1110	902	.719	.095	54.11	62.92

quite good(~%5) where as for others there is a discrepancy of up to %25. This discrepancy likely results from errors in the calculation of the exact far field coupling efficiency, which can be sensitive to simulation param-

eters, or difficulties in accurately producing a purely Gaussian excitation source due to simulation imperfections.

7.4 Excitation Volume Reduction

Microcavities have the additional advantage of exhibiting greatly reduced mode volumes as compared to diffraction-limited excitation in bulk material. Excitation volume typically plays a significant role in achieving a high signal-to-noise ratio in scanning confocal microscopy of single emitters. This results from the fact that single emitter luminescence typically saturates at a fixed optical input power whereas most background contributions scale linearly with power and excitation volume [171]. For a given optical intensity distribution with its maximum at the position of the emitter, a smaller excitation volume yields less bulk background emission[172], leading to better signal-to-noise ratios and reduced multi-photon emission probabilities in single photon sources. As has been demonstrated previously with III-V quantum dot systems [148], exciting higher order modes coupled to the defects absorption sideband in conjunction with collection from a fundamental mode coupled to the ZPL may facilitate the efficient, background free production of single photons from individual defects with lower probabilities of multi-photon generation. A reduced excitation vol-

ume can also limit the number of locally excited background charge fluctuations that induce spectral diffusion of the single emitter's relevant optical transitions.[48] [49]

The excitation volume of a focused Gaussian beam in a bulk material is approximated by the expression[173]:

$$V_m = 3.28\Big(\frac{\pi}{2}\Big)^{3/2}\frac{nw^3}{NA} \tag{7.26}$$

where n is the index of refraction and w is the beamwaist given by the expression for the minimum spot radius:

$$w_{min} = \frac{.61\lambda}{NA} \tag{7.27}$$

For the objective lens (NA=.7) used in this work, the ideal beam waist, and the index of refraction of 2.64 for SiC, this yields an diffraction limited excitation volume in the bulk of 22.04 μm^3.

For an ideally focused input beam exciting a thin 300 nm film like those used in this work, the intensity profile along the optical axis is set by the thickness of the membrane and is reduced to approximately .44 μm^3

However, due to optical aberrations or non-optimal filling of the microscope back aperture, the spot size can deviate from the ideal, diffraction limited value. We performed a beam profiling measurement by scanning our excitation spot over the edge of an alignment mark consisting of a void

adjacent to a freestanding membrane and measure the reflectance versus position. This results in a knife edge measurement of the beam diameter and measure a beam waist of 1.1 μm at the sample surface by fitting the reflectance to an error function. For bulk and thin film excitation, this beam waist yields an excitation volume of 32.41 μm^3 and .57 μm^3, respectively.

Excitation of the local photonic cavity, however, provides an effective mode cleaning with respect to the input beam. For a given local intensity maximum, the cavity yields a mode volume of .050 μm^3 for the basic L3 cavity design without Q optimization, irrespective of the input profile for resonant excitation (although the input coupling efficiency varies between different input profiles). Additionally, the actual excitation volume is further reduced by taking into account the lack of overlap between the emitters in the material and the evanescent fields of the mode present in the holes and just outside the surfaces of the membrane. The excitation volume of the cavity V_{ec} is defined as the fraction of the mode volume confined to the active material, the "confinement factor" Γ_{cv}, multiplied by the mode volume: $V_e = \Gamma_{cv} V_m$. For the basic L3 cavity, we calculate a value of $\Gamma_{cv} = .91$. Thus, in this instance, we produce a 706-fold reduction in the excitation mode volume as compared to bulk and an 12.4-fold reduction

in the excitation volume with respect to the unprocessed film. Table 7.2 summarizes these values.

Table 7.2: Excitation Volume Comparisons

Structure	V_e (μm^3)	V_e/V_{ec}
Bulk, ideal	22.04	480
Thin film, ideal	.44	9.59
Bulk, measured	32.41	706
Thin film, measured	.57	12.4
Cavity (V_{ec})	.046	1

Table 7.2. Comparison between the excitation volumes for different sample geometries for ideal diffraction limited excitation optics and for the measured beam parameters.

Figure 7.2 compares the intensity profiles of the Gaussian excitation beam used to excite the cavities and the cavity mode.

7.5 Experimental Details

All measurements were performed in a home-built scanning confocal microscope outfitted with a helium flow cryostat capable of achieving temperatures between 5K and 300K (see Figure 7.3). A 60x window corrected microscope objective with a numerical aperture of 0.7 was used to excite

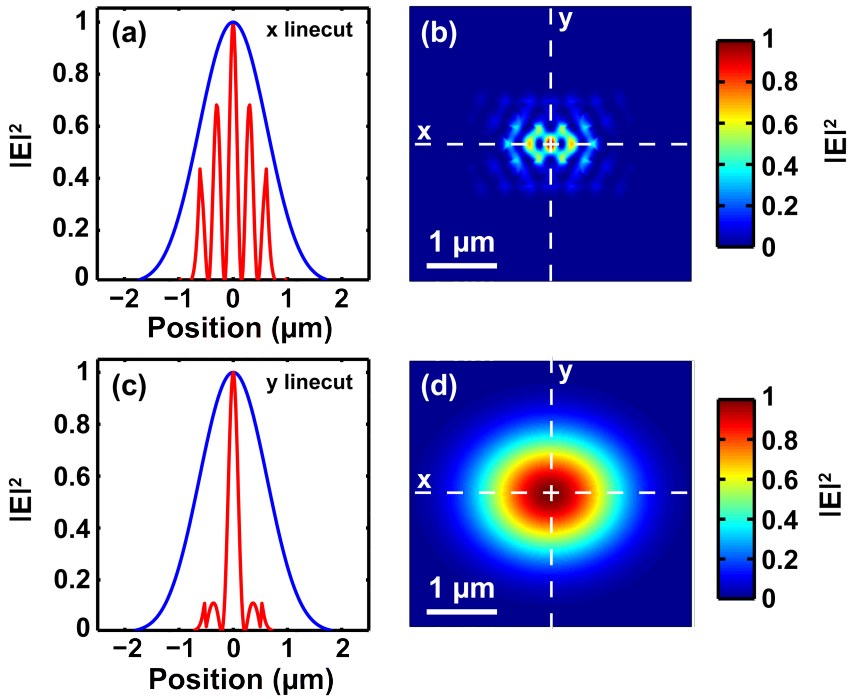

Figure 7.2: (a) A linecut of the field intensity along the dashed white line delineating the x-direction in (b) and (d) comparing the cavity mode to a Gaussian excitation beam with a waist as measured in our experimental configuration. (c) Simulated field intensity distribution of the basic L3 cavity mode. (d) A linecut of the field intensity along the dashed white line delineating the y-direction in (b) and (d) comparing the cavity mode to a Gaussian excitation beam as described above. (d) Simulated field intensity distribution of the focused Gaussian excitation beam used for the field enhancement calculations and simulations.

the sample and scattered light and PL were collected back through the same lens. The 1 mm thick cryostat window was anti-reflection coated for the near infrared to minimize loss of excitation power and PL due to the window interfaces. The cryostat is kept fixed and the excitation is spatially scanned with respect to the sample through the use of a series of mechanical stages for coarse positioning and a fast steering mirror (FSM) for finer, higher bandwidth (up to 580 Hz) spatial scanning with ~1 μm resolution. A periscope mounted on the objective stage prevented the excitation beam from moving off the back aperture of the microscope objective during lateral positioning. A lens pair between the FSM mirror and the microscope back aperture performed the same function for FSM spatial scanning. A white light source and CCD camera were used for wide field imaging of the sample surface and could be added or removed from the optical path with a beamsplitter on a flip mount.

The helium flow cryostat included custom installed microwave coaxial cabling to deliver microwave signals to the sample space. The sample was mounted on the end of a copper coldfinger with a coaxial cable terminated at a gold-plated printed circuit board stripline. The stripline was wirebonded directly to on-chip metalization pads to provide strong, local microwave fields at the location of the photonic crystal cavities. On-chip

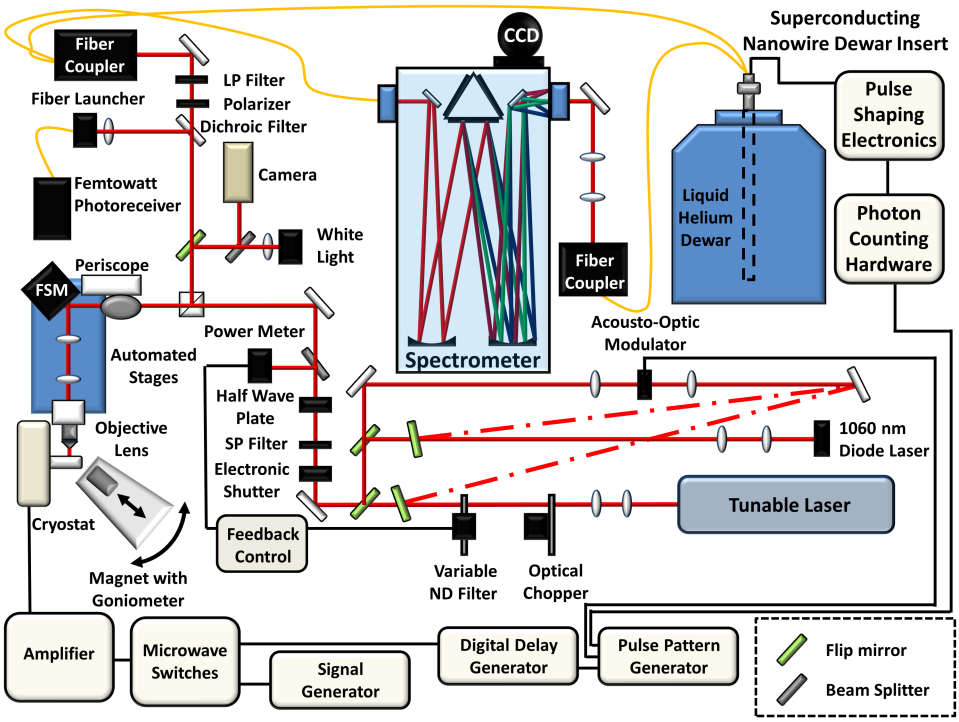

Figure 7.3: Schematic of the modified confocal microscope setup.

metalization was necessary in order to achieve AC magnetic fields strong enough to induce Rabi oscillations with periods comparable to the relatively short T_2^* time of the defects' ground state transitions (~50 ns). The setup also included a Neodymium magnet mounted on a goniometer stage capable of providing up to 700G magnetic fields along the <111> defect axis, although the measurements in this work were performed at zero magnetic field.

A 1060 nm fiber coupled diode laser was used for off resonant excitation of PL through the defects absorption sideband. A <300 kHz linewidth

Littman-Metcalf tunable diode laser with a wavelength range of 1090-1180 nm was used to resonantly excite the defects' ZPL transitions (centered at 1118 nm) or for exciting cavity modes and cross-polarized resonant scattering spectroscopy[174]. In order to compensate for wavelength-dependent power output from the tunable diode laser, we utilized an active feedback loop using a power meter and variable filter wheel in order to reduce output power fluctuations to below 1 percent of total power. A series of short pass filters removed spectral emission from the laser that fell within the detection wavelength range ($\lambda > 1175$ nm). This was especially crucial for removing unpolarized gain medium fluorescence output from the tunable diode laser as this emission swamped the PL signal in the absence of careful filtering. Mirrors on flip mounts in both the 1060 nm and tunable diode laser path allowed both beams to be passed through an acousto-optic modulator with a 10 ns rise time for time-dependent measurements.

The excitation beams passed through a polarizing beamsplitter (PBS) and the cross-polarized PL and scattered laser light were reflected by the beamsplitter to a series of filters and detectors. A half-wave plate in the excitation path prior to the PBS rotated the incident beam's polarization to maximize transmission through the beamsplitter and to the sample. The samples were mounted with the cavity axis (and therefore, far field

emission polarization) at 45 degrees with respect to the input laser polarization to enable cross-polarized resonant scattering spectroscopy. For off-resonantly excited PL measurements that required analysis of signals of both polarizations or for larger signals, the PBS was replaced with a 1064 nm dichroic beamsplitter.

For on-resonant (ZPL or cavity) excitation of PL, a series of 1150 and 1175 nm long pass and long-wave pass dichroic filters in the collection path spectrally rejected the excitation laser light and the gain medium fluorescence originating from the laser cavity. For off-resonant PL measurements, the filtered 1060 nm diode laser signal was passed to a photodiode in order to provide a 20 μm by 20 μm spatial reflectivity map for determining the position of the cavity prior to obtaining a PL spectrum. Alternatively, for cross-polarized resonant scattering spectroscopy, the filters were removed and scattered laser light was passed to a photodiode. An optical chopper incorporated into the excitation path was used as a reference signal for lock-in detection at $\sim$ 1 kHz.

A 1m focal length spectrometer was used to obtain sample PL spectra and as a scanning monochromator with $\sim$.1 nm resolution around 1100 nm. A single or multimode fiber passed PL from the collection path to the input of the spectrometer. Wideband spectra were obtained with an In-

GaAs CCD array in conjunction with an electronic shutter for background subtraction. When using the spectrometer as a scanning monochromator, the light was collected out of an alternate exit port, collimated, and focused into a single mode fiber leading to a superconducting nanowire single photon detector (SNSPD). Alternatively, for PL excitation measurements where the entire phonon sideband was detected, the filtered PL was fiber coupled directly to the SNSPD. A fiber-based polarization rotator matched the signal polarization to the optimal detection polarization of the SNSPD. The SNSPD operated in a liquid helium bath at an operating temperature of 1.8K. It demonstrated a quantum efficiency of ~25%, a rise time jitter of < 50 ps, and a maximum counting rate of up 100 MHz. The high bandwidth of this detection method allows for measurements of fluorescence dynamics on fast time scales. These time scales are inaccessible to the sensitive but low bandwidth (20 Hz to 1 kHz) femtowatt photoreceivers previously used for studying SiC defects.

For time-dependent measurements, a combination a pulse pattern generator, a function generator, and a digital delay generator were used to synchronize the acousto-optic modulator, microwave switches, and photon counting hardware. A microwave signal generator produced continuous wave (CW), GHz range microwave signals that were used for CW electron

spin resonance or passed through a series of microwave switches for pulsed spin manipulation. Both CW and pulsed microwave signals were amplified by a high frequency, 30W microwave amplifier and passed through vacuum tight SMA feedthroughs to the cryostat's internal coaxial cabling. The digital delay generator set the timing delay between optical, microwave, and time correlated single photon counting (TCSPC) unit trigger pulses. The function generator modulated both the microwave pulses and the routing of the photon signal pulses to two separate counting channels in order to subtract non-spin dependent signals from the measured signal. In order to count the photon signal pulses out of the SNSPD, the pulses were converted to either 20 ns long TTL pulses or NIM pulses to match the input requirements of the DAQ counters or the TCSPC PCI card, respectively.

7.6 Photoluminescence Signal Enhancements

We determine the position of the cavity resonances by measuring the PL spectrum of emitters localized within the cavity under off-resonant 1060 nm excitation. The Ky5 color center emission spectrum consists of an inhomogeneously broadened ZPL around 1118 nm and a red-shifted phonon

sideband extending out to approximately 1300 nm. The measured structures' geometries are designed such that the cavity resonances fall within the extent of the Ky5 ZPL, resulting in a Lorentzian-shaped spectral enhancement of luminescence at the resonance wavelength (see Figure 7.4). In order to observe the defects' response to the cavity resonant excitation, we tune the excitation wavelength to the cavity resonance peak and collect red-shifted sideband PL. Special care is taken is spectrally filter and cross-polarize the excitation and collection paths to fully suppress any scattered laser emission from that might couple to the SNSPD. As a result, we only collect 55% of the total emission sideband (λ >1175). Figure 7.4 shows the basic premise of the cavity enhanced PL excitation spectroscopy measurement. The inset shows the measured response of the defect sideband PL as the excitation laser is swept over the cavity resonance. The total amount of measured PL is greater when the laser is resonant with the cavity due to enhanced absorption and the spectral dependence of this enhancement matches the cavity mode wavelength profile as determined independently by measuring the off-resonantly excited PL spectrum and via cross-polarized resonant scattering spectroscopy. The Q's of the measured structures were typically around 900 with simulated mode volumes of .679 $(\lambda/n)^3$ and far field coupling efficiencies to external, free space Gaussian

modes of 9.6% . This same approach for resonant excitation can be applied to cavities with wavelengths within the defects' absorption sideband for applications that require enhanced off-resonant excitation and may be particularly beneficial for excitation wavelengths that overlap weakly with the defects' absorption spectrum.

To determine the total PL signal enhancement with respect to the unpatterned, released membrane, we perform a series of spatial scans over the photonic crystal area and compare the overall cavity signal to that of the surrounding membrane. Figure 7.5 (a-c) shows a series of 15 μm by 15 μm spatial scans over an L3 photonic crystal cavity with a resonance at 1117.1 nm for the wavelengths designated in the Figure 7.5 (d). The photonic crystal extent is delineated in the images by the white dashed lines and the bright spot in the middle corresponds to the position of the cavity. Figure 7.5 (d) shows the excitation wavelength-dependent PL signal originating from the cavity location. Figure 7.5 (e) shows a line cut of the PL map corresponding to the red, dashed line in the part (b). At this wavelength corresponding to the cavity maximum, the PL signal is approximately $\Gamma_e \approx 30$ times higher than the PL signal on the membrane, where we have defined Γ_e as the ratio of the resonantly excited cavity signal to the membrane signal at the same excitation wavelength. For H1 designs,

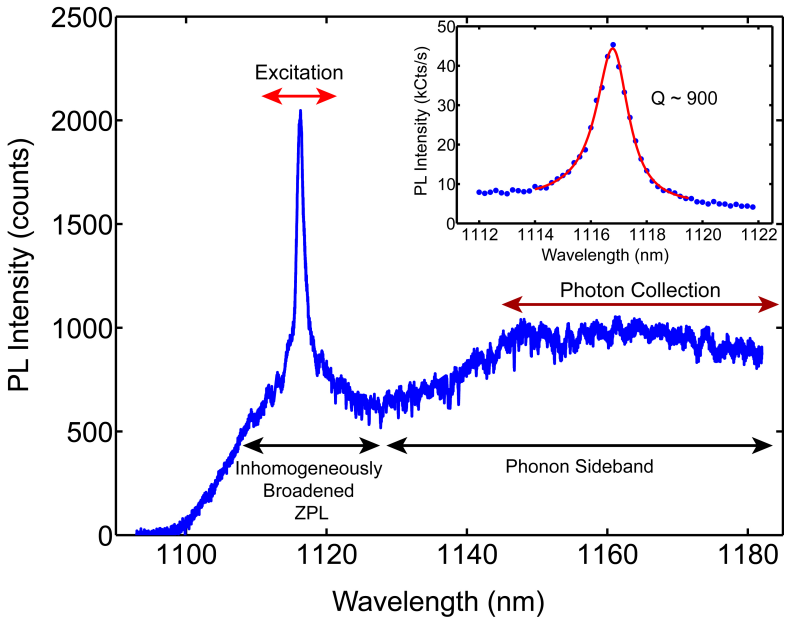

Figure 7.4: Diagram depicting the cavity enhanced PL excitation scheme. The main figure shows the off-resonantly excited PL spectrum of an L3 cavity with incorporated Ky5 emitters at 20K with the fundamental mode of the cavity tuned to the peak of the inhomogeneously broadened (FWHM of 28.2 nm) ZPL centered at 1118 nm. The small scale structure in the spectrum is primarily due to detector noise and discrete water absorption lines. To measure the cavity enhanced excitation, a narrow linewidth laser is scanned over the cavity resonance while photons from the phonon sideband for λ>1175 nm are collected for detection. The inset shows the PL excitation spectrum measured using this method.

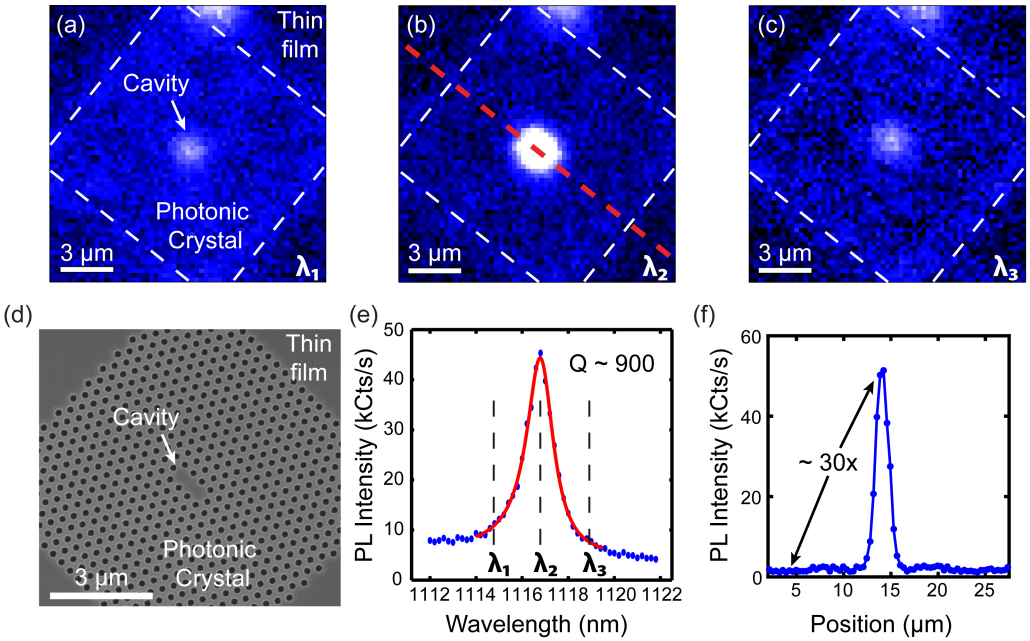

Figure 7.5: (a-c) 15 μm by 15 μm spatial scans of the sideband PL intensity signal for the three different excitation wavelengths depicted in (e)((a) λ_1=1115.1nm, (b) λ_2=1117.1nm, (c) λ_3=1119.1nm). The white dashed lines indicate the extent of the photonic crystal. (d) SEM image of the L3 cavity. (e) Linecut depicted in the center spatial scan by the dashed red line.

we observe a lower maximum $\Gamma_e \approx 13$ due to a smaller degree of input coupling for a Gaussian input beam for this design.

A number of differing factors between the bare membrane and the cavity determine the total signal increase that we measure. These factors include the magnitude of the cavity field intensity enhancement, the excitation volume, the far field coupling of the sideband PL, local heating of the structure and many as of yet unknown factors like the effects of surface

proximity on defect charge stability. Additionally, many of these factors vary across the excitation volume and thus ensemble averaging prevents a direct, quantitative comparison with the predicted field enhancement values. An isolated single emitter within the cavity probed at an excitation intensity below saturation is necessary for a quantitative comparison.

When measuring color center fluorescence under conditions of resonant excitation, it was crucial that the scattered laser light and laser gain-medium fluorescence be prevented from dominating the signal measured by the sensitive superconducting nanowire single photon detector. These measurements were performed in a configuration allowing cross-polarized resonant scattering spectroscopy such that the resonant laser was maximally scattered into the collection path when resonant with the cavity wavelength. Additionally, the laser cavity gain-medium exhibited un-polarized broadband fluorescence throughout the photoluminescence spectrum of the Ky5 defects. In order to suppress these two contributions, we used a series of 1150 nm short pass filters in the excitation path to eliminate the excitation beam's long wavelength components and then used a series of 1150 and 1175 nm long pass filters in the collection path to suppress any short wavelength components in the measured signal. Long pass filtering at 1175 nm passes ~55 percent of the total spectral weight of the defect emission

band. Additionally, an extra linear polarizer in the collection path helped further eliminate scatter that exhibited polarizations that did not coincide with the linear polarization of the PBS exit port.

As mentioned previously, we observe an increase in the ODMR signal by a factor that corresponded to the observed increase in signal intensity (see Figure 7.8). This confirms that the increased signal results from fluorescence, not scattered excitation light. To further corroborate this conclusion, we also perform the same signal enhancement measurements at room temperature. Because the defect luminescence is non-radiatively quenched as the temperature approaches 295K whereas the cross-polarized resonant scattering signal is observable at all temperatures, this allows us to determine the contribution to the signal from the scattered laser excitation. See Figure 7.6 for results from the L3 cavity design considered in the above and Figure 7.7 for the results for an H1 cavity on the same sample measured under the same conditions.

Figure 7.6 (a) shows the cavity photoluminescence and PL excitation spectrum for the L3 cavity design discussed in the above. Spatial scans of the cavity, surrounding photonic crystal, and membrane allow for the determination of the relative optical response of the sample structure. For this structure, we observe a photoluminescence signal enhancement of 24

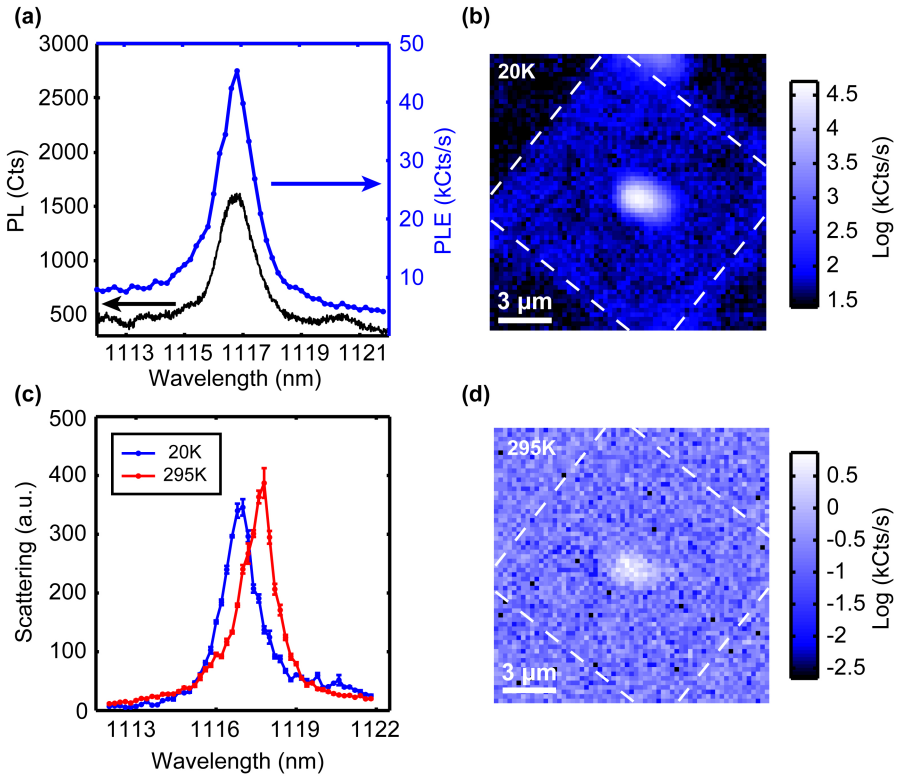

Figure 7.6: (a) PL (black line) and cavity enhanced PL excitation (blue line and dots) spectra for a basic L3 cavity at 20K. (b) Spatial map of the sideband photoluminescence signal under cavity resonant excitation at 20K. (c) Cross-polarized resonant scattering spectra of the cavity at 20K (blue line and dots) and 295 K (red line and dots). (d) Spatial map of the sideband photoluminescence signal under cavity resonant excitation for the same region and experimental conditions as (b).

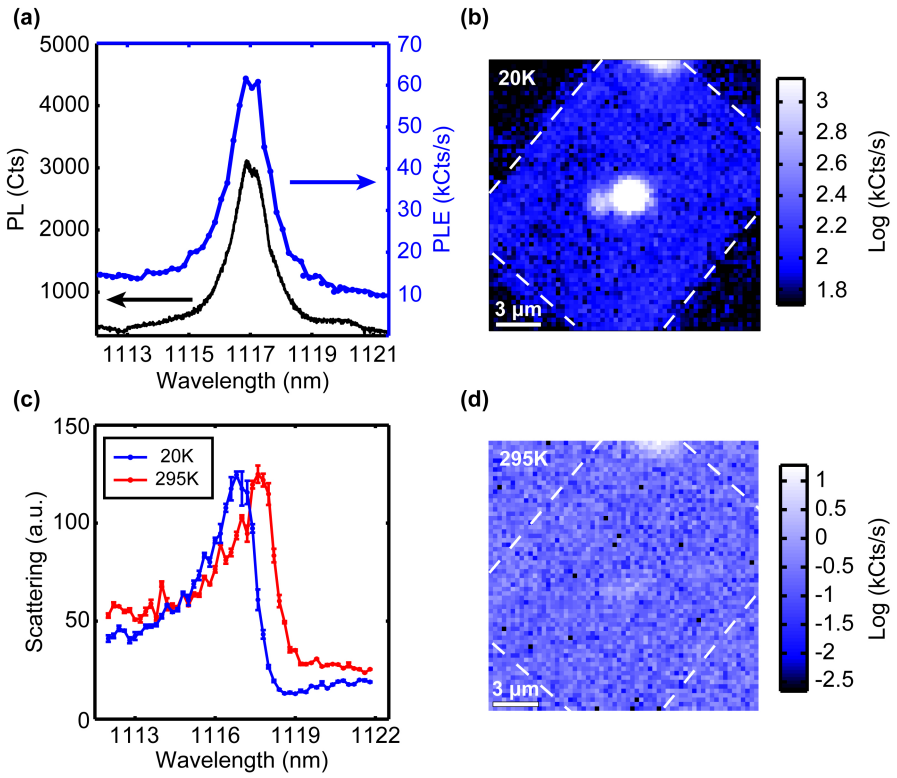

Figure 7.7: (a) PL (black line) and cavity enhanced PL excitation (blue line and dots) spectra for an H1 cavity at 20K. (b) Spatial map of the sideband photoluminescence signal under cavity resonant excitation at 20K. (c) Cross-polarized resonant scattering spectra of the cavity at 20K (blue line and dots) and 295 K (red line and dots). (d) Spatial map of the sideband photoluminescence signal under cavity resonant excitation for the same region and experimental conditions as (b).

times the membrane fluorescence (see Figure 7.6 (b)). The cavity resonance shifts by approximately 1 nm between 20 K and 295 K so in order to accurately determine the signal contribution from resonant scattering that isn't completely rejected by the filters, we use cross-polarized resonant scattering spectroscopy to determine the cavity resonance wavelength at room temperature (see Figure 7.6 (c)). Figure 7.6 (d) shows a spatial scan of the same region at room temperature. While the cavity is indeed still visible as a result of scattered laser light, the measured count rate of 1.5 kCts/s above the background is tiny compared to the signal measured at low temperature (107 kCts/s). This indicates that the contribution from the scattered laser excitation in the low temperature measurements is only 1.4% of the measured signal.

Figure 7.7 (a) shows the photoluminescence and PL excitation signal resulting from an H1 cavity design on the same sample. This cavity design, in general, exhibits a brighter cavity enhanced photoluminescence signal under off-resonant excitation than the L3 design due to a greater percentage of far field emission into the numerical aperture of the microscope objective. However, this design also exhibits an anti-symmetric electric field profile with respect to one axis of the photonic crystal cavity, resulting in a much weaker coupling to the Gaussian input beam. As a result,

the resonantly excited signal enhancement is approximately a factor of 2-3 lower as compared to the L3 cavity (a factor of 13.4, see Figure 7.7 (b)). This same effect also results in a weaker cross-polarized resonant scattering spectrum and a more pronounced Fano-type lineshape due to interference between the reflected and scattered beams as shown in Figure 7.7 (c). Figure 7.7 (d) shows a spatial scan over the same region at room temperature with the excitation laser tuned to the peak of the cross-polarized resonant scattering spectrum. The signal at the position of the spatial cavity is indistinguishable from the background, corroborating the conclusion that the low temperature signal is entirely a result of defect photoluminescence for this structure design.

7.7 Spin-dependent Measurements

The observed PL signal enhancements provide a means to greatly increase the signal amplitude in ODMR measurements that probe the defect level structure or for sensing applications. In order to perform spin dependent measurements on defects within the cavity structure, we performed an additional fabrication step that adds a metalization layer to the sample surface. Figure 7.8 shows an optical micrograph of an array of released

films patterned with photonic crystal cavities with a 50 μm wide gold wire positioned 50 μm away from the structure for applying intense local microwave fields to the sample. Due to the strength of the freestanding SiC films, the metalization can be applied prior to or after the release step. Microwave signals are fed through a vacuum tight feedthrough to coaxial cable internal to the helium flow cryostat and terminate in a stripline that is wirebonded direct to the sample. The use of on-chip metalization was found to be necessary for applying sufficiently intense microwave fields in order to achieve coherent spin manipulation (Rabi oscillations) on time scales faster than the defects T_2^* of $\sim$ 50 ns[121]. Technical limitations limited our applied π pulses to a length of $\sim$30 ns.

Figure 7.8 (b) compares the ODMR signal for the same excitation power with the beam incident on the membrane (red line and dots) and the photonic crystal cavity (blue line and dots) at zero magnetic field. The red data is multiplied by a factor of three so as to be visible on this scale. The overall ODMR signal enhancement matches the PL signal observed for this cavity ($\Gamma_e \approx 20$), further confirming that the enhanced signals on resonance originate from defect PL, not scattered laser light. Similar results are observed in the time domain. By synchronizing pulsed optical excitation using an acousto-optic modulator with pulsed microwave excitation, we

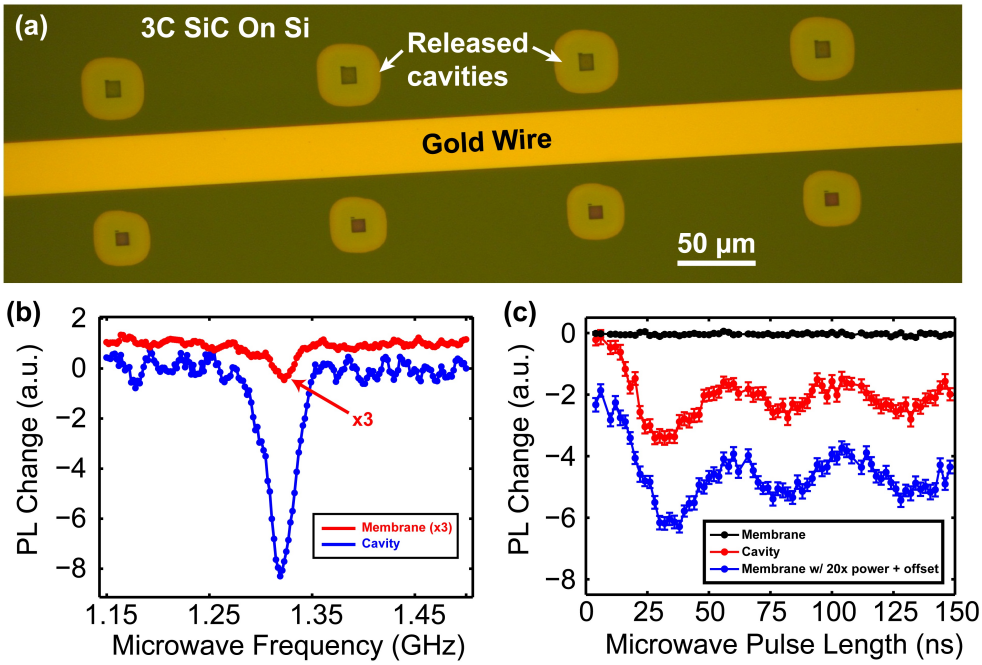

Figure 7.8: (a) Optical image of a photonic crystal cavity array with local 50 μm wide 10 nm/300nm Ti/Au metallization positioned 50 μm away from the cavities for applying microwave fields for spin manipulation. (b) ODMR signal at 1.319 GHz for the same incident optical power at a wavelength tuned to the cavity resonance wavelength on the photonic crystal cavity structure (blue line and dots) and on the membrane (red line and dots). The red line is multiplied by a factor of 3 for clarity. The peak is ~20 times larger and is equal to the measured Γ_e for this cavity. (c) Pulsed ODMR measurements demonstrating coherent control (Rabi oscillations) for a defect ensemble within the optical cavity (red line and dots) as compared to the same signal for defects in the membrane at the same distance from the metalization under the same excitation conditions (black line and dots). The blue line and dots shows the same measurement for defects within the membrane for a higher excitation power with an added offset for clarity. A π pulse corresponds to approximately 30 ns.

observe coherent Rabi oscillations between the $m_s = 0$ and $m_s = \pm 1$ sublevels of the defect's ground states for emitters excited via the cavity or in the bare membrane, as shown in Figure 7.8 (c). As with continuous wave ODMR, the Rabi oscillation signal amplitude is greatly enhanced under resonant excitation due to a combination of brighter PL and faster ground state spin polarization. These large signal enhancements may find applications in on-chip sensing architectures where significant losses in power can result from free-space to on-chip coupling or for studying the variation in spin properties for defects with differing strain environments resulting in distinct ZPL wavelengths or polarizations.

7.8 Studying Inhomogeneity

In addition to improving measurements of single emitters, cavity enhanced PL excitation spectroscopy on the inhomogeneously broadened ZPL of a large ensemble can facilitate studies of spectral inhomogeneity.[89] Utilizing the cavity for enhanced collection and excitation with a small mode volume as compared to the membrane facilitates the isolation of a smaller number of spectral lines within a given spectral window due to the fact that this spectral fine structure and its emission polarization can vary through-

out the crystal due to random local structural defects. [145]

All samples measured earlier in this chapter were implanted at a relatively high ion implantation dose of 10^{13} cm^{-2}. As discussed in [157], this dose was observed empirically to produce the brightest defect PL signal for the range of doses we tested (10^{10} cm^{-2}-10^{15} cm^{-2}). Higher doses were found to decrease the overall defect signal, indicating that above 10^{13} cm^{-2} the sample may exhibit more non-radiative pathways or the bulk properties are changed in such a way as to suppress defect formation. For the ion dose measured in the above (10^{13} cm^{-2}), the combination of a high defect density and random local strain resulting from the proximity to the silicon growth interface results in a large degree of inhomogeneous broadening of the defect ensemble ZPL. The FWHM of the ZPL in this sample was 28.2 nm. For the same implantation dose in a 3.85 μm thick film the FWHM was measured to be 4.6 nm. Figure 7.9 compares ZPL spectra of thick film and a thin film for the same implantation dose. The spectral density of the broadened ZPL exhibited an approximately Lorentzian lineshape, although some discrete features result from moisture in the air throughout this spectral range. While the inhomogeneous broadening present in the material grown close to the silicon interface may be detrimental to future applications, the material farther from the interface shows significantly

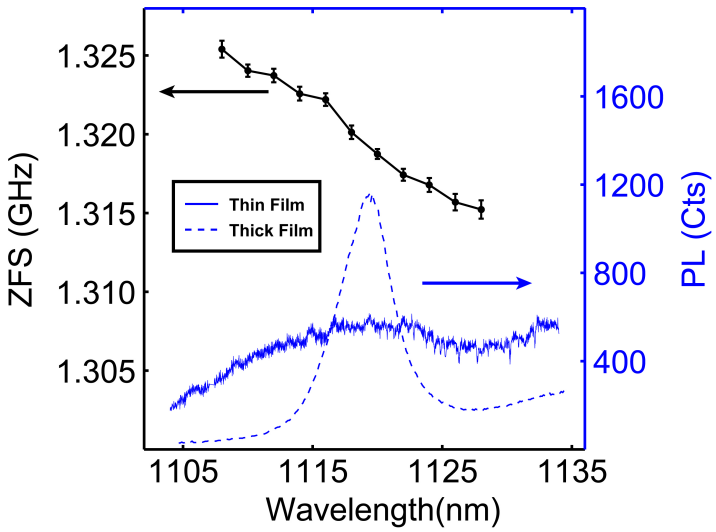

Figure 7.9: Extracted ZFS for defects excited at different wavelengths throughout the inhomogeneously broadened ZPL (black line and dots) and the corresponding PL spectra for a 300 nm thick film (solid blue line) and a 1 μm thick film (dashed blue line) implanted and annealed under identical conditions at an ion dose of 10^{13} cm^{-2}.

improved crystalline quality. Accordingly, the ability to easily back etch through the silicon substrate using wet etches or the Bosch process allows for one to produce photonic structures in higher quality material at the top of a thick grown film.

Resonant excitation provides a means to study this inhomogeneity through techniques like spectral hole burning or fluorescence line narrowing. We utilize this resonant excitation to selectively excite a spectrally narrow distribution of defects within the ZPL in an unprocessed membrane following the same methods used in the above for PLE. Figure 7.9

also shows the results of this selective excitation as applied to studying the ground state optically detected magnetic resonance (ODMR) spectra of the defect subensembles. The black line and dots show the resulting variation in zero field splitting (ZFS) measured for spectrally distinct subensembles plotted vs. excitation wavelength. The ZFS and the ZPL energy correlate as a result of the strain dependence of the ground state and excited state Hamiltonian of the defects. The ZFS shifts by 10 MHz between 1108 nm excitation and 1128 nm excitation resulting in a shift of .5 MHz/nm. Additionally, the ODMR linewidths vary by 30-40% over this same excitation wavelength range (see Figure 7.10). While a quantitative analysis of the exact details of this shift is difficult without a more precise knowledge of the local strains involved, this provides an example of the types of spectral inhomogeneity that can be more easily studied with the signal enhancements provided by enhanced cavity resonant excitation and has been observed previously in NV center systems.[89]

In lower implantation dose samples (10^{12} cm^{-2}), the defect ensemble ZPL no longer exhibits a smooth Lorentzian lineshape. Instead, as shown in Figure 7.11, the spectrum exhibits polarization-dependent fine structure. While water absorption still affects this spectrum, this lower dose shows a series of pronounced discrete emission lines on top of the broad-

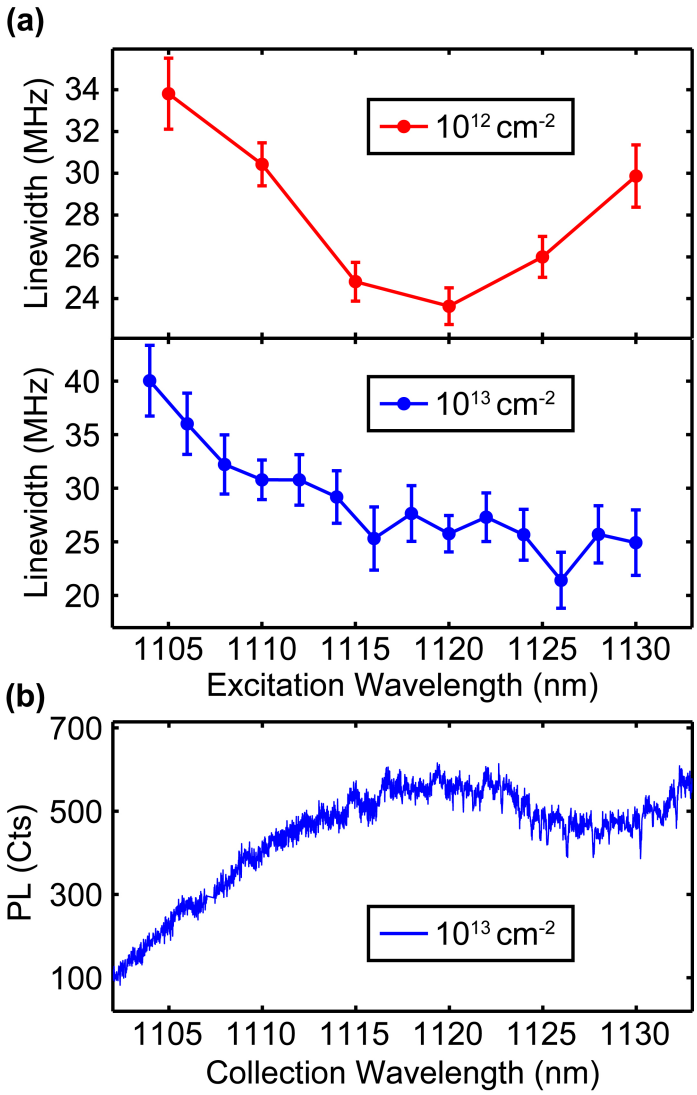

Figure 7.10: Extracted ODMR linewidths for defects excited at different wavelengths throughout the inhomogeneously broadened ZPL. The blue line shows the inhomogeneously broadened ZPL measured for a sample implanted at an ion dose of 10^{13} cm^{-2}. The blue line and dots depict the variation in the ODMR linewidth for different excitation wavelengths for a sample implanted at a dose of 10^{13} cm^{-2}. The red line and dots depict the variation in the ODMR linewidth for different excitation wavelengths for sample implanted at a dose of 10^{12} cm^{-2}.

ened ZPL distribution. This behavior becomes clearer when the emitters are present inside a cavity. Figure 7.11 shows the spectrum of a typical H1 cavity in a 300 nm thin film implanted at an ion dose of 10^{12} cm^{-2}. In this case, we focus on the H1 cavity design because even though it exhibits suppressed coupling to far field Gaussian modes, the overall emission pattern is weighted more heavily within the solid angle subtended by the numerical aperture of the objective lens, producing a ~10x brighter off-resonantly excited PL signal as compared to L3 structures within the same sample. While these narrow lines are visible in the bare membrane, the overall signal intensity is very low (~2-5 counts per second above the background-see Figure 7.11), making it difficult to perform measurements on feasible time scales. The cavity enhances the collection efficiency by approximately a factor of 10 for our H1 design, but only for spectral lines within the linewidth of the cavity and for emitters whose polarizations couple to the local cavity mode polarization (see Figure 7.12). This assists in isolating and enhancing these spectrally distinct emission lines. No narrow emission lines are observed for cavities turned to the phonon sideband due to the large homogeneous broadening in the sideband transitions. Additionally, the use of cavity resonant excitation as described previously allows for even further increases in signal strength as compared to off-resonantly

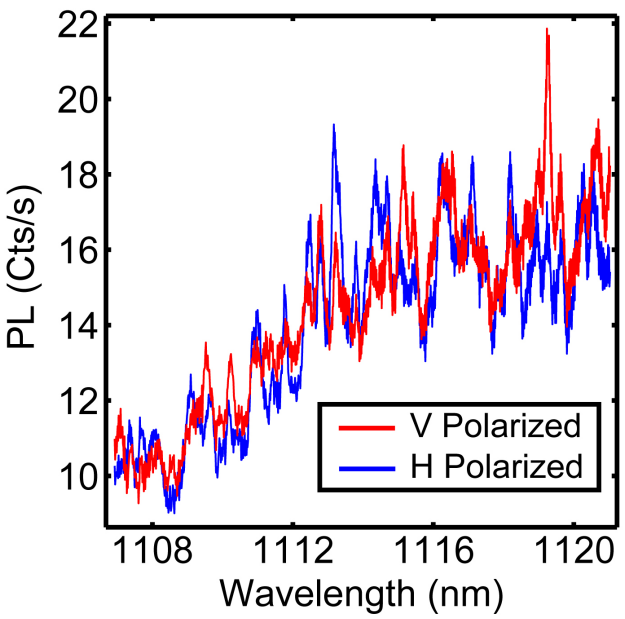

Figure 7.11: Vertically polarized (red line) and horizontally polarized (blue line) fine structure within the Ky5 ZPL in a 300 nm thick membrane implanted at an ion dose of 10^{12} cm^{-2}.

excited PL and also excites only emitters thats are contained within the small mode volume of the cavity and match the local cavity polarization.

Figure 7.13 shows a plot comparing cavity resonant PL excitation spectroscopy with PL measurements on the set of narrow emission lines coupled to a cavity resonance shown in Figure 7.12. The cavity resonant PL excitation technique has a resolution of ~300 kHz while the resolution of the spectrometer and CCD combination was measured to be 25 GHz (.1 nm). This measurement confirms the ~25 GHz linewidth observed for

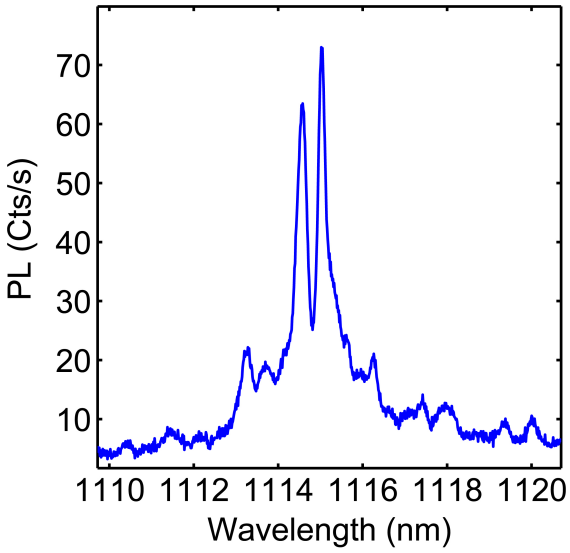

Figure 7.12: Off-resonantly excited PL spectrum of a representative H1 cavity in a thin film implanted at an ion dose of 10^{12} cm^{-2}.

the narrowest lines that we observed. Additionally, the count rates corresponding to the PL excitation measurements are significantly higher than the count rates for off-resonant excitation with spectral filtering for comparable excitation powers. The PL excitation scans shown in Figure 7.13 were obtained for a ~1.5 μW incident on the sample while the off-resonantly excited PL spectrum was obtained ~3.2 mW incident power. For a typical narrow line enhanced by the cavity mode, no PL signal above the detector dark counts (~10 cts/s) can be observed for off-resonant excitations powers below ~100 μW. For the PL excitation measurement depicted in Figure 7.13, the feature at ~1115.1 nm exhibits ~1400 cts/s for 1.5 μW incident

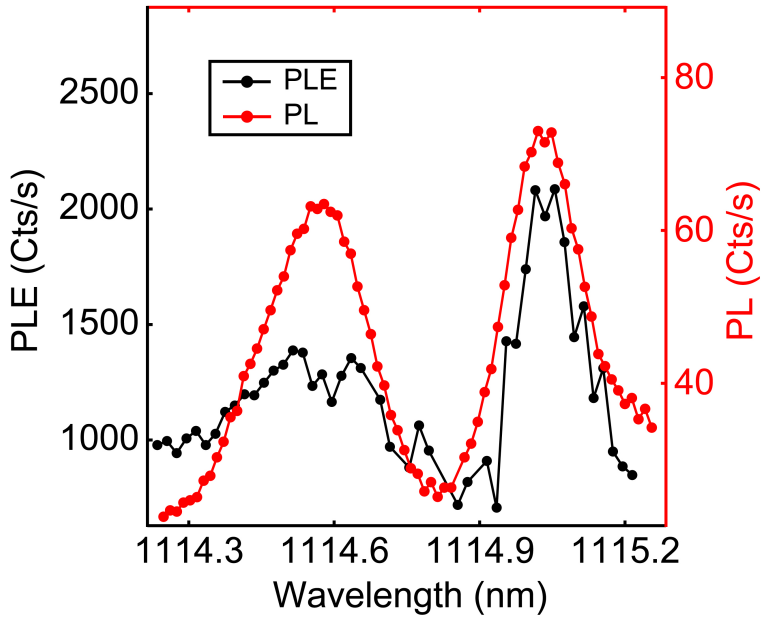

Figure 7.13: Comparison between the PL excitation (black line and dots) and PL (red line and dots) spectrum of the narrow emission lines coupled to the H1 cavity mode depicted in Figure 7.12.

power.

We speculate that these narrow spectral lines originate from sub-ensembles of defects within the inhomogeneously broadened ensemble that experience similar local strain environments. Figure 7.14 compares a typical PL spectrum in this sample to the cross-polarized resonant scattering measurement on the same structure, confirming that this fine structure is not a high Q resonant mode. Furthermore, Figure 7.15 shows the same PL excitation spectrum measured previously in Figure 7.13 as compared

to another spectrum taken at a higher power. If these narrow lines do result from subensembles consisting of a smaller number of defects, then they should exhibit saturation at higher powers and the signal should eventually be dominated by defects that are off-resonantly excited (i.e. still responding linearly), leading to a smooth absorption spectra. We observe that under off-resonant excitation, these narrow peaks don't begin to saturate until approximately 5 mW. Figure 7.15 confirms this behavior and shows that the cavity resonant PL excitation spectra exhibits the lineshape of the cavity mode at higher excitation powers (~37.5 μW). Figure 7.16 shows a wider cavity enhanced PL excitation scan of a similar cavity taken at higher excitation power (~75 μW) as compared to the off-resonantly excited PL spectra from the same cavity.

7.9 Photoluminescence Dynamics

In addition to providing enhanced signal intensities, the excitation enhancement provided by the resonant cavity can also be used to enhance the rate of optically induced spin polarization in the defects' ground state. To observe this enhancement, we measure the time-dependent response of the defects PL in conjunction with interleaved microwave π pulses. A series

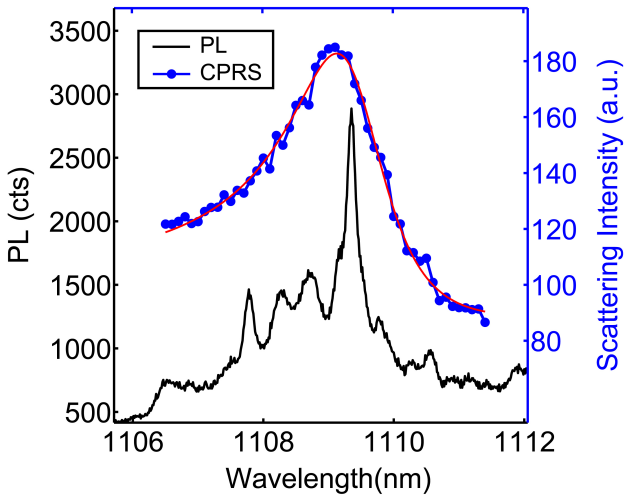

Figure 7.14: Comparison between the PL (black line) and cross-polarized resonant scattering spectra (CRPS)(blue line and dots) for an H1 cavity that exhibits narrow emission lines.

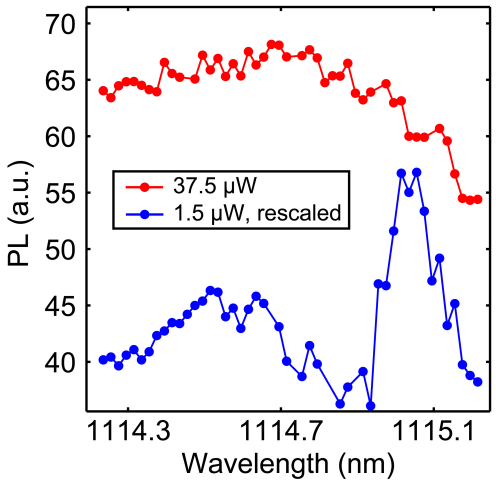

Figure 7.15: PL excitation spectra for the H1 cavity in Figure 7.12 for an incident power of 1.5 μW (blue lines and dots, rescaled for clarity) and 37.5 μW (red line and dots).

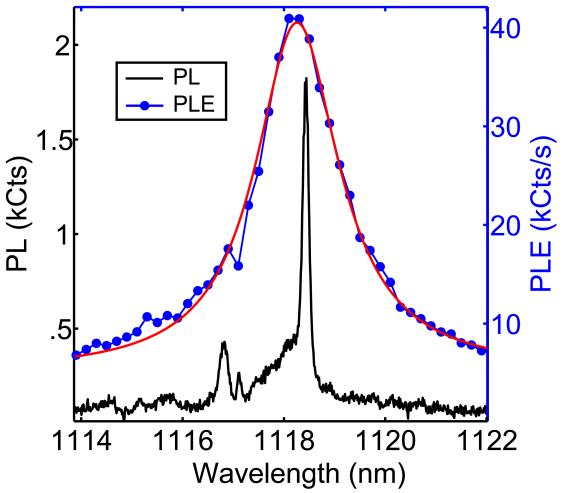

Figure 7.16: Comparison between the PL spectrum (black line) and PL excitation spectrum (blue line and dots) for an incident power of 75 μW for a typical H1 cavity in a sample implanted at an ion dose of 10^{12} cm^{-2}

of optical pulses with a variable length from 250 to 1500 ns are applied to excite the system from the ground state to the excited state where they experience a spin-dependent chance to relax back to the ground state via the intersystem crossing (ISC) transitions. As a result, for a period of time immediately after the turn-on of the optical pulse, the system will fluorescence more or less brightly depending on the degree of ground state spin polarization immediately prior to the optical pulse. Prior to half of the optical pulses, we apply a microwave π pulse to invert the ground state spin polarization. We collect the PL signal for a fixed time period of 100 ns immediately after the turn-on of the optical pulse and measure the dif-

ference in PL resulting from optical pulses that immediately followed a π pulse and those that did not. This differential PL signal provides a relative measure of the ground state spin polarization which is dependent on the length of the optical pulse. The same intersystem crossing process that allows for spin-dependent optical state readout also polarizes the ground state spin such that lengthening the pulse produces a higher degree of ground state polarization. [44] [96] Additionally, a more intense laser pulse also induces more optical cycling to the excited state and therefore a faster rate of ground state polarization. A 'dark' period of at least 500 ns follows every optical pulse to allow for population with in the ISC to fully relax to the ground state.

Figure 7.17 (a) shows the time-dependent difference in PL between a system initially prepared in either the $m_s = 0$ state or the $m_s = \pm 1$ states for two different excitation rates, as predicted by a PL dynamics model based on those used to model NV center fluorescence.[44] The figure also depicts the measurement scheme described above and the approximately exponential decay of the difference signal for laser pulse lengths longer than the collection time. This corresponds to an exponentially saturating ground state spin polarization and exponentially saturating PL difference

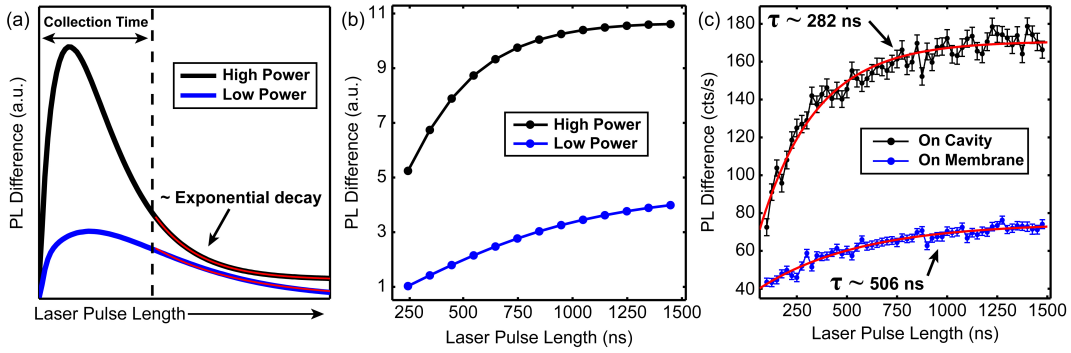

Figure 7.17: (a) Schematic indicating the difference in PL signal for the model of optical dynamics that is expected to apply for the Ky5 defects for two different excitation powers. The red lines depict exponential fits to the limiting behavior of the dynamics. The black curve is offset for clarity. (b) Simulations of the measured PL difference signal for the variable laser pulse length measurement indicated in (a) for two different excitation powers. (c) Measured PL difference signal for an ensemble of Ky5 defects within a basic L3 photonic crystal cavity excited on resonance (black line and dots) as compared to an ensemble excited at the same power and wavelength within the unpatterned membrane at the same distance from the metalization (blue line and dots).

signal measured within the collection time. Figure 7.17 (b) shows the results of simulations of this difference signal for varying laser pulse lengths for two different excitation rates based on this model. Figure 7.17(c) shows the results of this measurement scheme for defects within a photonic crystal cavity excited on resonance with the mode and defects incorporated into an unpatterned membrane. The observed saturation behavior qualitatively matches the modeled behavior and exhibits an enhanced rate of ground state polarization from ~500 ns to ~280 ns. This rate enhancement is relatively small because of the transitions are near saturation and would

be more significant for lower excitation rates.

While the variable laser pulse length measurement does provide a measure of the polarization rate of the defects, time correlated single photon counting (TCSPC) techniques are a more common method of measuring PL dynamics. Both methods exhibit different advantages and disadvantages for a variety of experimental parameters like count rate, pulse sequence repetition rate, timing precision, etc. Here we utilize TCSPC measurements to confirm the behavior observed with the variable laser pulse length measurements and provide further qualitative insight into the spin-dependent PL dynamics of the defect states. These measurements do, however, suffer from effects resulting from ensemble averaging and further detailed measurements on single defects or ensembles are necessary to accurately determine exact details of the system.

Figure 7.18 shows the pulse sequences utilized for the variable laser pulse length and the TCSPC measurements. For the variable laser pulse length measurements, the repetition rate of the experiment is set by a function generator that produces a square wave with a 5 microsecond period that alternatively routes photon count pulses through a microwave switch to two separate counting channels of a DAQ; one channel counts photons from optical pulses that were immediately preceded by a microwave π pulse

and the other channel counts photons from optical pulses without the π pulse. This subtractive measurement removes any non-spin dependent time dynamics and avoids low frequency noise and drifts. The function generator also triggers a pulse pattern generator and digital delay generator that send pulses to a series of microwave switches set the collection time of 100 ns, the microwave pulse length of the π pulse to drive population from the $m_s = 0$ states to $m_s = \pm 1$ states, and to gate the pulsed optical excitation. The measurement is averaged over many repetitions of the pulse sequence. For measurements performed on the cavity, a feedback loop scans and repositions the laser spot at the position of the cavity between each sequence repetition.

For TCSPC measurements, a function generator is used to produce a pulse to trigger the synchronization input of the TCSPC PCI card (Becker and Hickle SPC630) at a rate determined by maximum measurement span of the card (2 μs). A synchronization output of the function generator triggers the pulse pattern generator which is used to gate the AOM 'On' for two 500 ns time periods separated by 500 ns and generate a microwave π pulse with a microwave switch. The SNSPD generates an asynchronous photon count rate that is attenuated to 1 percent of the measurement repetition rate of 500 kHz to avoid skewed statistics resulting from electronics

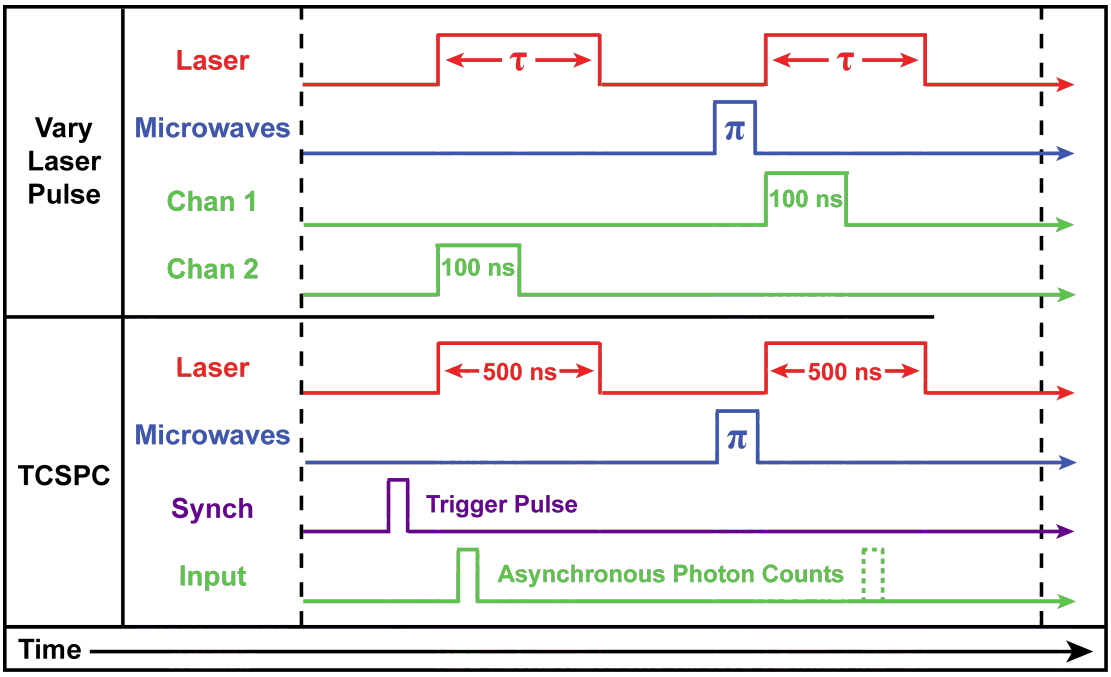

Figure 7.18: Pulse sequences for ground state spin polarization dynamics measurements performed by varying the excitation laser pulse or using TCSPC methods.

dead time(the 'pile-up' effect). While this method of observing time dependent PL is more straight forward to interpret than the variable laser pulse length method, it suffers from a limited timing window of 2 μs set by the TCSPC card, low count rates to avoid the pileup effect, and non-linearities in the Time-to-Amplitude converter that can obscure the data.

We also in the course of the work performed PL lifetime measurements on the defect emission band with pulsed, off-resonant excitation at 920 nm using a mode locked Ti:Sapphire laser. Because the pulse repetition rate exceeded the maximum synchronization rate of the photon counting

card and the inter-pulse period was comparable to PL lifetime, we used an electro-optic modulator pulse picker to reduce the inter-pulse spacing to about 130 ns. PL decay curves were obtained using the TCSPC photon counting unit. The signal counting rate is again reduced to roughly 1 percent of the synchronization rate to avoid statistical errors.

Figure 7.19 shows the time dependent PL for the first 350 ns of a laser pulse with a π pulse immediately preceding it as measured for defects excited on the cavity resonance (blue points) and for defects within the unprocessed membrane (navy points). The PL increase shows approximately exponential behavior as the defects are optically pumped into the $m_s = 0$ state, similar to what was observed in the variable laser pulse length measurements. The cavity polarization time constant is ~73 ns while the membrane time constant is ~169 ns. This degree of enhancement of the rate of polarization is similar to what was observed with the previous method.

To confirm that the variable laser pulse length dynamics result from spin-dependent optical pumping into the $ms = 0$ ground state, we perform a control measurement without the interleaved π pulse. This measurement is shown in Figure 7.20. As expected, there is no difference in time dependence between the pulses, thus resulting in no observable time-dependent difference signal. Similarly, no difference is seen between the two pulses

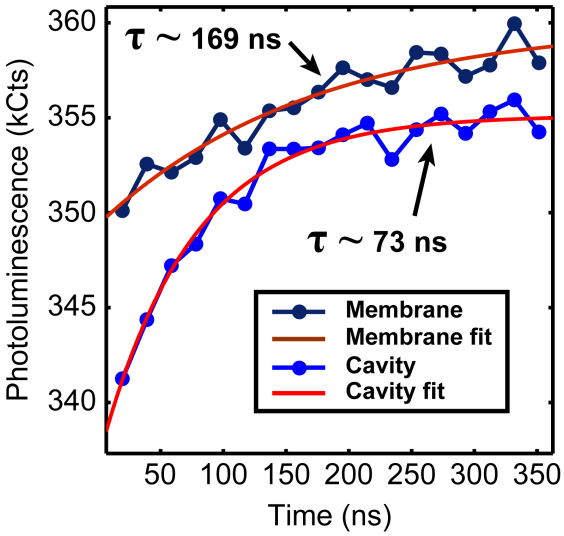

Figure 7.19: Saturation of PL intensity demonstrating ground state spin polarization dynamics for the bare membrane (navy line and dots) and cavity (blue line and dots) under identical excitation conditions as measured with TCSPC.

using TCSPC methods if no π pulse is applied during the pulse sequence.

Direct measurements of luminescence dynamics performed using TCSPC methods can also provide insight into the details of optical polarization dynamics of the defects[96]. A completely accurate determination of details of the optical dynamics of the defects is beyond the scope of this work but we do note qualitative agreement between our data and a model consisting of the seven level model originally proposed by Manson et. al.[44], albeit with modified values for the exact model parameters. This model's assumed level structure and various input parameters are de-

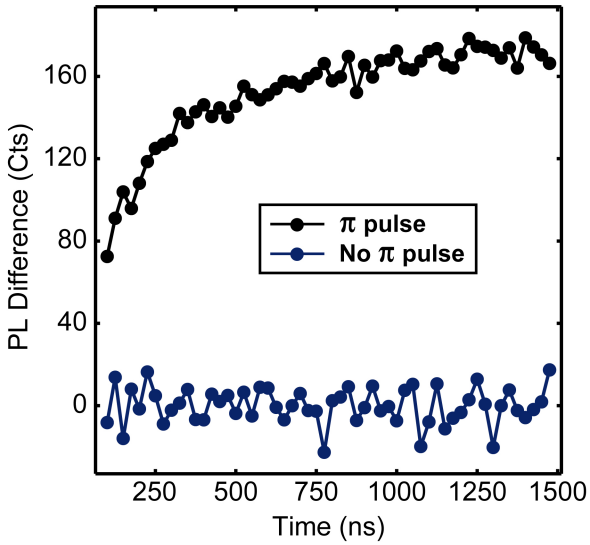

Figure 7.20: Variable laser pulse length measurements of the ground state spin polarization dynamics with resonant cavity excitation with (black line and dots) and without (navy line and dots) the interleaved microwave π pulse.

fined in Figure 7.21.

Levels 1 and 3 represent the $m_s = 0$ ground and excited states. Levels 2 and 4 consist of the $m_s = \pm 1$ ground and excited state levels and are grouped together to form a degenerate doublet with equal sets of rates. Level 5 consists of the intersystem crossing levels. The model consist of a series of classical rate equations defined by

$$\frac{dn_i}{dt} = \sum_j k_{ij} n_j - k_{ji} n_i \tag{7.28}$$

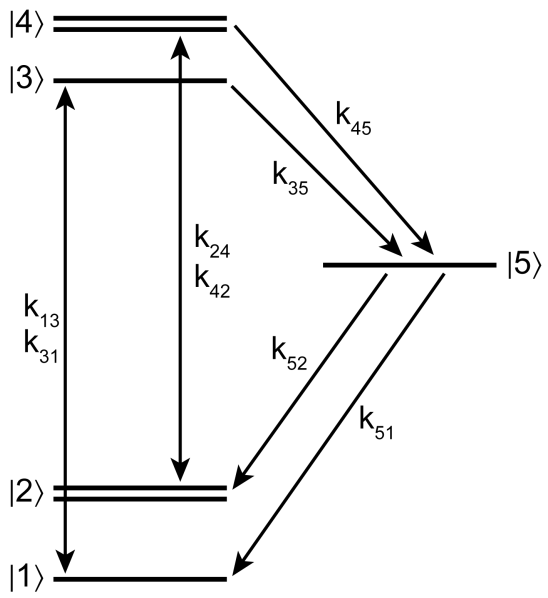

Figure 7.21: Electronic level structure used for rate equation modeling.

where n_i represents the occupation probability of a given level and k_{ij} represents the transition rate from level i to level j. All transitions are treated as radiative so that all rates from a lower energy level to a higher energy level are zero except for k_{13} and k_{24} which represent the optical excitation. Once the transition rates have been chosen, the resulting dynamics can be easily generated by a numerical ordinary differential equation solver.

The excited state to ground state transition rates can determined from the TCSPC luminescence lifetime measurements described above. Figure 7.22 shows the results of such measurements at 20K for a 300 nm thin

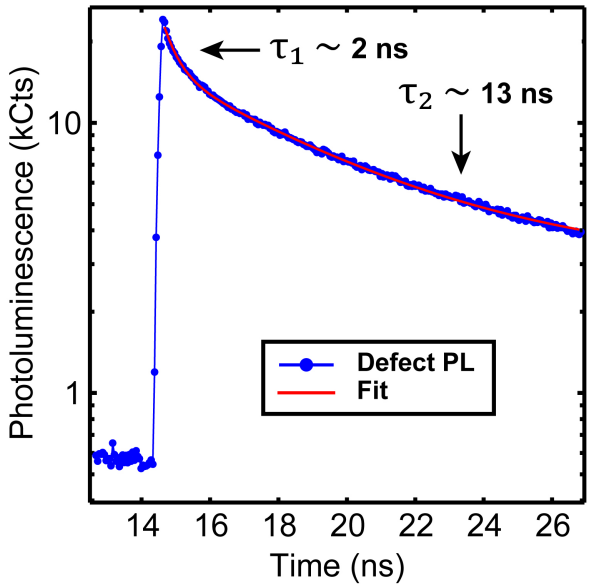

Figure 7.22: Fluorescence decay curve of the Ky5 luminescence band.

film implanted at an ion dose of 10^{12} cm^{-2}. The decay exhibits a fast ~ 2 ns component that is not atypical of most lifetime decay measurements [175] and may be related to background PL. The decay also exhibits a ~13 ns lifetime, similar to the excited state lifetime of the negatively charged nitrogen vacancy, further corroborating our assumptions that the two systems have similar electronic structure. This determines rates k_{31} and k_{42}.

Figure 7.23 shows representative PL dynamics from an unpatterned 10^{12} cm^{-2} dose implanted 300 nm thin film. The model qualitatively matches the behavior of the observed dynamics despite the fact that the model assumes a population undergoing uniform excitation and the mea-

surements consist of an ensemble of emitters that may be experiencing variable excitation powers. For the curves generated in Figure 7.23, the model also includes the experimental non-idealities such as the incomplete population inversion resulting from a non-ideal π pulse due to the short T_2^* time, the incomplete polarization resulting from each pulse, and the pulse repetition. The pulse repetition is included in the model by iterating the simulations in sequence using the ending polarization from the previous sequence. This is repeated until a steady state has been reached. The model's results for each pulse are then scaled by the same factor to match the total signal magnitude. The model qualitatively matches the overall timescale of the dynamics and the difference in count rates between the two pulses and produces a measured optimal pulsed ODMR measurement contrast of ~3 percent. For the simulation parameters that we determine, for ideal measurement conditions (a perfect π pulse and longer pulse length to ensure complete optical polarization) a maximum contrast of approximately 5.5 percent is achievable. Table 7.3 presents the values required to produce the curves in Figure 7.23. To reiterate, this agreement is only qualitative and more detailed measurements on single defects or homogeneously excited ensembles are required to determine whether or not the system truly exhibits NV center-like dynamics and if so, what the system

parameters are.

Table 7.3: NV Center Dynamics Model

Transition	Rate(μs^{-1})
$k_{13} = k_{24}$	77
$k_{14} = k_{23}$	0
k_{45}	10
k_{35}	0
$k_{51} = k_{52}$	40

Table 7.3 Parameters used for the rate equation modeling in Figure 7.23.

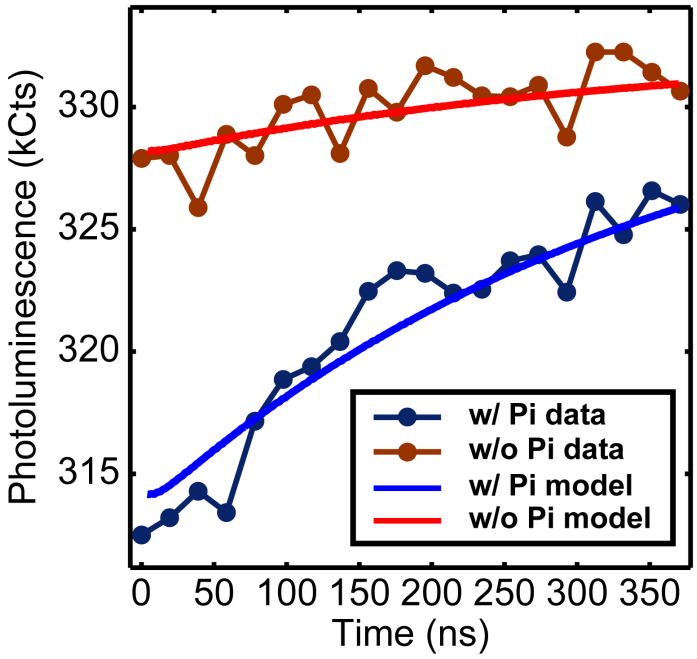

Figure 7.23: TCSPC measurements of Ky5 luminescence dynamics for an applied optical pulse with (navy line and dots) and without (dark red line and dots) a preceding π pulse.

Chapter 8

Conclusion

The work presented in the previous chapters represents a new direction for research in defect qubit approaches to solid state quantum information applications. This direction focuses on searching for and utilizing NV center analogues in other materials that may circumvent the pervasive challenges that are currently holding back progress in NV center-based applications. Chapters 2 and 3 presented a brief overview the aspects of solid state defect qubits that are relevant for quantum information applications and the details of the NV center, the model system on which we base our studies of defect qubits. Chapter 4 presented some of the first work on identifying and studying defect qubits based on divacancy and divacancy-related defects in 4H and 6H SiC. Chapter 5 presented subsequent work on defect qubits in a very technologically promising form of SiC: 3C SiC.

Chapter 6 detailed the work we did on producing the some of the first photonic cavities in 3C SiC and the first ones to incorporate defect qubits into the structures themselves. Chapter 7 then went on to use these structure to enhancement measurements of the defects and their ground state spin sub-levels; this represents one of (if not, the) first uses of high Q, small mode volume cavities to enhance measurements of defect qubits. All this work represents an early step along the route leading towards the goal of expanding the functional capabilities of defect qubit systems for quantum information or sensing applications. Of course, this alternate route forward is by no means a given; although other materials or defect systems may provide some clear advantages over diamond and NV centers, there are many yet undiscovered 'unknown unknowns'.[176] The primary reason for taking this risk is the likely possibility that any undiscovered challenges will be offset by the advantages afforded by these systems. If we knew what we were doing, it would not be called research, would it? [177]

Although one important milestone has recently been reached in the discovery of single divacancies [149] and other defect qubits in SiC [30], much work remains. Very little is known about the properties of these defects. It still remains to be seen as to how their optical dynamics/ISC process compares to the NV center, whether the excited state level struc-

ture is the same (are there any good cycling transitions or are non-spin conserving transitions significant?), or if they are more or less photostable than the NV center in bulk and near surfaces. Additionally, practical concerns need to be addressed such as how to enhance the relatively low count rate (3-5 kcts/s above background) of these single defects, whether devices can really be fabricated more easily in bulk SiC than diamond, and a definitive identification of the origin of many of the defects has yet to be performed. This, of course, is no where near an exhaustive list of unknowns that need to be probed in order to assess the long term prospects of SiC defect qubit research.

Defect qubits in 3C SiC face some of their own unique challenges. The most pressing challenge is determining what effects the crystalline defects that result from the lattice mismatch with silicon have on defect properties. Spectral inhomogeneity is clearly a potential problem, but this is also true for fabricated diamond where large residual strains are observed for defects in thin diamond films. Post-release annealing may provide a pathway towards healing some of the residual lattice imperfections. Furthermore, homogeneous linewidths and non-radiative recombination must be studied in order to determine the likelihood that these defects can be reproducibly used for photonic applications or at room temperature. It should also be

noted that another defect with an NV center-like spectrum has been observed near the telecom C-band (λ ~1500 nm) [178] and may act as another promising defect qubit in a wavelength range for which resonant lasers are more widely available.

Fabrication of photonic structures in 3C SiC will likely progress rapidly in the near future. Prior to 2013, there were no reports of resonant cavities in 3C SiC and now at least four research groups around the country are actively working on developing these structures for a variety of applications. Improving the Q's for the structures we have already demonstrated can likely be achieved by further process development. As discussed previously, achieving sidewalls that are more vertical is likely necessary for achieving Q's anywhere near the values simulated with FDTD and etching procedures exist that may allow this [139]. Alternatively, one-dimensional photonic crystal cavities seem to exhibit less sensitivity to sidewall angle and may significantly out-perform their 2-D counterparts. In any case, the structure parameters that have already been demonstrated may be used for the alternative applications of nanocavities discussed in previous chapters.

The recent discovery NV center analogues and development of devices interfacing with these defects has ushered in an exciting time for the study of defect qubits. Enough information is available to inform re-

searchers on the myriad of possible research directions but not so much is known as to make it difficult to find unexplored pathways forward. Much work still remains for developing our understanding of these defects and for incorporating them into photonic, mechanical, and electrical architectures. However, clear potential exists for developing scalable single photon sources or nanoscale sensors in order to produce some of the first widely available quantum technologies.

Appendix A

Cryogenics Tips and Tricks

Here are some tips on working with cryogenics:

- Safety: In general, safety should always be the primary concern. Cryogenics can be dangerous if not handled properly. Consult any 'Spectromag' manual or local safety resource for instructions on proper handling of cryogenics. In general, it is a good idea to always wear the proper gloves and eyewear in case of a spill or if one has to touch a particularly cold surface. In particular, vessels for handling liquid nitrogen occasionally pressurize in such a way that droplets can spontaneously ejected from the container and one should be prepared for such instances.
- Indium: It is not obvious, but metal-on-metal connections are frequently poor thermal junctions. For instance, a temperature increase

of almost 7K was observed (5K to 12K) at the cold finger of the Cold-Edge cryostat without proper treatment of the connection between copper braid connecting to the bottom cold stage and the sample mount. It is generally a good idea to provide some sort of means of improving the thermal link. The two most common substances uses for this purpose are Apiezon N grease and Indium. Both have their advantages and disadvantages. A detailed comparison has been prepared by NASA and can be found at [179]. In summary, Indium is generally preferable if one can provide enough force to the metal junction. Thin indium foil, however, can be quite expensive.

- Filters: Any constriction through which cryogens flow (like needle valves or capillary tubes) should be protected as much as possible with fine mesh brass filters. This is particularly important as a result of the recent drastic increase in the amount of ice and/or particulates found in the dewars provided by helium suppliers in North America. This contamination has led to many hours of wasted research time and even ruined expensive equipment. McMaster-Carr sells very fine mesh filters that can be utilized as additional safeguards when fitted to transfer lines.
- Sample mounting: Proper sample mounting is an art, especially con-

sidering the diverging opinions on how best to achieve a good thermal and mechanical joint. It is generally very important to make a careful choice in order to maximize the thermal connection to the cold finger, minimize the chance that the sample will detach under thermal cycling, and minimize background fluorescence. I personally found that rubber cement showed the least fluorescence in the IR as compared to GE varnish and silver paint under 975 nm excitation, but was the least reliable for thermal cycling and achieving a good thermal joint. Silver paint generally provided the best and most reliable thermal connection but was messy and difficult to completely clean away. GE varnish tended to be somewhat fluorescent but fairly reliable for thermal connections.

- Overpressure: In general, it is a good idea to be mindful of keeping good overpressures in any cryogenic space in order to minimize any backflow of oxygen or nitrogen in the air into a space that might eventually be at liquid helium temperatures.
- Minding leaks: This could be classified under safety but it is generally true that small leaks are difficult to completely remove so one should always be weary of warming up any cold space under vacuum. If a small leak has introduced a significant amount of nitrogen into the

space that subsequently condensed, this can cause an overpressure upon warming and provided a thermal pathway between the cold parts of the cryostat and the outside. In particular, it is a good idea to flow dry nitrogen over the cryostat window whenever one warms up in order to minimize condensation on the window which can effect the AR coating or leave residue.

- Monitor wirebond resistance: It is a good idea to be mindful of what the room and low temperature resistances are of your completely wirebonded up sample within your cryostat. Monitoring these values can clue you in when your wirebonds break or help with troubleshooting unknown microwave problems.
- Mounting temperature sensors: the type of temperature sensors we typically use from Lakeshore are intended to be mounted in such a way that minimizes strain on the sensor and the chance of electrical shorts. Accordingly, one should typically mount any temperature sensors with a mechanical means to lightly press the sensor to the desired substrate, typically with a piece of indium to make a good thermal contact.
- PCB sample mounts: don't use them. Always mount directly to copper to achieve the best thermal link to the substrate for low tem-

perature measurements.

Appendix B

Optics Tips and Tricks

Here are some tips on working with optics:

- Safety: It is very easy to stop taking optics safety seriously when you work around them long enough. A few general safety habits like never putting your head at table level (assuming one has kept the beam at table level) and putting up beam blocking shields will go along way to insuring no one ever damages their eyes. One should generally be exra careful around IR lasers that are invisible without an IR viewer.
- Alignment references: Our home built confocal microscope setups are generally rather complex and utilize a number of mechanical parts to steer the beam from source to sample. As a result, these setups can very easily become misaligned due to either human error or laser drift.

The counteract this, it is a good idea to place a series of alignment references throughout the setup in order to have an easy means of realignment without the need to start from scratch. Irises placed at key points in the setup are a good means to accomplish this and the use of fiber optics (especially single mode fibers) in the collection path can minimize the required to 'tweak' up the signal. The use of horizontal translation stages at a few key points in the optical path can greatly facilitate beam steering to compensate for optics drifts.

- Cameras and spectrometers: The spectrometers and CCD arrays were typically use from Princeton instruments and Acton are very sensitive and powerful but their firmware can be incredibly frustrating to interface with. I have generally found that unless you want to spend a weekend swearing at the camera, spectrometer, and Labview, it is a good idea to setup the camera and spectrometer once on a dedicated computer and never touch it again, resulting in a dedicated computer for each camera and spectrometer. We generally always have enough older unused computers that this is not a significant drain on lab resources. Other users can couple to the spectrometer through a fiber and use a TCP/IP interface to talk to the spectrometer.

- Calibrating at-sample polarization: In general, once one has achieved a particular light polarization through the use of a waveplate, that polarization will be altered by any optics the beam passes through on its way to the sample. To fix this, one can use a variable waveplate on a rotation mount to adjust the polarization until the correct one is achieved at the sample. To calibrate circular polarization, one can typically replace the sample with a mirror and use a 'Faraday isolator' geometry to compensate for deviations from circular polarization. Linear polarization is a bit easier can be fixed by introducing small amounts of circular polarization with a variable waveplate. Typically, linear polarizations won't be messed up by downstream optics as long as you stick to horizontal or vertical polarizations (even non-polarizing beamsplitters will introduce phase shifts to a beam that isn't S or P polarized).
- Spectral filtering: Proper spectral filtering can solve many background issues when dealing with sensitive photodetectors and faint fluorescence signals. Good long pass filtering is obvious but generally one should use a series of short pass filters int the excitation path as well. Many lasers produce significant gain medium fluorescence that can fall within the spectral window of interest and many optics

will also fluorescence when excited by your excitation laser. Careful use of short pass filters goes a long way towards eliminating these annoyances which can often swamp your signal of interest.

- Pellicles: If funds allow it, pellicle beamsplitters and optics are significantly easier to use than cube/plate optics. The pellicles eliminate extra reflections that can sometimes result in one maximizing the wrong signal or in the case of sample imaging with a white light source, swamp the image of interest.
- Checking the quantum efficiency of a sensitive detector: Due to the fact that they are fiber coupled with single mode fibers, checking the quantum efficiency of a SNSPD can be tricky. The important part of this task is that one needs to account for all losses and attenuation resulting from the input coupling, including mode-mismatch with the single mode fiber. Therefore, one has to take care not to alter the input mode when setting up the final measurement after calibrating the input attenuation. This is best accomplished by coupling the measurement light source out of a single mode fiber before coupling it into the detector fiber and then altering the input power by adjusting the input coupling to this additional fiber. This way, you in no way alter the mode being coupled into the detector fiber because you

always get a single mode out of a single mode fiber when operating above the cut-off wavelength. One can measure the power at the output of this additional fiber via a short free-space path in order to properly measure the power incident on the attenuation and the detector for proper signal level calibration.

Appendix C

Microwave Hardware Tips and Tricks

Here are some tips on working with microwave hardware:

- Avoiding damage: Many of the CW and pulsed microwave electronics that we use are sensitive to reflections at their inputs. As careful as one is to impedance match, it is a good idea to use ample attenuation whenever possible in order to attenuate back reflections that could damage something expensive. While I have never seen anything get destroyed in this manner, I have had high power attenuators used to damp reflections die presumably due to reflected microwave power.
- Cryogenic attenuators: the use of attenuators at cryogenic temperature is sometimes useful to provide a thermal link between the central

pin of the coaxial lines and the shield. However, some attenuators are made up of materials that go superconducting at low temperatures. Some members of the Martinis group found that attenuators sold by Boston Electronics do not superconduct at low temperature and should be used for the above mentioned applications.

- Pulse conversion: It is not uncommon to have to convert between a positive voltage spike, a NIM pulse, and a TTL pulse for interfacing photon counting detectors with photon counting hardware. Most TCSPC systems require NIM logic inputs that can be obtained from SNSPD or APD signals with attenuators and pulse inverters supplied by Boston Electronics or Picoquant. Converting to TTL from other pulse shapes is a little trickier. To accomplish this, I found the following work-around: for the SNSPD output (a few hundred millivolt pulse that is positive-going and a few nanoseconds wide), one can first pass the signal through a Gaussian (or Bessel) low pass filter (I used a 30 MHz Bessel low pass filter) and send the input to a fast voltage comparator that outputs a TTL level. By adjusting the comparison voltage, you can adjust the pulse width to the desired width. This was necessary to alter the SNSPD output in order to produce a pulse that could be counted by the TTL inputs of the counters

on the NI DAQ used for photon counting. Gaussian or Bessel filters are important to minimize 'after pulsing' that can produce extra counts. Alternatively, one can sometimes buy direct pulse converters for making such conversions.

- Pulsed electronics tips: Often one can play tricks to get more channels out a combination of digital delay generators and triggered function generators/arbitrary waveform generators. With the amount of pulsed electronics around the lab, one can generally find some combination of electronics with the right triggering characteristics to get more channels or more functions if the connection are chosen carefully. Furthermore, when combining with other triggered electro-optic components like the pulse pickers and Coherent synchrolock system, you can do fun things like implement arbitrary electronic delay lines.
- Cryogenics: adding coaxial cabling to cryogenic systems can be tricky. I have generally found it useful to add internal connector mounts at key stages to minimize the need for replacing the entire cable line if one part of the line breaks. It is generally a good idea to thermally sink the cable shielding to cold sections in stages and use stainless steel cable to minimize the thermal connection between stages. If the

outside of the cryostat experiences condensation or icing due to the connection to the cold stages, adding extra stainless steel connectors can remedy this by increasing the thermal resistance.

- Proper semi-rigid coax connectorization: see the following instructions adapted from the Martinis group for easy and robust coaxial cable connectorization (adjust the procedure as needed for the connectors you purchased or per your own personal preferences).

Coaxial Cable Connectorization:

Materials:

1. A clear work space

2. Coaxial cable Make sure that you have more than you think youll need because mistakes are bound to happen.

3. SMA connectors Digikey part no. ACX1177-ND. Manufactured by APL Connex, part number 132101. These come individually packaged in small plastic bags. Each bag should contain a hex nut with a cylindrical dielectric inside, a center pin, and a small plastic spacer ring.

4. Solder Anything thin enough to fit inside the SMA connector center pin will work. We used 0.015" solder for the ADR wiring.

5. Solder Flux

6. Soldering Iron I used a large chisel tip. Temperature = 580 F. Note that the soldering irons seem to read a lower temperature than the real value.

7. Razor Blade Make sure its sharp.

8. Small Vice

9. Second Hands Anything that can hold an SMA center pin vertically for you, like the alligator clips shown in the photographs below.

10. Isopropyl Alcohol

11. Wire cutters

12. Wire bender In the red toolbox in the DR lab. This is basically just a small circular stump of metal that you use to ensure that the bends you put in your cable arent too tight.

13. SMA connector toolkit This is in the electronics room in the BNC/SMA drawer. It contains several tools needed for soldering SMA connectors to the cable.

14. Some kind of abrasive Steel wool or sandpaper will work.

15. Small pliers

Procedure

1. Cut a length of cable from the stock and bend it into the desired shape:

Cut the cable to be an inch longer than you need so that if you make a mistake you can chop the end off and continue. Cables used in cryostats must have bends in them so that as they are cooled and develop mechanical stress they don't rip out their connectors. There should be enough bend between connection points so that you can easily flex the cable by a few millimeters.

2. Wipe the cable with isopropyl alcohol: The difference between a good solder joint and a bad solder joint is often the cleanliness of the involved surfaces, so make sure the cable is clean before you try to solder anything.

3. Choose an end of the cable to work on and make sure that it is cut flush: use a large wire stripper to cut the outer conductor of the cable and then a wire cutter to cut the inner conductor. The end should now be flush. Its ok if there are some burrs on the end of the outer conductor because you are about to cut them off.

4. Use the scoring tool to cut a groove in the outer conductor of the cable. Press the lever in the side of the tool and insert the cable into the hole in the white plastic face of the tool. Release the lever, and while applying firm pressure to keep the cable pressed as far as it can go into the tool rotate the cable (or the tool itself) slowly approximately ten times. (It is fine to do additional turns to ensure a deeper groove.) A blade inside the

tool will score a groove in the outer conductor of the cable. This groove should be 3.6 mm from the end of the cable (This value is approximate no need to use calipers to measure). If this distance is incorrect adjust the scoring tool.

a. Loosen the knob on the side of the tool

b. Turn the knob on the face of the tool opposite the hole in which you inserted the cable. Turn clockwise to reduce the distance of the groove, counterclockwise to increase the distance. Tighten the knob on the side of the tool.

5. Break off the outer conductor up to the scored groove: If the groove is nice and deep this should be easy. With small pliers grab the outer conductor near the cut edge of the cable and slowly bend. The outer conductor should break off at the scored groove. Once it does pull the broken part off with the pliers.

6. Cut off the exposed dielectric: Press the edge of a sharp razor into the exposed dielectric right where it meets the outer conductor and rotate the cable so that the razor cuts into the dielectric. Once the dielectric is completely cut use the razor to push the dielectric away from the outer conductor and off the center conductor so that it is removed. Be careful not to cut a groove in the center conductor while completing this step.

The cable should now have 3.6 mm of exposed center conductor protruding from otherwise intact cable.

7. Heat the end of the cable and remove any extra dielectric that extrudes: Hold the soldering iron tip against the outer conductor at the end of the cable. As the dielectric heats up it will expand and protrude from the cut end of the outer conductor. When this happens repeat step 6 to remove this extra dielectric. This step significantly improves the success rate of step 15.

8. Place a plastic spacer from the SMA connector package onto the exposed center conductor and push it up against the outer conductor.

9. Prepare the center pin: Place the center pin vertically in the alligator clip second hands so that the hole it pointed upwards. Cut a small piece of solder, approximately 2.5mm, and drop it into the center pin. Now hold the soldering iron against the pin for a few seconds to melt the solder. Make sure there is no excess ball of solder on the outside of the pin. There is special .3mm OD solder for very small central pins in the electronics area by the silver paste.

10. Solder the center pin to the exposed center conductor. Place the jig vertically into the vice with the jig's clamping mechanism at the top, screw the center pin holder into the jig, and place the center pin into the center

pin holder with its hole pointed upward. Apply a small amount of flux to the center pin. Place the cable into the jig clamping mechanism and close the clamp loosely around the cable. Let the exposed center conductor of the cable fall into the center pin. Hold the soldering iron against the center pin while gently pushing the cable downward into the pin. When the solder in the pin melts the cable will fall farther downward into the pin. Make sure that the cable is as far down as it can go, and then remove the heat and allow the parts to cool. Once cool, check the connection by pulling on the center pin; it should not come off of the cable. Clean off any remaining flux.

11. Use abrasive to rough up the outer conductor: This helps improve the solder joint that you're going to make.

12. Push the cable into the SMA hex nut: Place the hex nut on the work-bench with the hold for the coaxial cable facing upwards. Push the cable, center pin facing downwards, into the hole. It is possible to push the cable in too far. Sometimes during this step the dielectric in the SMA hex nut pops out. If this happens use the stop to push it back in. You can keep the stop in place while you push the cable into the hex nut to keep the dielectric from popping out.

13. Place solder on the cable: Wrap three turns of solder around the cable

near the hex nut and cut the loops off from the rest of the spool of solder. Push these three loops of solder up against the hex nut.

14. Prepare to solder the cable to the hex nut. Take the center pin holder out of the jig and put the stop in the jig. Feed the cable with the attached hex nut down onto the stop so that the center pin goes into the small hole in the stop. Tighten the jig clamp all the way. Firmly screw the stop upward toward the cable to ensure that the stop is pressed against the dielectric inside the hex nut. Place solder flux on the four turns of solder that are sitting above the hex nut; try to get it to go between the turns of solder and the outer conductor of the cable.

15. Solder the hex nut to the cable: With the soldering iron at ~580 F, heat the hex nut near where it attaches to the cable until the turns of solder melt and fall into the space between the cables outer conductor and the hex nut. Once this happens squirt isopropyl alcohol on the solder joint to cool it off so that the center pin doesnt fall out. Another school of thought on this step is to use a hotter soldering iron to try to get the solder turns to melt more quickly, but I had more luck with a cooler iron. Note that when the cable heats up the dielectric inside may extrude out and push the dielectric out of the hex nut. This is why in step 7 we pre-heated and cut the dielectric. While heating the connector, moving the iron around

the circumference several times will help give a more uniform heat profile which will help the solder flow better. Not doing this can lead to areas with too little solder opposite the iron.

The connection is now done: Inspect the solder joint for a good connection. If there's a problem put the cable back in the jig and try to fix it. If the center pin falls out or if the dielectric gets pushed out you may have to cut off the connector and start over. This is why it's a good idea to cut the cable longer than you think you need. If everything is good repeat these steps for the other end of the cable and viola! you have a semirigid coax. You can use the network analyzer to check that your cables have good microwave properties.

Appendix D

Fabrication Tips and Tricks

Here are some tips on cleanroom processing:

- Safety: As with cryogenics, safety is always the first concert. There are many dangerous chemicals involved in cleanroom processing and one should never be careless with them.
- Checklists: It is incredibly easy to forget steps in a process, especially with the odd hours that are often kept by people who frequent the cleanroom. Checklists provide a reliable means of checking one's actions at every step along the way. In general, one should always double and triple check parameters in order to minimize wasted samples and time.
- Always check recipes!: When in doubt, check the recipe. Never trust your gut or do anything with less than 100 percent certainty. You

will regret any lack of care that will inevitably lead to mistakes.

- Process characterization: Although it can be time consuming(and sometimes variable), it is generally a good idea to characterize each step in your process (SEM, AFM, so on) in order to be certain that the sample is turning out the way it should at each step along the way. This will often allow you to easily determine what has gone wrong should a sample exhibit flaws.
- Process reliability: Whenever possible, one should choose process steps in order to minimize the sensitivity of that step to process fluctuations that results from sample or tool variations. This is easier said than done and there is no systematic way to accomplish this. Nevertheless, one should attempt this whenever possible. For instance, one step the greatly improved our process reliability was coating the sample with AquaSave prior to the EBeam writing. This minimized sample charging effects that resulted from poor electrical conduction to the sample mount as a result of resist edge beads.
- Cleaning samples: Cleanroom processes like plasma etches can often leave residues that affect later steps. It is a good idea to clean samples when it is prudent. Obviously, exposing photoresist to solvents ruins the process so cleaning also needs to be intelligently introduced into

the appropriate places in a process.

- Plasma Homogeneity: It is especially important that one achieves a homogeneous plasma when performing etches on small samples. Sample edges can affect this homogeneity. It is a good idea to mount a series of samples of exactly the same height around the etched sample in order to achieve a plasma that is homogeneous over most, if not all, of the sample. However, one does need to take care that the surrounding samples don't negatively affect the main sample(see the next point).
- Silicon nanoparticles: The aggressive SF_6 etch used to etch SiC also aggressively etches Si. This process has been observed to coat the sample in Si or SiO nanoparticles that can result in micromasking. We generally used thick SiC films to surround the sample in order to avoid this. Also, exposing the sample to HF and XeF_2 at the end of the process is a good means of removing these particles.
- Bosch process: In order to effectively remove the fluorescence from the silicon substrate below the 3C SiC layer, I developed a process based on the Bosch process in order to produce a freestanding membrane. See Figure D.1 for the process flow.

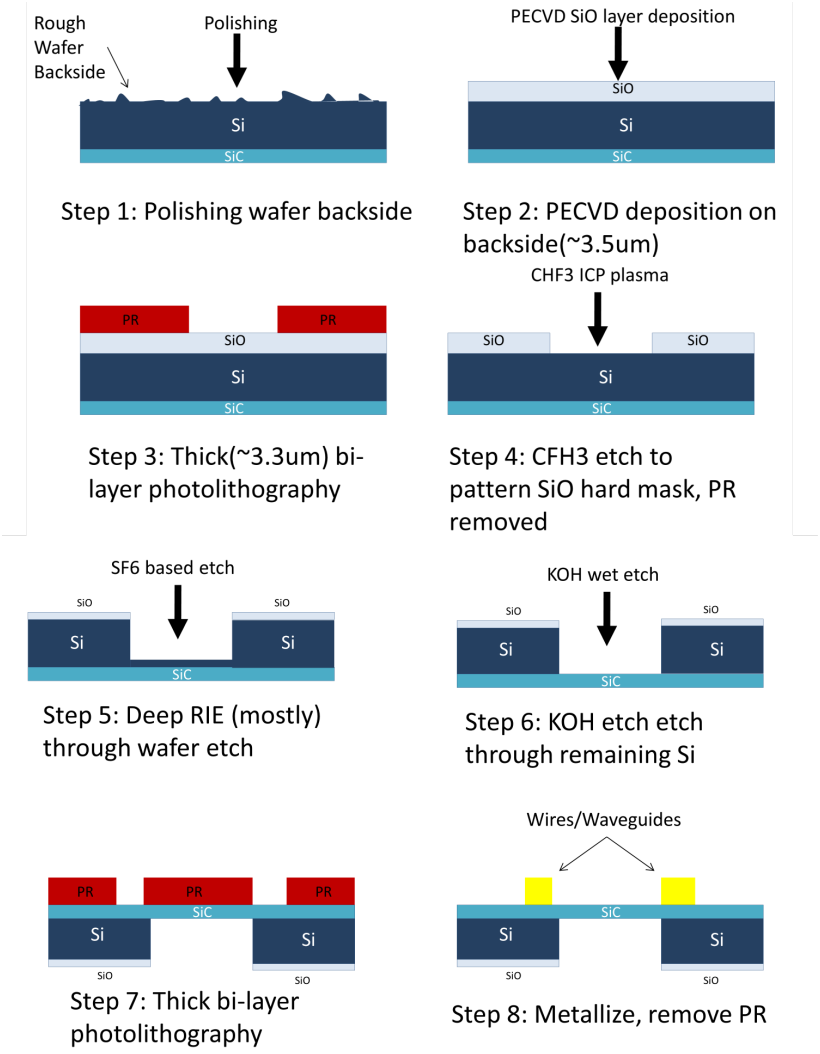

Figure D.1: Process for creating windows in 3C SiC through a back-etch process.

The follow tables give the etch recipes used for producing 3C SiC photonic crystal cavities:

Table D.1: 200W SF_6 etch

Parameter	Step 1	Step 2	Step 3	Step 4	Step 5	Step 6
BCl_3	0	0	0	0	0	0
Cl_2	0	0	0	0	0	0
SF_6	40	40	40	0	0	0
O_2	0	0	0	0	0	0
Ar	0	0	0	0	0	0
N_2	0	0	0	100	100	0
Pre.	2.00	.8	.8	2.5	2.5	0
Vacing TM	0	0	:15	:15	0	0
RF Wait TM	:15	0	0	:15	0	0
SRC FWD	900	900	900	100	50	0
SRC REF						
BIAS FWD	0	0	200	0	0	0
BIAS REF						
Dead Time	:05	:05	:05	:10	:05	0
EPM	None	None	None	None	None	None
Step Time	:05	:05	**Etch Time**	:10	:05	0
Over Etch	0	0	0	0	0	0
Over Etch	0	0	0	0	0	0

Etch rates:

SiC: ~400nm/min

Ma-N: ~800nm/min

PECVD SiO2: ~220nm/min

Table D.2: 50W SF_6 etch (~200 nm/min)

Parameter	Step 1	Step 2	Step 3	Step 4	Step 5	Step 6
BCl_3	0	0	0	0	0	0
Cl_2	0	0	0	0	0	0
SF_6	40	40	40	0	0	0
O_2	0	0	0	0	0	0
Ar	0	0	0	0	0	0
N_2	0	0	0	100	100	0
Pre.	2.00	.8	.8	2.5	2.5	0
Vacing TM	0	0	:15	:15	0	0
RF Wait TM	:15	0	0	:15	0	0
SRC FWD	900	900	900	100	50	0
SRC REF						
BIAS FWD	0	0	50	0	0	0
BIAS REF						
Dead Time	:05	:05	:05	:10	:05	0
EPM	None	None	None	None	None	None
Step Time	:05	:05	**Etch Time**	:10	:05	0
Over Etch	0	0	0	0	0	0
Over Etch	0	0	0	0	0	0

Etch rates:

SiC: ~200nm/min

Etch rates:

PMMA: ~500nm/min

ZEP: ~340nm/min

Ma-N: ~200nm/min

Aluminum: ~350nm/min

Etch rates:

SiC: ~80 nm/min

Here is the complete process recipe we used for producing photonic crystal cavities:

1. Surround the sample with SiC samples of the same height in order to produce a uniform etch plasma and to facilitate resist spinning.

2. Etch the sample to the appropriate thickness. For the 200W SF6 recipe, the etch rate is about 400 nm per minute. Check the thickness with ellipsometer, perform the appropriate etch combination to reach desired pre-fab thickness of about 300nm.

3. Perform the implantation and annealing process, if desired.

4. Deposit 5 nm of titanium to as a stiction layer and to getter any contaminants in the evaporation chamber. Deposit 100 nm aluminum in Ebeam 3 at a rate of 1 Angstrom per second. Cap with 10 nm of Titanium (1 A/sec). Be prepared to move the sample to the drybox immediately after the deposition and spin Ebeam resist as soon as possible.

5. Spin 100% ZEP520 at 5K RPM and then bake at 180 degrees C for 5 minutes to produce an approximately 340 nm thick layer of ZEP Ebeam resist.

6. Spin AquaSAVE at 3K RPM and bake for 30s at 90 degree C.

7. Write the pattern with the JEOL ebeam writer. Use the 5th lens, 100pA Aperture 3. The approximate dose is 500 uC/cm2 for ZEP520 with the 100 KeV JEOL.

8. Rinse the sample in DI water for 30s to remove the AquaSAVE. Develop the Ebeam resist for 90 seconds in 3:1 MIBK:IPA and rinse for 30 seconds with IPA. Blow dry with N2 and return the sample immediately

to the dry box. Perform the dry etch as soon as possible after development.

9. Perform the Martinis group BCL3/CL2 etch with the ICP set to SF6 and with the 200W SF6 Process immediately following the Martinis group etch. The last two CF4 steps in the Martinis Group BCL3/CL2 etch will instead be performed with SF6 and likely do not matter since they are so short. The 200W SF6 should be set to etch all the way through the 3C-SiC layer with some (but not too much) overshoot. Typically our film is about 350 nm thick and we perform a 1 minute process that would etch about 400 nm of SiC. This etches all the way through the SiC film and into the Si underneath.

10. Strip the photoresist in either acetone or 1165 for at least a few hours.

11. First, leave the sample in aluminum etchant for 15 minutes at 50 degrees C. Then, leave the sample in titanium etchant for 5 minutes at room temperature. Finally, leave the sample in buffered HF for 5 minutes to remove any remaining residues and eliminate any oxidized silicon layers within the holes. This will remove the remaining hard mask materials, any SiO particles on the sample, and remove the 'nano onion rings'.

12. At this point, inspect the sample in the SEM. Avoid imaging the ideal cavities since they may be affected by carbon deposition from the SEM. Determine the film thickness.

13. Perform the XeF2 undercut etch with the following spec's: 5 cycles, pressure: 4 torr, 60s cycle time.

14. To get the sample to the right membrane thickness after the membrane thickness is determined and the resonances have been observed, perform a thinning etch for the desired amount of time (we typically used the Ar/CL2 etch with a rate of about 80 nm per minute).

Here is the bilayer lithography process used to metalize the photonic crystal samples:

1. Mount the piece on a carrier wafer with wax surrounded by silicon pieces of the same height.

2. Dehydration bake the wafer at 180 degree C for 5 minutes.

3. Oxygen plasma etch the surface for 1 minute using te standard process.

4. Perform the bi-layer stepper process: Spin HDMS at 4000 RPM for 30 seconds. Spin LOL2000 at 4000 rpm for 30 seconds. Bake at 180 degrees C for 5 minutes. Spin SPR955 .9 microns at 4000 RPM for 30 seconds. Soft bake the sample at 100 degrees C for 2 minutes.

5. Do the standard exposure on the desired row (for single wires) or pattern (for multiple wires).

6. Do a post exposure bake at 110 degrees C for 60 seconds.

7. Develop for 90 seconds in AZ300MIF.

8. Descum for 60 seconds using the standard procedure.

9. Evaporate 10 nm Ti followed by 300 nm of Au in Ebeam 3.

10. Place the sample in 1165 over night and then delicately induce the

metal to liftoff the sample by agitating the sample and beaker.

11. Descum again for 2 minutes to remove any remaining photoresist.

Table D.3: Aluminum(BCl_3/Cl_2) etch (~350 nm/min)

Parameter	Step 1	Step 2	Step 3	Step 4	Step 5	Step 6
BCl_3	20	20	20	0	0	0
Cl_2	40	40	40	0	0	0
CF_4	0	0	0	50	50	0
O_2	0	0	0	0	0	0
Ar	0	0	0	0	0	0
N_2	0	0	0	0	0	0
Pre.	3.00	.7	.7	2.0	2.0	0
Vacing TM	0	0	:45	0	:45	0
RF Wait TM	:15	0	0	:10	0	0
SRC FWD	300	300	300	700	700	0
SRC REF						
BIAS FWD	0	0	70	0	20	0
BIAS REF						
Dead Time	:05	:05	:05	:10	:30	0
EPM	None	None	None	None	None	None
Step Time	:05	:05	**Etch Time**	:05	:05	0
Over Etch	0	0	0	0	0	0
Over Etch	0	0	0	0	0	0

Table D.4: Ar/Cl_2(slow SiC) etch (~80 nm/min)

Parameter	Step 1	Step 2	Step 3	Step 4	Step 5	Step 6
BCl_3	0	0	0	0	0	0
Cl_2	10	10	10	0	0	0
CF_4	0	0	0	0	0	0
O_2	0	0	0	0	0	0
Ar	40	40	40	0	0	0
N_2	0	0	0	100	100	0
Pre.	2.00	.7	.7	2.50	2.50	0
Vacing TM	0	0	:15	0	:15	0
RF Wait TM	:15	0	0	:15	0	0
SRC FWD	500	500	500	500	50	0
SRC REF						
BIAS FWD	0	0	100	0	0	0
BIAS REF						
Dead Time	:10	:20	:20	:10	:10	0
EPM	None	None	None	None	None	None
Step Time	:05	:05	**Etch Time**	:10	:10	0
Over Etch	0	0	0	0	0	0
Over Etch	0	0	0	0	0	0

Appendix E

Simulation Tips and Tricks

Here are some tips on proper implementation of FDTD simulations that are mostly for Lumerical (but some also apply in general to FDTD simulations):

- Use a cluster: FDTD simulations can become very time consuming, especially when testing for convergence with small time and spatial steps. Using a cluster will typically provide a large reduction in computation time, largely limited by the ability of the cluster machines to communicate memory elements. I typically noticed a factor of reduction in simulation time when using he CNSI Knot cluster as opposed to a 64 bit dual core, ~2 GHz processor with 8 gigs of RAM.
- Check your simulations: One should always check any simulation for convergence by increasing time steps and decreasing spatial resolu-

tion. This is crucial to achieving reliable results. If one can, they should also compare to trusted literature examples, although it can be difficult to be certain that the authors also checked for convergence (I have found examples that made me think otherwise when checking other author's result).

- Carefully set up sources: To avoid artifacts and achieve reliable results, it is a good idea to carefully check the setup of your sources. When exciting photonic crystal cavity modes with internal dipole sources, one has to be careful to avoid placing the excitation at a node of the cavity mode. For external Gaussian excitation, I observed that it was important place he excitation a a large distance (1-2 microns) from the structure to achieve reliable results. In the time domain, it is vitally important that one makes sure that the source has zero field amplitude at the beginning and end of the simulation time. Otherwise, the field monitor normalizations are not maintained(which is a big problem for calculating the steady state optical response of a photonic crystal cavity).
- Apodization: similar the sources, it is important to properly apodize field monitors to achieve the desired temporal overlap between sources and field monitors. For determining structure parameters, I avoided

any temporal between the sources and monitors. For calculating steady state responses, it doesn't matter as a result of the field normalization.

- Far field calculations: In order to calculate the field emission pattern of the cavity so as to determine the input coupling efficiency, I used Lumerical's far field vector calculation tool to determine the far field S and P polarization components. I then performed the same analysis for the input beam. Lumerical outputs a map of the real and imaginary components of the vector field which I then used to calculate the mode overlap integral numerically in Matlab.
- Adding in imperfections: Lumerical includes many geometric structures that are produced through algorithms that can be altered to induce structure imperfections. Random number generators can be used to induce random fluctuations or cones can be drawn in place of cylinders to simulate angled etching. One should run any randomly generated simulations many times in order to generate proper statistics.

References

[1] M. Nielsen and I. Chuang. *Quantum Computation and Quantum Information*. Cambridge Series on Information and the Natural Sciences. Cambridge University Press, (2000).

[2] C. H. Bennett and G. Brassard. In *Proceedings of the IEEE International Conference on Computers, Systems and Signal Processing*, 175–179, (1984).

[3] D. Budker and D. Kimball. *Optical Magnetometry*. Optical Magnetometry. Cambridge University Press, (2013).

[4] R. Schirhagl, K. Chang, M. Loretz, and C. L. Degen, Annual Review of Physical Chemistry **65**, 83–105 (2014). PMID: 24274702.

[5] B. Lounis and M. Orrit, Reports on Progress in Physics **68**, 1129 (2005).

[6] I. M. Georgescu, S. Ashhab, and F. Nori, Rev. Mod. Phys. **86**, 153–185 (2014).

[7] R. Blatt and C. F. Roos, Nat Phys **8**, 277–284 (2012).

[8] L. M. K. Vandersypen, M. Steffen, G. Breyta, C. S. Yannoni, M. H. Sherwood, and I. L. Chuang, Nature **414**, 883–887 (2001).

[9] B. Ellis, M. A. Mayer, G. Shambat, T. Sarmiento, J. Harris, E. E. Haller, and J. Vuckovic, Nat Photon **5**, 297–300 (2011).

[10] R. J. Warburton, Nat Mater **12**, 483–493 (2013).

[11] A. Politi, J. C. F. Matthews, and J. L. O'Brien, Science **325**, 1221 (2009).

[12] E. Lucero, R. Barends, Y. Chen, J. Kelly, M. Mariantoni, A. Megrant, P. O/'Malley, D. Sank, A. Vainsencher, J. Wenner, T. White, Y. Yin, A. N. Cleland, and J. M. Martinis, Nat Phys **8**, 719–723 (2012).

[13] A. Reiserer, N. Kalb, G. Rempe, and S. Ritter, Nature **508**, 237–240 (2014).

[14] D. Kim, Z. Shi, C. B. Simmons, D. R. Ward, J. R. Prance, T. S. Koh, J. K. Gamble, D. E. Savage, M. G. Lagally, M. Friesen, S. N. Coppersmith, and M. A. Eriksson, Nature **511**, 70–74 (2014).

[15] F. A. Zwanenburg, A. S. Dzurak, A. Morello, M. Y. Simmons, L. C. L. Hollenberg, G. Klimeck, S. Rogge, S. N. Coppersmith, and M. A. Eriksson, Rev. Mod. Phys. **85**, 961–1019 (2013).

[16] W. Tittel, M. Afzelius, T. Chanelire, R. Cone, S. Krll, S. Moiseev, and M. Sellars, Laser & Photonics Reviews **4**, 244–267 (2010).

[17] R. Kolesov, K. Xia, R. Reuter, R. Sthr, A. Zappe, J. Meijer, P. Hemmer, and J. Wrachtrup, Nat Commun **3**, 1029 (2012).

[18] A. D. OConnell, M. Hofheinz, M. Ansmann, R. C. Bialczak, M. Lenander, E. Lucero, M. Neeley, D. Sank, H. Wang, M. Weides, J. Wenner, J. M. Martinis, and A. N. Cleland, Nature **464**, 697–703 (2010).

[19] T. D. Ladd, F. Jelezko, R. Laflamme, Y. Nakamura, C. Monroe, and J. L. O'Brien, Nature **464**, 45–53 (2010).

[20] J. L. O'Brien, A. Furusawa, and J. Vuckovic, Nature Photon. **3**, 687–695 (2009).

[21] K. K. Mehta, A. M. Eltony, C. D. Bruzewicz, I. L. Chuang, R. J. Ram, J. M. Sage, and J. Chiaverini, Applied Physics Letters **105**, – (2014).

[22] H. J. Kimble, Nature **453**, 1023–1030 (2008).

[23] K.-M. C. Fu, S. M. Clark, C. Santori, C. R. Stanley, M. C. Holland, and Y. Yamamoto, Nat Phys **4**, 780–784 (2008).

[24] A. M. Tyryshkin, S. Tojo, J. J. L. Morton, H. Riemann, N. V. Abrosimov, P. Becker, H.-J. Pohl, T. Schenkel, M. L. W. Thewalt, K. M. Itoh, and S. A. Lyon, Nat Mater **11**, 143–147 (2012).

[25] M. P. Hedges, J. J. Longdell, Y. Li, and M. J. Sellars, Nature **465**, 1052–1056 (2010).

[26] http://physics.nist.gov/PhysRefData/Star/Text/ESTAR.html.

[27] www.gel.usherbrooke.ca/casino/index.html.

[28] K. Ohno, F. Joseph Heremans, L. C. Bassett, B. A. Myers, D. M. Toyli, A. C. Bleszynski Jayich, C. J. Palmstrm, and D. D. Awschalom, Applied Physics Letters **101**, 082413 (2012).

[29] J. Steeds, G. Evans, L. Danks, S. Furkert, W. Voegeli, M. Ismail, and F. Carosella, Diamond and Related Materials **11**, 1923 – 1945 (2002).

[30] M. Widmann, S.-Y. Lee, T. Rendler, N. T. Son, H. Fedder, S. Paik, N. Zhao, S. Yang, I. Booker, A. Denisenko, M. Jamali, S. A. Momenzadeh, T. Ohshima, A. Gali, E. Janzn, and J. Wrachtrup. eprint,arXiv:1407.0180.

[31] www.srim.org.

[32] D. M. Toyli, C. D. Weis, G. D. Fuchs, T. Schenkel, and D. D. Awschalom, Nano Letters **10**, 3168–3172 (2010). PMID: 20698632.

[33] W. E. Carlos, N. Y. Graces, E. R. Glaser, and M. A. Fanton, Phys. Rev. B **74**, 235201 (2006).

[34] Y. Chu, N. de Leon, B. Shields, B. Hausmann, R. Evans, E. Togan, M. J. Burek, M. Markham, A. Stacey, A. Zibrov, A. Yacoby, D. Twitchen, M. Loncar, H. Park, P. Maletinsky, and M. Lukin, Nano Letters **14**, 1982–1986 (2014).

[35] A. Batalov, V. Jacques, F. Kaiser, P. Siyushev, P. Neumann, L. J. Rogers, R. L. McMurtrie, N. B. Manson, F. Jelezko, and J. Wrachtrup, Phys. Rev. Lett. **102**, 195506 (2009).

[36] L. Robledo, L. Childress, H. Bernien, B. Hensen, P. F. A. Alkemade, and R. Hanson, Nature **477**, 574–578 (2011).

[37] B. B. Buckley, G. D. Fuchs, L. C. Bassett, and D. D. Awschalom, Science **330**, 1212–1215 (2010).

[38] N. T. Son, J. Appl. Phys. **79**, 3784–3786 (1996).

[39] MizuochiN., MakinoT., KatoH., TakeuchiD., OguraM., OkushiH., NothaftM., NeumannP., GaliA., JelezkoF., WrachtrupJ., and YamasakiS., Nat Photon **6**, 299–303 (2012).

[40] F. Fuchs, V. A. Soltamov, S. Vth, P. G. Baranov, E. N. Mokhov, G. V. Astakhov, and V. Dyakonov, Sci. Rep. **3**, 1637 (2013).

[41] J. H. N. Loubser and J. A. van Wyk, Reports on Progress in Physics **41**, 1201 (1978).

[42] G. Pensl and W. Choyke, Physica B: Condensed Matter **185**, 264 – 283 (1993).

[43] D. J. Meyer, P. M. Lenahan, and A. J. Lelis, Applied Physics Letters **86**, 023503 (2005).

[44] N. B. Manson, J. P. Harrison, and M. J. Sellars, Phys. Rev. B **74**, 104303 (2006).

[45] R. T. Harley, M. J. Henderson, and R. M. Macfarlane, Journal of Physics C: Solid State Physics **17**, L233 (1984).

[46] K. Holliday, X.-F. He, P. T. H. Fisk, and N. B. Manson, Opt. Lett. **15**, 983–985 (1990).

[47] A. Gruber, A. Drbenstedt, C. Tietz, L. Fleury, J. Wrachtrup, and C. v. Borczyskowski, Science **276**, 2012–2014 (1997).

[48] L. Robledo, H. Bernien, I. van Weperen, and R. Hanson, Phys. Rev. Lett. **105**, 177403 (2010).

[49] L. C. Bassett, F. J. Heremans, C. G. Yale, B. B. Buckley, and D. D. Awschalom, Phys. Rev. Lett. **107**, 266403 (2011).

[50] P. V. Klimov, A. L. Falk, B. B. Buckley, and D. D. Awschalom, Phys. Rev. Lett. **112**, 087601 (2014).

[51] E. R. MacQuarrie, T. A. Gosavi, N. R. Jungwirth, S. A. Bhave, and G. D. Fuchs, Phys. Rev. Lett. **111**, 227602 (2013).

[52] P. Ovartchaiyapong, K. W. Lee, B. A. Myers, and A. C. B. Jayich, Nat Commun **5**, 4429 (2014).

[53] J. P. Hadden, J. P. Harrison, A. C. Stanley-Clarke, L. Marseglia, Y.-L. D. Ho, B. R. Patton, J. L. OBrien, and J. G. Rarity, Applied Physics Letters **97**, – (2010).

[54] T. M. Babinec, H. J. M., M. Khan, Y. Zhang, J. R. Maze, P. R. Hemmer, and M. Loncar, Nat Nano **5**, 195–199 (2010).

[55] J. T. Choy, B. J. M. Hausmann, T. M. Babinec, I. Bulu, M. Khan, P. Maletinsky, A. Yacoby, and M. Loncar, Nat Photon **5**, 738–743 (2011).

[56] A. Faraon, P. E. Barclay, C. Santori, K.-M. C. Fu, and R. G. Beausoleil, Nat Photon **5**, 301–305 (2011).

[57] A. Faraon, C. Santori, Z. Huang, V. M. Acosta, and R. G. Beausoleil, Phys. Rev. Lett. **109**, 033604 (2012).

[58] J. Riedrich-Moller, L. Kipfstuhl, C. Hepp, E. Neu, C. Pauly, F. Mucklich, A. Baur, M. Wandt, S. Wolff, M. Fischer, S. Gsell, M. Schreck, and C. Becher, Nat Nano **7**, 69–74 (2012).

[59] K. V. Kepesidis, S. D. Bennett, S. Portolan, M. D. Lukin, and P. Rabl, Phys. Rev. B **88**, 064105 (2013).

[60] S. Kolkowitz, A. C. Bleszynski Jayich, Q. P. Unterreithmeier, S. D. Bennett, P. Rabl, J. G. E. Harris, and M. D. Lukin, Science **335**, 1603–1606 (2012).

[61] C. Wang, C. Kurtsiefer, H. Weinfurter, and B. Burchard, Journal of Physics B: Atomic, Molecular and Optical Physics **39**, 37 (2006).

[62] S. Castelletto, B. C. Johnson, C. Zachreson, D. Beke, I. Balogh, T. Ohshima, I. Aharonovich, and A. Gali, ACS Nano **8**, 7938–7947 (2014). PMID: 25036593.

[63] S.-Y. Lee, M. Widmann, T. Rendler, M. W. Doherty, T. M. Babinec, S. Yang, M. Eyer, P. Siyushev, B. J. M. Hausmann, M. Loncar, Z. Bodrog, A. Gali, N. B. Manson, H. Fedder, and J. Wrachtrup, Nat Nano **8**, 487–492 (2013).

[64] H. Bernien, B. Hensen, W. Pfaff, G. Koolstra, M. S. Blok, L. Robledo, T. H. Taminiau, M. Markham, D. J. Twitchen, L. Childress, and R. Hanson, Nature **497**, 86–90 (2013).

[65] S. Benjamin, B. Lovett, and J. Smith, Laser & Photonics Reviews **3**, 556–574 (2009).

[66] A. Beveratos, R. Brouri, T. Gacoin, A. Villing, J.-P. Poizat, and P. Grangier, Phys. Rev. Lett. **89**, 187901 (2002).

[67] A. Sipahigil, M. L. Goldman, E. Togan, Y. Chu, M. Markham, D. J. Twitchen, A. S. Zibrov, A. Kubanek, and M. D. Lukin, Phys. Rev. Lett. **108**, 143601 (2012).

[68] M. T. Rakher, L. Ma, O. Slattery, X. Tang, and K. Srinivasan, Nat Photon **4**, 786–791 (2010).

[69] M. W. McCutcheon, D. E. Chang, Y. Zhang, M. D. Lukin, and M. Loncar, Opt. Express **17**, 22689–22703 (2009).

[70] A. Faraon, A. Majumdar, D. Englund, E. Kim, M. Bajcsy, and J. Vučković, New Journal of Physics **13**, 055025 (2011).

[71] K.-M. C. Fu, C. Santori, P. E. Barclay, L. J. Rogers, N. B. Manson, and R. G. Beausoleil, Phys. Rev. Lett. **103**, 256404 (2009).

[72] S. Buckley, K. Rivoire, and J. Vu?kovi, Reports on Progress in Physics **75**, 126503 (2012).

[73] M. Scully and S. Zubairy. *Quantum Optics*. Cambridge University Press, (1997).

[74] L. Li, T. Schrder, E. H. Chen, M. Walsh, I. Bayn, J. Goldstein, O. Gaathon, M. E. Trusheim, M. Lu, J. Mower, M. Cotlet, M. L. Markham, D. J. Twitchen, and D. Englund. eprint, arXiv:1409.1602, (2014).

[75] C. Santori, D. Fattal, and Y. Yamamoto. *Single-photon Devices and Applications*. Wiley-VCH, (2010).

[76] S. Ritter, C. Nolleke, C. Hahn, A. Reiserer, A. Neuzner, M. Uphoff, M. Mucke, E. Figueroa, J. Bochmann, and G. Rempe, Nature **484**, 195–200 (2012).

[77] L.-M. Duan and H. J. Kimble, Phys. Rev. Lett. **92**, 127902 (2004).

[78] H. Kim, R. Bose, T. C. Shen, G. S. Solomon, and E. Waks, Nat Photon **7**, 373–377 (2013).

[79] T. G. Tiecke, J. D. Thompson, N. P. de Leon, L. R. Liu, V. Vuletic, and M. D. Lukin, Nature **508**, 241–244 (2014).

[80] A. Lenef and S. C. Rand, Phys. Rev. B **53**, 13441–13455 (1996).

[81] A. T. Collins, M. F. Thomaz, and M. I. B. Jorge, Journal of Physics C: Solid State Physics **16**, 2177 (1983).

[82] M. W. Doherty, N. B. Manson, P. Delaney, F. Jelezko, J. Wrachtrup, and L. C. Hollenberg, Physics Reports **528**, 1 – 45 (2013). The nitrogen-vacancy colour centre in diamond.

[83] L. Childress, M. V. Gurudev Dutt, J. M. Taylor, A. S. Zibrov, F. Jelezko, J. Wrachtrup, P. R. Hemmer, and M. D. Lukin, Science **314**, 281–285 (2006).

[84] K. Ohno, F. Joseph Heremans, C. F. de las Casas, B. A. Myers, B. J. Alemn, A. C. Bleszynski Jayich, and D. D. Awschalom, Applied Physics Letters **105**, 052406 (2014).

[85] G. D. Fuchs, G. Burkard, P. V. Klimov, and D. D. Awschalom, Nat Phys **7**, 789–793 (2011).

[86] E. V. Oort and M. Glasbeek, Chemical Physics Letters **168**, 529 – 532 (1990).

[87] P. Tamarat, T. Gaebel, J. R. Rabeau, M. Khan, A. D. Greentree, H. Wilson, L. C. L. Hollenberg, S. Prawer, P. Hemmer, F. Jelezko, and J. Wrachtrup, Phys. Rev. Lett. **97**, 083002 (2006).

[88] F. Dolde, H. Fedder, M. W. Doherty, T. Nobauer, F. Rempp, G. Balasubramanian, T. Wolf, F. Reinhard, L. C. L. Hollenberg, F. Jelezko, and J. Wrachtrup, Nat Phys **7**, 459–463 (2011).

[89] E. van Oort and M. Glasbeek, Journal of Luminescence **53**, 88 – 91 (1992).

[90] G. Davies and M. F. Hamer, Proceedings of the Royal Society of London. Series A, Mathematical and Physical Sciences **348**, pp. 285–298 (1976).

[91] V. M. Acosta, E. Bauch, M. P. Ledbetter, A. Waxman, L.-S. Bouchard, and D. Budker, Phys. Rev. Lett. **104**, 070801 (2010).

[92] D. M. Toyli, C. F. de las Casas, D. J. Christle, V. V. Dobrovitski, and D. D. Awschalom, Proceedings of the National Academy of Sciences **110**, 8417–8421 (2013).

[93] F. Kaiser, V. Jacques, A. Batalov, P. Siyushev, F. Jelezko, and J. Wrachtrup. e-print, arXiv:0906.3426, (2009).

[94] N. Reddy, N. Manson, and E. Krausz, Journal of Luminescence **38**, 46 – 47 (1987).

[95] F. Jelezko, I. Popa, A. Gruber, C. Tietz, J. Wrachtrup, A. Nizovtsev, and S. Kilin, Applied Physics Letters **81**, 2160–2162 (2002).

[96] L. Robledo, H. Bernien, T. van der Sar, and R. Hanson, New Journal of Physics **13**, 025013 (2011).

[97] M. Steiner, P. Neumann, J. Beck, F. Jelezko, and J. Wrachtrup, Phys. Rev. B **81**, 035205 (2010).

[98] S. Takahashi, R. Hanson, J. van Tol, M. S. Sherwin, and D. D. Awschalom, Phys. Rev. Lett. **101**, 047601 (2008).

[99] P. L. Stanwix, L. M. Pham, J. R. Maze, D. Le Sage, T. K. Yeung, P. Cappellaro, P. R. Hemmer, A. Yacoby, M. D. Lukin, and R. L. Walsworth, Phys. Rev. B **82**, 201201 (2010).

[100] G. Balasubramanian, P. Neumann, D. Twitchen, M. Markham, R. Kolesov, N. Mizuochi, J. Isoya, J. Achard, J. Beck, J. Tissler, V. Jacques, P. R. Hemmer, F. Jelezko, and J. Wrachtrup, Nat Mater **8**, 383–387 (2009).

[101] L. Childress, J. M. Taylor, A. S. Sørensen, and M. D. Lukin, Phys. Rev. Lett. **96**, 070504 (2006).

[102] J. M. Taylor, P. Cappellaro, L. Childress, L. Jiang, D. Budker, P. R. Hemmer, A. Yacoby, R. Walsworth, and M. D. Lukin, Nat Phys **4**, 810–816 (2008).

[103] A. Dréau, M. Lesik, L. Rondin, P. Spinicelli, O. Arcizet, J.-F. Roch, and V. Jacques, Phys. Rev. B **84**, 195204 (2011).

[104] J. R. Maze, P. L. Stanwix, J. S. Hodges, S. Hong, J. M. Taylor, P. Cappellaro, L. Jiang, M. V. G. Dutt, E. Togan, A. S. Zibrov, A. Yacoby, R. L. Walsworth, and M. D. Lukin, Nature **455**, 644–647 (2008).

[105] J. R. Weber, W. F. Koehl, J. B. Varley, A. Janotti, B. B. Buckley, C. G. Van de Walle, and D. D. Awschalom, Proceedings of the National Academy of Sciences **107**, 8513–8518 (2010).

[106] P. Baranov, I. Ilin, E. Mokhov, M. Muzafarova, S. Orlinskii, and J. Schmidt, Journal of Experimental and Theoretical Physics Letters **82**, 441–443 (2005).

[107] N. Son, E. Srman, M. Singh, W. Chen, C. Hallin, O. Kordina, B. Monemar, J. Lindstrm, and E. Janzn, Diamond and Related Materials **6**, 1378 – 1380 (1997). Proceeding of the 1st European Conference on Silicon Carbide and Related Materials (ECSCRM 1996).

[108] N. T. Son, P. N. Hai, M. Wagner, W. M. Chen, A. Ellison, C. Hallin, B. Monemar, and E. Janzn, Semiconductor Science and Technology **14**, 1141 (1999).

[109] N. T. Son, E. Sörman, W. M. Chen, C. Hallin, O. Kordina, B. Monemar, E. Janzén, and J. L. Lindström, Phys. Rev. B **55**, 2863–2866 (1997).

[110] W. Carlos, E. Glaser, and B. Shanabrook, Physica B: Condensed Matter **340342**, 151 – 155 (2003). Proceedings of the 22nd International Conference on Defects in Semiconductors.

[111] N. T. Son, Physica B **376-377**, 334–337 (2006).

[112] N. T. Son, P. Carlsson, J. ul Hassan, E. Janzén, T. Umeda, J. Isoya, A. Gali, M. Bockstedte, N. Morishita, T. Ohshima, and H. Itoh, Phys. Rev. Lett. **96**, 055501 (2006).

[113] A. Gali, physica status solidi (b) **248**, 1337–1346 (2011).

[114] B. Magnusson and E. Janzen, Mater. Sci. Forum **483-485**, 341–346 (2005).

[115] R. J. Epstein, F. M. Mendoza, Y. K. Kato, and D. D. Awschalom, Nat Phys **1**, 94–98 (2005).

[116] P. G. Baranov, A. P. Bundakova, A. A. Soltamova, S. B. Orlinskii, I. V. Borovykh, R. Zondervan, R. Verberk, and J. Schmidt, Phys. Rev. B **83**, 125203 (2011).

[117] R. Hanson, O. Gywat, and D. D. Awschalom, Phys. Rev. B **74**, 161203(R) (2006).

[118] G. de Lange, Z. H. Wang, D. Riste, V. V. Dobrovitski, and R. Hanson, Science **330**, 60–63 (2010).

[119] E. van Oort and M. Glasbeek, Chem. Phys. **143**, 131–140 (1990).

[120] N. T. Son, Mater. Sci. Forum **527-529**, 527–530 (2006).

[121] A. L. Falk, B. B. Buckley, G. Calusine, W. F. Koehl, V. V. Dobrovitski, A. Politi, C. A. Zorman, P. X.-L. Feng, and D. D. Awschalom, Nat Commun **4**, 1819 (2013).

[122] A. L. Falk, P. V. Klimov, B. B. Buckley, V. Ivády, I. A. Abrikosov, G. Calusine, W. F. Koehl, A. Gali, and D. D. Awschalom, Phys. Rev. Lett. **112**, 187601 (2014).

[123] S. Yamada, B.-S. Song, S. Jeon, J. Upham, Y. Tanaka, T. Asano, and S. Noda, Opt. Lett. **39**, 1768–1771 (2014).

[124] V. Bratus, R. Melnik, S. Okulov, V. Rodionov, B. Shanina, and M. Smoliy, Physica B: Condensed Matter **404**, 4739 – 4741 (2009).

[125] W. F. Koehl, B. B. Buckley, F. J. Heremans, G. Calusine, and D. D. Awschalom, Nature **479**, 84–87 (2011).

[126] B.-S. Song, S. Yamada, T. Asano, and S. Noda, Opt. Express **19**, 11084–11089 (2011).

[127] S. Yamada, B.-S. Song, J. Upham, T. Asano, Y. Tanaka, and S. Noda, Opt. Express **20**, 14789–14796 (2012).

[128] A. P. Magyar, D. Bracher, J. C. Lee, I. Aharonovich, and E. L. Hu, Applied Physics Letters **104**, 051109 (2014).

[129] J. Cardenas, M. Zhang, C. T. Phare, S. Y. Shah, C. B. Poitras, B. Guha, and M. Lipson, Opt. Express **21**, 16882–16887 (2013).

[130] X. Lu, J. Y. Lee, P. X.-L. Feng, and Q. Lin, Opt. Lett. **38**, 1304–1306 (2013).

[131] X. Lu, J. Y. Lee, P. X.-L. Feng, and Q. Lin, Applied Physics Letters **104**, 181103 (2014).

[132] M. Radulaski, T. M. Babinec, S. Buckley, A. Rundquist, J. Provine, K. Alassaad, G. Ferro, and J. Vučković, Opt. Express **21**, 32623–32629 (2013).

[133] S. Johnson and J. Joannopoulos, Opt. Express **8**, 173–190 (2001).

[134] S. Tomljenovic-Hanic, M. J. Steel, C. M. de Sterke, and J. Salzman, Opt. Express **14**, 3556–3562 (2006).

[135] Y. Akahane, T. Asano, B.-S. Song, and S. Noda, Nature **425**, 944–947 (2003).

[136] L. C. Andreani, D. Gerace, and M. Agio, Photonics and Nanostructures - Fundamentals and Applications **2**, 103 – 110 (2004).

[137] www.novasic.com.

[138] S. Ahn, S. Han, J. Lee, J. Moon, and B. Lee, Metals and Materials International **10**, 103–106 (2004).

[139] R. M. K. J. K. N. L. D. J. A. L. Hiller, T. Stauden and J. Pezoldt, Materials Science Forum **717-720**, 901 (2012).

[140] T. Asano, B.-S. Song, and S. Noda, Opt. Express **14**, 1996–2002 (2006).

[141] M. Galli, S. L. Portalupi, M. Belotti, L. C. Andreani, L. OFaolain, and T. F. Krauss, Applied Physics Letters **94**, 071101 (2009).

[142] J. Hagemeier, C. Bonato, T.-A. Truong, H. Kim, G. J. Beirne, M. Bakker, M. P. van Exter, Y. Luo, P. Petroff, and D. Bouwmeester, Opt. Express **20**, 24714–24726 (2012).

[143] D. Englund, A. Faraon, I. Fushman, N. Stoltz, P. Petroff, and J. Vuckovic, Nature **450**, 857–861 (2007).

[144] S. Yamada, B.-S. Song, T. Asano, and S. Noda, Opt. Lett. **36**, 3981–3983 (2011).

[145] M. Bosi, G. Attolini, M. Negri, C. Frigeri, E. Buffagni, C. Ferrari, T. Rimoldi, L. Cristofolini, L. Aversa, R. Tatti, and R. Verucchi, Journal of Crystal Growth **383**, 84 – 94 (2013).

[146] Y. Tanaka, T. Asano, Y. Akahane, B.-S. Song, and S. Noda, Applied Physics Letters **82**, 1661–1663 (2003).

[147] S. Buckley, M. Radulaski, J. Petykiewicz, K. G. Lagoudakis, J.-H. Kang, M. Brongersma, K. Biermann, and J. Vučković, ACS Photonics **1**, 516–523 (2014).

[148] M. Nomura, S. Iwamoto, T. Nakaoka, S. Ishida, and Y. Arakawa, Applied Physics Letters **88**, 114108 (2006).

[149] D. J. Christle, A. L. Falk, P. Andrich, P. V. Klimov, J. ul Hassan, N. T. Son, E. Janzn, T. Ohshima, and D. D. Awschalom. eprint, arXiv:1406.7325.

[150] A. Powell, Int. J. High Speed Electron. Syst. **16**, 751–777 (2006).

[151] C. Zetterling and I. of Electrical Engineers. *Process Technology for Silicon Carbide Devices*. EMIS processing series. INSPEC, (2002).

[152] M. Lončar and A. Faraon, MRS Bulletin **38**, 144–148 (2013).

[153] I. J. Luxmoore, N. A. Wasley, A. J. Ramsay, A. C. T. Thijssen, R. Oulton, M. Hugues, S. Kasture, V. G. Achanta, A. M. Fox, and M. S. Skolnick, Phys. Rev. Lett. **110**, 037402 (2013).

[154] J. E. Kennard, J. P. Hadden, L. Marseglia, I. Aharonovich, S. Castelletto, B. R. Patton, A. Politi, J. C. F. Matthews, A. G. Sinclair, B. C. Gibson, S. Prawer, J. G. Rarity, and J. L. O'Brien, Phys. Rev. Lett. **111**, 213603 (2013).

[155] G. Reithmaier, S. Lichtmannecker, T. Reichert, P. Hasch, K. Muller, M. Bichler, R. Gross, and J. J. Finley, Sci. Rep. **3**, 1901 (2013).

[156] J. Vučković, D. Fattal, C. Santori, G. S. Solomon, and Y. Yamamoto, Applied Physics Letters **82**, 3596–3598 (2003).

[157] G. Calusine, A. Politi, and D. D. Awschalom, Applied Physics Letters **105**, 011123 (2014).

[158] H.-J. Chang, S.-H. Kim, Y.-H. Lee, E. P. Kartalov, and A. Scherer, Opt. Express **18**, 24163–24177 (2010).

[159] R. Bose, D. Sridharan, G. S. Solomon, and E. Waks, Applied Physics Letters **98**, 121109 (2011).

[160] R.-J. Shiue, X. Gan, Y. Gao, L. Li, X. Yao, A. Szep, D. Walker, J. Hone, and D. Englund, Applied Physics Letters **103**, 241109 (2013).

[161] K. Jensen, N. Leefer, A. Jarmola, Y. Dumeige, V. M. Acosta, P. Kehayias, B. Patton, and D. Budker, Phys. Rev. Lett. **112**, 160802 (2014).

[162] X. Gan, K. F. Mak, Y. Gao, Y. You, F. Hatami, J. Hone, T. F. Heinz, and D. Englund, Nano Letters **12**, 5626–5631 (2012).

[163] T. van Leest and J. Caro, Lab Chip **13**, 4358–4365 (2013).

[164] C. Davis. *Lasers and Electro-optics: Fundamentals and Engineering.* Cambridge University Press, (1996).

[165] J. Ye and T. W. Lynn. volume 49 of *Advances In Atomic, Molecular, and Optical Physics*, 1 – 83. Academic Press (2003).

[166] S. Groblacher, J. T. Hill, A. H. Safavi-Naeini, J. Chan, and O. Painter, Applied Physics Letters **103**, 181104 (2013).

[167] C. Manolatou, M. Khan, S. Fan, P. R. Villeneuve, H. Haus, and J. Joannopoulos, Quantum Electronics, IEEE Journal of **35**, 1322–1331 (1999).

[168] www.Lumerical.com.

[169] A. Faraon, E. Waks, D. Englund, I. Fushman, and J. Vučković, Applied Physics Letters **90**, 073102 (2007).

[170] S. L. Portalupi, M. Galli, C. Reardon, T. Krauss, L. O'Faolain, L. C. Andreani, and D. Gerace, Opt. Express **18**, 16064–16073 (2010).

[171] W. E. Moerner and D. P. Fromm, Review of Scientific Instruments **74**, 3597–3619 (2003).

[172] R. Oulton, B. D. Jones, S. Lam, A. R. A. Chalcraft, D. Szymanski, D. O'Brien, T. F. Krauss, D. Sanvitto, A. M. Fox, D. M. Whittaker,

M. Hopkinson, and M. S. Skolnick, Opt. Express **15**, 17221–17230 (2007).

[173] M. Bass, E. W. Van Stryland, and D. R. Williams. *Handbook of optics. vol. 2 vol. 2*. McGraw-Hill, New York, (1995).

[174] M. W. McCutcheon, G. W. Rieger, I. W. Cheung, J. F. Young, D. Dalacu, S. Frdrick, P. J. Poole, G. C. Aers, and R. L. Williams, Applied Physics Letters **87**, 221110 (2005).

[175] B. J. M. Hausmann, T. M. Babinec, J. T. Choy, J. S. Hodges, S. Hong, I. Bulu, A. Yacoby, M. D. Lukin, and M. Lončar, New Journal of Physics **13**, 045004 (2011).

[176] D. Rumsfeld.

[177] A. Einstein.

[178] V. e. a. Bratus, Materials Science Forum **740-742**, 417 (2013).

[179] http://ntrs.nasa.gov/archive/nasa/casi.ntrs.nasa.gov/19940009554.pdf.